uOttawa

Adsorption Separation of CO_2 in Low Concentrations for Applications in Direct Air Capture and Excimer Gas Separation

By

Sean Wilson

Submitted to the School of Graduate Studies and Research

in partial fulfillment of requirements

for degree of Ph.D. in Chemical Engineering

Department of Chemical and Biological Engineering, Faculty of Engineering

University of Ottawa, Ottawa, Canada

Abstract

Adsorption Separation of CO_2 in Low Concentrations for Applications in Direct Air Capture and Excimer Gas Separation

The overall objective of this thesis is to evaluate the fundamentals of current low concentration CO_2 separation technologies and to provide an alternate method using adsorption technology with existing as well as new adsorbents. Two different applications for the adsorption of CO_2 are explored; Direct Air Capture (DAC) and excimer gas purification. The investigation of aerogels as possible adsorbent for these applications was also explored.

The first application, DAC of CO_2 using adsorbents, addresses climate change by reducing the amount of atmospheric CO_2 levels that are directly correlated to global warming. Because of DAC being carbon negative, this field has gained significant attention in the literature. DAC as a CO_2 reduction strategy was approached in two ways:

1. Chapter 2 investigates capturing and concentrating CO_2 from 0.04% in the air to 95% to be able to sequester it into the ground. This research began by doing an adsorbent selection using pure gas gravimetric measurements on seven different commercially available type X zeolites that were determined to have potential for this separation. Breakthrough experiments were then carried out with the most promising zeolite by perturbing the bed with compressed ambient air. In the process studied, a basic four step temperature vacuum swing adsorption (TVSA) cycle was investigated comprising the following steps: pressurization, adsorption, blowdown, and desorption. Four different regeneration temperatures were tested along with four different gas space velocities. With this cycle configuration, CO_2 was concentrated to 95% from 0.04% with total capture fractions as high as 81%. This study highlighted methods to reduce the energy consumption per ton of CO_2 captured in the system as well as the potential of using low Si/Al ratio faujasite structured zeolites in DAC of CO_2 for greenhouse gas reduction.
2. Chapter 3 expands on the research of Chapter 2 by capturing CO_2 from 0.04% in the air and concentrating it to high purity CO_2 levels where the cost for operating the process will be reimbursed through the value of the produced CO_2. The goal of this research was to increase the CO_2 to as high as possible because the purer the CO_2, the more valuable it is. This research started by conducting an in-depth investigation into the pure gas adsorption of CO_2, N_2, O_2, and Ar on the most promising zeolite from Chapter 2. The data was then fitted to the TD-Toth model which allowed for the evaluation of the TVSA cycle and showed the potential of reducing the pressure and/or elevating the temperature during the blowdown step in order to produce high purity CO_2. To confirm this, the TVSA cycle was run on a fixed bed breakthrough experiment where high purity CO_2 was produced between a concentration of 99.5% and 99.96% by lowering the blowdown pressure. By controlling the blowdown temperature, the concentration of the product was increased from 99.8% to 99.95%, however with a

significant loss of CO_2. This effect of N_2, O_2, and Ar desorbing during the blowdown step with CO_2 desorbing during the evacuation step is shown graphically by measuring the concentration and flow rate of the exiting gas species. The results from this study show the potential for producing a valuable product of high purity CO_2 from atmospheric concentrations.

The second application in this thesis that is explored in Chapter 4 is the purification of trace impurities of CO_2, CF_4, COF_2, and O_2 from F_2, Kr, and Ne for applications in excimer lasers. Due to the incompatibility of many adsorbents to F_2 and HF, aluminas and polymeric adsorbents were selected as potentially compatible materials. To increase the compatibility of these adsorbents, the use of a cryo-cooler was determined to be feasible to precool the feed stream before separation, which increases the adsorption capacity and compatibility of the material to F_2 and HF. To determine the adsorption potential in the low concentration of these adsorbents, the concentration pulse chromatographic technique was chosen to determine the Henry's Law constants of CO_2, CF_4, and O_2. This data was then plotted on the van't Hoff plot and extrapolated to colder temperatures to determine the benefit of using a cryo-cooler. From this study, it was determined that HayeSep Q was the best polymeric adsorbent with significant adsorption of CO_2 at temperatures below -50°C while being the best performing CF_4 adsorbent. AA-300 was the best performing alumina in this study while having significant adsorption of CF_4 at temperatures below -135°C. However, from a compatibility standpoint, both of these materials need to be tested to determine their robustness in the presence of F_2 and HF at room and reduced temperatures.

Chapters 5 & 6 in this thesis explore the fundamentals of adsorption on aerogels as a prelude to using aerogels as possible adsorbents for DAC of CO_2. This investigation into aerogels looks at silica aerogels and carbon aerogels, which are both industrially produced and explores their adsorption with relation to like materials such as silica gel and activated carbons. Both of these Chapters utilize experimentally determined adsorption isotherms of CO_2, N_2, O_2, and Ar as well as characterization to determine adsorption trends in the materials. Some major conclusions for silica aerogels were that common surface modifications to make the material more resilient against water adsorption impacts the adsorption of CO_2 significantly with roughly 4 fold difference in adsorption capacity. For carbon aerogels some major conclusions were that the adsorption was increasingly dominated by the heterogeneous nature of the surface at lower pressures and increasingly dominated by the pore size at the higher pressures. Both chapters discuss the adsorption of air along with ideas such as the influence of gas thermal conductivity in the pores with respects to adsorption.

Resume

La séparation par adsorption du CO_2 à faible concentration pour des applications pour la capture directe dans l'air et la séparation des gaz excimères

L'objectif général de cette thèse est d'évaluer les principes fondamentaux des technologies actuelles de séparation du CO_2 à faible concentration et de fournir une méthode alternative utilisant la technologie d'adsorption avec des adsorbants actuels ainsi que d'en découvrir de nouveaux. Deux applications différentes pour l'adsorption du CO_2 ont été explorées; la capture directe dans l'air ambient (CAD) et la purification des gaz excimères, ainsi que la recherche d'aérogels comme adsorbant possible pour ces applications.

La première application, le CAD du CO_2 utilisant des adsorbants, pourrait répondre aux changements climatiques puisque les niveaux de CO_2 atmosphérique sont directement corrélés au réchauffement climatique. Dernièrement, le CAD a fait l'objet d'une attention particulière en tant que stratégie de réduction du CO_2, par conséquent, deux voies différentes ont été explorées dans cette thèse:

1. Le chapitre 2 étudie la capture et la concentration du CO_2 de 0,04% dans l'air à 95% afin de pouvoir l'enfermer dans la terre. Pour ce faire, une sélection d'adsorbant a été effectué en utilisant des mesures gravimétriques à gaz pur sur sept zéolithes de type X disponibles dans le commerce qui ont été déterminés comme ayant un potentiel pour cette séparation. Des expériences révolutionnaires ont ensuite été réalisées avec la zéolite la plus prometteuse en perturbant le lit avec de l'air ambiant comprimé. Dans le processus étudié, un cycle basique à quatre étapes d'adsorption modulée en température et pression (AMTP) a été étudié, comprenant les étapes suivantes: pressurisation, adsorption, purge et désorption. Quatre températures de régénération différentes ont été testées ainsi que quatre vitesses spatiales de gaz différents. Avec cette configuration de cycle, le CO_2 était concentré à 95% de 0,04% avec des fractions de capture totales aussi élevées que 81%. Cette étude a mis en évidence des méthodes pour réduire la consommation d'énergie par tonne de CO_2 captée dans le système ainsi que le potentiel d'utilisation de zéolithes structurées à base de faujasite à faible rapport Si/Al dans le CAD du CO_2 pour la réduction des gaz à effet de serre.
2. Le chapitre 3 approfondit les recherches du chapitre 2 en capturant le CO_2 de 0,04% dans l'air et en le concentrant à des niveaux de très haute pureté où le processus sera remboursé par la valeur du CO_2 produit. L'objectif de cette partie était d'augmenter la pureté du CO_2 le plus possible car plus le CO_2 est pur, plus il est précieux. Une enquête approfondie sur l'adsorption de gaz pur de CO_2, N_2, O_2 et Ar sur la zéolite la plus prometteuse du chapitre 2. Les données ont ensuite été ajustées au modèle TD-Toth qui a permis d'évaluer le cycle AMTP et a montré le potentiel de réduire la pression et/ou d'élever la température pendant l'étape de purge afin de produire du CO_2 de haute pureté. Pour confirmer cela, le cycle AMTP a été fait par le biais d'une expérience dans un lit fixe où du CO_2 de haute pureté a été produit entre une concentration de 99,5% et 99,96% en abaissant la pression de purge. En contrôlant la température de purge, la concentration du produit est passée de 99,8% à 99,95%, mais avec une

perte importante de CO_2. Cet effet de la désorption de N_2, O_2 et Ar pendant l'étape de purge avec la désorption du CO_2 pendant l'étape d'évacuation est illustré graphiquement en mesurant la concentration et le débit des espèces de gaz sortant. Les résultats de cette étude montrent le potentiel de production d'un produit précieux de CO_2 de haute pureté à partir des concentrations atmosphériques.

La deuxième application de cette thèse qui est explorée au Chapitre 4 est la purification des traces d'impuretés de CO_2, CF_4, COF_2 et O_2 de F_2, Kr et Ne pour des applications dans les lasers à excimère. En raison de l'incompatibilité de nombreux adsorbants avec le F_2 et le HF, les alumines et les adsorbants polymères ont été sélectionnés comme matériaux potentiellement compatibles. Pour augmenter la compatibilité de ces adsorbants, l'utilisation d'un cryoréfrigérant a été jugée possible pour pré-refroidir le flux d'alimentation avant la séparation, ce qui augmente la capacité d'adsorption et la compatibilité du matériau en F_2 et HF. Pour déterminer le potentiel d'adsorption dans la faible concentration de ces adsorbants, la technique de chromatographie pulsée de concentration a été choisie pour déterminer les constantes de la loi de Henry de CO_2, CF_4 et O_2. Ces données ont ensuite été tracées sur le graphique van't Hoff et extrapolées à des températures plus froides pour déterminer les avantages de l'utilisation d'un cryoréfrigérant. À partir de cette étude, il a été déterminé que HayeSep Q était le meilleur adsorbant polymère avec une adsorption significative de CO_2 à des températures inférieures à -50 ° C tout en étant l'adsorbant CF_4 le plus performant. L'AA-300 était l'alumine la plus performante de cette étude tout en ayant une adsorption significative de CF_4 à des températures inférieures à -135 °C. Cependant, du point de vue de la compatibilité, ces deux matériaux doivent être testés pour déterminer leur robustesse en présence de F_2 et de HF à température ambiante et réduite.

Les chapitres 5 et 6 explorent les principes fondamentaux de l'adsorption sur les aérogels en prélude à l'utilisation d'aérogels comme adsorbants possibles pour le CAD du CO_2. Cette enquête sur les aérogels examine les aérogels de silice et les aérogels de carbone, qui sont tous les deux fabriqués industriellement et explore leur adsorption par rapport à des matériaux similaires tels que le gel de silice et les charbons actifs. Ces deux chapitres utilisent des isothermes d'adsorption déterminés expérimentalement de CO_2, N_2, O_2 et Ar ainsi que la caractérisation pour déterminer les tendances d'adsorption dans les matériaux. Certaines conclusions majeures pour les aérogels de silice étaient que les modifications de surface courantes pour rendre le matériau plus résistant à l'adsorption d'eau ont un impact significatif sur l'adsorption de CO_2 avec une différence d'environ 4 fois dans la capacité d'adsorption. Pour les aérogels de carbone, certaines conclusions majeures étaient que l'adsorption était de plus en plus dominée par la nature hétérogène de la surface à des pressions plus faibles et de plus en plus dominée par la taille des pores aux pressions plus élevées. Les deux chapitres discutent de l'adsorption d'air ainsi que des idées telles que l'influence de la conductivité thermique du gaz dans les pores en ce qui concerne l'adsorption.

Dedication

I wish to dedicate this thesis to my parents Deborah and Timothy Wilson for whom I would not have been dealt such a loving hand in life. Ever since I was young, they have been supporting and nurturing my sense of creativity, allowing me to come up with my own ideas and reasoning for the world that is around me which has given me a passion for learning and pushing the frontier of knowledge. They have also been supporting during my doctorate with my parents being there during the struggles of null hypotheses allowing themselves to be sound boards to the coming up ideas on the fly. I know for my parents that me taking on the mantle of being a chemical engineer is enough for them but I would still like to say "Thank-you", I will always treasure your unconditional love towards me.

Acknowledgements

Even though this thesis is the end result of four years, the journey along the way has been astounding and I have developed many relationships, working and personal. These relationships made up my day to day experience and I would like to acknowledge their importance. Firstly, I would like to thank Vida Gabriel, who was an amazing partner to me personally and academically. Personally, she has helped me stay healthy by being active and laughing together while making the most delicious donuts and other nourishments. Academically, she is an intelligent ruthless debater, offering me her time and knowledge, particularly in characterization, which has helped me produce this work.

I would also like to thank my academic supervisor Dr. F. Handan Tezel, whom gave me freedom to explore my own ideas and thoughts throughout these past 4 years. When I approached her before my enrolment, I proposed that I do a doctorate on a few ideas that I had for DAC of CO_2. Those ideas blossomed into this PhD thesis. And for that, I would like to say thank-you. I would also like to acknowledge the hard work on her part required to editing all the chapters of this thesis as the sole supervisor.

I am incredibly thankful for the many friends that I have from the University of Ottawa and in the Ottawa region over the last 4 years. These includes childhood friends Patrick, Dan, and Phil and high school friends Kyle and Michael who have seen me evolve with time and are always gems to hang out with. For my University of Ottawa friends, I wish to one day work in an environment with humans as wonderful as you. I would like to especially thank David Carter, Charbel Atallah, Fahad Chowdhury, and Dean Kennedy whose crosswording, complaining, smashing, company, fishing, gymnasticing, drinking, idea bouncing, and camaraderie have really made my time here special.

Collaboration

I hereby declare that all ideas in this thesis are my own. This thesis is a collection of my works and I am the sole author of this thesis. I defined the problem and procedures, executed all experiments and analyses unless otherwise stated. During my thesis, my supervisor Dr. F. Handan Tezel held meetings once every two weeks, and provided the editorial comments of this thesis. Other than this, I have acknowledged other sources of information and assistance in data collection and analyses where applicable.

For Chapter 5, Vida A. Gabriel did the ^{29}Si solid-state nuclear magnetic resonance (NMR) characterization of the three silica samples along with the analysis of the NMR data. She also wrote the accompanying section of the NMR data. Vida A. Gabriel also helped with the collection of the Fourier-Transform Infrared Spectroscopy (FTIR) data for this Chapter.

For Chapter 6, Vida A. Gabriel collected the FTIR characterization data for the eight carbon samples along with analysing the data. She also wrote the majority of the accompanying section. Fatma Al-Enzi ran the gravimetric experiments and collected the isotherm data for the eight carbon samples for four gases and five temperatures.

Table of Contents

Table of Figures

Table of Tables

Hypotheses and Thesis Structure

The overall goal of this thesis is to apply existing adsorbents for the removal of CO_2 in low concentration applications as well as to discover new ones. This research will particularly look into two different applications for the adsorption purification of CO_2; DAC of CO_2 and excimer gas purification, and will investigate aerogels as a possible adsorbent for these applications.

Hypotheses

1. It is hypothesized that adsorbents such as low Si/Al ratio faujasite structured zeolite or other adsorbents can be used for DAC of CO_2 and offer many benefits over the alternative research in that field due to the fast uptake rate, proven stability and reliability of adsorbents. By conducting adsorption experiments on these adsorbents, the potential for DAC can be analysed for applications in greenhouse gas reduction as well as for the production of high purity CO_2.
2. It is hypothesized that silica aerogel or carbon aerogel could be potential adsorbents and by extension of that, for applications in either DAC of CO_2 or for purification of excimer gases. This hypothesis can be tested by conducting isotherms of CO_2 as well as N_2, O_2, and Ar as well as doing characterization of the aerogels. This will give insights into the adsorption potential of aerogels as adsorbents for these two applications.
3. It is hypothesized that adsorbents could be used potentially to reduce the amount of impurities within excimer gas, in particular CO_2, which is present within the laser as a bi-product of fluorine reactions. This is going to be tested by GC concentration pulse chromatography to determine Henry's Law constants for the potential of a variety of different adsorbents.

Thesis Structure

This paper based thesis consists of 7 chapters. Chapter 1 is the Introduction which discusses adsorption, DAC of CO_2, excimer gas purification, and aerogels in-depth while reviewing the literature in the field. Chapters 2 to 6 each represents an individual article published in or prepared for submission to a peer-reviewed academic journal. In this thesis, repetition of some ideas and elements was inevitable, such as materials and methods. This thesis ends with Chapter 7 which provides an overview, conclusions, and recommendations for future work that pertains to the entirety of this thesis. At the end of each chapter contains their own separate abbreviations, nomenclature, and bibliographies.

Chapter 2

Direct Dry Air Capture of CO_2 using VTSA with Faujasite Zeolites

The capture and concentration of CO_2 from a dry ambient air stream by temperature vacuum swing adsorption (TVSA) has been experimentally demonstrated in a small scale by using a single bed system packed with 20 g of zeolite X. 7 different commercially available type X zeolites were investigated and one of them was chosen for a more comprehensive study. Breakthrough experiments were carried out by

perturbing the He saturated bed with compressed ambient air with CO_2 of around 410 to 440 ppm. In the process studied, a basic four step TVSA cycle comprising the following steps: pressurization with feed, adsorption, blowdown, and desorption was investigated first. Four different regeneration temperatures were tested along with four different gas space velocities. With this cycle configuration, CO_2 was concentrated to 95% from 400 ppm with total capture fractions as high as 81%. The energy consumption per ton of CO_2 captured in the system are discussed for the different process configuration. The results from this study are discussed on how to improve the possibility of using low Si/Al ratio faujasite structured zeolites in direct air capture of CO_2.

Chapter 3
High Purity CO_2 from Direct Air Capture using a Single Cycle TVSA with Na-X Zeolites

The capture and concentration of 0.04% CO_2 from a dry ambient air stream by temperature vacuum swing adsorption (TVSA) was investigated in order to produce high purity CO_2. Initial investigation into the pure gas adsorption of CO_2, N_2, O_2 and Ar was measured and these results were used to model the temperature dependant Toth equation. This model allowed for the evaluation of the TVSA cycle and showed the potential of reducing the pressure and/or elevating the temperature during the blowdown step in order to produce high purity CO_2. A fixed bed adsorption desorption breakthrough curves to model the TVSA cycle to investigate the pressure and temperature effects on the blowdown step. From the experimental results, high purity CO_2 was produced between a concentration of 99.5% and 99.96% by lowering the blowdown pressure. By controlling the blowdown temperature, the concentration of the product was increased from 99.8% to 99.95%, however with a significant loss of CO_2. This effect of N_2, O_2, and Ar desorbing during the blowdown step with CO_2 desorbing during the evacuation step is shown graphically by measuring the concentration and flow rate of the exiting gas species. The results from this study show the potential for producing a valuable product of high purity CO_2 from atmospheric concentrations, which can be used in many applications, particularly ones where CO_2 infrastructure does not exist or where there is a burden in utilizing a CO_2 cylinder.

Chapter 4
Adsorption Separation of CF_4, O_2, CO_2, and COF_2 from an Excimer Gas Mixture

The use of adsorbents is explored as an option for the removal of trace impurities of CO_2, CF_4, COF_2, and O_2 from F_2, Kr, and Ne for applications in excimer lasers. Due to the incompatibility of many adsorbents to F_2 and HF, aluminas and polymeric adsorbents were selected as potentially compatible materials. To determine the adsorption potential of these adsorbents in the low concentration region, the concentration pulse chromatographic technique was chosen to determine the Henry's Law constants of CO_2, CF_4, and O_2 gases on three polymeric adsorbents (HayeSep Q, HayeSep B, and Fluorinated DVB) and two aluminas

(AA-300, and Alumina A). The results were plotted and compared on van't Hoff plots with the heat of adsorption values being calculated from the lines of best fit for all gases and adsorbents tested in this study. Due to the large energies required to operate the excimer lasers, a cryo-cooler was determined to be feasible to precool the feed stream before separation, which increases the adsorption capacity and the compatibility of the adsorbents to F_2 and HF. The van't Hoff plots were extrapolated to colder temperatures to determine the Henry's Law constants to analyze the potential of using the cryo-cooler. From this study, it was determined that HayeSep Q was the best polymeric adsorbent with significant adsorption of CO_2 at temperatures below -50°C while being the best performing CF_4 adsorbent. AA-300 was the best performing alumina in this study while having significant adsorption of CF_4 at temperatures below -135°C. However, from a compatibility standpoint, both of these materials need to be tested to determine their robustness in the presence of F_2 and HF at room and reduced temperatures.

Chapter 5
Adsorption of Components from Air on Silica Aerogels

Aerogels are porous media that have large internal surface areas causing them to have significant gas adsorption. The adsorption isotherms of carbon dioxide, nitrogen, oxygen, and argon with a tetramethoxysilane (TMOS) silica aerogel, a [trimethylsilyl]oxy (TMS)-modified silica aerogel, and a silica gel were measured in the pressure range of 0 to 6.5 atm at 10°C, 30°C, 50°C, 70°C, and 90°C. These isotherms were fitted to Langmuir, Freundlich, Sips, and Toth isotherms, as well as the temperature dependent Toth model and their cumulative adsorption of the components of air were discussed. Isosteric heats of adsorption were quantified. With this data, we can see the impact of the surface groups on adsorption as well as the pore size, with a significant increase in the quantity and strength of adsorption of CO_2 reported between silanol and TMS groups. The relationship between adsorption capacity and the thermal properties of silica aerogels were also discussed in this study.

Chapter 6
Effect of Pore Size and Heterogeneous Surface on the Adsorption of CO_2, N_2, O_2, and Ar on Carbon Aerogel, RF Aerogel, and Activated Carbons

Aerogels are porous super materials that have many desirable properties including high surface areas which cause them to have significant gas adsorption. In this study, carbon aerogel and resorcinol-formaldehyde (RF) aerogel are compared with six commercial activated carbons (Derived from wood, coconut shells, polymers, and bituminous coal). This study investigates many intrinsic properties of these carbons including surface area, pore size, presence and type of surface groups, as well as ash content and determines their influence on the adsorption of CO_2, N_2, O_2, and Ar using pure gas adsorption isotherms. This study noted that there was no trend for ash content but a strong correlation existed between the

adsorption capacity and the pore size in the higher pressure region according to Dubinin's micropore volume filling theory. In the lower pressure range, the heterogeneous nature of the surface dominates the adsorption particularly for CO_2 which has the strongest polarizability and quadrupole moment of the probe molecules investigated. The two aerogel samples were then further investigated by determining their adsorption in the presence of air using the temperature dependant Toth model with N_2 and O_2 being adsorbed significantly more than CO_2 and Ar at ambient conditions.

Chapter 1

Introduction

1.1 Preamble

In industry, adsorption processes are widely used due to their abilities to perform separations that are impossible, impractical, or uneconomical by conventional separation techniques such as distillation, membranes, and absorption. This is due to the advantage of adsorption which can be optimized to operate at ambient system conditions, therefore leading to less intensive process for the separation. As environmental constraints increase over time, stricter quality standards are needed. Adsorption will be investigated as a possible solution to many new separation problems. In order to determine which adsorbent could be used to solve a problem, many commercially available adsorbents can be investigated, and in most cases, these adsorbents perform reasonably for the separation. However, new adsorbents are continuously being developed that have higher surface areas, faster diffusions, larger capacities, and better properties which translates into improved performance for the targeted separation.

Adsorption is a surface phenomenon where the surface of the adsorbent interacts with the fluid which can be a liquid or a gas. Separation in adsorption occurs when one component of the fluid stream is more affinitive to the adsorbent surface than the others, leading to one component being preferentially adsorbed. Since this is a surface phenomenon, the larger the surface area, the more adsorption happens. Therefore commercially available adsorbents have large surface areas in the hundreds of meters squared per gram of adsorbent. It is a common indication that if a material has high surface area that was measured using the Brunauer-Emmett-Tellor (BET) method, the possibility of it being applicable as an adsorbent is good.

Adsorption falls underneath two main types: bulk separation and purification. Bulk separation is defined as the adsorption of a large concentration of the total stream (above 10 wt%) [1]. Some industrial applications of bulk separation using adsorbents include normal paraffins from iso-paraffins, N_2 from O_2, refinery hydrogen generation, and H_2O from ethanol. Purification in adsorption, the subject of this thesis, is defined as separating less than 2 wt% of the adsorbed component [1]. Due to the nature of adsorbents being in fixed beds, adsorption is ideally suited for application in purification and has many different uses in industry. Adsorbents that are useful for purification processes have high Henry's Law constants which allow for adsorption of the adsorbate at very low concentrations as the gas proceeds down the column, purifying the stream of that adsorbate.

The required shape of the isotherm for a purification compared to a bulk separation can be seen in Figure 1.1. For the bulk adsorption of CO_2 from processes such as biogas upgrading, syngas processing, and flue gas treatment, the desired isotherm shape is less rectangular than that for purification of CO_2 in applications of CO_2 removal in confined spaces and direct air capture. This is because there is an optimal interaction between the adsorbent and the adsorbate.

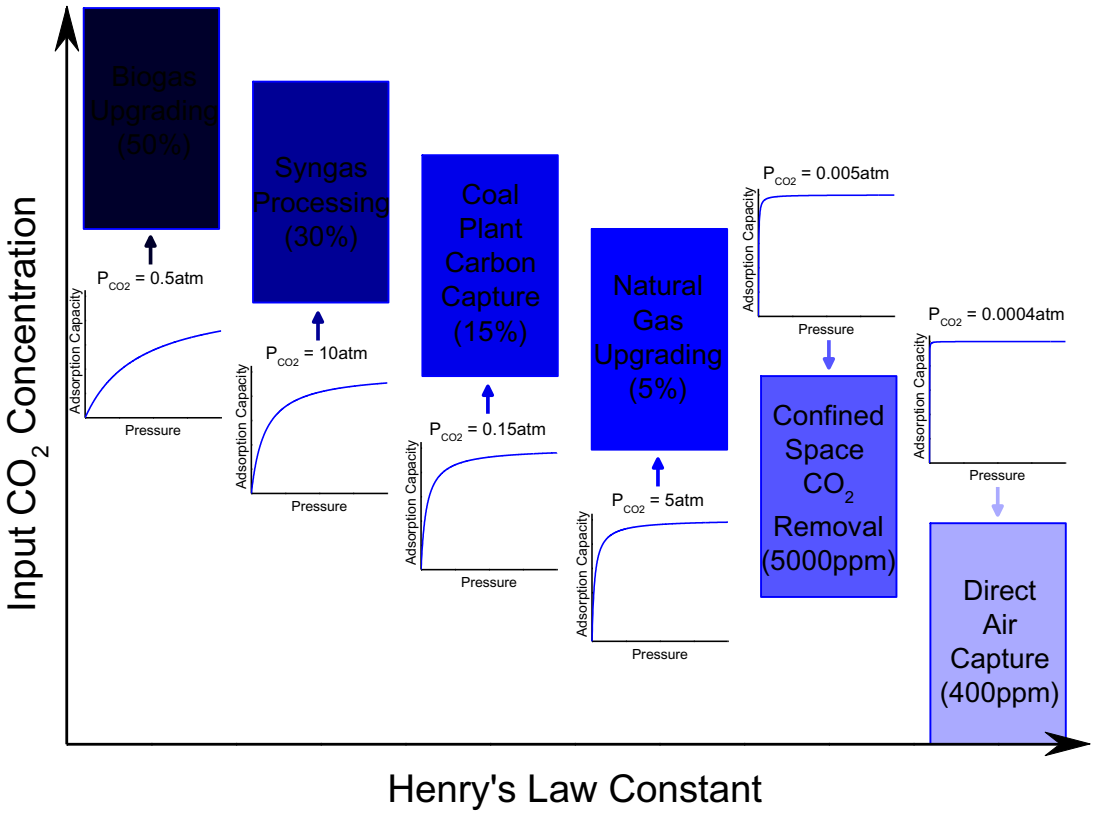

Figure 1.1 – Desired adsorption isotherm shape for adsorption of CO_2 from different applications adapted from Belmabkhout et al (2016) [2].

This thesis will be looking into the adsorption of CO_2 within the purification range for two different applications: Direct Air Capture (DAC) of CO_2 for greenhouse gas mitigation as well as for the production of high purity CO_2; and the purification of excimer gas from low levels of CO_2.

Adsorbents have been used by industry for the adsorption purification of CO_2 in applications including landfill and natural gas treatment, purifying hydrocarbons, air prepurification, and hydrogen gas production [3]. These applications all require CO_2 to be brought down to ppm levels. On the contrary, the two applications in this thesis rconsider the adsorption of CO_2 in the ppm range as the feed into the process, with DAC requiring the capture of low concentration of CO_2 from the air, and excimer gas requiring the scrubbing of CO_2 from the rest of the gas mixture at low concentrations.

1.2 Direct Air Capture (DAC)

Increasing levels of CO_2 in the atmosphere has been shown to correlate to the increasing average global surface temperature (Figure 1.2) which has led many researchers to invest time and effort into finding ways to effectively reduce the amount of CO_2 entering the environment or to capture CO_2 directly from the air. The latter, the subject of this study, has been dubbed DAC from pioneering research done by Lackner et al. in 1999, and looks into capturing CO_2 directly from the air in concentrations around 400 ppm and

concentrating it as a means to reduce global warming [4]. Thanks to that study, this field has significantly gained interest as a true carbon negative strategy to reduce the amount of CO_2 in the atmosphere [5–7]. DAC, although thermodynamically less favourable than capturing CO_2 from large stationary post combustion point sources [8,9], has some important benefits. The three main benefits of CO_2 capture from air over conventional carbon capture is:

- CO_2 emissions from any sector, including automobiles, small CO_2 point sources, and airplanes, can be captured in a separate location from the emission source. It would otherwise be impractical to capture the CO_2 directly from these sources.
- A commercial plant for direct CO_2 capture from atmospheric air can be made any size and put in any location due to it not being an addition to a power plant. This allows for scales of economy for the size of the plant to be taken into consideration which would allow governments to put a fixed price on carbon.
- CO_2 from past emissions can also be captured.

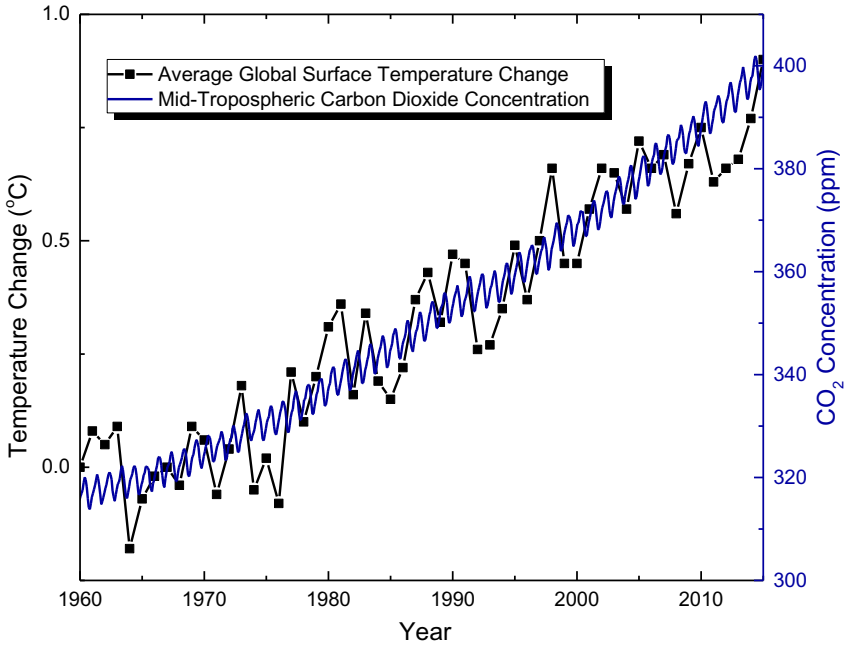

Figure 1.2 – Correlation between the average global surface temperature change and the concentration of carbon dioxide measured at the mid-tropospheric. This NOAA ESRL data was freely provided by NASA.

This however, comes at the price of having to put in additional energy to remove the CO_2 from a more dilute source in order to concentrate it up to the desired purity than Post Combustion Capture (PCC) if all other conditions are similar [10–12]. Studies have shown that using methods such as the Reverse Water Gas Shift reaction in tandem with Fischer-Tropsch process, could allow DAC of CO_2 to be used to generate hydrocarbon fuels instead of traditional sources, which would allow for the continuing use of the transportation infrastructure well into the future [13–15].

The DAC of CO_2 at around 400 ppm is less thermodynamically favourable than coal fired PCC at 10 – 15% CO_2, or natural gas carbon capture (NGCC) at 5 – 8% CO_2. This is because the more disordered systems require more energy to concentrate it. This can be derived from the second law of thermodynamics and is shown in Equation 1 as the minimum energy required to separate the CO_2 at a particular concentration and concentrate it to pure CO_2 (W_{min}). The derivation of this equation can be seen in works from American Physical Society (APS) [11].

$$W_{min} = -\frac{RT}{yM_{CO2}}(y \ln y + (1-y)\ln(1-y)) \quad (1)$$

Where R is the gas constant, M_{CO2} is the molar mass of carbon dioxide, and y is the initial concentration of CO_2. This difference in minimum work required to separate the CO_2 from DAC, NGCC, and PCC is shown in Figure 1.3. Even though the minimum energy required to separate out the CO_2 from air is 2 to 3 times that of PCC and NGCC, that difference in energy is no more than 1-2 US$/ton$CO_2$ [8].

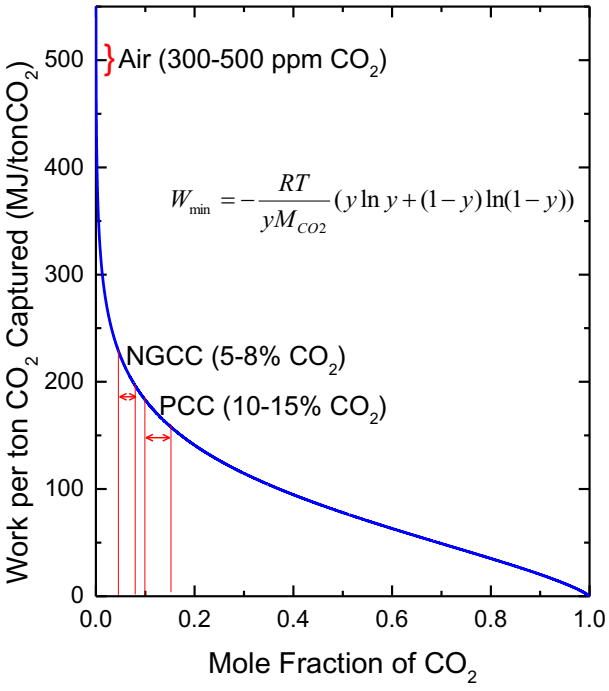

Figure 1.3 – Minimum work required to separate all of the CO_2 at a particular concentration and concentrate it up to 100%.

With DAC gaining scientific interest, the scientific challenge of implementation is finding a low cost sorbent that has high uptakes, selective for CO_2, and fast kinetics, with strong physical and chemical stabilities, whose regeneration is not overly energy intensive. Research efforts into finding a promising sorbent can fall under four main categories: amine based sorbents [16–24], zeolites [18,19], absorption using caustic solutions [6,25–33], and metal organic frameworks (MOFs) [18,34–36]. Researchers first investigated using absorption systems such as sodium hydroxide solutions to absorb CO_2 [6,25] but since then amines bound onto solid supports have gained significant traction in the scientific community as the solution to DAC [16,37–39]. This transition of

thinking occurred due to the energy intensive nature of pumping a dilute source of CO_2, where solid sorbents provided significantly lower pressure drops and therefore lower pumping costs. Continuing with this logic, adsorbents and in particular zeolites, could be potential materials for the DAC of CO_2 with many such materials known for having very fast CO_2 adsorption kinetics and therefore require shorter beds and less energy to pump gas through the beds.

Zeolites in literature have yet to be thoroughly investigated for DAC due to their hydrophilic nature. This is because the tolerance of zeolites, a hydrophilic material, to water is poor and will decrease the overall adsorption capacity of CO_2 in the presence of H_2O because of competitive adsorption [18,19,36,37]. A guard bed using a desiccant however, can be placed before the zeolite bed which would solve the problem by removing H_2O from the air stream before it contacts the zeolite [1]. Zeolites have many benefits for DAC that should not be overlooked and should be given an appropriate investigation before being dismissed. Zeolites, unlike amine based sorbents and MOFs for DAC of CO_2, are commercially available, are very well studied, and proven in industry due to their physical and chemical stabilities for many different situations. This, coupled with faujasite structured zeolites being known to have very high capacities, favourable selectivities, and strong adsorption of CO_2, has made them excellent candidates for similar separations to DAC such as PCC projects [40–43]. It is also important to note that Na-X has been used and proven in industry for capturing CO_2 from air since the early 1980's in air prepurification processes in order to reduce CO_2 to less than the ppm level [44,45]. Another benefit that faujasite structured zeolites have, when compared to other promising technologies, is very fast uptake rates, allowing for beds to be optimized to have lower overall pressure drops. This is important because air compression can cost $22 per kPa increase per ton of CO_2 captured which can make up the majority of the cost for DAC for the technology [19].

In this present thesis, we look at investigating zeolites' potential for the DAC of CO_2 while outlining clear positives and negatives of such a system. This will be done by using pure gas adsorption analysis along with breakthrough experimentation in order to determine optimal adsorption and desorption conditions for a Temperature Vacuum Swing Adsorption (TVSA) system. This work was inspired by previous literature from Ralph T. Yang's student who investigated Li-LSX, K-LSX, and amine-grafted SBA-15, and was able to increase the concentration of CO_2 in dry air using TVSA from 0.0395% to 93%, 94%, and 98%, respectively, for these three different sorbents [19]. Another inspiration for this research is the constant reliability that zeolite 13X has for DAC of CO_2 which, after many runs shows its robustness for being implemented in such a technology [18].

1.2.1 Adsorption of CO_2 for DAC

Activated carbons, zeolites, silica gels, and activated aluminas have dominated the adsorption commercial market [1] and therefore, are readily available and relatively cheap to acquire. This makes them more attractive for use in DAC then alternatives which would need to be produced in-house. There are many like processes to DAC that remove CO_2 in low concentrations. Air prepurification, used as a means to remove

CO_2 and water to below the ppm level before cryogenic distillation in air separation plants, uses adsorbents. A survey of air prepurification literature shows that the most common adsorbents are γ-alumina and low Si/Al faujasite structured zeolites used in pressure swing adsorption (PSA) or temperature swing adsorption (TSA) for this separation [44–48]. Na-Y has also been patented as an alternative for low Si/Al faujasite zeolite due to lower blowdown energies during regeneration [49–52].

The adsorption of CO_2 at 30°C is shown in Figure 1.4 for activated carbons, zeolites, silica gels, and activated aluminas. Due to the nature of DAC being a purification process, the adsorption of CO_2 by the adsorbent is desired to have a high Henry's Law constant. This Henry's Law constant can be seen by the shape of the isotherm with more rectangular isotherms indicating a larger Henry's Law constant. In Figure 1.4, the adsorption of CO_2 is the strongest with zeolites and activated aluminas in comparison to activated carbons and silica gels. This strength of adsorption for CO_2 is why zeolites and activated aluminas are used in air prepurification and not activated carbons or silica gels.

For zeolites, different structures, Si/Al ratios, and cations that are present affect the adsorption of CO_2. There are 248 currently identified different structures of zeolites and the International Zeolite Association has a very well done data base showing the structure of each one of them. Out of these structures, faujasite and Linde Type A have seen applications in low concentration CO_2 removal due to their high Henry's Law constants. Faujasite structured zeolites are denoted as "X" or "Y" zeolites with the difference between them being the Si/Al ratio with "X" encompassing Si/Al ratios below 2, and "Y" has more than 2. For "X" zeolites that are approximately a 1/1 ratio of Si/Al are denoted as Low Silica X (LSX) is common. In Figure 1.4, faujasite structured zeolites are Ca-X, APG-III, Nitroxy 5, Nitroxy SXSDM, Na-LSX, Na-Y, and H-Y. Linde Type A zeolites are denoted as "A" and in Figure 1.4 are labelled as 5A and 4A. For "A" zeolites, the number that precedes the designation indicates the approximate pore size with 5A having a pore size around 5Å, and 4A having a pore size around 4Å [53]. A useful in-depth review by Bonenfant et al. describes the effect that cations and Si/Al ratio within the zeolite have on the adsorption of CO_2 [54] and explains the CO_2 adsorption behaviour seen in Figure 1.4 for the zeolite samples.

For aluminas, different structures of the Al_2O_3 framework and pH level affect the adsorption of CO_2. There are two different structures of alumina's investigated for adsorption; γ-alumina and a-alumina which are calcinated at 400-600 °C and 1050-1100 °C with surface areas of 266 m^2/g and 5 m^2/g, respectively. γ-alumina's which have higher surface areas than a-alumina's, are marked as activated alumina and are the aluminas of interest for CO_2 adsorption.

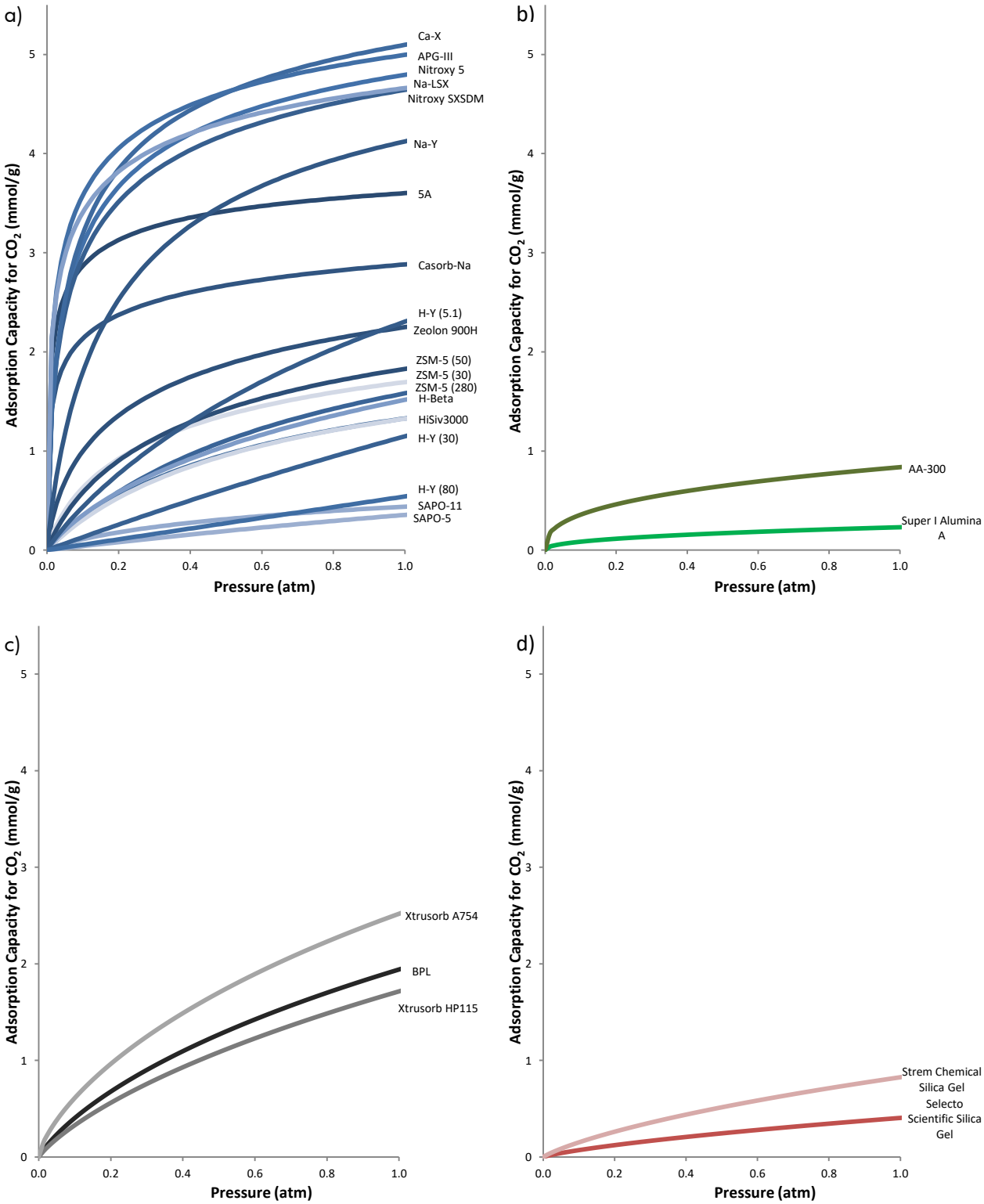

Figure 1.4 – Modelled adsorption isotherms of CO_2 at 30°C for a) zeolites, b) activated aluminas, c) activated carbons, and d) silica gels [55,56].

The pH of an activated alumina also affects the adsorption of CO_2, an acidic molecule [1]. This can be seen in Figure 1.4, with the two activated aluminas AA-300 being a neutral activated alumina, and Super I Alumina A having a pH of 4. Due to AA-300 being more basic, the adsorption with CO_2 is stronger which is a similar trend to that seen in zeolites [57]. The adsorption of CO_2 on the surface of activated alumina is complex with there being different types of adsorption sites [58]. Studies have shown that this complex adsorption is due to a combination of physisorption and chemisorption, with chemisorption forming bicarbonates, bidentate and monodentate carbonate, and bridging carbonate groups with the alumina [59].

In ambient air, there is approximately 405 ppm of CO_2 according to NASA with the rest of the components being 78.09% N_2, 20.95% O_2, and 0.93% Ar. This puts the amount of CO_2 present in air approximately within the Henry's Law region of the isotherm. Figure 1.5 shows a line approximation for the adsorption of CO_2 within the Henry's Law region from a variety of sources for zeolites, solid supported amines, and MOFs. All three sorbents can potentially be used for DAC of CO_2 with specific examples in Figure 1.5 of each sorbent type showing adsorption greater than 1 mmol/g.

Zeolites have been tested within the Henry's Law region for CO_2 adsorption with a wide range of reported capacities. Low Si/Al faujasite structured zeolites "X" and "LSX" have the highest CO_2 adsorption capacity when compared to higher Si/Al faujasite structured zeolite "Y". Other zeolite structures such as clinoptilolite and pentasil have significantly lower adsorption capacities for CO_2 within the 400 ppm and are therefore not promising candidates for DAC. Two important points within the data in Figure 1.5 can be observed. One is the fact that similarly classified zeolites (NaX and 13X) can have very different adsorption capacities. This difference in adsorption capacities between different NaX samples can be due to multiple reasons including the process, materials, or binders used to make them, or the difference in Si/Al ratio within the material. The other observation from Figure 5 is that Li^+ as a cation improved the adsorption capacity in the Henry's Law region more than Na^+ cation. The cation within the zeolite affects the acid-base properties, with Cs > Rb > K > Na > Li in terms of basicity [57]. With CO_2 being a slightly acidic molecule, the general rule is that increase in basicity, increases the strength of CO_2 adsorption. However, even though lithium is the least basic alkali metal of all cation exchanged forms of zeolite "X", due to CO_2 being a very polarizable molecule, the small Li^+ ion size induces a stronger interaction with CO_2 which has been observed in literature [19,60].

Amine-functionalized porous solids are also promising sorbents for CO_2 capture and have been proposed to be used in space craft as a means of closed circuit breathing systems [22,61]. However, amine sorption is influenced by many parameters and these parameters typically feature trade-offs. The primary advantage of amine functionalized sorbents is their high capacity which can be seen in Figure 1.5 with 9.9 mmol/g Amine Loading having a high sorption capacity for CO_2 of 1.72 mmol/g at 400 ppm of CO_2. However, these amine materials have very slow kinetics which require hours to reach saturation which has been commented in literature [34]. This is due to the loss of the porous nature of the support structure to which the amine is impregnated or grafted onto as well as pore plugging from the amine occupying a pore entrance. Choi et al reported surface areas of 45 m^2/g, 234 m^2/g, and 314 m^2/g, for amine loadings of 9.9

mmol/g, 5.3 mmol/g, and 2.9 mmol/g, respectively, from an initial support structure surface area of 840 m^2/g [20]. This decrease in surface area is due to an increase in the amine loading which significantly reduces the sorption kinetics. The humidity of the air also affects the sorption of CO_2 in amine functionalized solids, with the amines able to co-sorb CO_2 and H_2O. However, a wet gas stream is required to ensure that the amine stays stable and does not degrade [62]. As seen in Figure 1.5, a change in humidity affected the amount of CO_2 adsorbed in the Henry's Law region which was reported by Wurzbacher et al [23]. This study showed a decrease in CO_2 capacity as humidity dropped from 80% to 60% to 40% to 20% with similar adsorption uptake rates for all humidities. The similar uptake rates for CO_2 for all humidities however was caused by the amine structure being pore plugged and having a low surface area of 12.2 m^2/g and therefore being surface reaction with the amine groups limited. Research by Stuckert & Yang however showed that if amines were grafted onto the surface of the support structure with care to ensure that there was no pore blocking, that dry amines would sorb CO_2 three times faster than wet amines [19].

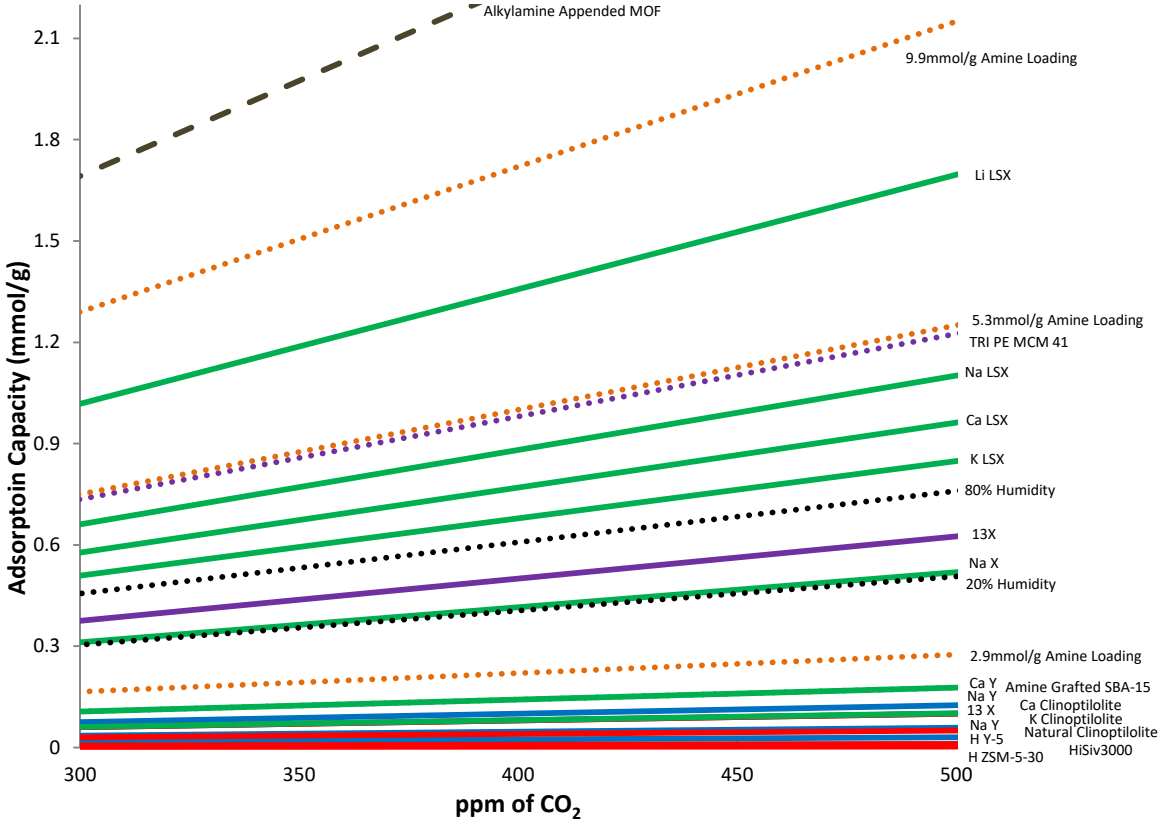

Figure 1.5 – A line approximation for the adsorption capacity for CO_2 within the Henry's Law region for zeolites (solid line), amines (dotted line), and MOFs (dashed line) at approximately room temperature. Source for data includes red [63], blue [45], green [19], purple [16], brown [34], black [23], and orange [20].

To overcome the sorption trade-off of increased amine loading vs pore plugging in amine functionalized solid sorbents, specially designed MOFs have been produced by McDonald et al. with amines grafted only

onto the metal substrate of the MOF [34]. This MOF is labelled alkylamine appended MOF in Figure 1.5. This research was proposed to allow for high surface areas and larger capacities at the same time. The results from this study show that sorption was around 2.2 mmol/g of CO_2 at 390 ppm in nitrogen. However, the surface area of the sample decreased from 3270 m^2/g to 70 m^2/g upon grafting the amine and further research was proposed to try other polyamines in the place of the chosen grated amine.

With low Si/Al ratio faujasite structured zeolites having high capacity for CO_2 at low concentration, high uptake rates in comparison to amine functionalized solid sorbents [19], industrially available, durable and robust, makes them excellent candidates for DAC of CO_2 for applications in concentrating CO_2 up to 95% for greenhouse gas mitigation, as well as for application in production of high purity CO_2.

1.2.2 Economics

The economic feasibility of a DAC technology is based on the operating cost, initial capital cost, integration into present technology, and the value of the product. Each one of these attributes affect the final cost per ton of CO_2 captured. A report on the feasibility of DAC using sodium hydroxide absorption processes by the APS estimated the cost at \$600/tonCO_2[11]. This report concluded that DAC was economically unfeasible but since this report, published papers from Carbon Engineering using a potassium hydroxide DAC pilot plant showed that cost can be as low as \$94/tonCO_2 [64,65]. Academic literature has also countered the report from the APS with studies investigating a solid sorbent system for DAC that would significantly drop the cost with one study predicting costs as low as \$100 per ton of CO_2 captured [17].

The operating cost of a DAC technology is based on the mechanical energy and the thermal energy requirements for the system. Mechanical energy is required to flow the air through the sorbent (E_f), as well as for the removal of wastes and products by vacuum (E_v), and energy to compress the product stream (E_c), which is generally provided by electricity. Thermal energy however, is required to desorb the CO_2 (E_D) by heating up the sorbent (E_S) but can be provided by electricity or by a waste heat stream. This would therefore allow DAC to become more economically feasible if incorporated into another process by reducing the thermal energy requirements of the system.

The required energy for the flow of air through the adsorbent bed is one of the most important parameters when determining the energy requirement for a DAC process and has been found to be the second most energy intensive portion of DAC for amine impregnated sorbents [17]. This is because of the low CO_2 content in air of 16.6 mmol of CO_2/m^3 of air (400 ppm of CO_2) and is heavily based on the percent captured and the rate of diffusion of the sorbent. In order to estimate the energy requirement for air flow, a simple correlation provided by the APS can be used (Equation 2).

$$E_f = \frac{P_{drop}}{\alpha_T C_{CO2}} \quad (2)$$

$$P_{drop} = 150\frac{v_S \mu (1-\varepsilon_B)^2 L}{(\emptyset d_v)^2 {\varepsilon_B}^3} + 1.75\frac{{v_S}^2 \rho_f (1-\varepsilon_B) L}{\emptyset d_v {\varepsilon_B}^3} \quad (3)$$

Where the P_{drop} is the pressure drop which can be derived from the Ergun equation for a packed bed (Equation 3), α_T is the total capture fraction of CO_2 from the air that flowed through the bed, and C_{CO2} is the concentration of CO_2 in the air which is 0.72 g/m^3 for 400 ppm of CO_2 at 25 °C and 1 atm. The capture fraction of CO_2 can then be defined from the characteristic length of the adsorbent L_o, which is similar to the concept to the mass transfer zone of a breakthrough curve.

$$\alpha = 1 - \exp(-\frac{L}{L_o}) \quad 4$$

$$L_o = \frac{\eta v_S \varepsilon_B {d_v}^2}{\mathcal{D}} \quad 5$$

Where L is the length of the bed, v_S is the superficial velocity, d_v is the diameter of the pellets, ε_B is the bulk void space in the bed, $\mathcal{D}$ is the molecular diffusion of CO_2 in air which is approximately $2.1 \cdot 10^{-5}$ m^2/s, and η is the dimensionless separation constant of the slowest decaying mode. The dimensionless separation constant parameter is a measure of the contribution of the external mass transfer resistance to the overall mass transfer in a packed bed.

$$\eta = f(d_v) \quad 6$$

Therefore, the energy requirement for the flow is a function of the system parameters (v_S, L), and the sorbent parameters (ε_S, d_v, $\emptyset$). When comparing different sorbents for DAC of CO_2, if system and sorbent parameters are constant, only diffusion influences the energy required for flow. This is convenient in sorbent selection due to the ability to investigate experimentally the rate of sorption of a single sorbate into a sorbent particle using the Linear Driving Force model [66].

The mechanical energy for the vacuum is considerably less than the energy that is required for flow which has been seen in literature [17]. This was seen to be due to the significantly larger flow required to capture the CO_2 compared to flow for the amount of CO_2 desorbed. Another finding from literature noted that if all gases desorbed from the bed were assumed to be CO_2 the energy for compression of the final product to 15 MPa would remain constant at approximately 417 MJ/tonCO_2 [17].

The total thermal energy required for a DAC system is the sum of the sensible energy to heat up the sorbent to the desorption temperature and the energy required to desorb the CO_2 along with the sensible energy to heat the gas to the desorption temperature.

$$E_D = M_A \Delta H_A + M_A C_{PA} \Delta T \quad 7$$

$$E_S = M_S C_{PS} \Delta T \quad 8$$

Where M_A is the mass of the adsorbed species, ΔH_A is the heat of adsorption, C_{PA} is the heat capacity of the adsorbed species, and C_{PS} is the heat capacity of the sorbent. A sorbent that can be regenerated at a lower temperature will therefore have a lower required change in temperature which will require less energy per ton of CO_2 adsorbed. For a cyclic process, another method to lower the cost per ton of CO_2

captured is to have a high working capacity of the sorbent. This is because of the loss of energy due to heating up the sorbent decreases as the working capacity of the sorbent increases.

The total energy of the system is the sum of the mechanical energy (energy to pump the air plus the energy for the vacuum of the system plus the energy for the compression of the CO_2 after concentration), and the thermal energy (the energy of desorption plus the sensible energy to heat up the sorbent and the sorbate), given by Equation 9.

$$E_T = (E_f + E_v + E_c) + (E_D + E_S) \quad 9$$

Ways to save energy can be included into these parameters. For instance, thermal energy can be saved using waste heat streams or direct heat streams. Examples of applications that could use the heat stream are concentrated solar power which operates at temperatures of higher than 200°C and would be sufficient to desorb the CO_2 from materials such as low Si/Al ratio faujasite structured zeolites. Incorporating concentrated solar power into DAC could be done by designing adsorption cycles to last throughout low sun output and desorption when sun output is high. This would therefore allow for CO_2 to be captured when it is the coldest, and desorbed when it is naturally the hottest.

One of the measurable DAC technology initial capital costs is the capital investment into the liquid or solid sorbents which is a function of the working capacity, cost of the sorbent, lifetime of the sorbent, and the swingtime of the process (Equation 10). Having a lower cost of sorbent consumption relative to amount of CO_2 captured is desirable and can only be achieved with high working capacities, fast cycles, and long lifetimes. High working capacities can be investigated by looking into the loadings in pure gas adsorption isotherms, with larger capacity differences over temperature and pressures indicating more desirable sorbent. Lifetime of the sorbent is harder to quantify in a laboratory setting, however. Lifetimes, unless degrading after dozens of cycles which has been identified in MOFs and hybrid ultramicroporous materials [18], are harder to measure, with amine impregnated sorbents being shown only up to 100's of repeated cycles [22]. Zeolites in industry last over 15 years in air separation processes.

$$\frac{Cost\ of\ Sorbent\ Consumption}{tonCO_2} = \frac{Sorbent\ Cost\ \times Swingtime}{Working\ Capacity\ \times Lifetime} \quad 10$$

1.2.3 Greenhouse Gas Mitigation

DAC of CO_2 for greenhouse gas mitigation has been growing rapidly but is still in its infancy in terms of technology. The larger industrial players such as Carbon Engineering (Squamish, British Columbia, Canada) which utilizes a KOH absorption unit was founded only in 2009, Climeworks (Zurich, Switzerland) which utilizes amines that are impregnated onto fiber supports being founded in 2009, and Global Thermostat (Huntsville, Alabama, United States) which uses amines that are impregnated onto ceramic supports being founded in 2006. Since these companies founding, they have commercialized their technology, begun sales, and have received significant funding due to the promise that their technology can

be a part of the solution to global warming. As of 2019, Carbon Engineering has acquired $68 million in private funding [67] and have announced a joint venture to capture 0.5 million tons of CO_2 per year based on their Squamish prototype [68]. Global Thermostat has raised $29.5 million for its pilot plant out of a total fundraising since inception of $70 million with plans to build a commercial project [68]. In 2018, Climeworks secured €30.5 million with a total funding of €50 million since there founding, with plans to produce CO_2 for products by Coca Cola under the brand name of "Valser" [68]. Other start-ups in the DAC of CO_2 include Prometheus fuels, Skytree, Soletair Power, Silicon Kingdom Holdings, Synhelion, and Sunfire. This rise of start-ups is due to global warming becoming more of a problem in the public perception, which therefore offers more support for carbon emission trading as well as carbon taxes.

The goal of all CO_2 mitigation technologies is set by the U.S. DOE, which is a technology that can achieve 90% capture at 95% purity from a coal fired power plant while limiting the increase cost of electricity to no more than 35% [69]. This equates to around 27-39 US$/ton$CO_2$ [70]. It is important to note that DAC of CO_2 does not need to meet the same recovery rate as PCC or NGCC which could translate into a thermodynamically more favourable separation. The initial baseline for this technology was set by anime absorption of flue gas with figures showing CO_2 capture costs between $40 - $100/ton$CO_2$ [71].

In order to compare different technologies for DAC of CO_2 for greenhouse gas mitigation, it is important to break down the operating energy requirements into the heating and the electrical energies. This is because these values determine if a process is fundamentally feasible. Also, these values can be compared across different processes. Care should be taken when comparing the final $/ton$CO_2$ of a DAC plant without first investigating the energy requirements because differences in methodology, cost of utilities, and capital costs of the equipment can significantly change the final $/ton$CO_2$. For example, Figure 1.6 shows the energy requirements of four different processes for DAC utilizing NaOH absorption (APS Report, 2011)[11], KOH absorption (Carbon Engineering, 2018)[64], fibers impregnated with amines (Climeworks AG, 2019)[72], and TRI-PE-MCM-41 (Kulkarni and Sholl, 2012)[17] with reported costs of $610-780/ton$CO_2$, $94-232/ton$CO_2$, $100-600/ton$CO_2$[73], and $88-163/ton$CO_2$, respectively. The estimated cost for a DAC NaOH absorption plant according to the APS Report was theoretically determined to be $610-780/ton$CO_2$ which utilizes fossil fuels for heating and $0.71/kWh for electricity with a total operating utility energy cost of $81/ton$CO_2$. The remainder of the $610-780/ton$CO_2$ is the capital costing of $370-500/ton$CO_2$ and operating costs excluding utility energy costs being $160-200/ton$CO_2$. The APS study considers the value of $610/ton$CO_2$ being optimistic for DAC of CO_2 and deemed the use of such technology as uneconomical which is an unscrupulous statement. This is because when comparing it to $/ton$CO_2$ determined from a real world pilot plant by Carbon Engineering which uses the same energy costs but changes the solution from NaOH to KOH, using a novel design, and accounting for renewable energy in the grid, Carbon Engineering study reported only a cost between $94-232/ton$CO_2$ from their pilot plant located in Squamish, British Columbia, Canada.

In literature and practise in the DAC of CO_2 for greenhouse gas mitigation, one trick used to reduce the heating costs is to utilize the burning of fossil fuels which provides cheap heat [11,17]. This is counter-intuitive

to the mitigation of green-house gases but savings in overall cost per ton of CO_2 can be significant. Kulkarni and Sholl (2012) showed differences in reported cost of \$181.7/tonCO_2 to \$92.7/tonCO_2 by utilizing fossil fuels instead of just wind electricity at a utility cost of \$0.097/kWh while accounting for the release of CO_2 from the burning of fossil fuels [17]. Carbon Engineering makes this a fundamental part of their process in their calciner which requires significant amount of thermal energy to break the CO_2 from the calcium carbonate [64]. Global Thermostat also mentioned in their patents that fossil fuels would be able to provide the heat required for their process [74,75].

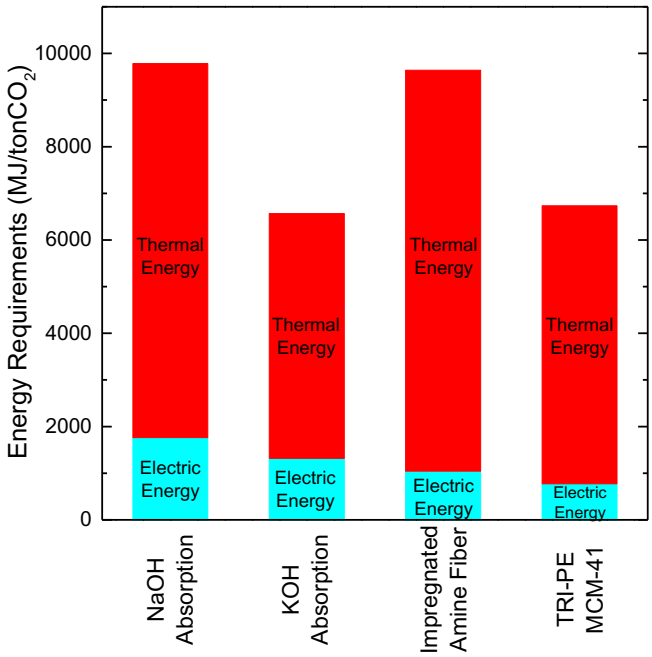

Figure 1.6 – The thermal and electrical energy requirements for DAC using NaOH absorption [11], KOH absorption [64], impregnated amine fiber [72], and TRI-PE-MCM-41 [17].

From a combination perspective of an environmentalist and a chemical engineer, utilizing a source of low grade heat that is not fossil fuel dependant would allow the DAC process to meet their thermal requirements while having minimal CO_2 impact. Two carbon free sources of low grade heat that are particularly interesting includes solar thermal plants and geothermal which has been noted in literature [76]. Both of these energy sources have renewable sources of heat and can also be used to produce electricity, effectively running the full DAC plant. Climeworks is currently partnered with Reykjavik Energy on an EU-funded project called CarbFix2 which looks to utilize Climework's DAC technology along with Reykjavik Energy's geothermal power plant to be able to capture and then sequester CO_2 utilizing renewable energy [77]. Global Thermostat has also expressed interest in utilizing solar thermal power in their DAC technology [74,75]. Combining green energy sources with DAC technologies, DAC becomes more economical with the potential to be used as a solution to global warming.

The potential of other green energy sources such as photovoltaic and wind for DAC have been investigated in literature, especially when they are located in regions with high energy potential [78–80]. For solar, this can

be utilized in regions along the Topic of Cancer or Tropic of Capricorn that have high solar energy densities. Breyer et al. demonstrated in their economic study that by utilizing photovoltaics in the Maghreb region in the Sahara can reduce the \$/kWh, which will therefore drop the \$/tonCO_2 significantly [79]. For wind, that can use utilize katabatic winds or trades winds such as the Roaring Forties which provide strong continuous winds that can be seen in maps of wind energy density. Goldberg et al. showed that locating a humidity swing DAC process on the Kerguelen Islands in the South Indian Ocean would offer cheap energy from wind to run their process, as well as a favourable location to sequester the CO_2 in the nearby Courbet Peninsula [80]. This matching of DAC technology with an inexpensive energy source is important for the potential to reduce the overall effect of greenhouse gas emissions on a global scale.

CO_2 can be captured from the air anywhere on the planet to reduce the overall world's emissions [6]. However, from a technological standpoint, the location of the DAC is very important for the viability of the technology. This is due to the dilute nature of the targeted adsorbate. In air, there is only 0.72 g/m^3 for 400 ppm of CO_2 (25 °C and 1 atm) and therefore would require substantial amount of air to capture 1 ton of CO_2. This makes it uneconomical to change the temperature, humidity, or pressure of the ambient air. For each particular DAC technology, there would be optimum conditions for the process to run. With DAC utilizing zeolites, this would be locations that would be considered dry due to the requirement to first remove water before separating the CO_2. By matching the ideal operating conditions for a DAC technology with potential locations, one can then therefore select a location near an ideal energy source, as well as a location to sequester the CO_2. By choosing a location this way, the \$/tonCO_2 can be reduced significantly which would increase the viability of removing CO_2 from the atmosphere using DAC.

1.2.4 Production of High Purity CO_2

Table 1.1 – Different Concentrations of CO_2 provided by CO_2meter [82].

Type	CO_2 Concentration
Medical	99.5%
Bone Dry	99.8%
Food and Beverage	99.9%
Anaerobic and Laser	99.95%
Supercritical Fluid	99.998%
Research	99.999%

The majority of DAC projects sequester CO_2 but projects that utilize the CO_2 from DAC will get reimbursed through the value of the carbon, increasing the economic viability of the process. Process such as Air to Fuels try to chemically convert the CO_2 into more valuable products [64] but due to CO_2 being the most oxidized version of carbon, have to overcome a large enthalpy [25]. One method to utilize CO_2 without chemically converting it is to increase the purity to the point where it becomes intrinsically more valuable. There are many different concentrations of high purity CO_2 in the market which can be seen in Table 1.1. These vary in value with higher values being attributed to higher purities. For medical grade CO_2 typical

charges are around $15 CAN for a cylinder of CO_2. For bone dry CO_2 that number is around $30 CAN, and the cost for research grade CO_2 is over $500 CAN per cylinder [81]. Therefore, depending on the purity of CO_2 being able to be achieved, different cost comparisons will be needed.

CO_2 has many applications that are currently being met with small scale solutions such as dewars and cylinders, or large scale solutions such as bulk supply tanks. These solutions are used for:

- **Food & beverage:** where CO_2 is used as a cryogenic agent for freezing, chilling, and cooling applications which protect the food's texture and taste. CO_2 is also used as a preservative in packaged products as well as for carbonation in beverages.
- **Healthcare:** where CO_2 is often mixed with air or oxygen as an inhalation stimulant to promote deep respiration. CO_2 is also used in cases where insufflation is required.
- **Pulp & paper:** where CO_2 is used to control the pH levels in alkaline digestion processes, reduce calcium carbonate dissolution, and during the washing of brown and bleached stock.
- **Wastewater treatment:** where CO_2 is used to reduce the wastewater's pH which is a safe alternative to mineral acids.
- **Welding & metal fabrication:** where CO_2 is used as a shielding gas to prevent atmospheric contamination of molten metal in electric arc welding processes.
- **Electronic:** where CO_2 is used in the removal of microscopic particles from electronics as well as to help prevent the photoresists collapsing during drying for semiconductor layers.
- **Pharmaceutical:** where CO_2 is used in bench top incubators as well as for the separation of chiral molecules using super-critical CO_2 fluid chromatography.

Providing high purity CO_2 for these applications using DAC has the benefit that since air is everywhere, CO_2 can be provided everywhere. The challenge is concentrating that CO_2 from air which is composed of 0.04% CO_2 to more than 99.5%. Experimentally in literature neither this concentration step change nor separation type has yet to be investigated using adsorbents. Kikkinides and Yang modelling investigated CO_2 separation using an activated carbon or carbon molecular sieve for PCC which demonstrated that CO_2 could potentially be concentrated to purities of 99.997% from 17% using a PSA cycle [83]. Similar modeling research has also showed that zeolite 13X can be used in PCC to concentrate CO_2 from 16% to over 99% using PSA [41]. One conclusion from these studies is that other than high working capacities which was discussed earlier in this thesis, high equilibrium selectivity is required between CO_2 and the other components in the air in order to produce high purity CO_2 [41]. This is important because after the adsorption step, significant amounts of N_2 and O_2 are co-adsorbed with the CO_2 due to the high quantities present in the feed stream. The blowdown step then occurs with the goal of removing the N_2 and O_2 while leaving the CO_2 present on the adsorbent so that only pure CO_2 is desorbed during the evacuation step. So if an adsorbent has a high equilibrium selectivity to CO_2, the adsorbent will be efficient in the blowdown step in removing the N_2 and O_2 while leaving CO_2 adsorbed. This thesis will be looking into the potential of utilizing low Si/Al ratio faujasite structured zeolites which have been shown in literature to have high

equilibrium selectivity to CO_2 and have been shown to be able to concentrate 400ppm of CO_2 to 93% and 94% for Li-LSX and K-LSX, respectively [19].

The value proposition for using DAC for the production of high purity CO_2 is not the \$/tonCO_2 but the convenience of having a continuous supply of CO_2 available as well as not requiring CO_2 transportation infrastructure to be put in place. The cost is not the value proposition because producing high purity CO_2 from air will require significant amounts of energy to run the process leading to significant \$/tonCO_2 and will not be able to compete on a \$/tonCO_2 against current means of production including purified CO_2 from hydrogen production, ammonia production, fermentation, and oxo-alkene production. However, the convenience of having a continuous supply of high purity CO_2 available has the value proposition according to the Lean Six Sigma mantra, of reduced waiting for replacement when CO_2 cylinder/tank run empty, reduced transportation into and out of the facility, reduced inventory requirement of CO_2, and minimizing personnel motions in the requirement of changing CO_2. Since only air and electricity are needed for the production of high purity CO_2, this means that high purity CO_2 can be produced even with a lack of CO_2 infrastructure in remote areas or places in poor/undeveloped regions in the world.

DAC companies have also seen the potential of producing high purity CO_2 with companies such as Global Thermostat which are selling captured CO_2 to soda companies, and Climeworks working with Coca Cola's brand "Valser" to carbonate their drinks with CO_2 from the air as well as selling CO_2 captured from air for sparkling water dispensers which are manufactured by Carbagas [68]. By utilizing the CO_2, DAC can help offer solutions to problems while allowing their businesses to acquire funding to develop their technology. This allows these companies a segue from smaller scale developments to larger solutions to global warming.

1.3 Excimer Gas

Excimer lasers are used to produce a specific wavelength of light which is in the ultraviolet spectrum and have applications in the production of semiconductors [84–86], eye surgery [87–90], and micromachining [91,92]. They work by exciting a noble gas (Ar, Kr, or Xe and sometimes Hg) with a reactive gas (F_2, Cl_2, or Br and sometimes I) into an exciplex [93]. This exciplex is created using high voltages with the exciplex producing a pulse of light which then dissociates into the original gas mixture. In this thesis the noble and reactive gases of interest are Kr and F, respectively, which when excited, produce a wavelength of 248 nm. In order to produce this exciplex, gases F_2 and Kr are needed at concentrations of 0.1% and 2% with a balance of neon within the laser chamber.

The issue with Kr–F excimer lasers is that the fluorine is very reactive and a build-up of by-products of CO_2, COF_2, CF_4, O_2, and HF are found within the laser. Technologies exist to chemically remove HF but 20 ppm, 350 ppm, and 150 ppm of CO_2, CF_4, and COF_2 are present in the laser with an unknown amount of O_2. These gases either absorb the 248 nm ultraviolet light or impede the formation of the exciplex [94]. To keep the laser operating at the same specification, the laser is programmed to ramp up the voltage required to

produce the desired intensity of light. This increase in voltage however, significantly decreases the life of the laser.

1.3.1 Separation of Impurities

Current and previous solutions to this problem include venting, cleaning, and injecting fresh excimer gases into the chamber, as well as utilizing liquid nitrogen to condense out the impurities in the process. Using liquid nitrogen was found to condense out significant amounts of krypton as well as be an inconvenience to the customers which has since been phased out as a solution [95]. The current solution of venting, cleaning, and injecting fresh excimer gas however, has become more expensive due to the increase cost of Ne and Kr in the world market.

One potential solution is scrubbing the excimer gas of the impurities as they build up by utilizing adsorbents. This would mean finding an adsorbent that would adsorb CO_2, CF_4, COF_2, and O_2 while letting F_2, Kr, and Ne pass through. By noting the internal adsorbate forces [96–100], CO_2 and COF_2 would have the strongest sorption due to their strong intermolecular forces in comparison to CF_4, O_2, and F_2 being weaker. Kr and Ne with little to no intermolecular forces, typically have the weakest adsorption.

The challenge with adsorbents is finding an adsorbent that has a high adsorption capacity, favourable selectivity, easily regenerable, fast kinetics, good chemical and physical stabilities, and low cost. Due to the reactiveness of F_2 and HF, many common industrial adsorbents could not be utilized. This includes activated carbons which have been found to break down to CO_2 and O_2 while scrubbing all the F_2, and the Si-O bond which is present in zeolites and silica gels which reacts spontaneously with fluorine [101–103]. It has been shown in literature that the reaction of activated carbons to F_2 and HF happens at room temperature [104]. However, this work by Tressaud et al. shows that the fluorination does not go untill completion but mainly reacts with the surface groups to C-F with some C-F_2. Therefore, fluorinated carbons could be prospective materials for this separation if it happens at room temperature or lower. Aluminum Phosphates (AlPO) have also been investigated for their stability to HF and F_2 exposure, with studies showing mixed results with decomposition occurring at room temperature for some AlPOs [105] and stability at temperatures above 400°C for others [106–108]. There has yet to be a paper discussing the stability of F_2 or HF to MOFs.

Two commercially available adsorbents which could be used for this separation are porous polymers and activated aluminas. Many polymers have been found to have good stability for F_2 and HF such as polytetrafluoroethylene (PTFE), polyfluorinated-ethylenepropylene, and polyperfluoroalkoxy [109]. PTFE has many brand named chromatography column packings [110] but has significantly less surface area than the most popular porous polymers which are divinylbenzene (DVB) based. DVB based porous polymers have surface areas in the order of $\approx$ 600 m^2/g which make them useful in chromatographic separations but has yet to be tested for its stability for F_2 or HF. Alumina have also been found to have decent stabilities to F_2 and because of this, are common materials for electrodes in excimer lasers. Activated aluminas, which are porous aluminas, can have different surface chemistries from basic to acidic, with either or both Brønsted and Lewis sites [1]. Some literature has shown that activated alumina can have stability up to 200°C to HF [111]

but a more thorough investigation into the effect of F_2 and HF on different surface chemistries is required before determining compatibility.

1.3.2 Potential of Colder Conditions

Due to the large amount of energy required producing the exciplex (6 kW of power for the excimer laser), it is feasible to cool down the feed stream using cryocoolers before separation. This would allow the use of materials that would otherwise not be able to handle fluorine or hydrofluoric acid at room temperature for long durations with the goal of having a continuous use service life of around 3 – 6 months. This can be seen with aluminas Al-O bond reaction with HF which has a strong correlation to temperature [111]. Lowering the temperature also increases the compatibility of HF and F_2 to polymeric materials which has been seen in literature [109].

Lowering the temperature would have the added benefit of increasing the adsorption capacity which can be seen from the van't Hoff equation (Equation 11) which relates the Henry's Law constant (K) to temperature (T). The rate at which K changes with respect to T is based on the heat of adsorption at zero loading (ΔH_0), with larger ΔH_0 creating a larger changes in K with respect to T.

$$lnK = -\frac{\Delta H_0}{R}\frac{1}{T} + lnK_0 \qquad 11$$

1.3.3 Adsorption of CO_2, COF_2, CF_4, and O_2

A part of this thesis will be investigating the adsorption of CO_2, COF_2, CF_4, and O_2 for the purification of Kr-F excimer laser gas. This separation has yet to be investigated in literature for adsorption but patents have been filed for using cryogenic condensation or sublimation of the impurities [112,113]. The adsorption of CO_2 and O_2 are very well studied in literature for applications in air separation, respectively [1]. For CF_4, the field of adsorption has mainly investigated its adsorption properties due to fluorocarbons having a high greenhouse gas potential [114–116]. No studies have been identified in the field of adsorption for COF_2. In this thesis, it is expected that COF_2 will have the strongest adsorption but due to COF_2 being a dangerous and hard to acquire gas, it will be negated from tests. The adsorption of $CO_2 > CF_4 > O_2$ is expected due to their relative intermolecular forces. This can be seen in the study by Branken et al. shows the adsorption trend of stronger interaction in order of $CO_2 > CF_4 > O_2$ on a wide variety of adsorbents including 13X, 5A, ShinCarbon ST, HayeSep N (highly polar porous polymer made of EGDMA and DVB), and Super Q [117]. Similar trend of greater adsorption of CF_4 over O_2 can be seen from work done by Yang et al. with Porapak Q (a DVB based porous polymer), silica gel, and 5A [118].

Since the impurities are present at low concentrations in this thesis, the adsorption behaviour can be best described by the Henry's Law region of the isotherm. Previous studies by our research group have investigated the Henry's Law region of CO_2, and CF_4 of many adsorbents including ones of interest for this section of this thesis, activated aluminas [63,115]. In the literature, there are also Henry's Law constants for the

adsorption behaviour of CO_2 and O_2 on activated aluminas [58,119,120]. There are no previously mentioned Henry's Law constants for porous polymers of adsorbates in this part of the thesis.

1.3.4 Concentration Pulse Gas Chromatography Technique

To investigate the Henry's Law constants of these impurities on activated aluminas and porous polymers, concentration pulse gas chromatography technique can be utilized. This technique has been widely used in literature since 1958 to measure the Henry's Law constants, diffusion properties, and the limiting heats of adsorption[121–124]. It is an isothermal approach where a pulse of strongly interacting component is put into the flow stream of a carrier gas which is a component that insignificantly interacts with the adsorbent (normally He but for this part of the thesis Ne was used). Using the response of the column to an impulse at the inlet the Henry's Law constant can be calculated from the recorded data by the gas chromatography's detector as concentration as a function of time. This event and response of the system are shown in Figure 1.7. By analysing the response, the Henry's Law constant can be calculated for a specific adsorbate at that temperature. By carrying out experiments at multiple temperatures, the limiting heats of adsorption for that specific adsorbate can be determined from the Henry's Law constants obtained at different temperatures.

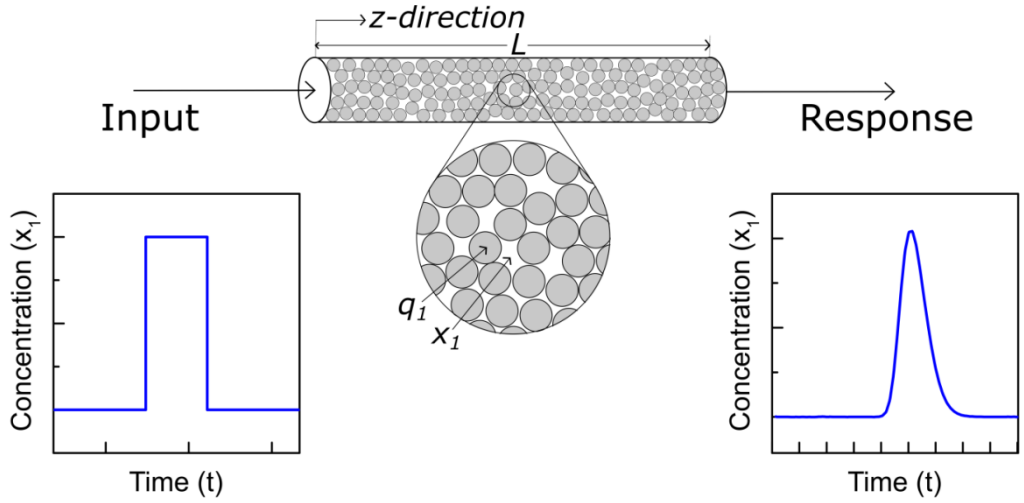

Figure 1.7 – Diagram of the concentration pulse gas chromatographic technique.

1.3.4.1 Henry's Law Constant

The derivation for this begins with the mass balance in the column ($x_1 + x_2 = 1$) for the component mole fraction in the gas phase of the strongly interacting component (x_1) and the component mole fraction in the gas phase of the weakly interacting component (x_2) which is shown in Equation 12 and Equation 13, respectively, assuming dispersed plug flow with negligible pressure drop.

$$-\mathcal{D}_L \frac{\partial^2 x_1}{\partial z^2} + v\frac{\partial x_1}{\partial z} + x_1\frac{\partial v}{\partial z} + \frac{\partial x_1}{\partial t} + \left(\frac{1-\varepsilon_B}{\varepsilon_B}\right)\frac{1}{c}\frac{\partial q_1}{\partial t} = 0 \quad (12)$$

$$-\mathcal{D}_L \frac{\partial^2 x_2}{\partial z^2} + v\frac{\partial x_2}{\partial z} + x_2\frac{\partial v}{\partial z} + \frac{\partial x_2}{\partial t} + \left(\frac{1-\varepsilon_B}{\varepsilon_B}\right)\frac{1}{c}\frac{\partial q_2}{\partial t} = 0 \quad (13)$$

With D_L being the axial dispersion coefficient, z being the direction along the length of the column, v being the interstitial gas velocity, ε_B being the void fraction of the bed, q_1 & q_2 being the adsorbed phase concentration of components 1 & 2 on a pellet basis, t being time, and c being the total gas phase concentration which is defined as $c = c_1/x_1 = c_2/x_2 = c_2/(1-x_1)$. This can be seen in literature [123] by summing Equations 12 and 13, for small changes in gas concentration denoted by X about an initially established equilibrium composition of x_1 gives

$$D_L\frac{\partial^2 X}{\partial z^2} - v\frac{\partial X}{\partial z} - \frac{\partial X}{\partial t} - \left(\frac{1-\varepsilon_B}{\varepsilon_B}\right)\frac{1}{c}\left\{(1-x_1)\frac{\partial q_1}{\partial t} - x_1\frac{\partial q_2}{\partial t}\right\} = 0 \qquad 14$$

Due to the change being small (such as those in the Henry's Law region), the equilibrium relationship can be denoted as linear, with q_1^* and q_2^* being the equilibrium values of q_1 and q_2 at a particular concentration.

$$q_1^* = \frac{\partial q_1^*}{\partial c_1}cX + constant \;\;\&\;\; q_2^* = -\frac{\partial q_2^*}{\partial c_2}cX + constant \qquad 15$$

By differentiating Equation 15 with respect to t gives the accumulation term $\frac{\partial q_1}{\partial t}$ and $\frac{\partial q_2}{\partial t}$ are formed.

$$\frac{\partial q_1}{\partial t} = \frac{dq_1^*}{dc_1}c\frac{\partial X}{\partial t} \;\;\&\;\; \frac{\partial q_2}{\partial t} = -\frac{dq_2^*}{dc_2}c\frac{\partial X}{\partial t} \qquad 16$$

By substituting Equation 16 into Equation 14, the effective equilibrium constant of components 1 and 2 can be obtained.

$$D_L\frac{\partial^2 X}{\partial z^2} - v\frac{\partial X}{\partial z} - \left\{1 + \left(\frac{1-\varepsilon_B}{\varepsilon_B}\right)\left[(1-x_1)\left(\frac{dq_1^*}{dc_1}\right) + x_1\left(\frac{dq_2^*}{dc_2}\right)\right]\frac{\partial X}{\partial t}\right\} = 0 \qquad 17$$

Where K_{eff} is the effective equilibrium constant of components 1 and 2,

$$K_{eff} = (1-x_1)\left(\frac{dq_1^*}{dc_1}\right) + x_1\left(\frac{dq_2^*}{dc_2}\right) \qquad 18$$

Therefore,

$$D_L\frac{\partial^2 X}{\partial z^2} - v\frac{\partial X}{\partial z} - \left\{1 + \left(\frac{1-\varepsilon_B}{\varepsilon_B}\right)K_{eff}\right\}\frac{\partial X}{\partial t} = 0 \qquad 19$$

The velocity of the concentration wave front as it moves through the bed (v^*) can be rearranged from the accumulation which can be expressed as the product of the velocity and the concentration gradient using the triple product rule,

$$X = f(t,z), \quad \left(\frac{\partial X}{\partial t}\right)_z = -\left(\frac{\partial z}{\partial t}\right)_X\left(\frac{\partial X}{\partial z}\right)_t = -v^*\left(\frac{\partial X}{\partial z}\right)_t \quad where\ v^* = \left(\frac{\partial z}{\partial t}\right)_X \qquad 20$$

By substituting the velocity of the concentration wave front from Equation 20 into Equation 19 we get,

$$D_L \frac{\partial^2 X}{\partial z^2} - \left\{ v - v^* \left[1 + \left(\frac{1 - \varepsilon_B}{\varepsilon_B} \right) K_{eff} \right] \right\} \left(\frac{\partial X}{\partial z} \right)_t = 0 \quad 21$$

At the inflection point of $(\partial^2 x_1 / \partial z^2)_t = 0$, the ratio of the interstitial velocity and the velocity of the concentration wave front can be given by,

$$\frac{v^*}{v} = \frac{1}{1 + \left(\frac{1 - \varepsilon_B}{\varepsilon_B} \right) K_{eff}} \quad 22$$

For a given length (L), the mean retention time (τ) is then given by,

$$\tau = \frac{L}{v^*} = \frac{L}{v} \left\{ 1 + \left(\frac{1 - \varepsilon_B}{\varepsilon_B} \right) K_{eff} \right\} \quad 23$$

From the gas chromatographs response, the mean retention time can be calculated from the difference in the baseline and the response peak at the exit of the column (Δc_1) given by Equation 24,

$$\tau = \frac{\int_0^\infty \Delta c_1 t \partial t}{\int_0^\infty \Delta c_1 \partial t} \quad 24$$

If the adsorption of the weakly interacting component (component 2) can be neglected with respect to the strongly interacting component (component 1) which is an acceptable assumption for most carrier gases (He and Ne), then as the mole fraction of component 1 approaches zero, the effective equilibrium constants of components 1 and 2 equate to the Henry's Law constant for component 1 (K_1). Therefore, by calculating the mean retention time from Equation 24 using the gas chromatograph response and substituting its value into Equation 23, for a small injection step change in the input of the column, the Henry's Law constant of component 1 can be calculated.

$$K_1 = \lim_{x_1 \to 0} K_{eff} = \frac{\partial q_1^*}{\partial c_1} \quad 25$$

To modify the Henry's Law constant (K_1) from the less common mol·m^{-3}/mol·m^{-3} to the more common units of $K_{P,1}$ of mmol g^{-1} atm^{-1}, the following conversion can be used.

$$K_{P,1} = \frac{K_1}{\rho_P R T} \quad 26$$

Where ρ_P is the pellet density in kg·m^{-3}, R is the gas constant in atm·m^3·mol^{-1}·K^{-1}, and T is temperature in K.

1.3.4.2 Limiting Heat of Adsorption

By doing multiple injections at different temperatures for an adsorbate, the limiting heat of adsorption can be determined by using the van't Hoff equation as follows,

$$\frac{\delta ln K_{P,1}}{\delta T} = \frac{\Delta H_0}{RT^2} \quad 27$$

Where $K_{P,1}$is the Henry's Law constant which were previously calculated for a specific T, and ΔH_0 is the limiting heat of adsorption. By assuming ΔH_0 is not a strong function of T, integrating Equation 27 gives,

$$ln K_{P,1} = -\frac{\Delta H_0}{R}\frac{1}{T} + ln K_0 \quad 28$$

Where K_0 is the pre-exponential constant. The slope of the line of best fit in the plot of $ln K_{P,1}$ versus $1/T$ in Equation 28 gives the limiting heat of adsorption for that adsorbate.

From the van't Hoff plot, the Henry's Law constant can be interpolated from the line of best fit within the range of experimental temperatures. For many circumstances however when the interaction between the adsorbent and adsorbate is strong enough to create a distended response at the temperature of interest, a solution is to elevate the analysis temperature and extrapolate to the desired range. This is done because for strong interactions between the adsorbent and the adsorbate, there is a large error between the baseline and the response on the gas chromatograph. Care should be taken when extrapolating values as the further the extrapolation, the greater the error.

1.4 Aerogels

Aerogels, by definition, are a class of mesoporous open-celled solid foams that are an assembly of interconnected nanostructures with porosity of greater than 50%. This class of materials have some exceptional properties making them the best insulating medium (0.016 W/m K), the lightest synthetic solid (0.0011 g/cm^3), have the lowest sound speed (70 m/s), have the lowest optical index of refraction (1.002), as well as having the lowest dielectric constant (1.008) [125]. Due to aerogels' high porosity (~80 to 99.8%) [126] particularly in the mesoporous range (2 – 50 nm), they have high surface areas typically between ~500 – 1200 m^2/g with reported values up to 3200 m^2/g for carbon aerogels that have been activated to further develop additional surface area [127]. This porosity and high surface area makes aerogel materials of interest for the field of adsorption.

Aerogels were first invented by S. Kistler in 1931 where aerogels of silica, alumina, nickel tartarate, stannic oxide, tungstic oxide, gelatine, agar, nitrocellulose, cellulose, and egg albumin were synthesised using three common steps, sol-gel process, aging, and then drying [128,129]. When S. Kistler invented aerogels he noted that he could see no reason why this list of aerogel materials may not be extended indefinitely. With great foresight, this list of materials was extended significantly to pure and composite materials of metal oxides (including most transition, lanthanide, and actinide metal oxide with several main group metal oxides), organic polymeric (such as resorcinol-formaldehyde, phenol-formaldehyde, polyurethanes, polyacrylates, polystyrenes, and epoxies), biological polymers (such as agar-agar, pectin, and gelatin), pure metals (such as copper and gold), and carbon (carbon nanotubes, and pyrolyzed biological or organic polymeric aerogels) [130]. This is significant for the field of adsorption with each aerogel material

having a unique surface chemistry. This surface chemistry interacts uniquely with the adsorbates' polarizability, quadrupole moment, and dipole moment potentially allowing an improved or new adsorption separation to occur between particular gases. For example, copper aerogels could be used as an adsorbent to adsorb CO from syngas production via π – bonding which would be a significant improvement compared to impregnating adsorbents with copper salts [1]. Other benefits of aerogels is that they increase the options for adsorption screening based on system compatibility, many aerogels are electrically conductive [125] allowing for electric swing adsorption [131], can be made to be monoliths, and they have a tuneable pore size [132,133].

Aerogels have yet to be thoroughly investigated in the field of adsorption which presents an opportunity for research. Currently, only a handful of investigations into gas adsorption separations have been done with the majority of studies investigating carbon aerogels. This includes gas adsorption separations into chemical air pollutants [134,135], use in hydrogen storage [136], for CO_2 capture [137–140], adsorption of ethane & ethylene [132], investigating adsorption of water [141], with many studies using adsorption for surface and pore size characterization (CO_2 and N_2 BET). Also, due to aerogels having a porous structure with a large surface area, many studies have investigated using them as support for grafting or impregnating a working material for a separation [142–147].

The future of aerogels made for adsorption will be different than aerogels made for other applications. This is because other applications favour having as light as possible aerogel and therefore, a very porous solid. However with adsorption, having a solid that is 99% porous would lead to adsorbent beds that have low volumetric productivities as well as challenges to meet adsorbed component product purities requirements. Therefore, aerogels made for adsorption should focus more on creating aerogels with high surface area and more defined pore size at the expense of low density.

1.5 Nomenclature

c	Total Gas Phase Concentration (mol m^{-3})
C_i	Concentration of Component I (ton of CO_2 m^{-3})
C_P	Heat Capacity (MJ kg^{-1} K^{-1})
$\mathcal{D}$	Molecular Diffusion (m^2 s^{-1})
$\mathcal{D}_L$	Axial Dispersion (m^2 s^{-1})
d_v	Diameter of Pellet (m)
E_c	Mechanical Energy Required to Compress Product Stream (MJ tonCO_2^{-1})
E_D	Heat Energy Required to Desorb CO_2 (MJ tonCO_2^{-1})
E_f	Mechanical Energy Required to Flow Air through the Sorbent (MJ tonCO_2^{-1})
E_S	Heat Energy Required to Heat up Sorbent (MJ tonCO_2^{-1})
E_v	Mechanical Energy Required to Remove Wastes and Products by Vacuum (MJ tonCO_2^{-1})
E_T	Total Energy Required for the System (MJ tonCO_2^{-1})
H_A	Heat of Adsorption (MJ kg^{-1})
H_0	Heat of Adsorption at Zero Loading (MJ kg^{-1})
K	Henry's Law Constant (mmol g^{-1} atm^{-1})
K_1	Henry's Law Constant for Strongly Adsorbed Species (mol m^{-3}/mol m^{-3})
K_{eff}	Effective Equilibrium Constant (mol m^{-3}/mol m^{-3})

K_P	Henry's Law Constant (mmol g^{-1} atm^{-1})
L	Length of the Adsorbent Bed (m)
L_0	Characteristic Length of the Adsorbent Bed (m)
M	Molar Mass (g mol^{-1})
M_A	Mass of the Adsorbed Species (kg)
P_{drop}	Pressure Drop (MJ m^{-3})
q_i	Concentration of Component i in the Pellets (mol m^{-3})
R	Ideal Gas Law Constant (m^3 atm K^{-1} mol^{-1})
t	Time (s)
T	Temperature (K)
v	Interstitial Velocity (m s^{-1})
v_s	Superficial Velocity (m s^{-1})
W_{min}	Minimum Energy (MJ tonCO_2^{-1})
x_i	Concentration of Component i in between the Pellets (mol m^{-3})
y	Mole Fraction in the Gas Phase (-)
z	Direction along the Length of the Column (m)
α_A	Adsorption Capture Fraction (-)
α_D	Desorption Capture Fraction (-)
α_T	Total Capture Fraction (-)
ε_B	Void Fraction of the Bed (-)
η	Dimensionless Separation Constant Parameter (-)
μ	Dynamic Viscousity (kg m^{-1} s^{-1})
ρ_f	Density of Fluid (kg m^{-3})
ρ_P	Density of Pellet (kg m^{-3})
τ	Mean Retention Time (s)
Ø	Sphericity (1 for perfect sphere) (-)

1.6 List of Abbreviations

APS	American Physical Society
BET	Brunauer-Emmett-Tellor
DAC	Direct Air Capture
DVB	Divinylbenzene
LSX	Low Silica X
MOFs	Metal Organic Frameworks
NGCC	Natural Gas Carbon Capture
PCC	Post Combustion Capture
PSA	Pressure Swing Adsorption
PTFE	Polytetrafluoroethylene
TSA	Temperature Swing Adsorption
TVSA	Temperature Vacuum Swing Adsorption

1.7 Bibliography

1. Yang, R. T. *Adsorbents: Fundamentals and Applications*. (John Wiley & Sons, 2003).
2. Belmabkhout, Y., Guillerm, V. & Eddaoudi, M. Low Concentration CO_2 Capture using Physical Adsorbents: Are Metal-Organic Frameworks Becoming the New Enchmark Materials? *Chem. Eng. J.* **296,** 386–397 (2016).
3. Gomes, V. G. & Yee, K. W. K. Pressure Swing Adsorption for Carbon Dioxide Sequestration from Exhaust Gases. *Sep. Purif. Technol.* **28,** 161–171 (2002).

4. Lackner, K. S., Ziock, H.-J. & Grimes, P. *Carbon Dioxide Extraction from Air: Is it an Option? Los Alamos National Laboratory*. (1999).
5. Lackner, K. S., Grimes, P. & Ziock, H. *Carbon Dioxide Extraction from Air? Los Alamos National Laboratory*. (1999).
6. Johnston, N. A. C., Blake, D. R., Rowland, F. S., Elliott, S., Lackner, K. S., Ziock, H. J., Dubey, M. K., Hanson, H. P. & Barr, S. Chemical Transport Modeling of Potential Atmospheric CO_2 Sinks. *Energy Convers. Manag.* **44,** 681–689 (2003).
7. Lackner, K. S. Capture of Carbon Dioxide from Ambient Air. *Eur. Phys. J. Spec. Top.* **176,** 93–106 (2009).
8. Lackner, K. S. The Thermodynamics of Direct Air Capture of Carbon Dioxide. *Energy* **50,** 38–46 (2013).
9. Keith, D. W., Ha-Duong, M. & Stolaroff, J. K. Climate Strategy with CO_2 Capture from the Air. *Clim. Change* **74,** 17–45 (2006).
10. House, K. Z., Baclig, A. C., Ranjan, M., van Nierop, E. A., Wilcox, J. & Herzog, H. J. Economic and Energetic Analysis of Capturing CO_2 from Ambient Air. *Proc. Natl. Acad. Sci.* **108,** 20428–20433 (2011).
11. Socolow, R., Desmond, M., Aines, R., Blackstock, J., Bolland, O., Kaarsberg, T., Lewis, N., Mazzotti, M., Pfeffer, A., Sawyer, K., Siirola, J., Smit, B. & Wilcox, J. *Direct Air Capture of CO_2 with Chemicals*. *American Physical Society - Panel on Public Affairs* (2011).
12. Ruthven, D. M., Farooq, S. & Brandani, S. Work of Separation in CO_2 Capture: Applicability of the Value Function. *Chem. Eng. Sci.* **126,** 604–607 (2015).
13. Zeman, F. S. & Keith, D. W. Carbon Neutral Hydrocarbons. *Philos. Trans. R. Soc. a-Mathematical Phys. Eng. Sci.* **366,** 3901–3918 (2008).
14. Olah, G. A., Prakash, G. K. S. & Goeppert, A. Anthropogenic Chemical Carbon Cycle for a Sustainable Future. *J. Am. Chem. Soc.* **133,** 12881–12898 (2011).
15. Graves, C., Ebbesen, S. D., Mogensen, M. & Lackner, K. S. Sustainable Hydrocarbon Fuels by Recycling CO_2 and H_2O with Renewable or Nuclear Energy. *Renew. Sustain. Energy Rev.* **15,** 1–23 (2011).
16. Belmabkhout, Y., Serna-Guerrero, R. & Sayari, A. Amine-Bearing Mesoporous Silica for CO2 Removal from Dry and Humid Air. *Chem. Eng. Sci.* **65,** 3695–3698 (2010).
17. Kulkarni, A. R. & Sholl, D. S. Analysis of Equilibrium-Based TSA Processes for Direct Capture of CO_2 from Air. *Ind. Eng. Chem. Res.* **51,** 8631–8645 (2012).
18. Kumar, A., Madden, D. G., Lusi, M., Chen, K.-J., Daniels, E. A., Curtin, T., Perry, J. J. & Zaworotko, M. J. Direct Air Capture of CO_2 by Physisorbent Materials. *Angew. Chemie Int. Ed.* **54,** 14372–14377 (2015).
19. Stuckert, N. R. & Yang, R. T. CO_2 Capture from the Atmosphere and Simultaneous Concentration Using Zeolites and Amine-Grafted SBA-15. *Environ. Sci. Technol.* **45,** 10257–10264 (2011).
20. Choi, S., Drese, J. H., Eisenberger, P. M. & Jones, C. W. Application of Amine-Tethered Solid Sorbents for Direct CO_2 Capture from the Ambient Air. *Environ. Sci. Technol.* **45,** 2420–2427 (2011).
21. Goeppert, A., Czaun, M., May, R. B., Prakash, G. K. S., Olah, G. A. & Narayanan, S. R. Carbon Dioxide Capture from the Air using a Polyamine Based Regenerable Solid Adsorbent. *J. Am. Chem. Soc.* **133,** 20164–20167 (2011).
22. Satyapal, S., Filburn, T., Trela, J. & Strange, J. Performance and Properties of a Solid Amine Sorbent for Carbon Dioxide Removal in Space Life Support Applications. *Energy and Fuels* **15,** 250–255 (2001).
23. Wurzbacher, J. A., Gebald, C., Piatkowski, N. & Steinfeld, A. Concurrent Separation of CO_2 and H_2O from Air by a Temperature-Vacuum Swing Adsorption/Desorption Cycle. *Environ. Sci. Technol.* **46,** 9191–9198 (2012).
24. Wurzbacher, J. A., Gebald, C., Brunner, S. & Steinfeld, A. Heat and Mass Transfer of Temperature-Vacuum Swing Desorption for CO_2 Capture from Air. *Chem. Eng. J.* **283,** 1329–1338 (2016).
25. Lackner, K. S. Carbonate Chemistry for Sequestering Fossil Carbon. *Annu. Rev. Energy Environ.* **27,** 193–232 (2002).
26. Zeman, F. Energy and Material Balance of CO_2 Capture from Ambient Air. *Environ. Sci. Technol.* **41,** 7558–7563 (2007).
27. Stolaroff, J. K., Keith, D. W. & Lowry, G. V. Carbon Dioxide Capture from Atmospheric Air using Sodium Hydroxide Spray. *Environ. Sci. Technol.* **42,** 2728–2735 (2008).
28. Zeman, F. Experimental Results for Capturing CO_2 from the Atmosphere. *AIChE J.* **54,** 1396–1399 (2008).
29. Mahmoudkhani, M. & Keith, D. W. Low-Energy Sodium Hydroxide Recovery for CO_2 Capture from Atmospheric Air-Thermodynamic Analysis. *Int. J. Greenh. Gas Control* **3,** 376–384 (2009).
30. Sherman, S. R. Nuclear Powered CO_2 Capture from the Atmosphere. *Environ. Prog. Sustain. Energy* **28,** 52–59 (2009).
31. Fee, J. P. H., Ph, D., Murray, J. M., Renfrew, C. W., Bedi, A., McCrystal, C. B., Jones, D. S. & Fee, H. J. P. Amsorb: A New Carbon Dioxide Absorbent for Use in Anesthetic Breathing Systems. *J. Am. Soc. Anesthesiol.* **91,** 1342 (1999).
32. Veselovskaya, J. V., Derevschikov, V. S., Kardash, T. Y., Stonkus, O. A., Trubitsina, T. A. & Okunev, A. G. Direct CO_2 Capture from Ambient Air using K_2CO_3/Al_2O_3 Composite Sorbent. *Int. J. Greenh. Gas Control* **17,** 332–340 (2013).
33. Wang, T., Lackner, K. S. & Wright, a. B. Moisture-Swing Sorption for Carbon Dioxide Capture from Ambient Air: A

Thermodynamic Analysis. *Phys. Chem. Chem. Phys.* **15,** 504–14 (2013).

34. McDonald, T. M., Lee, W. R., Mason, J. A., Wiers, B. M., Hong, C. S. & Long, J. R. Capture of Carbon Dioxide from Air and Flue Gas in the Alkylamine-Appended Metal-Organic Framework mmen-Mg_2(dobpdc). *J. Am. Chem. Soc.* **134,** 7056–7065 (2012).
35. Shekhah, O., Belmabkhout, Y., Chen, Z., Guillerm, V., Cairns, A., Adil, K. & Eddaoudi, M. Made-to-Order Metal-Organic Frameworks for Trace Carbon Dioxide Removal and Air Capture. *Nat. Commun.* **5,** 4228 (2014).
36. Liang, Z., Marshall, M. & Chaffee, A. L. CO_2 Adsorption-Based Separation by Metal Organic Framework (Cu-BTC) Versus Zeolite (13X). *Energy and Fuels* **23,** 2785–2789 (2009).
37. Franchi, R. S., Harlick, P. J. E. & Sayari, A. Applications of Pore-Expanded Mesoporous Silica. 2. Development of a High-Capacity, Water-Tolerant Adsorbent for CO_2. *Ind. Eng. Chem. Res.* **44,** 8007–8013 (2005).
38. Harlick, P. J. E. & Sayari, A. Applications of Pore-Expanded Mesoporous Silicas. 3. Triamine Silane Grafting for Enhanced CO_2 Adsorption. *Ind. Eng. Chem. Res.* **45,** 3248–3255 (2006).
39. Harlick, P. J. E. & Sayari, A. Applications of Pore-Expanded Mesoporous Silica. 5. Triamine Grafted Material with Exceptional CO_2 Dynamic and Equilibrium Adsorption Performance. *Ind. Eng. Chem. Res.* **46,** 446–458 (2007).
40. Krishnamurthy, S., Rao, V. R., Guntuka, S., Sharratt, P., Haghpanah, R., Rajendran, A., Amanullah, M., Karimi, I. A. & Farooq, S. CO_2 Capture from Dry Flue Gas by Vacuum Swing Adsorption: A Pilot Plant Study. *Sep. Mater. Devices Process.* **60,** 1830–1842 (2014).
41. Chue, K. T., Kim, J. N., Yoo, J., Cho, S. H. & Yang, R. T. Comparison of Activated Carbon and Zeolite 13X for CO_2 Recovery from Flue Gas by Pressure Swing Adsorption. *Ind. Eng. Chem. Res.* **34,** 591–598 (1995).
42. Choi, S., Drese, J. H. & Jones, C. W. Adsorbent Materials for Carbon Dioxide Capture from Large Anthropogenic Point Sources. *ChemSusChem* **2,** 796–854 (2009).
43. Reza, H., Nilam, R., Rajendran, A., Farooq, S. & Karimi, I. A. Cycle Synthesis and Optimization of a VSA Process for Postcombustion CO_2 Capture. *AIChE J.* **59,** 4735–4748 (2013).
44. Sircar, S. & Kratz, W. C. Patent 4249915 - Removal of Water and Carbon Dioxide from Air. (1981).
45. Rege, S. U., Yang, R. T. & Buzanowski, M. A. Sorbents for Air Prepurification in Air Separation. *Chem. Eng. Sci.* **55,** 4827–4838 (2000).
46. Kumar, R. Removal of Water and Carbon Dioxide from Atmospheric Air. (1987).
47. Jain, R. Pre Purification of Air for Separation. 8 (1993).
48. Rege, S. U., Yang, R. T., Qian, K. & Buzanowski, M. A. Air-Prepurification by Pressure Swing Adsorption using Single / Layered Beds. *Chem. Eng. Sci.* **56,** 2745–2759 (2001).
49. Leavitt, F. W. PSA Gas Purifier and Purification Process. 6 (1998).
50. Golden, T. C., Kalbassi, M. A., Taylor, F. W. & Allam, R. J. Use of Zeolites and Alumina in Adsorption Processes. 12 (1998).
51. Kumar, R., Deng, S., Bulow, M., Fitch, F., Ojo, A. F. & Gittleman, C. S. Air Purification Process. 4 (1993).
52. Kanazirev, V. I. & Latus, D. G. Composite Adsorbents for Air Purification. 6 (2003).
53. Ruthven, D. M. *Principles of Adsorption and Adsorption Processes*. (John Wiley & Sons, 1984).
54. Bonenfant, D., Kharoune, M., Niquette, P., Mimeault, M. & Hausler, R. Advances in Principal Factors Influencing Carbon Dioxide Adsorption on Zeolites. *Sci. Technol. Adv. Mater.* **9,** 1–7 (2008).
55. Wilson, S. M. W. Adsorption Separation of CO2 from CO in Syngas: Improving the Conversion of the Reverse Water Gas Shift Reaction. (University of Ottawa, 2015).
56. Wilson, S. M. W., Kennedy, D. A. & Tezel, F. H. Adsorbent Screening for CO_2/CO Separation for Applications in Syngas Production. *Separation and Purification Technology* **236,** (Elsevier, 2020).
57. Barthomeuf, D. Conjugate Acid-Base Pairs in Zeolites. *J. Phys. Chem.* **88,** 42–45 (1984).
58. Manchado, M. C., Guil, J. M., Masia, A. P., Paniego, A. R. & Menayo, J. M. T. Adsorption of H_2, O_2, CO, and CO_2 on a Gamma-Alumina: Volumetric and Calorimetric Studies. *Langmuir* **10,** 685–691 (1994).
59. Mao, C.-F. & Vannice, M. A. High Surface Area Alpha Alumina 1: Adsorption Properties and Heats of Adsorption of Carbon Monoxide Carbon Dioxide and Ethylene. *Appl. Catal. A Gen.* **111,** 151–173 (1994).
60. Walton, K. S., Abney, M. B. & LeVan, M. D. CO_2 Adsorption in Y and X Zeolites Modified by Alkali Metal Cation Exchange. *Microporous Mesoporous Mater.* **91,** 78–84 (2006).
61. Schladt, M. J., Filburn, T. P., Helble, J. J. & Hartford, W. Supported Amine Sorbents under Temperature Swing Absorption for CO_2 and Moisture Capture. *Ind. Eng. Chem. Res.* **46,** 1590–1597 (2007).
62. Sayari, A. & Belmabkhout, Y. Stabilized Amine-Containing CO_2 Adsorbents and Related Systems and Methods. (2016).
63. Harlick, P. J. E. & Tezel, F. H. An Experimental Adsorbent Screening Study for CO_2 Removal from N_2. *Microporous*

Mesoporous Mater. **76,** 71–79 (2004).

64. Keith, D. W., Holmes, G., St. Angelo, D. & Heidel, K. A Process for Capturing CO_2 from the Atmosphere. *Joule* 1–22 (2018). doi:10.1016/j.joule.2018.05.006
65. Holmes, G., Nold, K., Walsh, T., Heidel, K., Henderson, M. A., Ritchie, J., Klavins, P., Singh, A. & Keith, D. W. Outdoor Prototype Results for Direct Atmospheric Capture of Carbon Dioxide. *Energy Procedia* **37,** 6079–6095 (2013).
66. Sircar, S. & Hufton, J. R. Why Does the Linear Driving Force Model for Adsorption Kinetics Work? *Adsorption* **6,** 137–147 (2000).
67. Engineering, C. *Carbon Engineering Concludes USD $ 68 Million Private Investment Round and Proceeds with Commercialization of Carbon Dioxide Removal Technology*. (2019).
68. Chalmin, A. Direct Air Capture: Recent Developments and Future Plans. *Geoengineering Monitor* 1–6 (2019).
69. Ciferno, J. P., Fout, T. E., Jones, A. P. & Murphy, J. T. Capturing Carbon from Existing Coal-Fired Power Plants. *Chem. Eng. Prog.* **105,** 33–41 (2009).
70. Davison, J. Performance and Costs of Power Plants with Capture and Storage of CO_2. *Energy* **32,** 1163–1176 (2007).
71. Merkel, T. C., Lin, H., Wei, X. & Baker, R. Power Plant Post-Combustion Carbon Dioxide Capture: An Opportunity for Membranes. *J. Memb. Sci.* **359,** 126–139 (2010).
72. Gebald, C., Repond, N. & Wurzbacher, J. A. US 10279306 B2 - Steam Assisted Vacuum Desorption Process for Carbon Dioxide Capture. 14 (2019).
73. Tollefson, J. Sucking Carbon Dioxide from Air is Cheaper than Scientists Thought. *Nature* **558,** 173 (2018).
74. Eisenberger, P. M. & Chichilnisky, G. US 9908080 B2 - System and Method for Removing Carbon Dioxide from an Atmosphere and Global Thermostat using the Same. 1–9 (2018).
75. Eisenberger, P. & Chichilnisky, G. US 20100319537 A1 - System and Method for Removing Carbon Dioxide from an Atmosphere and Global Thermostat using the Same. 1–16 (2010).
76. Creutzig, F., Breyer, C., Hilaire, J., Minx, J., Peters, G. P. & Socolow, R. The Mutual Dependence of Negative Emission Technologies and Energy Systems. *Energy Environ. Sci.* **12,** 1805–1817 (2019).
77. Gutknecht, V., Snaebjornsdottir, S. O., Sigfusson, B., Aradottir, E. S. & Charles, L. Creating a Carbon Dioxide Removal Solution by Combining Rapid Mineralization of CO_2 with Direct Air Capture. *Energy Procedia* **146,** 129–134 (2018).
78. Fasihi, M., Olga, E. & Breyer, C. Techno-economic Assessment of CO_2 Direct Air Capture Plants. *J. Clean. Prod.* **224,** 957–980 (2019).
79. Breyer, C., Fasihi, M. & Aghahosseini, A. Carbon Dioxide Direct Air Capture for Effective Climate Change Mitigation based on Renewable Electricity: A New Type of Energy System Sector Coupling. *Mitig. Adapt. Strateg. Glob. Chang.* 1–23 (2019).
80. Goldberg, D. S., Lackner, K. S., Han, P., Slagle, A. L. & Wang, T. Co-Location of Air Capture, Subsea floor CO2 Sequestration, and Energy Production on the Kerguelen Plateau. *Environ. Sci. Technol.* **47,** 7521–7529 (2013).
81. Linde Canada Ltd. Pricing Chart. (2017).
82. Pringle, J. Why the Grade of CO_2 Gas you are Using is Important. *Web Article* 1 (2015). Available at: https://www.co2meter.com/blogs/news/16831989-why-the-grade-of-co2-gas-you-are-using-is-important. (Accessed: 1st April 2017)
83. Kikkinides, E. S., Yang, R. T. & Cho, S. H. Concentration and Recovery of $C0_2$ from Flue Gas by Pressure Swing Adsorption. *Ind. Eng. Chem. Res.* **32,** 2714–2720 (1993).
84. Aoki, T., Hatanaka, Y. & Look, D. C. ZnO Diode Fabricated by Excimer-Laser Doping. *Appl. Phys. Lett.* **76,** 3257–3258 (2000).
85. Tsukazaki, A., Ohtomo, A., Onuma, T., Ohtani, M., Makino, T., Sumiya, M., Ohtani, K., Chichibu, S. F., Fuke, S., Segawa, Y., Ohno, H., Koinuma, H. & Kawasaki, M. Repeated Temperature Modulation Epitaxy for P-Type Doping and Light-Emitting Diode Based on ZnO. *Nat Mater* **4,** 42–46 (2005).
86. Nomura, K., Ohta, H., Takagi, A., Kamiya, T., Hirano, M. & Hosono, H. Room-Temperature Fabrication of Transparent Flexible Thin-Film Transistors using Amorphous Oxide Semiconductors. *Nature* **432,** 488–492 (2004).
87. Trokel, S. L., Srinivasan, R. & Braren, B. Excimer Laser Surgery of the Cornea. *Am. J. Ophthalmol.* **96,** 710–715 (1983).
88. Puliafito, C. A., Steinert, R. F., Deutsch, T. F., Hillenkamp, F., Dehm, E. J. & Adler, C. M. Excimer Laser Ablation of the Cornea and Lens. *Ophthalmology* **92,** 741–748 (1985).
89. Sakimoto, T., Rosenblatt, M. I. & Azar, D. T. Laser Eye Surgery for Refractive Errors. *Lancet* **367,** 1432–1447 (2006).
90. Munnerlyn, C. R., Koons, S. J. & Marshall, J. Photorefractive Keratectomy: A Technique for Laser Refractive Surgery. *J. Cataract Refract. Surg.* **14,** 46–52 (1988).
91. Pedraza, A. J., Fowlkes, J. D. & Lowndes, D. H. Silicon Microcolumn Arrays Grown by Nanosecond Pulsed-Excimer Laser Irradiation. *Appl. Phys. Lett.* **74,** 2322–2324 (1999).

92. Dongre, S., Gujrathi, A. & Nandan, H. A Review of Laser Micromachining. *Int. J. Eng. Sci.* **6,** 2416–2420 (2016).

93. Lakoba, I. S. & Yakovlenko, S. I. Active Media of Exciplex Lasers (Review Article). *Kvantovaya Elektron.* **7,** 677–719 (1980).

94. Sumitani, A., Andoua, S., Watanabea, T., Konishi, M., Egawa, S., Ohta, T., Terashimab, K., Suzukib, N., Enamib, T. & Mizoguchi, H. Output Stabilization Technology with Chemical Impurity Control on ArF Excimer Laser. *Analyzer* **4000,** 1424–1434 (2000).

95. Basting, D. *Excimer Laser Technology*. (Springer Science & Business Media, 2005).

96. Stogryn, D. E. & Stogryn, A. P. Molecular Multipole Moments. *Mol. Phys.* **11,** 371–393 (1966).

97. Griskey, R. G. *Transport Phenomena and Unit Operations: A Combined Approach*. (John Wiley & Sons, 2005).

98. Sircar, S. Basic Research Needs for Design of Adsorptive Gas Separation Processes. *Ind. Eng. Chem. Res.* **45,** 5435–5448 (2006).

99. Granville, A. & Hall, P. G. Adsorption of Krypton and Nitric Oxide on Alkali Metal Chloride Films. *Trans. Faraday Soc.* **63,** 701–707 (1967).

100. Gough, K. M., Yacowar, M. M., Cleve, R. H. & Dwyer, J. R. Analysis of Molecular Polarizabilities and Polarizability Derivatives in H_2, N_2, F_2, CO, and HF, with the Theory of Atoms in Molecules. *Can. J. Chem.* **74,** 1139–1144 (1996).

101. Flamm, D. L., Donnelly, V. M. & Mucha, J. A. The Reaction of Fluorine Atoms with Silicon. *J. Appl. Phys.* **52,** 3633–3639 (1981).

102. Standaert, T. E. F. M., Hedlund, C., Joseph, E. a., Oehrlein, G. S. & Dalton, T. J. Role of Fluorocarbon Film Formation in the Etching of Silicon, Silicon Dioxide, Silicon Nitride, and Amorphous Hydrogenated Silicon Carbide. *J. Vac. Sci. Technol. A Vacuum, Surfaces, Film.* **22,** 53 (2004).

103. Kirsch, W. B. & Laurent, S. M. US:4557921 Purification of Halide. (1985).

104. Tressaud, A., Guimon, C., Gupta, V. & Moguet, F. Fluorine-Intercalated Carbon fibers: II: An X-Ray Photoelectron Spectroscopy Study. *Mater. Sci. Eng. B* **30,** 61–68 (1995).

105. Rampersadh, P. Removal of Hydrogen Fluoride from Gas Streams. (Faculty of Science, University of Witwatersrand, Johannesburg, 2005).

106. Takita, Y., Ninomiya, M., Miyake, H., Wakamatsu, H., Yoshinaga, Y. & Ishihara, T. Catalytic Decomposition of Perfluorocarbons Part II. Decomposition of CF_4 over $AlPO_4$ Rare Earth Phosphate Catalysts. *Phys. Chem. Chem. Phys.* **1,** 4501–4504 (1999).

107. Takita, Y., Ninomiya, M., Matsuzaki, R., Wakamatsu, H., Nishiguchi, H. & Ishihara, T. Decomposition of Chlorofluorocarbons over Metal Phosphate Catalysts Part I. Decomposition of CCl_2F_2 over Metal Phosphate Catalysts. *Phys. Chem. Chem. Phys.* **1,** 2367–2372 (1999).

108. Takita, Y., Wakamatsu, H., Li, G. L., Moro-Oka, Y., Nishiguchi, H. & Ishihara, T. Decomposition of Chlorofluorocarbons over Metal Phosphate Catalysis. II. Origin of the Stability of $AlPO_4$ and the Location of CE as a Promoter. *J. Mol. Catal. A Chem.* **155,** 111–119 (2000).

109. Cornell. Chemical Compatibility Guide. Available at: http://sevierlab.vet.cornell.edu/resources/Chemical-Resistance-Chart-Detail.pdf.

110. Barry, E. F. & Grob, R. L. *Columns for Gas Chromatography: Performance and Selection*. (John Wiley & Sons, 2007).

111. Scokart, P. O., Selim, S. A., Damon, J. P. & Rouxhet, P. G. The Chemistry and Surface Chemistry of Fluorinated Alumina. *J. Colloid Interface Sci.* **70,** 209–222 (1979).

112. Bedwell, D. J. US 5090020 - Apparatus for Controlling the Composition of a Laser Gas or Gas Mixture. 1–7 (1992). doi:10.1074/JBC.274.42.30033.(51)

113. Jursich, G. M. & Von Drasek, W. A. US 5897847 - Method for Extending the Gas Lifetime of Excimer Lasers. 1–6 (1999). doi:10.1074/JBC.274.42.30033.(51)

114. Senkovska, I., Barea, E., Navarro, J. A. R. & Kaskel, S. Adsorptive Capturing and Storing Greenhouse Gases such as Sulfur Hexafluoride and Carbon Tetrafluoride using Metal-Organic Frameworks. *Microporous Mesoporous Mater.* **156,** 115–120 (2012).

115. Singh, S., Tezel, F. H. & Harlick, P. J. E. Adsorption of Tetrafluoromethane and Nitrogen on Various Adsorbents. *Sep. Sci. Technol.* **37,** 2763–2784 (2002).

116. Furmaniak, S., Terzyk, A. P., Gauden, P. A., Kowalczyk, P., Harris, P. J. F. & Koter, S. Applicability of Molecular Simulations for Modelling the Adsorption of the Greenhouse Gas CF4 on Carbons. *J. Phys. Condens. Matter* **25,** 1–9 (2013).

117. Branken, D. J., le Roux, J. P., Krieg, H. M. & Lachmann, G. A Dual-Channel Gas Chromatography Method for the Quantitation of Low and High Concentrations of NF_3 and CF_4 to Study Membrane Separation of the Two Compounds. *J. Chromatogr. A* **1307,** 180–190 (2013).

118. Ou Yang, C. F., Kam, S. H., Liu, C. H., Tzou, J. & Wang, J. L. Assessment of Removal Efficiency of Perfluorocompounds (PFCs) in a Semiconductor Fabrication Plant by Gas Chromatography. *Chemosphere* **76,** 1273–1277 (2009).

119. Cao, D. V & Sircar, S. Heats of Adsorption of Pure SF_6 and CO_2 on Silicalite Pellets With Alumina Binder. *Ind. Eng. Chem. Res.* **40,** 156–162 (2001).

120. Rosynek, M. P. Isotherms and Energetics of Carbon Dioxide Adsorption on Gamma-Alumina at 100-300 Degrees. *J. Phys. Chem.* **79,** 1280–1284 (1975).

121. Greene, S. A. & Pust, H. Determination of Nitrogen Dioxide by Gas-Solid Chromatography. *Anal. Chem.* **30,** 1039–1040 (1958).

122. Habgood, H. W. Adsorptive and Gas Chromatographic Properties of Various Catonic Forms of Zeolite X. *Can. J. Chem.* **42,** 2340–2350 (1964).

123. Ruthven, D. M. & Kumar, R. An Experimental Study of Single-Component and Binary Adsorption Equilibria by a Chromatographic Method. *Ind. Eng. Chem. Fundam.* **19,** 27–32 (1980).

124. Ma, Y. H. & Mancel, C. Diffusion Studies of CO_2, NO, NO_2, and SO_2 on Molecular Sive Zeolites by Gas Chromatography. *AIChE J.* **18,** 1148–1153 (1972).

125. Hrubesh, L. W. Aerogel Applications. *J. Non. Cryst. Solids* **225,** 335–342 (1998).

126. Maleki, H. Recent Advances in Aerogels for Environmental Remediation Applications : A Review. *Chem. Eng. J.* **300,** 98–118 (2016).

127. Kabbour, H., Baumann, T. F., Satcher, J. H., Saulnier, A. & Ahn, C. C. Toward New Candidates for Hydrogen Storage: High-Surface-Area Carbon Aerogels. *Chem. Mater.* **18,** 6085–6087 (2006).

128. Kistler, S. S. Coherent Expanded Aerogels and Jellies. *Nature* **127,** 741 (1931).

129. Kistler, S. S. Coherent Expanded-Aerogels. *J. Phys. Chem.* **36,** 52–64 (1931).

130. Du, A., Zhou, B., Zhang, Z. & Shen, J. A Special Material or a New State of Matter: A Review and Reconsideration of the Aerogel. *Materials (Basel).* **6,** 941–968 (2013).

131. Ribeiro, R. P. P. L., Grande, C. A. & Rodrigues, A. E. Electric Swing Adsorption for Gas Separation and Purification: A Review. *Sep. Sci. Technol.* **49,** 1985–2002 (2014).

132. Tamon, H., Ishizaka, H., Araki, T. & Okazaki, M. Control of Mesoporous Structure of Organic and Carbon Aerogels. *Carbon N. Y.* **36,** 1257–1262 (1998).

133. Horikawa, T., Hayashi, J. & Muroyama, K. Controllability of Pore Characteristics of Resorcinol-Formaldehyde Carbon Aerogel. *Carbon N. Y.* **42,** 1625–1633 (2004).

134. Fairen-Jimenez, D., Carrasco-Marin, F. & Moreno-Castilla, C. Adsorption of Benzene, Toluene, and Xylenes on Monolithic Carbon Aerogels from Dry Air Flows. *Langmuir* **23,** 10095–10101 (2007).

135. Štandeker, S., Novak, Z. & Knez, Ž. Removal of BTEX Vapours from Waste Gas Streams using Silica Aerogels of Different Hydrophobicity. *J. Hazard. Mater.* **165,** 1114–1118 (2009).

136. Tian, H. Y., Buckley, C. E., Wang, S. B. & Zhou, M. F. Enhanced Hydrogen Storage Capacity in Carbon Aerogels Treated with KOH. *Carbon N. Y.* **47,** 2128–2130 (2009).

137. Alhwaige, A. A., Ishida, H. & Qutubuddin, S. Carbon Aerogels with Excellent CO_2 Adsorption Capacity Synthesized from Clay-Reinforced Biobased Chitosan-Polybenzoxazine Nanocomposites. *ACS Sustain. Chem. Eng.* **4,** 1286–1295 (2016).

138. Jeon, D.-H., Min, B.-G., Oh, J. G., Nah, C. & Park, S.-J. Influence of Nitrogen Moieties on CO_2 Capture of Carbon Aerogel. *Carbon Lett.* **16,** 57–61 (2015).

139. Marques, L. M., Carrott, P. J. M. & Carrott, M. M. L. R. Carbon Aerogels used in Carbon Dioxide Capture. *Bol. Grup. Español Carbón* **40,** 9–12 (2016).

140. Hao, G. P., Li, W. C., Qian, D. & Lu, A. H. Rapid Synthesis of Nitrogen-Doped Porous Carbon Monolith for CO_2 Capture. *Adv. Mater.* **22,** 853–857 (2010).

141. Knez, Z. & Novak, Z. Adsorption of Water Vapor on Silica, Alumina, and Their Mixed Oxide Aerogels. *J. Chem. Eng. Data* **46,** 858–860 (2001).

142. Fan, H., Wu, Z., Xu, Q. & Sun, T. Flexible, Amine-Modified Silica Aerogel with Enhanced Carbon Dioxide Capture Performance. *J. Porous Mater.* **23,** 131–137 (2016).

143. Wörmeyer, K., Alnaief, M. & Smirnova, I. Amino functionalised Silica-Aerogels for CO_2 Adsorption at Low Partial Pressure. *Adsorption* **18,** 163–171 (2012).

144. Linneen, N., Pfeffer, R. & Lin, Y. S. CO_2 Capture using Particulate Silica Aerogel Immobilized with Tetraethylenepentamine. *Microporous Mesoporous Mater.* **176,** 123–131 (2013).

145. Cui, S., Cheng, W., Shen, X., Fan, M. & Russell, T. Mesoporous Amine-Modified SiO_2 Aerogel: A Potential CO_2 Sorbent. *Energy Environ. Sci.* **4,** 2070–2074 (2011).

146. Begag, R., Krutka, H., Dong, W., Mihalcik, D., Rhine, W., Gould, G., Baldic, J. & Nahass, P. Superhydrophobic Amine Functionalized Aerogels as Sorbents for CO_2 Capture. *Greenh. Gases Sci. Technol.* **3,** 30–39 (2013).

147. Amonette, J. E. & Matyáš, J. Functionalized Silica Aerogels for Gas-Phase Purification, Sensing, and Catalysis: A Review. *Microporous Mesoporous Mater.* **250,** 100–119 (2017).

Chapter 2

Direct Dry Air Capture of CO_2 using VTSA with Faujasite Zeolites

Sean M.W. Wilson, and F. Handan Tezel

Department of Chemical and Biological Engineering, University of Ottawa, 161 Louis-Pasteur, Ottawa, Ontario K1N 6N5 Canada,

Accepted by: Industrial & Engineering Chemistry Research 2020

2.1 Abstract

The capture and concentration of CO_2 from a dry ambient air stream by temperature vacuum swing adsorption (TVSA) has been experimentally demonstrated in a small scale by using a single bed system packed with 20 g of zeolite X. 7 different commercially available type X zeolites were investigated and one of them was chosen for a more comprehensive study. Breakthrough experiments were carried out by perturbing the He saturated bed with compressed ambient air with CO_2 of around 410 to 440 ppm. In the process studied, a basic four step TVSA cycle comprising pressurization with feed, adsorption, blowdown, and desorption steps, was investigated first. Four different regeneration temperatures were tested along with four different gas space velocities. With this cycle configuration, CO_2 was concentrated to 95% from 400 ppm with total capture fractions as high as 81%. The energy consumption per ton of CO_2 captured in the system are discussed for the different process configuration. The results from this study are discussed on how to improve the possibility of using low Si/Al ratio faujasite structured zeolites in direct air capture of CO_2.

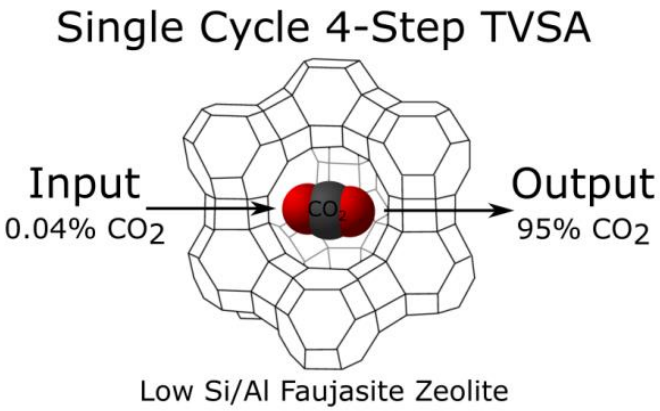

Keywords: CO_2 Capture, Zeolite 13X, Faujasite Zeolite, Temperature Vacuum Swing Adsorption, Direct Air Capture, Process Energy Requirements

2.2 Introduction

Increasing levels of CO_2 in the atmosphere has been shown to correlate to the increasing average global surface temperature which has led many researchers to invest time and effort into finding ways to effectively reduce the amount of CO_2 entering the environment or to capture CO_2 directly from the air. The latter, the subject of this study, has been dubbed Direct Air Capture (DAC) and has significantly gained interest as a true carbon negative strategy to reduce the amount of CO_2 in the atmosphere.[1–3] DAC, although thermodynamically less favourable than capturing CO_2 from large stationary post combustion point sources [4,5], has important benefits including; all greenhouse gas emissions (including transportation emissions) can be captured from one spot, previous CO_2 emissions can be captured, and the location as well as the size are not limited unlike post combustion capture of a power plant. Additionally, studies have shown that using methods such as the Reverse Water Gas Shift reaction in tandem with Fischer-Tropsch process, could allow DAC of CO_2 to be used to generate hydrocarbon fuels instead of traditional sources, which would allow for the continuing use of the transportation infrastructure well into the future.[6–8]

With DAC gaining interest, the scientific challenge of implementation is finding a low cost sorbent that has high uptakes, selectivity for CO_2, and fast kinetics, with strong physical and chemical stabilities, whose regeneration is not overly energy intensive. Research efforts into finding a promising sorbent can fall under four main categories: anime based sorbents [9–17], zeolites [9,10], absorption using caustic solutions [2,18–25], and metal organic frameworks (MOFs). [9,26–28]

Zeolites in literature have yet to be thoroughly investigated due to their hydrophilic nature for DAC. This is because of the low tolerance of zeolites, a hydrophilic material, to water which will decrease the overall adsorption capacity of CO_2 in its presence because of competitive adsorption [9,10,28,29]. A guard bed using a desiccant however, can be placed before the zeolite bed which would solve the problem by removing H_2O from the air stream before it contacts the zeolite [30]. Zeolites have many benefits that should not be overlooked and should be given an appropriate investigation before being dismissed. Zeolites, unlike amine based sorbents and MOFs for DAC of CO_2, are commercially available, are very well studied, and proven in industry due to their physical and chemical stabilities for many different situations. This coupled with faujasite structured zeolites being known to have very high capacities, favourable selectivities, and strong adsorption of CO_2, has made them excellent candidates for similar separations to DAC such as post combustion carbon capture projects [31–34]. It is also important to note that Na-X has been used and proven in industry for capturing CO_2 from air since the early 1980's in air prepurification processes in order to reduce CO_2 to less than the ppm level [35,36]. Another benefit that faujasite structured zeolites have, when compared to other promising technologies, is very fast uptake rates, allowing for beds to be optimized to have lower overall pressure drops [10]. This is important because air compression can cost $22 per kPa increase per ton of CO_2 captured which can make up the majority of the cost for DAC for the technology (assuming an energy cost of $0.06 kW/h) [10].

In this present study, we look at investigating zeolites' potential for the DAC of CO_2 as a means of producing 95% pure CO_2 for carbon sequestration while outlining clear positives and negatives of such a system. This will be done by using pure gas adsorption analysis along with breakthrough experimentation in order to determine optimal adsorption and desorption conditions for a temperature vacuum swing adsorption (TVSA) system. This work was inspired by previous work in the literature which investigated Li-LSX, K-LSX, and amine-grafted SBA-15, and was able to increase the concentration of CO_2 in dry air using TVSA from 0.000395% to 93%, 94%, and 98%, respectively, for the three different sorbents [10]. Another inspiration for this research is the constant reliability that faujasite zeolites have for DAC of CO_2 which, after many runs show their robustness for being implemented in such a technology [9].

2.3 Materials and Methods

2.3.1 Materials

CO_2, N_2, O_2, and Ar pure gases were obtained from Linde Canada (Burlington, Ontario, Canada) at purities of 99.99%, 99.999%, 99.994%, and 99.9993%, respectively. Adsorbent materials were chosen from a group of commercially available faujasite structured adsorbents which were acquired from Zeochem (Rüti, Switzerland), CECA Arkema Group (La Garenne-Colombes, France), Hengye (Houston, Texas, United States), and Honeywell UOP (Des Plaines, Illinois, United States). APG-III, and Z10-02ND were chosen because they are marketed for their use in air pre-purification, G5CO2M, Z10-01, and Na-X HP as standard 13X zeolites, and Ca-X and Na-LSX to give some variety. The details of these adsorbents are given in Table 2.1.

Table 2.1 – Commercially available 8 x 12 MESH faujasite structured zeolite samples used in this study with their respective manufacturer, trademark name, structure and cation.

Manufacturer	Name	Ion*	ρ_P [T] (g/mL)	Comments
CECA Arkema	G5CO2M	Na	1.03	Standard 13X
Honeywell UOP	APG-III	Na	1.07	Air prepurification
Zeochem	Ca-X	Ca	1.04	
Zeochem	Na-LSX	Na	1.08	Low Silica X
Zeochem	Z10-01	Na	1.04	Standard 13X
Zeochem	Z10-02ND	Na	0.98	Air prepurification
Hengye	Na-X HP	Na	1.07	Standard 13X

[T] Determined experimentally
* Major cation component in the crystalline structure (full data included in Table 2.2)

The chemical compositions of the samples were measured using energy-dispersive X-ray spectroscopy and are presented in Table 2.2. Since pellets were analysed, some binder composed of silica or alumina might be present which would inflate either the silica or alumina numbers.

2.3.2 Methods

2.3.2.1 Equilibrium Isotherms

Pure component isotherms were measured using a VTI Scientific Instruments (Hialeah, Florida, United States) GHP gravimetric system for CO_2, N_2, O_2, and Ar adsorption at 22°C for all samples. These were conducted by first weighing then regenerating the samples at 350°C under a vacuum pressure of approximately 10^{-8} atm until there was negligible weight change. Samples were then evaluated at increasing pressures of up to 6 atm. This was done using a microbalance with an accuracy of ± 5 ×10^{-7} g, and two pressure transducers, one from 0 to 1000 Torr with an accuracy of ± 0.25 % of reading, and another from 0 to 6 atm with an accuracy of ± 0.02 atm. Desorption was then performed by decreasing the pressure to check for any hysteresis. Buoyancy corrections were performed using helium at similar pressure and temperatures. A schematic drawing of the setup is included in the Supporting Information in Appendix I (Figure AI.1).

Table 2.2 – Chemical composition of faujasite structured zeolites used in this study in atomic percentages for cations within the lattice structure of the zeolite determined using SEM-EDS.

	Cation					Lattice Structure	
Adsorbent	Na^+	K^+	Mg^{2+}	Ca^{2+}	Fe^{2+}	Si^{4-}	Al^{3-}
G5CO2M	9.75	0.533	2.16	0.128	0.163	17.5	10.9
APG-III	11.15	0.083	1.01	0.360	0.275	16.6	12.1
Ca-X	2.65	0.148	0.758	5.25	0.223	17.5	12.4
Na-LSX	10.8	0.495	1.26	0.403	0.263	16.0	12.2
Z10-01	10.7	0.045	1.08	0.30	0.248	17.0	11.8
Z10-02ND	11.5	0.018	0.855	0.345	0.168	16.5	12.2
Na-X HP	11.5	0.06	0.67	0.178	0.210	17.2	11.9

The adsorption isotherms were then fitted to the Langmuir, Freundlich, Sips, and Toth models using the sum of least squares method. The isotherm model with the highest coefficient of determination (R^2) was used to reflect the isotherm. These models were then used to analyse the ideal selectivity between the different adsorbents. Equations for the isotherm models and ideal selectivity are included in the Supporting Information in Appendix I (Table AI.1, and Equation AI.1, respectively).

Rates of adsorption were calculated from pressure steps of vacuum to approximately 1.3 · 10^{-2} atm for all adsorbents tested. The equations for the diffusion into the particle using the Linear Driving Force (LDF) model are included in the Supporting Information in Appendix I (Equations AI.6 and AI.7). They are also sourced here [37].

2.3.2.2 Fixed Bed Adsorption Breakthrough Curves

Fixed bed adsorption-desorption breakthrough curves were used in order to determine the multicomponent gas adsorption behaviour of CO_2 separation from air. A schematic diagram of the breakthrough setup is

included in the Supporting Information in Appendix I (Figure AI.2). Breakthrough experiments were carried out by first packing the adsorbent column and using a piece of quartz wool on either end of the column. The column was then degassed at (350°C) with a helium purge for at least 24 hours. The feed gas for the experiment was ambient air from Ottawa that was compressed to 20 psi and pre-purified to remove moisture using calcium sulphate and any oils from the compressor using activated carbon. The flow rate of the air entering the column was controlled using a 10000 ± 100 sccm mass flow controller. The prepurified atmospheric air would then enter the packed bed adsorption column at conditions presented in Table 2.3. Eight temperature probes were used to monitor the bed temperature with one probe located each at the inlet and the outlet, and six located along the outside of the packed column. Column pressure was monitored with two pressure gauges (0 to 7 atm ± 0.02 atm) located at the inlet and outlet. The column outlet gas composition was measured as a function of time in tandem with a Model 410i IR (10'000 ppm CO_2) from Thermo Electron Corporation (Waltham, Massachusetts, United States) and a model 580 gas chromatograph from GOW-MAC (Bethlehem, Pennsylvania, United States) which was equipped with a thermal conductivity detector and a Porapak Q column.

Table 2.3 – Column properties and operating conditions for adsorption-desorption breakthrough curves obtained in this study.

Parameter	Value
Column Properties	
Column length, L	30 cm
Inner column diameter, D_{in}	1.09 cm
Outer column diameter, D_{out}	1.27 cm
Volume of column, V_c	28.1 cm^3
Void fraction, ε	0.4
Adsorption Operating Conditions for Case Study	
Total feed volumetric flow rate, Q	1250 – 10000 sccm
Average column pressure, P	1.25 atm
Average pressure drop, ΔP_{exp}	0.35 atm
Average temperature, T	23.5°C
CO_2 feed concentration, y_{CO2}	409 – 441 ppm
N_2 feed concentration, y_{N2}	78.1%
O_2 feed concentration, y_{O2}	20.9%
Ar feed concentration, y_{Ar}	0.93%

Once the outlet gas composition from the packed adsorption column reached the same as the inlet gas composition, the breakthrough was complete. Desorption of the column would then begin by reducing the pressure. Once a pressure of 0.1 atm was detected, the column would then start heating up (up to 261°C) while applying a vacuum. Exiting gas flow rates were analysed using a 50 ± 0.5 or 1000 ± 10 sccm mass flow meter. Once desorption was completed, the cycle would be repeated.

2.3.2.3 Four Step TVSA Cycle

Many commercial applications use a combined vacuum swing adsorption and temperature swing adsorption called a temperature vacuum swing adsorption (TVSA) [30]. This process is examined in the present work in order to determine the feasibility of producing a 95% CO_2 concentration desorption product from a feed stream of air. This specification of 95% was determined based on the required CO_2 concentration to pipeline CO_2 to the desired sequestration site [38,39].

Desorbed gas quantities were calculated using the measured flow rate and the measured concentration from both gas analysing instruments (GC and IR). These desorbed amounts were used to calculate the purity of the gas, which is shown in Equation 1. With DAC of CO_2 for greenhouse gas reduction, a purity of 95% CO_2 in the product stream is important to meet the specification for pipelines and compression. However, the recovery of CO_2 is less important and more importance should be given to reduce the overall energy per ton of CO_2 captured. Lower recoveries, also called capture fractions, theoretically have also been shown to have higher thermodynamic efficiencies [40], however, smaller capture fractions of CO_2 require larger pumping energies which is discussed later. The definitions for the capture fraction of CO_2 during adsorption (α_A) and during desorption (α_D) are shown in Equations 2 and 3.

$$Purity = \frac{Moles\ of\ CO_2\ from\ Desorption\ Step}{Total\ Moles\ of\ Gas\ from\ Desorption\ Step} \times 100\% \quad (1)$$

$$\alpha_A = \frac{Moles\ of\ CO_2\ Adsorbed\ during\ Adsorption\ and\ Pressurization\ Steps}{Total\ Moles\ of\ Gas\ that\ Entered\ the\ Column\ during\ \ Adsorption\ and\ Pressurization\ Steps} \quad (2)$$

$$\alpha_D = \frac{Moles\ of\ CO_2\ from\ Desorption\ step}{Total\ Moles\ of\ CO_2\ from\ Desorption\ and\ Blowdown\ Steps} \quad (3)$$

The total capture fraction of the process (α_T) is the product of these two capture fractions, assuming that moles of CO_2 adsorbed during adsorption and pressurization steps are equal to the total moles of CO_2 coming out from the desorption and blowdown steps. For the four step TVSA cycle, a single adsorption bed was used. The bed was first pressurized quickly from vacuum to the adsorption pressure and then the adsorption step would take place. The adsorption step would last until the column outlet concentration of CO_2 reached the inlet concentration at which time the column was completely saturated with CO_2. Once the column is saturated, the co-current regeneration would be started. This was composed of a blowdown step where the pressure would be slowly decreased to 0.1 atm over the course of 5.3 ± 1.1 min, followed by the desorption step where the column would be heated up to its regeneration temperature while maintaining the vacuum. In total, the blowdown and the desorption steps took 3 hours. Regeneration temperatures of 261°C, 194°C, 116°C, and 62°C all with an applied vacuum and just a vacuum were tested for an adsorption gas hourly space velocity (GHSV) of 13400 h^{-1}. GHSV is defined in the Supporting Information in Appendix I (Equation AI.9). GHSVs of 34400 h^{-1}, 27000 h^{-1}, 13400 h^{-1}, and 6720 h^{-1} after a regeneration temperature of 194°C were tested as well. The fixed GHSV and regeneration temperatures were chosen as the middle point values studied in this work.

2.3.2.4 Estimation of Energy Requirements

The economic feasibility of a DAC technology is based on the operating cost, initial capital cost, integration into present technology, and the value of the product. Each one of these attributes has an effect on the final cost per ton of CO_2 captured. A recent report on the feasibility of DAC using sodium hydroxide absorption processes by the American Physical Society estimated the cost at \$600/tonCO_2 [40]. This report concluded that DAC was economically unfeasible but studies quickly countered that using a solid sorbent system for DAC would significantly drop the cost to around as low as \$100/tonCO_2 [15]. Also, a very recent study has shown that using innovative solutions for NaOH solutions could also drop the cost to as low as \$94/ton of CO_2 captured which has been demonstrated in a 9 year pilot plant study [41].

The operating cost of a DAC technology is based on the mechanical energy and the thermal energy requirements for the system. Mechanical energy is generally provided by electricity, and is composed of three components: (E_f) for air flow through the sorbent, (E_v) for the removal of wastes and products by vacuum, and (E_c) energy to compress the product stream. Thermal energy can be provided by electricity or by a waste heat stream and is composed of two components: (E_S) the energy required to heat up the sorbent, and (E_D) the energy required to desorb the CO_2. By incorporating a waste heat stream, DAC would become more economically feasible by reducing the overall thermal energy requirements of the system.

The required energy for the flow of air through the adsorbent bed is one of the most important parameters when determining the energy requirement for a DAC process and has been found to be the most mechanical energy intensive portion of DAC for amine impregnated sorbents [15]. This is because of the low CO_2 content in air of 16.3 mmol of CO_2/m^3 of air (at 400 ppm of CO_2) and is heavily based on the total capture fraction of CO_2 from the process and the rate of diffusion of the sorbent. In order to estimate the energy requirement for air flow, a simple correlation which was derived and provided by the American Physical Society can be used (Equation 4)[40].

$$\boldsymbol{E_f = \frac{P_{drop}}{\alpha_T C_{CO2}}} \quad 4$$

$$P_{drop} = 150\frac{v\mu(1-\varepsilon)^2 L}{(\emptyset d_v)^2\varepsilon^3} + 1.75\frac{v^2\rho_f(1-\varepsilon)L}{\emptyset d_v\varepsilon^3} \quad 5$$

where the P_{drop} is the pressure drop which can be derived from the Ergun equation for a packed bed (Equation 5), α_T was calculated as the product of α_A and α_D using Equations 2 and 3, and C_{CO2} is the concentration of CO_2 in the air which is 0.72 g/m^3 for 400 ppm of CO_2 at 25°C and 1 atm. Where L is the length of the bed, v is the superficial velocity, d_v is the diameter of the pellets, ε is the void fraction in the bed. $\emptyset$ is the sphericity which was taken to be unity in this study.

A theoretical method can be used to calculate the capture fraction of CO_2 during adsorption which can then be defined from the characteristic length of the adsorbent, L_O, which is similar to the concept of the

mass transfer zone of a breakthrough curve shown in Equations 6 and 7 [40]. It is essential to highlight the importance of kinetics in adsorption systems.

$$\boldsymbol{\alpha_A = 1 - exp(-\frac{L}{L_o})} \quad 6$$

$$L_o = \frac{\eta v \varepsilon {d_v}^2}{\mathcal{D}} \quad 7$$

$\mathcal{D}$ is the molecular diffusion of CO_2 in air which is approximately $2.1 \cdot 10^{-5}$ m^2/s, and η is the dimensionless separation constant (Equation 8).

$$\boldsymbol{\eta = f(D_p)} \quad 8$$

The dimensionless separation constant parameter depends on the effective adsorption of the CO_2 into the wall of the pellet, and is equal to 0.068 for the case of diffusion from the gas to the pellet being slower than the diffusion from the surface of the pellet to the inside of the pellet, D_p [40].

Therefore, the energy requirement for the flow is mainly a function of the system parameters (v, L), and the sorbent parameters (D_p, ε, d_v, $\emptyset$). In order to compare different sorbents, system parameters should be maintained constant, which would only leave diffusion properties to be compared. This is convenient in sorbent selection due to the ability to investigate the rate of sorption of a single sorbate into a sorbent particle using the LDF (Linear Driving Force) model experimentally [37].

The mechanical energy for the vacuum is considerably less than the required energy for flow which has been observed in literature [15]. This was due to the significantly larger flow required to capture the CO_2 compared to the flow for the amount of CO_2 desorbed. Assuming only pure CO_2 is being pulled from the bed, this energy cost would only be 22.4 MJ/tonCO_2 [15]. Another finding from literature noted that, if all gases desorbed from the bed were assumed to be CO_2, the energy for compression of the final product to 15 MPa would remain constant at approximately 417 MJ/tonCO_2 [15]. This article assumed a vacuum pump and the compressor efficiency of 80%.

The total thermal energy required for a DAC system is the sum of the energy required to desorb the CO_2 along with the sensible energy to heat the gas to the desorption temperature (Equation 9) and the sensible energy to heat up the sorbent to the desorption temperature (Equation 10) [40].

$$\boldsymbol{E_D = (M_A \Delta H_A + M_A C_{PA} \Delta T)/\alpha_D} \quad 9$$

$$E_S = M_S C_{PS} \Delta T / \alpha_D \quad 10$$

where M_A is the mass of the adsorbed species, M_S is the mass of the adsorbent, ΔH_A is the heat of adsorption, C_{PA} is the heat capacity of the adsorbed species, and C_{PS} is the heat capacity of the sorbent. A sorbent that can be regenerated at a lower temperature will therefore have a lower required change in

temperature which will require less energy per ton of CO_2 captured. For a cyclic process, other strategies to lower the cost per ton of CO_2 captured are to have a lower heat of adsorption as well as to have a high adsorption capacity for the sorbent. The latter in particular can reduce energy requirement since the loss of energy due to heating up the sorbent decreases per adsorption cycle as the working capacity of the sorbent increases which can be seen in Equation 10.

One of the measurable initial capital cost for DAC technology is the capital investment for the liquid or solid sorbents. This capital cost is a function of the sorbent's working capacity, the sorbent's working lifetime, and the swingtime of the process as shown in Equation 11.

$$\frac{\boldsymbol{Cost\ of\ Sorbent\ Consumption}}{\boldsymbol{tonCO_2}} = \frac{\boldsymbol{Sorbent\ Cost}(\$/\boldsymbol{kg}) \times \boldsymbol{Swingtime}(\boldsymbol{hr})}{\boldsymbol{Working\ Capacity}(\boldsymbol{tonCO_2/kg}) \times \boldsymbol{Lifetime}(\boldsymbol{hr})} \quad 11$$

Having a lower cost of sorbent consumption relative to amount of CO_2 captured is desirable and can only be achieved with high working capacities, fast cycles, and long lifetimes. High working capacities can be investigated by looking into the loadings in pure gas adsorption isotherms, with larger capacity differences over temperature and pressures indicating more desirable sorbents. Lifetime of the sorbent is harder to quantify in a laboratory, however. Lifetimes, unless degradating after dozens of cycles which has been identified in the majority of MOFs and hybrid ultramicroporous materials [9], are harder to measure, with amine impregnated sorbents being shown only up to 100's of repeated cycles in the presence of water [14]. Zeolites in industry are shown to last over 10 years in air separation processes.

2.4 Results

2.4.1 Equilibrium Adsorption Isotherms

The pure component adsorption isotherms of CO_2, N_2, O_2, and Ar with faujasite structured zeolites at 22°C can be seen in Figure 2.1. Solid lines in the figure represent the adsorption isotherm model with the highest coefficient of determination. All isotherms tested showed no hysteresis indicating that the isotherms are completely reversible. At all pressures, carbon dioxide was the most adsorbed gas, followed by nitrogen, then oxygen, and argon was the least adsorbed species. This was the same trend that was shown in literature with other sodium based faujasite structured zeolites [42,43]. The adsorption equilibrium of CO_2 and N_2 was compared to previous literature with similar results for similar adsorbents with deviations of up to 13 % [44,45]. Adsorption isotherm data points (Tables AI.2 to AI.8) and isotherm model parameters (Table AI.9) are included in the Supporting Information in Appendix I.

For adsorption at 22°C and a concentration of 400 ppm of CO_2, adsorption capacity was predicted to be between 0.13 to 0.51 mmol/g of adsorbent calculated from the isotherm model with the low SiO_2/Al_2O_3 ratio zeolites having the highest adsorption capacities. This adsorption capacity is within the range of those measured from literature with Na-X at 0.41 mmol/g [10] and 13X at 0.2 mmol/g [36] at 395 ppm of CO_2. However, Stuckert and Yang (2011)[10] reported better zeolitic materials such as Li-LSX, Na-LSX, and Ca-LSX

with adsorption capacities of 1.34, 0.87, and 0.76 mmol/g at 395 ppm of CO_2 at 298 K. This made in house zeolite would have significantly increased efficacy because increased adsorption capacity reduces the energy requirement to heat up the sorbent (E_S) per ton of CO_2 captured.

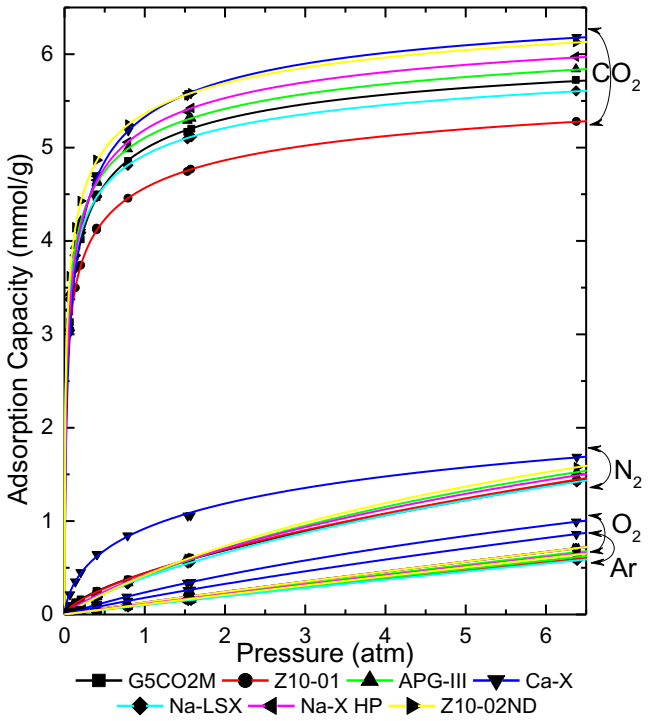

Figure 2.1 – CO_2, N_2, O_2, and Ar pure adsorption isotherms at 22°C for CECA Arkema Group's G5CO2M, Honeywell UOP's APG-III, Hengye's Na-X HP, and Zeochem's Ca-X, Na-LSX, Z10-01, and Z10-02ND. Each isotherm is fitted to Langmuir, Freundlich, Sips, and Toth and is represented by the model with the best fit.

2.4.2 CO_2 Selectivity

As can be seen from the equilibrium isotherms, faujasite structured zeolites are very selective for carbon dioxide. This can be more clearly seen in Figure 2.2 where the ideal selectivity is shown for in a part for part basis at different total pressures for air having 780840 ppm of N_2, 20960 ppm of O_2, and 9300 ppm of Ar and 400 ppm of CO_2. The selectivity is calculated as the ratio of CO_2 pure gas adsorption capacity corresponding to a relative partial pressure of 400 ppm over the summation of the pure gas adsorption capacities for N_2, O_2, and Ar at their corresponding relative partial pressures at 780840 ppm, 20960 ppm, and 9300 ppm, respectively. This was calculated from the isotherm models that best represented each isotherm. Z10-02ND, APG-III, and Na-LSX have the highest selectivity values for CO_2 out of the adsorbents tested. This is not surprising since two of these adsorbent (Z10-02ND and APG-III) are marketed for air prepurification. They are also the adsorbents with the lowest SiO_2/Al_2O_3 ratios, indicating that the more heterogeneous the surface, the greater the ideal adsorption selectivity for CO_2. One thing of interest is that the ideal selectivity of CO_2 decreases as pressure increases for these adsorbents, indicating that a CO_2 separation from the air will not benefit from selectivity at higher pressures for the best performing

adsorbents. This is due to the sharp rectangular nature of the CO_2 isotherms for highly selective adsorbents compared to the other ones. At even very low partial pressures of CO_2 in air (400 ppm), CO_2 seems to be favourably adsorbed compared to nitrogen.

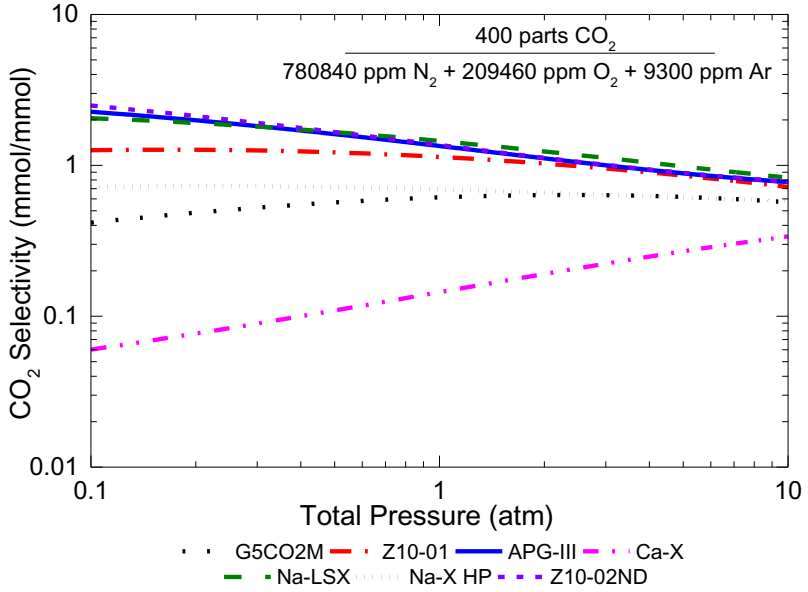

Figure 2.2 – The adsorption capacity ratio of CO_2 at 400 ppm over the summation of adsorption capacities of N_2, O_2 and Ar at 780840, 209460, and 9300 ppm, respectively, at different total pressures calculated from their isotherms at 22°C.

2.4.3 Adsorption Rates

Adsorption uptake rates are important parameters for the economic viability of DAC of CO_2 with higher uptake rates having steeper breakthroughs as well as higher capture fractions. This relationship can be seen in Equations 4 and 5 in Section 3. With higher capture fractions (α_T), less energy per ton of CO_2 captured is required.

The LDF model was used to model the diffusion of CO_2 into the particles using the uptake rates from the constant pressure gravimetric experiments from the initial equilibrium data point on the isotherms. Graphs showing the uptake rates for all zeolites are included in the Supporting Information in Appendix I (Figure AI.4) along with the equations for the diffusion time constant into the particle using the LDF model which are sourced from literature [37]. The calculated values in Table 2.4 show good agreement with values calculated in the literature [10]. The diffusion time constants of CO_2 into the particle are the highest for Z10-02ND and APG-III, which are the adsorbents designed for air prepurification and the lowest for G5CO2M and Z10-01 which are basic 13X zeolites. However, all of these faujasite structured zeolites perform two orders of magnitude better than amine-grafted SBA-15 data from literature with a diffusion time constant of $0.043 \cdot 10^{-2}$ s^{-1} [10]. With grafted amines typically having significantly higher surface areas than impregnated amines, impregnated amines would be hypothesized to have worse kinetics.

Table 2.4 – CO_2 LDF mass transfer coefficients into the particle calculated from the LDF model for the adsorbents studied.

	G5CO2M	Z10-01	APG-III	Ca-X	Na-LSX	Na-X HP	Z10-02ND
100·kL (s^{-1})	1.76	1.69	1.87	1.76	1.78	1.81	1.90

2.4.4 Fixed Bed Breakthrough Curves

APG-III was selected for further breakthrough experimentation due to its highest adsorption capacity predicted from the isotherm model, one of the highest CO_2 selectivity at 1 atm, and second highest diffusivity compared to the other adsorbents tested in this study. Due to the CO_2 selectivity ratio being only 1.35, a simple two stage adsorption cycle would not yield a high enough purity of 95% for carbon sequestration (since the amount of N_2, O_2, and Ar that would be co-adsorb would dilute the product gas). Therefore, a four stage TVSA cycle was chosen. This cycle includes a pressurization, adsorption, blowdown, and desorption steps where the DAC of CO_2 will happen during the pressurization and adsorption steps, the majority of N_2, O_2, and Ar within the column will be evacuated during the blowdown step, and the CO_2 will be recovered as a product gas during the desorption step. After the desorption step, the column would be cooled in ambient air before starting the pressurization step. A design note: It was observed that by starting pressurization step immediately with a hot column the thermal front would advance and exit the column relatively quickly without impacting concentration front during the adsorption step.

Four regeneration temperatures were tested to determine their effects on the DAC of CO_2. This include regeneration temperatures of 60°C, 116°C, 194°C, and 261°C with vacuum, as well as one run where only a vacuum was applied at room temperature. The blowdown and desorption steps were cumulatively three hours long. Figure 2.3 show the breakthrough curves after the blowdown and desorption steps for air passing through the column at a GHSV of 13400 h^{-1}. Corresponding adsorption and desorption temperature profiles are included in the Supporting Information in Appendix I (Figure AI.5).

Breakthrough times after desorption using a regeneration temperature of 261°C is the longest, with lower regeneration temperatures having sooner breakthroughs. This is due to more CO_2 being able to escape the column at higher temperatures than at lower temperatures over the 3 hours regeneration period. For regeneration temperature of 60°C, the effluent concentration wave front of CO_2 happened immediately. For a regeneration temperature of 261°C, 0.41 ± 0.02 mmol of CO_2/g of APG-III was released, with the coupled breakthrough adsorbing 0.40 ± 0.04 mmol of CO_2/g of APG-III, and as the regeneration temperature decreased, the breakthrough adsorption capacity decreases. This effect can be seen in Figure 2.4 which shows the breakthrough adsorption capacity. Figure 2.4 shows both the adsorption and desorption breakthrough capacity for APG-III for the different temperatures tested. The calculation for this is

described in the Supporting Information in Appendix I. The error bars in Figure 2.4 were determined from replicate runs showing the reproducibility of these results.

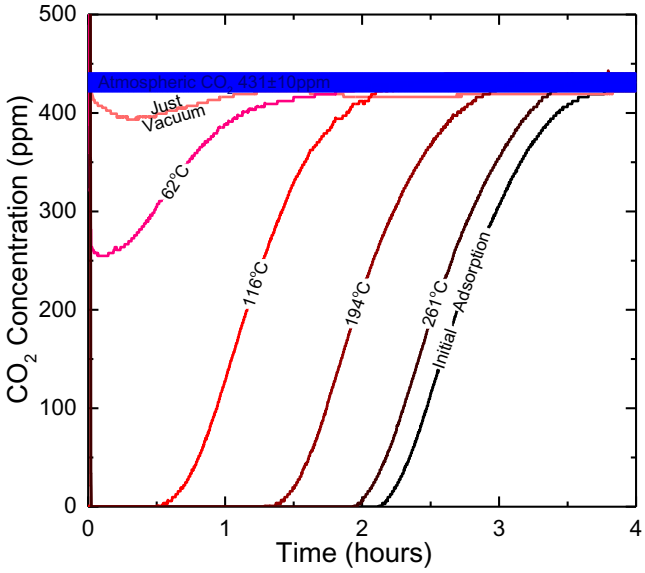

Figure 2.3 – Breakthrough curves for a column packed with APG-III with a positive CO_2 concentration step of 431 ± 10 ppm of CO_2 (indicated in blue) at 23.5°C and a GHSV of air at 13400 h^{-1}. These breakthroughs happened after regeneration temperatures of 62°C, 116°C, 194°C, and 261°C while applying a vacuum over the course of three hours.

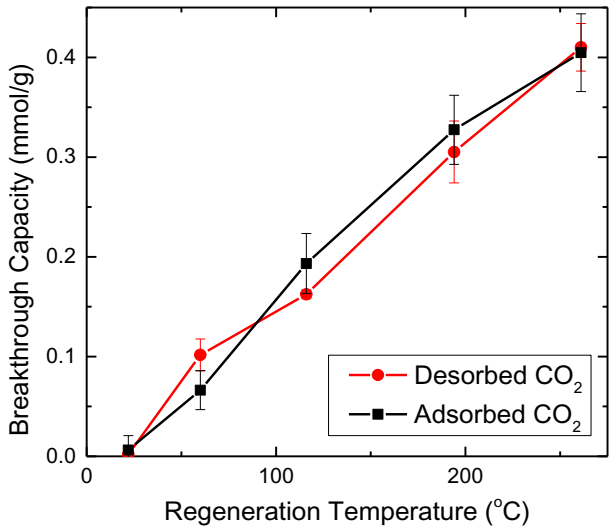

Figure 2.4 – Breakthrough adsorption and desorption capacity of CO_2 for APG-III in the column for the adsorbed CO_2 during the adsorption and pressurization steps as well as the desorbed CO_2 during the combined blowdown and desorption steps.

The initial adsorption after a complete regeneration using a helium flow and temperature of around 350°C over 24 hours with a He purge had a breakthrough adsorption capacity of 0.42 ± 0.04 mmol of CO_2/g of adsorbent. This is less than the predicted adsorption capacity from the isotherms which was 0.51 mmol of CO_2/g of adsorbent. From Figure 2.3, using a regeneration temperature of 261°C the adsorbent bed was

not able to fully regenerate. This can be seen in Figure 2.3 with the breakthrough curves for 261°C breaking through before the initial adsorption. This difference is due to the high affinity of CO_2 to APG-III within the adsorption column even at vacuum pressures of 0.010 ± 0.002 atm and elevated temperatures which has been seen in literature with 13X [46]. This affinity for CO_2 from APG-III can also be seen from just applying a vacuum of 0.008 ± 0.002 atm to the column during regeneration where almost no CO_2 loss was observed. This effect can be used to optimize the purity while reducing the loss of CO_2 during the blowdown and the desorption step by using the vacuum to first remove the N_2, O_2, and Ar from the adsorption column and subsequently desorb the CO_2 with additional heat.

This affinity for CO_2 can also be seen in the sharp shock wave of the effluent concentration after regeneration temperatures of 116°C, 194°C, and 261°C. This sharpness in the breakthrough's shape is due to the favourable rectangular shape of the isotherm as well as the fast adsorption kinetics of CO_2 for APG-III which causes a self-sharpening mass transfer zones as it moves through the bed. This effect has been seen within literature [30] with similar shaped CO_2 breakthroughs for Li-LSX and K-LSX from air [10]. However, these breakthroughs do show some dispersion in the trailing edge of the shockwave which is also impacted on the use of glass wool or void space within the experimental setup. The slight change in the exiting gas temperature due to the exothermic nature of adsorption of 0.75°C would also make the trailing edge distended which can be seen in the temperature profiles included in the Supporting Information in Appendix I (AI.Figure 5). The sharpness of the effluent concentration after regeneration temperatures of 116°C, 194°C, and 261°C are very similar.

The effect of GHSV on the breakthrough on APG-III at 6720 h^{-1}, 13400 h^{-1}, 27000 h^{-1}, and 34400 h^{-1} were tested each using the same regeneration temperature of 194°C. These results are presented in Figure 2.5. The experimental pressure drop was determined to be 18, 35, 65, and 82 kPa for flow rates of 6720 h^{-1}, 13400 h^{-1}, 27000 h^{-1}, and 34400 h^{-1}, respectively. This pressure drop is much greater than the theoretical pressure drop of 2, 5, 15, and 21 kPa respectively, due to the glass wool, fittings, and bends in the equipment. All GHSV's had statistically similar breakthrough adsorption capacities with an average of 0.32 mmol/g along with similar sharpness in the shock wave. However, there is a slight trend in the breakthroughs being sharper at faster GHSVs. This can be seen with the leading edge of the wave front being smaller for faster GHSVs than slower ones in Figure 2.5. This is not surprising due to the nature of self-sharpening wave front with even the fastest GHSV of 34400 h^{-1} having a clean breakthrough.

2.4.5 Energy Requirements for Greenhouse Gas Reduction

In order to mitigate CO_2 in the atmosphere, CO_2 must be pipelined and sequestered at concentrations of 95% and pressures of 14 MPa [15,38,39]. For a 95% CO_2 purity for the product stream during the desorption step, capture fractions for a combined blowdown and desorption step (α_D) were calculated from the experimental data and are presented in Figure 2.6 for desorption temperatures of 116°C, 194°C, and 261°C. For 60°C, insufficient CO_2 was released. The purity fluctuated for the 116°C, 194°C, and 261°C due to human error in manually slowly opening in the valve during the blowdown step. To correct this,

shifting the time in which the desorption step started in the calculations by ± 1.3 min make sure that the purity was 95% according to Equation 1. This figure shows that the capture fraction for desorption increases from 96% at a regeneration temperature of 116°C to 99% at a regeneration temperature of 261°C. This is due to similar amount of CO_2 being desorbed during the blowdown step, but more CO_2 being released during the desorption step as regeneration temperature increases.

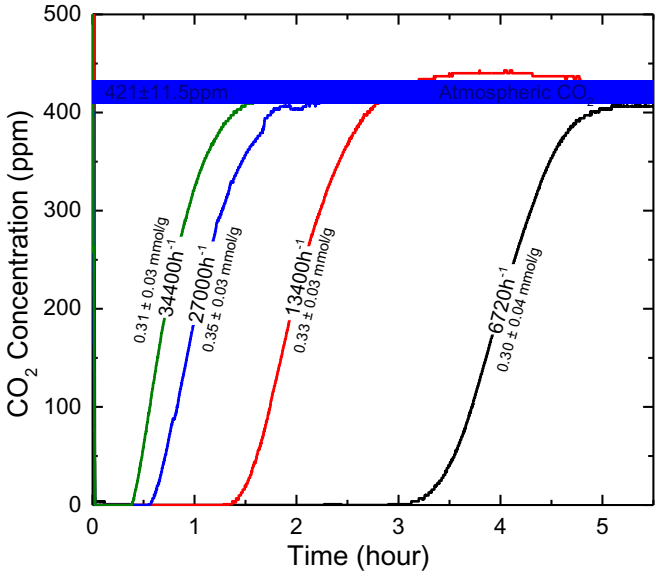

Figure 2.5 – Breakthrough curves for a column packed with APG-III with a positive CO_2 concentration step of 421 ± 11.5 ppm of CO_2 (indicated in blue) at 23.5°C after a regeneration temperature of 194°C and vacuum over the course of three hours for GHSV of air of 34400 h^{-1}, 27000 h^{-1}, 13400 h^{-1}, and 6720 h^{-1}. Corresponding breakthrough adsorption capacities are next to the displayed GHSVs.

Adsorption capture fractions were calculated from the beginning of the pressurization until the effluent concentration reached 95% of the input concentration during the adsorption breakthrough. The adsorption capture fraction increased as the regeneration temperature increased, with this effect being more significant than the same trend with the desorption capture fraction. The adsorption capture fractions changed from 0.64 after regeneration at 116°C to 0.79 after regeneration at 261°C as can be seen in Figure 2.6. Although the length of unused bed (LUB) for different regeneration temperatures are the same, the difference in adsorption capture fractions come from the fact that columns regenerated at higher temperatures have higher adsorption capacities, leading to later breakthroughs.

Energy costs per ton of CO_2 captured are important for the viability of a DAC process. Figure 2.7 shows the total energy per ton of CO_2 captured which are composed of the mechanical energy for the flow, vacuum, and compression to 14 MPa, and the thermal energy for heating during the desorption and the sensible heating requirements for the sorbent to be heated up to the desorption temperature for APG III.

For the mechanical energy, if the vacuum and the compression are assumed to be applied to pure CO_2, the energy requirement of 430 MJ/ton of CO_2 is constant. The energy requirement for flow is a function of the total capture fraction and the pressure drop which was calculated using Equation 2 which was 2950 Pa for

a GHSV of 13400 h^{-1} (which is equivalent to a flow of 2500 sccm). With the pressure drop being constant over these experiments, the energy cost for flow mirrors the same trend shown in Figure 2.6. This trend shows that with increasing regeneration temperatures during desorption having higher values for the total capture fraction reduces the energy cost of flow E_f per ton of CO_2 captured. Overall, mechanical energy requirements for DAC are only 30% to 39% of the total energy requirement.

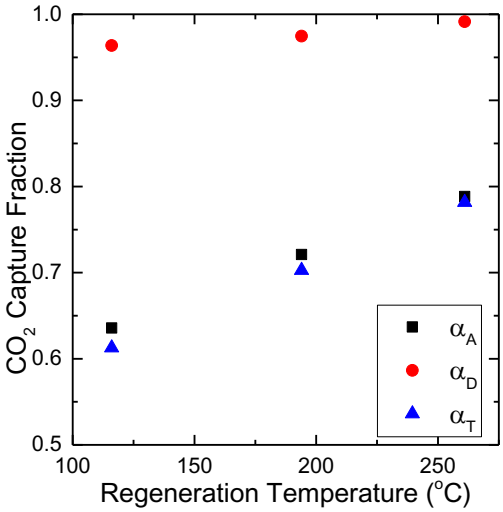

Figure 2.6 – CO_2 capture fractions for the adsorption at 95% effluent concentration/input concentration composed of the pressurization and adsorption step (α_A), desorption with a CO_2 purity of 95% composed of the blowdown and desorption steps (α_D) and the total capture rate of all four steps (α_T) at a GHSV of 13400 h^{-1} and temperatures of 116°C, 194°C, and 261°C for APG-III.

Thermal energy requirements to capture one ton of CO_2 was calculated using Equations 9 and 10. The sensible heating requirements for the sorbent, E_S, were found to be the most energy intensive part making up between 56% and 64% of the total energy requirements. This energy requirement per ton of CO_2 captured was higher at higher regeneration temperatures and lower at lower regeneration temperatures. The same trend was also observed for the desorption energy requirements E_D. However, this value is significantly smaller than E_S, with E_D making up only 4% to 5% of the total energy requirements. The energy cost of E_S for APG-III is significantly larger than that for the E_S for amine solid sorbents when compared to literature [15]. This is in part due to the higher temperatures required for CO_2 desorption from low Si/Al ratio faujasite structure zeolites (~200°C) compared to the temperature required to desorb CO_2 from amines solid sorbents (~120°C) [33,47]. However, due to amine solid sorbents forming chemisorption bonds with CO_2 [33,47] the energy for desorption is higher with impregnated amines such as MEA, DEA, and PEI requiring 81 kJ/mol, 65 kJ/mol, and 69 kJ/mol [48], respectively, compared to APG-III which was calculated to be 31.7 ± 1.3 kJ/mol (calculations shown in Supporting Information, Figure AI.3). This gives APG-III a lower E_D when compared to the E_D for amine solid sorbents from literature [15,48].

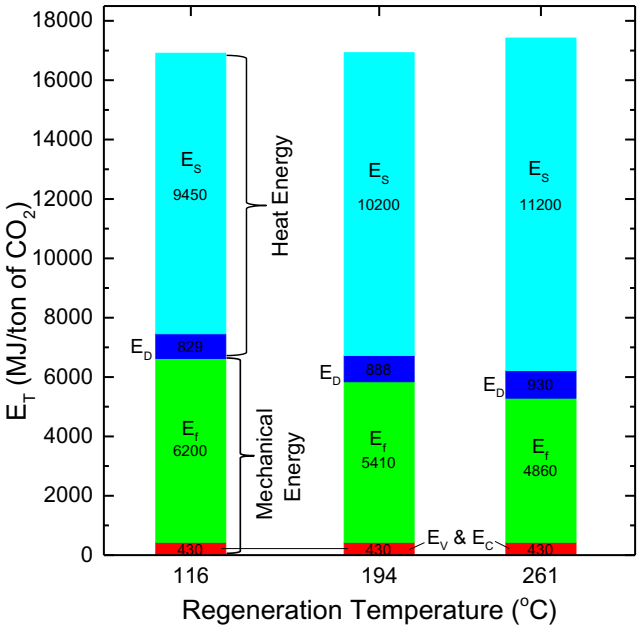

Figure 2.7 – Energy cost per ton of captured CO_2 at a GHSV of 13400 h^{-1} at 23.5°C and temperatures of 116°C, 194°C, and 261°C calculated using Equations 4, 5, 9, and 10 for APG-III.

One benefit of higher regeneration temperatures is that the volume productivities (CO_2 captured per cubic meter) are better than those at lower regeneration temperatures. This is because there are larger CO_2 adsorption breakthrough capacities at higher regeneration temperatures than at lower ones allowing more CO_2 per kg of adsorbent. Lower volume productivities means more dead volume must be evacuated per ton of CO_2 captured which will increase the vacuum energy requirements.

The effect of the GHSV on the energy consumption for flow was also investigated and is presented in Figure 2.8 for APG-III. This figure shows that as the GHSV decreases, the pressure drop across the bed decreases requiring less energy per ton of CO_2 captured compared to higher GHSV values. This effect is compounded by slower GHSV having higher adsorption capture fractions. This is due to the length of the equilibrium section of the breakthrough curve is much higher relative to the LUB section at low GHSV conditions. With slower GHSV having lower pressure drops and higher adsorption capture fractions, the energy requirement for flow decreases significantly from 21400 MJ/ton of CO_2 to 2160 MJ/ton of CO_2 for 34400 h^{-1} to 6720 h^{-1}, respectively. This is a reduction of 10 times the energy cost, however, by reducing the flow rate, the amount of CO_2 that is captured per day reduces due to the longer adsorption step that is required to saturate the adsorbent bed. With the energy for flow requiring mechanical energy often provided by electricity, reducing this energy cost will help make DAC of CO_2 much more viable.

There are three additional strategies that could be utilized to reduce the energy cost required for flow. One strategy is utilizing a shortened length of adsorbent bed which would reduce the overall pressure drop (can be seen from Equation 5), but this would also reduce the capture fraction. Another strategy would be ordered packed beds which would significantly reduce the energy cost for flow to capture CO_2. Ordered packed beds have been investigated in literature in recent years using 3D printing fusion deposition

modeling for many applications [49–52]. This would particularly be beneficial to DAC due to the low concentration of CO_2 in the air requiring large pumping requirements. Lastly, utilizing larger adsorbent particles could possibly reduce the energy required to pump air through the adsorbent bed per ton CO_2 captured. Larger particles would reduce the pressure drop across the bed but have been shown to have higher mass transfer resistances which leads to a more dispersed breakthrough [53] reducing the adsorption capture fraction.

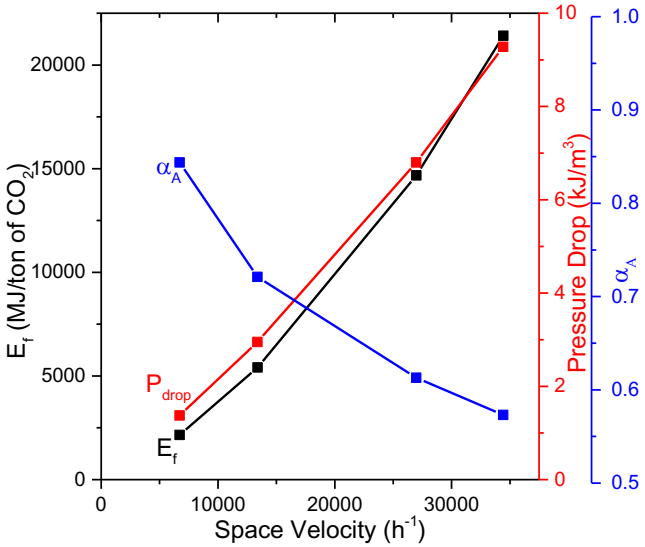

Figure 2.8 – The effect of GHSV on the energy for flow at 23.5°C, pressure drop, and the adsorption capture fraction for a regeneration temperature of 194°C.

2.4.6 Moisture Effect

Water must first be removed from the air before CO_2 can be captured using zeolite materials. This is due to the hydrophilic nature of zeolites competitively adsorbing water preferentially over CO_2. This is in contrast to absorbent materials which require a moist stream of air to not damage the materials in the case of solid supported amines [29,54,55] or have to deal with evaporation losses of water which happens with NaOH solutions [19,20].

To overcome this problem, a desiccant bed such as silica gel or 3A which do not significantly adsorb or are kinetically hindered would allow the CO_2 to pass through but would capture the humidity in the air. This would then allow a low Si/Al ratio faujasite zeolite such as APG-III to subsequently capture the CO_2 from the air. This required additional process would have an additional energy cost and would make a large impact on the economics of DAC using zeolites.

This additional energy cost would be the E_f to push the air additionally through the desiccant bed, E_D to desorb the water and elevate its temperature from the adsorption temperature to the desorption temperature, and E_S to elevate the sorbent temperature from its adsorption temperature to its desorption temperature. 3A and silica gel have different desiccant process parameters outlined in Table 2.5. This

difference in parameters has been noted in literature making silica gel more suited as a desiccant at higher H_2O partial pressures and 3A more suited at lower H_2O partial pressures [56].

Table 2.5 – Desiccants 3A and silica gel parameters for the desorption temperature, density, heat capacity, H_2O heats of adsorption, and TD-Toth parameters for the H_2O adsorption capacity.

Desiccant	T_D (°C)	Density (kg/m³)	C_P (kJ•kg⁻¹•K⁻¹)	ΔH_A (kJ/mol)	Water Adsorption Capacity TD-Toth Parameters [57]				
					a_0 (mol•kg⁻¹•kPa⁻¹)	b_0 (kPa⁻¹)	E (K)	t_0	c (K)
Silica Gel	110	720	1.13	2980 [58]	176.7	$2.787 \cdot 10^{-5}$	1093	$-1.19 \cdot 10^{-3}$	22.13
Zeolite 3A	175	780	0.836	3400 [59]	$1.106 \cdot 10^{-8}$*	$4.714 \cdot 10^{-10}$*	9955*	0.3548*	-51.14*

*TD Toth parameters for 5A were used as an approximation to 3A due to no available estimation data for the desired temperature range due to their similar water adsorption capacities which was validated through literature [59,60].

This impact on the energy consumption per ton of CO_2 captured to remove H_2O has been estimated and shown in Figure 2.9 for APG-III. This was estimated for air containing 431 ppm of CO_2 for APG-III regeneration temperature of 194°C, an adsorption GHSV of 13400 h^{-1}, which has an adsorption capacity of 0.33 mmol of CO_2 per gram of APG-III. This was determined by the H_2O saturation vapour pressure in air using a temperature dependant empirical equation from literature [61], estimating the H_2O adsorption capacity of the desiccant using the TD-Toth equations, using the parameters that are shown Table 2.5, with Equations 4, 9, and 10. Information about the calculations for this is included in the Supporting Information in Appendix I. This estimate however, did not take into consideration the change in adsorption capacity for CO_2 of APG-III with respect to temperature. In Figure 2.9, the energy requirements for both 3A and silica gel to remove water from air are shown. From this figure, 3A or silica gel can be chosen depending on the feed air temperature and the relative humidity level to have the least energy requirement for the removal of the moisture. In accordance with literature, lower partial pressures of H_2O which occur at lower temperatures and humidity levels are more energy efficient to remove with 3A than with silica gel.

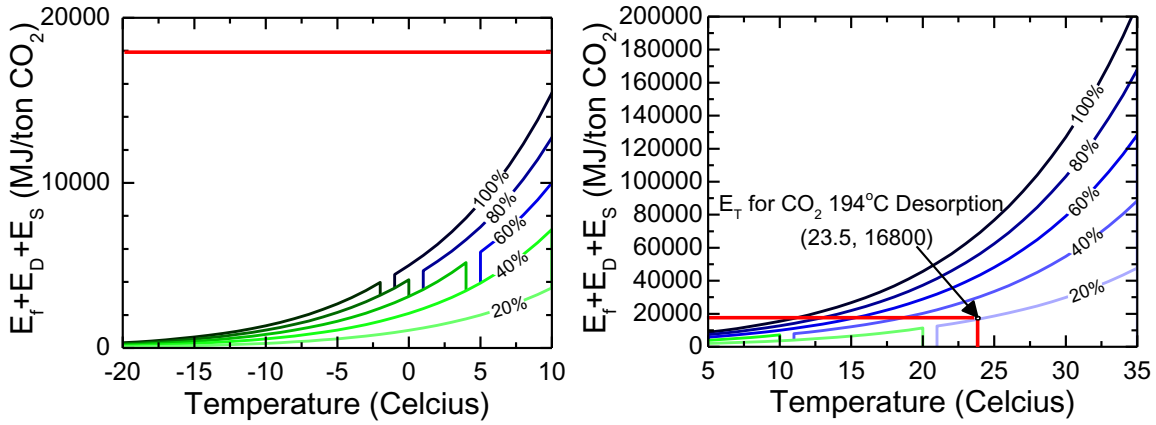

Figure 2.9 - Energy required to remove water from air for the DAC of CO_2 using APG-III using either silica gel (blue) or zeolite 3A (green) as a function of temperature and humidity levels 20%, 40%, 60%, 80% and 100% between the temperature of -20°C to 10°C (left) and 5°C to 35°C (right).

The energy requirement to remove water from air is lower when the temperature is lower and the humidity is lower. This effect is significant with the difference in humidity and temperature effectively determining the success of using APG-III as a DAC of CO_2 adsorbent. For example, earlier experimentation taking place at 23.5°C with a GHSV of 13400 h^{-1} and a regeneration temperature of 194°C required 16800 MJ/ton CO_2 captured. This is the same energy required to remove water from air at a humidity level of 22.3%. The energy required to dehumidify the air is composed of thermal energy which makes up between 92% and 97% and electrical energy which makes up between 3% and 8% of the total energy requirements. Similar to the capturing CO_2, utilizing a waste heat source would help significantly reduce the energy required to remove water from the air.

2.4.7 Capital Cost and Location

Operating a DAC of CO_2 process can potentially happen anywhere on the planet due to all air on the planet containing CO_2. This allows some flexibility in terms of operating costs to run such a process by selecting a location that has desirable operating conditions. This problem has been investigated before for DAC of CO_2 for NaOH in literature [2]. Low humidity places are desirable which can be found in desert locations due to their low humidity levels. Deserts can also be beneficial because of the low cloud cover allowing for solar panels to capture significant amounts of energy which can provide the heating requirements as well as electrical requirements to run the process. Deserts also have cold nights and warm days to design adsorption and desorption steps around. They are locations where instillation of such a unit would not affect the environment significantly. Colder temperature places are also beneficial which can be found closer to the poles as well as at higher elevations. Running this process with cool air would also improve the amount of CO_2 adsorbed which might also decrease the energy required for this process making it more economical. However, further studies would be required to determine this.

Investigating different locations on the planet concludes polar deserts are excellent locations for this process. This is because polar deserts are arid frigid locations which would reduce the energy required to dehydrate the air as well as provide higher CO_2 adsorption capacities at lower temperatures. One advantageous place in particular is the super arid McMurdo Dry Valley in the Antarctic which has a yearly average temperature of -20°C and an average humidity of 54% [62]. This particularly dry artic weather is due to the katabatic winds [63] which could be harnessed to provide energy to run the DAC process. Another ideal location is the Atacama Desert located in Chile. This 105,000 km^2 elevated desert located on the Tropic of Capricorn has temperatures and humidity levels between -5°C to 20°C, and 5% to 20%, respectively, near the top of Cerro Paranal [64]. Due to its location and aridness, the Atacama Desert is one of the best locations for solar power which houses both photovoltaic and concentrated solar power plants [65]. These energy sources could be used to significantly reduce the energy requirements for the DAC process.

Another important consideration for location is that the DAC plant is near a CO_2 sequestration site. These can be oil, gas, or unminable coal reserves or geological formations such as saline formations. Saline

formations located in the sedimentary basins are relatively common and have a high prospective use for CO_2 sequestration which is extensively explained by Bradshaw and Dance (2005) [66]. By locating the DAC plant near the sequestration site, the capital and energy cost to build and pump the CO_2 to from the DAC plant to the sequestration site can be reduced.

Keeping the capital costs low is important for the viability of DAC using zeolites. Faujasite structured zeolites are relatively cheap with costs in the 100's per ton for non-specialized versions and with their long life times in the 10 to 20 year range of operation in air prepurification. For an adsorbent cost of \$500/ton and lifetime of 20 years, using the conditions for 194°C regeneration and a cycle time of 6 hours, the capital cost of the adsorbent would be only \$1.20/tonCO_2. This is a fraction of the cost per tonCO_2 captured incurred in comparison to the operational costs.

2.5 Conclusions

DAC of CO_2 using low Si/Al ratio faujasite zeolites such as APG-III has been shown to have a high uptake of CO_2 0.42 mmol/g, fast kinetics leading to sharp breakthroughs, quite high selectivity towards CO_2 allowing for CO_2 purities that can be compressed, piped, and stored, and have strong physical and chemical stabilities allowing their long term use. However, due to the high temperature to desorb CO_2, a majority of the energy is used to heat up the adsorbent during the regeneration process. This along with the requirement to remove water before the capture of CO_2 are the two biggest challenges for DAC using low Si/Al ratio faujasite type structured zeolites. These two challenges however can be overcome by capturing CO_2 in a low humidity level environment and by using waste heat streams while integrating heat recovery into the process. Another way to optimize DAC of CO_2 is the reduction of the amount of electrical energy to do mechanical work which can be done by reducing pressure drop using future zeolite monolith beds technology or by reducing the flow rates which was shown in this article. For the effect of regeneration temperature, increasing the regeneration temperature increases the thermal energy per ton of CO_2 captured, but decreases the electrical energy per ton of CO_2 captured.

2.6 Nomenclature

C_i	Concentration of Component I (ton of CO_2 m^{-3})
C_P	Heat Capacity (MJ kg^{-1} K^{-1})
d_v	Diameter of Pellet (m^3)
D_{in}	Inner Column Diameter (cm)
D_{out}	Outer Column Diameter (cm)
E_c	Energy Required for Compression (MJ tonCO_2^{-1})
E_D	Energy Required for Desorption (MJ tonCO_2^{-1})
E_f	Energy Required for Flow (MJ tonCO_2^{-1})
E_S	Energy Required for Sorbent (MJ tonCO_2^{-1})
E_V	Energy Required for Vacuum (MJ tonCO_2^{-1})
H_A	Heat of Adsorption (MJ ton^{-1})

k_L	Linear Driving Force Mass Transfer Coefficient (s^{-1})
L	Column Length (cm)
L_0	Characteristic Length of the Adsorbent Bed (m)
M_A	Mass of the Adsorbed Species (ton)
M_S	Mass of the Required Sorbent (ton tonCO_2^{-1})
P	Pressure (atm)
P_{drop}	Pressure Drop (MJ m^{-3})
Q	Standard Total Feed Volumetric Flow Rate (sccm)
T	Temperature (K)
T_D	Desorption Temperture (°C)
v	Velocity (m s^{-1})
V_C	Volume of Column (cm^3)
y_i	Molar Component Fraction (-)
α_A	Adsorption Capture Fraction (-)
α_D	Desorption Capture Fraction (-)
α_T	Total Capture Fraction (-)
ε	Bed Void Fraction (-)
η	Dimensionless Separation Constant (-)
μ	Dynamic Viscosity (kg m^{-1} s^{-1})
ρ_f	Density of Fluid (kg m^{-3})
Ø	Sphericity (1 for perfect sphere)
$\mathcal{D}$	Molecular Diffusion (m^2 s^{-1})

2.7 Abbreviations

DAC	Direct Air Capture
DEA	Diethanolamine
FAU	Faujasite
GHSV	Gas Hourly Space Velocities
LDF	Linear Driving Force
LSX	Low Silica X
LUB	Length of Unused Bed
MEA	Monoethanolamine
MOFs	Metal Organic Frameworks
PEI	Polyethyleneimine
TD-Toth	Temperature Dependant Toth
TVSA	Temperature Vacuum Swing Adsorption

2.8 Bibliography

1. Lackner, K. S., Grimes, P. & Ziock, H. *Carbon Dioxide Extraction from Air? Los Alamos National Laboratory*. (1999).
2. Johnston, N. A. C., Blake, D. R., Rowland, F. S., Elliott, S., Lackner, K. S., Ziock, H. J., Dubey, M. K., Hanson, H. P. & Barr, S. Chemical Transport Modeling of Potential Atmospheric CO_2 Sinks. *Energy Convers. Manag.* **44,** 681–689 (2003).
3. Lackner, K. S. Capture of Carbon Dioxide from Ambient Air. *Eur. Phys. J. Spec. Top.* **176,** 93–106 (2009).
4. Lackner, K. S. The Thermodynamics of Direct Air Capture of Carbon Dioxide. *Energy* **50,** 38–46 (2013).
5. Keith, D. W., Ha-Duong, M. & Stolaroff, J. K. Climate Strategy with CO_2 Capture from the Air. *Clim. Change* **74,** 17–45

(2006).

6. Zeman, F. S. & Keith, D. W. Carbon Neutral Hydrocarbons. *Philos. Trans. R. Soc. a-Mathematical Phys. Eng. Sci.* **366,** 3901–3918 (2008).
7. Olah, G. A., Prakash, G. K. S. & Goeppert, A. Anthropogenic Chemical Carbon Cycle for a Sustainable Future. *J. Am. Chem. Soc.* **133,** 12881–12898 (2011).
8. Graves, C., Ebbesen, S. D., Mogensen, M. & Lackner, K. S. Sustainable Hydrocarbon Fuels by Recycling CO_2 and H_2O with Renewable or Nuclear Energy. *Renew. Sustain. Energy Rev.* **15,** 1–23 (2011).
9. Kumar, A., Madden, D. G., Lusi, M., Chen, K.-J., Daniels, E. A., Curtin, T., Perry, J. J. & Zaworotko, M. J. Direct Air Capture of CO_2 by Physisorbent Materials. *Angew. Chemie Int. Ed.* **54,** 14372–14377 (2015).
10. Stuckert, N. R. & Yang, R. T. CO_2 Capture from the Atmosphere and Simultaneous Concentration Using Zeolites and Amine-Grafted SBA-15. *Environ. Sci. Technol.* **45,** 10257–10264 (2011).
11. Choi, S., Drese, J. H., Eisenberger, P. M. & Jones, C. W. Application of Amine-Tethered Solid Sorbents for Direct CO_2 Capture from the Ambient Air. *Environ. Sci. Technol.* **45,** 2420–2427 (2011).
12. Goeppert, A., Czaun, M., May, R. B., Prakash, G. K. S., Olah, G. A. & Narayanan, S. R. Carbon Dioxide Capture from the Air using a Polyamine Based Regenerable Solid Adsorbent. *J. Am. Chem. Soc.* **133,** 20164–20167 (2011).
13. Belmabkhout, Y., Serna-Guerrero, R. & Sayari, A. Amine-Bearing Mesoporous Silica for CO2 Removal from Dry and Humid Air. *Chem. Eng. Sci.* **65,** 3695–3698 (2010).
14. Satyapal, S., Filburn, T., Trela, J. & Strange, J. Performance and Properties of a Solid Amine Sorbent for Carbon Dioxide Removal in Space Life Support Applications. *Energy and Fuels* **15,** 250–255 (2001).
15. Kulkarni, A. R. & Sholl, D. S. Analysis of Equilibrium-Based TSA Processes for Direct Capture of CO_2 from Air. *Ind. Eng. Chem. Res.* **51,** 8631–8645 (2012).
16. Wurzbacher, J. A., Gebald, C., Piatkowski, N. & Steinfeld, A. Concurrent Separation of CO_2 and H_2O from Air by a Temperature-Vacuum Swing Adsorption/Desorption Cycle. *Environ. Sci. Technol.* **46,** 9191–9198 (2012).
17. Wurzbacher, J. A., Gebald, C., Brunner, S. & Steinfeld, A. Heat and Mass Transfer of Temperature-Vacuum Swing Desorption for CO_2 Capture from Air. *Chem. Eng. J.* **283,** 1329–1338 (2016).
18. Zeman, F. Energy and Material Balance of CO_2 Capture from Ambient Air. *Environ. Sci. Technol.* **41,** 7558–7563 (2007).
19. Stolaroff, J. K., Keith, D. W. & Lowry, G. V. Carbon Dioxide Capture from Atmospheric Air using Sodium Hydroxide Spray. *Environ. Sci. Technol.* **42,** 2728–2735 (2008).
20. Zeman, F. Experimental Results for Capturing CO_2 from the Atmosphere. *AIChE J.* **54,** 1396–1399 (2008).
21. Mahmoudkhani, M. & Keith, D. W. Low-Energy Sodium Hydroxide Recovery for CO_2 Capture from Atmospheric Air-Thermodynamic Analysis. *Int. J. Greenh. Gas Control* **3,** 376–384 (2009).
22. Sherman, S. R. Nuclear Powered CO_2 Capture from the Atmosphere. *Environ. Prog. Sustain. Energy* **28,** 52–59 (2009).
23. Fee, J. P. H., Ph, D., Murray, J. M., Renfrew, C. W., Bedi, A., McCrystal, C. B., Jones, D. S. & Fee, H. J. P. Amsorb: A New Carbon Dioxide Absorbent for Use in Anesthetic Breathing Systems. *J. Am. Soc. Anesthesiol.* **91,** 1342 (1999).
24. Veselovskaya, J. V., Derevschikov, V. S., Kardash, T. Y., Stonkus, O. A., Trubitsina, T. A. & Okunev, A. G. Direct CO_2 Capture from Ambient Air using K_2CO_3/Al_2O_3 Composite Sorbent. *Int. J. Greenh. Gas Control* **17,** 332–340 (2013).
25. Wang, T., Lackner, K. S. & Wright, a. B. Moisture-Swing Sorption for Carbon Dioxide Capture from Ambient Air: A Thermodynamic Analysis. *Phys. Chem. Chem. Phys.* **15,** 504–14 (2013).
26. McDonald, T. M., Lee, W. R., Mason, J. A., Wiers, B. M., Hong, C. S. & Long, J. R. Capture of Carbon Dioxide from Air and Flue Gas in the Alkylamine-Appended Metal-Organic Framework mmen-Mg_2(dobpdc). *J. Am. Chem. Soc.* **134,** 7056–7065 (2012).
27. Shekhah, O., Belmabkhout, Y., Chen, Z., Guillerm, V., Cairns, A., Adil, K. & Eddaoudi, M. Made-to-Order Metal-Organic Frameworks for Trace Carbon Dioxide Removal and Air Capture. *Nat. Commun.* **5,** 4228 (2014).
28. Liang, Z., Marshall, M. & Chaffee, A. L. CO_2 Adsorption-Based Separation by Metal Organic Framework (Cu-BTC) Versus Zeolite (13X). *Energy and Fuels* **23,** 2785–2789 (2009).
29. Franchi, R. S., Harlick, P. J. E. & Sayari, A. Applications of Pore-Expanded Mesoporous Silica. 2. Development of a High-Capacity, Water-Tolerant Adsorbent for CO_2. *Ind. Eng. Chem. Res.* **44,** 8007–8013 (2005).
30. Yang, R. T. *Adsorbents: Fundamentals and Applications*. (John Wiley & Sons, 2003).
31. Krishnamurthy, S., Rao, V. R., Guntuka, S., Sharratt, P., Haghpanah, R., Rajendran, A., Amanullah, M., Karimi, I. A. & Farooq, S. CO_2 Capture from Dry Flue Gas by Vacuum Swing Adsorption: A Pilot Plant Study. *Sep. Mater. Devices Process.* **60,** 1830–1842 (2014).
32. Chue, K. T., Kim, J. N., Yoo, J., Cho, S. H. & Yang, R. T. Comparison of Activated Carbon and Zeolite 13X for CO_2 Recovery from Flue Gas by Pressure Swing Adsorption. *Ind. Eng. Chem. Res.* **34,** 591–598 (1995).

33. Choi, S., Drese, J. H. & Jones, C. W. Adsorbent Materials for Carbon Dioxide Capture from Large Anthropogenic Point Sources. *ChemSusChem* **2,** 796–854 (2009).

34. Reza, H., Nilam, R., Rajendran, A., Farooq, S. & Karimi, I. A. Cycle Synthesis and Optimization of a VSA Process for Postcombustion CO_2 Capture. *AIChE J.* **59,** 4735–4748 (2013).

35. Sircar, S. & Kratz, W. C. Patent 4249915 - Removal of Water and Carbon Dioxide from Air. (1981).

36. Rege, S. U., Yang, R. T. & Buzanowski, M. A. Sorbents for Air Prepurification in Air Separation. *Chem. Eng. Sci.* **55,** 4827–4838 (2000).

37. Sircar, S. & Hufton, J. R. Why Does the Linear Driving Force Model for Adsorption Kinetics Work? *Adsorption* **6,** 137–147 (2000).

38. de Visser, E., Hendriks, C., Barrio, M., Mølnvik, M. J., de Koeijer, G., Liljemark, S. & Le Gallo, Y. Dynamis CO_2 Quality Recommendations. *Int. J. Greenh. Gas Control* **2,** 478–484 (2008).

39. Wetenhall, B., Race, J. & Downie, M. The Effect of CO_2 Purity on the Development of Pipeline Networks for Carbon Capture and Storage Schemes. *Int. J. Greenh. Gas Control* **30,** 197–211 (2014).

40. Socolow, R., Desmond, M., Aines, R., Blackstock, J., Bolland, O., Kaarsberg, T., Lewis, N., Mazzotti, M., Pfeffer, A., Sawyer, K., Siirola, J., Smit, B. & Wilcox, J. *Direct Air Capture of CO_2 with Chemicals*. *American Physical Society - Panel on Public Affairs* (2011).

41. Keith, D. W., Holmes, G., St. Angelo, D. & Heidel, K. A Process for Capturing CO_2 from the Atmosphere. *Joule* 1–22 (2018). doi:10.1016/j.joule.2018.05.006

42. Jayaraman, A., Yang, R. T., Cho, S. H., Bhat, T. S. G. & Choudary, V. N. Adsorption of Nitrogen, Oxygen and Argon on Na-CeX Zeolites. *Adsorption* **8,** 271–278 (2002).

43. Sebastian, J. & Jasra, R. V. Sorption of Nitrogen, Oxygen, and Argon in Silver-Exchanged Zeolites. *Ind. Eng. Chem. Res.* **44,** 8014–8024 (2005).

44. Harlick, P. J. E. & Tezel, F. H. An Experimental Adsorbent Screening Study for CO_2 Removal from N_2. *Microporous Mesoporous Mater.* **76,** 71–79 (2004).

45. Cavenati, S., Grande, C. A. & Rodrigues, A. E. Adsorption Equilibrium of Methane, Carbon Dioxide, and Nitrogen on Zeolite 13X at High Pressures. *J. Chem. Eng. Data* **49,** 1095–1101 (2004).

46. Su, F. & Lu, C. CO_2 Capture from Gas Stream by Zeolite 13X using a Dual-Column Temperature/Vacuum Swing Adsorption. *Energy Environ. Sci.* **5,** 9021 (2012).

47. Samanta, A., Zhao, A., Shimizu, G. K. H., Sarkar, P. & Gupta, R. Post-Combustion CO_2 Capture using Solid Sorbents: A Review. *Ind. Eng. Chem. Res.* **51,** 1438–1463 (2012).

48. Quang, D. V., Dindi, A., Rayer, A. V., El Hadri, N., Abdulkadir, A. & Abu-Zahra, M. R. M. Impregnation of Amines onto Porous Precipitated Silica for CO_2 Capture. *Energy Procedia* **63,** 2122–2128 (2014).

49. Couck, S., Cousin-Saint-Remi, J., Van der Perre, S., Baron, G. V., Minas, C., Ruch, P. & Denayer, J. F. M. 3D-Printed SAPO-34 Monoliths for Gas Separation. *Microporous Mesoporous Mater.* **255,** 185–191 (2018).

50. Couck, S., Lefevere, J., Mullens, S., Protasova, L., Meynen, V., Desmet, G., Baron, G. V. & Denayer, J. F. M. CO_2, CH_4, and N_2 Separation with a 3DFD-Printed ZSM-5 Monolith. *Chem. Eng. J.* **308,** 719–726 (2017).

51. Thakkar, H., Eastman, S., Hajari, A., Rownaghi, A. A., Knox, J. C. & Rezaei, F. 3D-Printed Zeolite Monoliths for CO_2 Removal from Enclosed Environments. *ACS Appl. Mater. Interfaces* **8,** 27753–27761 (2016).

52. Thakkar, H., Eastman, S., Al-Mamoori, A., Hajari, A., Rownaghi, A. A. & Rezaei, F. Formulation of Aminosilica Adsorbents into 3D-Printed Monoliths and Evaluation of Their CO_2 Capture Performance. *ACS Appl. Mater. Interfaces* **9,** 7489–7498 (2017).

53. Yang, R. T. *Gas Separation by Adsorption Processes*. (Butterworth-Heinemann, 2013).

54. Sayari, A. & Belmabkhout, Y. Stabilization of Amine-Containing CO_2 Adsorbents: Dramatic Effect of Water Vapor. *J. Am. Chem. Soc.* **132,** 6312–6314 (2010).

55. Sayari, A., Belmabkhout, Y. & Serna-Guerrero, R. Flue Gas Treatment via CO_2 Adsorption. *Chem. Eng. J.* **171,** 760–774 (2011).

56. Ahn, H. & Lee, C. H. Adsorption Dynamics of Water in Layered Bed for Air-Drying TSA Process. *AIChE J.* **49,** 1601–1609 (2003).

57. Wang, Y. & LeVan, M. D. Adsorption Equilibrium of Binary Mixtures of Carbon Dioxide and Water Vapor on Zeolites 5A and 13X. *J. Chem. Eng. Data* **55,** 3189–3195 (2010).

58. Chua, H. T., Ng, K. C., Chakraborty, A., Oo, N. M. & Othman, M. A. Adsorption Characteristics of Silica Gel + Water Systems. *J. Chem. Eng. Data* **47,** 1177–1181 (2002).

59. Lalik, E., Mirek, R., Rakoczy, J. & Groszek, A. Microcalorimetric Study of Sorption of Water and Ethanol in Zeolites 3A and 5A. *Catal. Today* **114,** 242–247 (2006).

60. Kim, K. M., Oh, H. T., Lim, S. J., Ho, K., Park, Y. & Lee, C.-H. Adsorption Equilibria of Water Vapor on Zeolite 3A, Zeolite 13X, and Dealuminated Y Zeolite. *J. Chem. Eng. Data* **61,** 1547–1554 (2016).

61. Buck, A. L. New Equations for Computing Vapor Pressure and Enhancement Factor. *Journal of Applied Meteorology* **20,** 1527–1532 (1981).

62. Keys, H. J. R. *Air Temperature, Wind, Precipitation, and Atmospheric Humidity in the McMurdo Region, Antarctic*. (1980).

63. Nylen, T. H., Fountain, A. G. & Doran, P. T. Climatology of Katabatic Winds in the McMurdo Dry Valleys, Southern Victoria Land, Antarctica. *J. Geophys. Res. Atmos.* **109,** 1–9 (2004).

64. ESO. *Paranal Site Information - Climate Information*. (2017).

65. Zhang, H. L., Baeyens, J., Degrève, J. & Cacères, G. Concentrated Solar Power Plants: Review and Design Methodology. *Renew. Sustain. Energy Rev.* **22,** 466–481 (2013).

66. Bradshaw, J. & Dance, T. Mapping Geological Storage Prospectivity of CO_2 for the World's Sedimentary Basins and Regional Source to Sink Matching. *Greenh. Gas Control Technol. 7* **1,** 583–591 (2005).

Chapter 3

High Purity CO_2 from Direct Air Capture using a Single Cycle TVSA with Na-X Zeolites

Sean M.W. Wilson, and F. Handan Tezel

Department of Chemical and Biological Engineering, University of Ottawa, 161 Louis-Pasteur, Ottawa, Ontario K1N 6N5 Canada

To be submitted: Industrial & Engineering Chemistry Research 2020

3.1 Abstract

The capture and concentration of 0.04% CO_2 from a dry ambient air stream by temperature vacuum swing adsorption (TVSA) was investigated in order to produce high purity CO_2. Initial investigation into the pure gas adsorption included the determination of CO_2, N_2, O_2 and Ar adsorption isotherms with NaX zeolite and their fit to the temperature dependent Toth isotherm model equation. These studies allowed for the evaluation of the TVSA cycle and showed the potential of reducing the pressure and/or elevating the temperature during the blowdown step in order to produce high purity CO_2. Fixed bed adsorption desorption breakthrough curves for TVSA cycle were obtained to investigate the pressure and temperature effects on the blowdown step. High purity CO_2 was experimentally produced between a concentration of 99.5% and 99.96% by lowering the blowdown pressure. By controlling the blowdown temperature, the concentration of the product was increased from 99.8% to 99.95%, however with a significant loss of CO_2. This effect of N_2, O_2, and Ar desorbing during the blowdown step with CO_2 desorbing during the evacuation step is shown graphically by measuring the concentration and flow rate of the exiting gas species. The results from this study show the potential for producing a valuable product of high purity CO_2 from atmospheric concentrations, which can be used in many applications, particularly ones where CO_2 infrastructure does not exist or where there is a burden in utilizing a CO_2 cylinder.

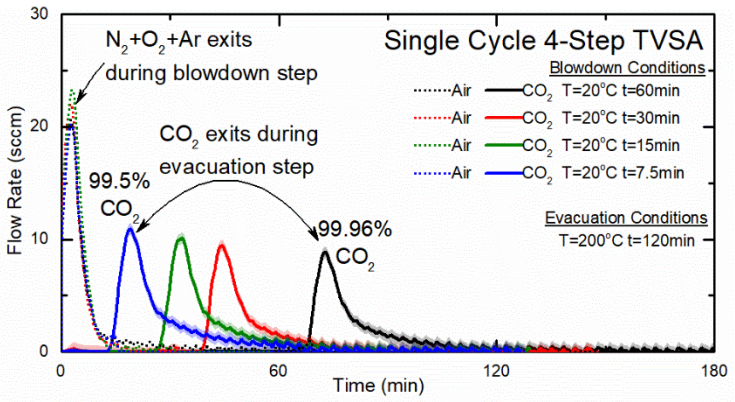

Keywords: CO_2 Capture, Zeolite Na-X, Faujasite Zeolite, Temperature Vacuum Swing Adsorption (TVSA), Direct Air Capture, High Purity CO_2, Blowdown Step

3.2 Introduction

The global warming phenomenon is the observed correlation between an increasing worldwide surface temperatures and the increase in CO_2 that is present within the atmosphere. This global warming causes many changes to the planet and has spurred interest into reducing the amount of CO_2 in the atmosphere back to the pre-industrial revolution levels. One strategy to do this is capturing the approximately 400 ppm of CO_2 from the other components in the air, which is referred to as direct air capture (DAC). The majority of DAC projects look into sequestering the CO_2, but projects that look into utilizing the CO_2 from DAC will get reimbursed through the value of the carbon, making the whole process more economical. Most utilization methods look into a chemical conversion route which is energy intensive because of the low chemical energy state of CO_2 which is the most oxidized version of carbon. Another way to get reimbursed from capturing CO_2 without having to chemically convert it is to increase the concentration of the CO_2 to the point that it becomes intrinsically more valuable. The value of the CO_2 increases as the purity of the CO_2 increases from medical, bone dry, beverage, and food grade CO_2 (which are between 99.5% and 99.9%) to anaerobic, laser, supercritical fluid, and research grade CO_2 (which are between 99.95% and 99.999%).

In literature, many studies have shown experimentally that relatively pure CO_2 can be produced via adsorption using activated carbons [1], and zeolites [2,3]. Chue et al. showed that the purity that can be achieved is a function of the shape of the isotherm and the inlet concentration of CO_2, with lower inlet concentrations requiring larger Henry's Law constants to achieve higher purities [4]. For DAC, this means that a potential adsorbent would need to have a large Henry's Law constant due to the diffuse nature of CO_2 in the air. Having a large Henry's Law constant is also important during the adsorption step of DAC with larger Henry's Law constants for CO_2 indicating larger loading capacities of the process making it more economical. Due to this requirement of a large Henry's Law constant, adsorbents such as certain zeolites [3] and metal organic frameworks (MOFs) [5] which have been shown in literature to have high CO_2 Henry's Law constants could be used as prospective materials for this separation. It is important that the materials also have high selectivity for CO_2 compared to other components in the air, fast kinetics, relatively low cost, are not overly energy intensive to regenerate, and have strong physical and chemical stabilities.

The number of adsorption steps and the type of adsorption swing process is important for the economic viability of DAC. Utilizing a significant number of steps in an adsorption cycle allows for higher recoveries for a set purity but requires more equipment to handle set productivities which has been shown in literature [6]. This is particularly important for DAC with CO_2 being so diffuse in the air. This happens, because in a simple two-step adsorption cycle, the amount of N_2, O_2, and Ar that would be co-adsorbed during the adsorption step would dilute the product gas during the desorption step producing a dilute CO_2 product. For these reasons, many studies in the literature looking into DAC, utilize more complex swing processes such as temperature vacuum swing adsorption (TVSA), rather than just temperature swing adsorption (TSA) or vacuum swing adsorption (VSA). With TVSA, the strong adsorption required to capture the CO_2 during the adsorption step can be overcome in the evacuation step with the aid of a combination of vacuum and

heat. The steps involved in a simple 4-step TVSA cycle are typically adsorption, blowdown, evacuation, and light product pressurization (LPP) with a temperature increase during the evacuation step, which are shown in Figure 3.1.

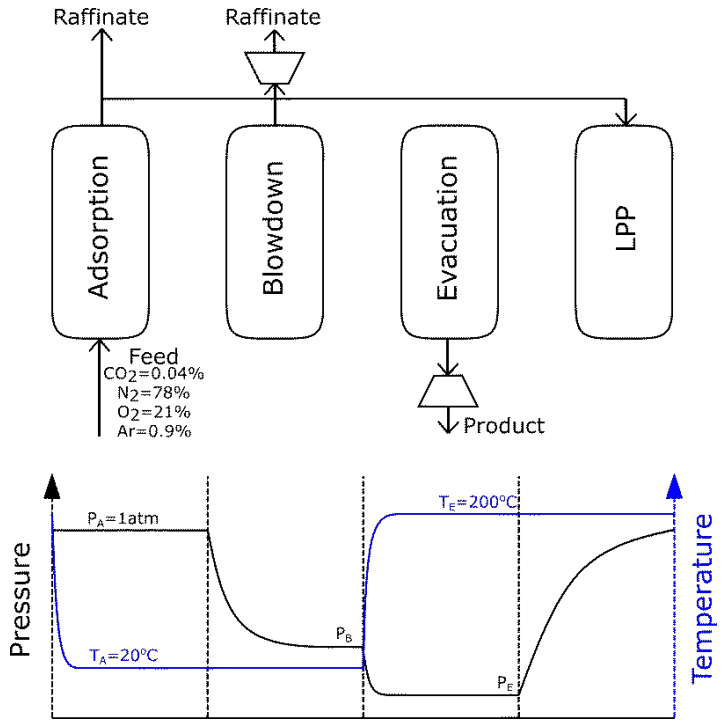

Figure 3.1 – Schematic diagram along with the graphical representation of the temperature and pressure of a 4-step TVSA.

In this study, we have looked at improving what has already been investigated for dry DAC of CO_2 using zeolites [3,7], and in particular sodium type low Si/Al ratio faujasite structured zeolites, and determining whether it is possible to concentrate the CO_2 from air to concentrations above 99.5% in one TVSA adsorption cycle composed of 4 steps. In this study, we have applied an additional controlled temperature increase to the blowdown step, and changed the blowdown duration, which would effectively supply a stronger vacuum. This investigation has included an initial pure gas isotherm study as well as breakthrough experiments. A single bed system has been used to demonstrate the TVSA cycle with the steps in the adsorption cycle being non- coupled.

3.3 Materials and Methods

3.3.1 Materials

CO_2, N_2, O_2, and Ar pure gases were obtained from Linde Canada (Burlington, Ontario, Canada) at purities of 99.99%, 99.999%, 99.994%, and 99.9993%, respectively. A cylinder of 383 ± 1 ppm certified CO_2 concentration in air acquired from Linde Canada was used to determine the steady state breakthrough. Air used for the breakthrough portion of this study was acquired from outdoor air in the

downtown Ottawa region, compressed, and then purified to remove any oils and water that was present. APG-III purchased from Honeywell UOP (Des Plaines, Illinois, United States), a sodium type low Si/Al ratio faujasite structured zeolite which will be referred to in this manuscript as Na-X, was chosen because it is marketed for its use in air pre-purification, and its relevance to previous DAC research [7]. The details of this Na-X are given along with the chemical composition, which was measured using energy-dispersive X-ray spectroscopy in the Supporting Information in Appendix II (Table AII.1 and Table AII.2, respectively).

3.3.2 Methods

3.3.2.1 Equilibrium Isotherms

Pure component isotherms were measured using a VTI Scientific Instruments GHP gravimetric system (Hialeah, Florida, United States) for CO_2, N_2, O_2, and Ar adsorption at 22°C, 50°C, 80°C, and 110°C for Na-X. These were conducted by first weighing then regenerating the sample at 350°C under a vacuum pressure of approximately 10^{-8} atm until there was negligible weight change. The sample was then evaluated at increasing pressures of up to 6 atm of the pure gas that was studied. This was done using a microbalance with an accuracy of $\pm 5 \times 10^{-7}$ g, and two pressure transducers, one with a range of 0 to 1000 Torr with an accuracy of ± 0.25 % of reading, and another with a range of 0 to 900 psi with an accuracy of ± 0.36 psi. To look at any possible hysteresis, desorption was then performed by decreasing the pressure after the adsorption data points and the data points are presented within the isotherms. Buoyancy corrections were performed using helium at similar pressures and temperatures as the isotherm data points. These were used to calculate the absolute isotherms from the excess amounts by assuming that helium does not adsorb to the surface during buoyancy correction. All isotherms presented in this study are shown as absolute isotherms. A more elaborate description of the calculations of absolute isotherms from excess amounts are presented in S. Cavenati et al [8]. A schematic drawing of the setup is included in the Supporting Information in Appendix II in Figure AII.1.

The adsorption isotherms were fitted to the Langmuir, Freundlich, Sips, and Toth models over the whole range of pressures by minimizing the sum of least squares, and the isotherm with the highest coefficient of determination (R^2) was used to represent the isotherm. These isotherm model equations are presented in the Supporting Information in Table AII.3 in Appendix II. The limiting heat of adsorption (ΔH_0) values were calculated using the van't Hoff plot (Henry's Law constant vs. 1/T) with the relationship of the heat of adsorption at zero loading given by Equation 1. The Henry's Law constants were derived from the linear section of the isotherms for N_2, O_2, and Ar and from the Langmuir parameters for CO_2.

$$lnK = -\frac{\Delta H_0}{R}\frac{1}{T} + lnK_0 \qquad 1$$

Temperature Dependant Toth (TD-Toth) was also used to represent the isotherms between temperatures of 20°C and 110°C from 0 to 6.5 atm pressures. The TD-Toth model equations are presented and explained in the Supporting Information in Appendix II (Table AII.4).

3.3.2.2 Fixed Bed Adsorption Breakthrough Curves

To determine the multicomponent adsorption behaviour of CO_2, N_2, O_2, and Ar, fixed bed adsorption-desorption breakthrough curves were used. The schematic diagram of the system used is shown in Figure AII.2 in the Supporting Information in Appendix II. Table AII.5 in the Supporting Information in Appendix II shows the column properties, and operating conditions used for these experiments. The experiment began by first packing the adsorption column with Na-X with a piece of quartz wool on either end of the column. The column was then placed into the setup and degassed at 250°C with a flow of 300 sccm of N_2 for over 48 hours to ensure any water was driven off the adsorbent. Once regenerated, the column was placed into the temperature controlled bath at 20°C and kept at isothermal conditions. The feed gas for the experiment was Ottawa, Canada air that was compressed, put through a layered adsorption bed of activated carbon and $CaSO_4$ to remove any water or oils from the feed. The flow of the gas was then controlled using a 10,000 ± 100 sccm mass flow controller (MFC). The gas would then enter the column during the adsorption step with its pressure (0 to 100 psi ± 0.25 psi) and temperature being measured. After exiting the column, the temperature and pressure were measured again and the gas would proceed to bypass the gas chromatograph (GC) and get measured by the Thermo Electron Corporation Model 410i 10,000ppm CO_2 Infrared Spectroscopy (IR) (Waltham, Massachusetts, United States) to determine the exiting CO_2 concentration. After the adsorption had completely broken through the column, the blowdown step would begin.

For this study, to increase the purity of the product during the evacuation step, the temperature and pressure during the blowdown step were modified. Instead of choosing a blowdown pressure, the duration of the blowdown step was chosen in which a vacuum pump would run. Therefore, longer blowdown durations would equate to lower pressures. Four blowdown temperatures of 20°C, 40°C, 60°C, and 80°C, and blowdown durations of 7.5 min, 15 min, 30 min, and 60 min were chosen. The conditions for each step are graphically shown in Figure 3.2 with the varying conditions for the blowdown step. Subscripts A, B, and E denote adsorption, blowdown, and evacuation, respectively, and T, t, and P denote temperature, time, and pressure, respectively.

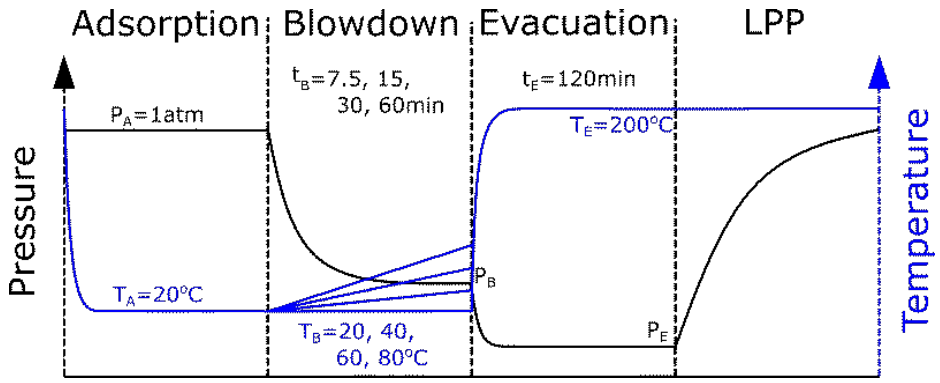

Figure 3.2 – The conditions in this study for the adsorption, blowdown, evacuation, and LPP steps of the TVSA cycle.

During blowdown and evacuation steps, the column would first be isolated by closing the valves around the column and placed into either the temperature controlled bath for blowdown temperature of 20°C or in the temperature controlled oven for blowdown temperatures of 40°C, 60°C, and 80°C. The system was designed to minimize the dead space around the column which would otherwise impact the purity obtained in this study. This dead space, excluding the void space between the pellets was 7.1 cm^3 and including it was 18.3 cm^3. The vacuum would then be applied by opening the exit valve during the blowdown step for 7.5 min, 15 min, 30 min, or 60 min. After the blowdown step, the column was placed inside the temperature controlled oven for the evacuation step, which was controlled at 200°C for 120 min. In order to evaluate the composition of the gases coming out during the blowdown and evacuation steps, the exiting gas being drawn out of the column would first pass though the GC GOW-MAC 580 (Bethlehem, Pennsylvania, United States). This GC was equipped with a thermal conductivity detector and a Porapak Q column to determine the CO_2 composition coming out of the column. Compositional analysis would occur every 3 minutes with a 6-port GC valve. The gas would then pass through the vacuum pump and enter the CO_2 IR spectroscopy and then the 50 ± 0.5 sccm mass flow meter (MFM). The flow rate of the exiting gas would be corrected based on the concentrations calculated from the interpolated GC readings and the thermal conductivities of the gases. In order to determine the purity of a particular run more accurately, the column after the blowdown step was isolated from vacuum using valves and allowed to be pressurized while the temperature increased to 200°C, and then sampled with the GC to determine the purity in a similar procedure to literature [3].

The goal of this study is to produce high purity CO_2. The definition of purity is given in Equation 2. With DAC using CO_2 from the air, more importance should be placed on producing CO_2 at a high purity inexpensively than with high capture fractions (also called recovery) since air is abundant [9]. Capture fraction is an important parameter to investigate due to lower capture fractions requiring larger pumping energies to capture the CO_2 from the air. In this study, there were two different capture fractions that were defined: capture fraction during the adsorption steps (α_A) and the capture fraction during the evacuation steps (α_E). They are defined in Equations 3 and 4.

$$Purity = \frac{Moles\ of\ CO_2\ from\ Evacuation\ Step}{Total\ Moles\ of\ Gas\ from\ Evacuation\ Step} \times 100\% \quad (2)$$

$$\alpha_A = \frac{Moles\ of\ CO_2\ Adsorbed\ during\ Adsorption\ and\ Pressurization\ Steps}{Total\ Moles\ of\ Gas\ that\ Entered\ the\ Column\ during\ \ Adsorption\ and\ Pressurization\ Steps} \quad (3)$$

$$\alpha_E = \frac{Moles\ of\ CO_2\ from\ Evacuation\ step}{Total\ Moles\ of\ CO_2\ from\ Evacuation\ and\ Blowdown\ Steps} \quad (4)$$

3.4 Results and Discussion

3.4.1 Equilibrium Adsorption Isotherms

The pure component isotherms of CO_2, N_2, O_2, and Ar with Na-X at 22°C, 50°C, 80°C, and 110°C are presented in Figure 3.3. The solid markers represent the adsorption data points, and the hollow markers represent the desorption data points. No significant hysteresis was observed, which is indicative that the isotherms are completely reversible. The solid lines in Figure 3.3 represent the isotherm model with the highest coefficient of determination. The adsorption equilibrium data presented is in good agreement within 1% of literature values for CO_2 adsorption at 22°C [10]. The adsorption isotherm data points and isotherm model parameters are presented in the Supporting information in Appendix II in Table AII.6 – AII.9 and Table AII.10, respectively.

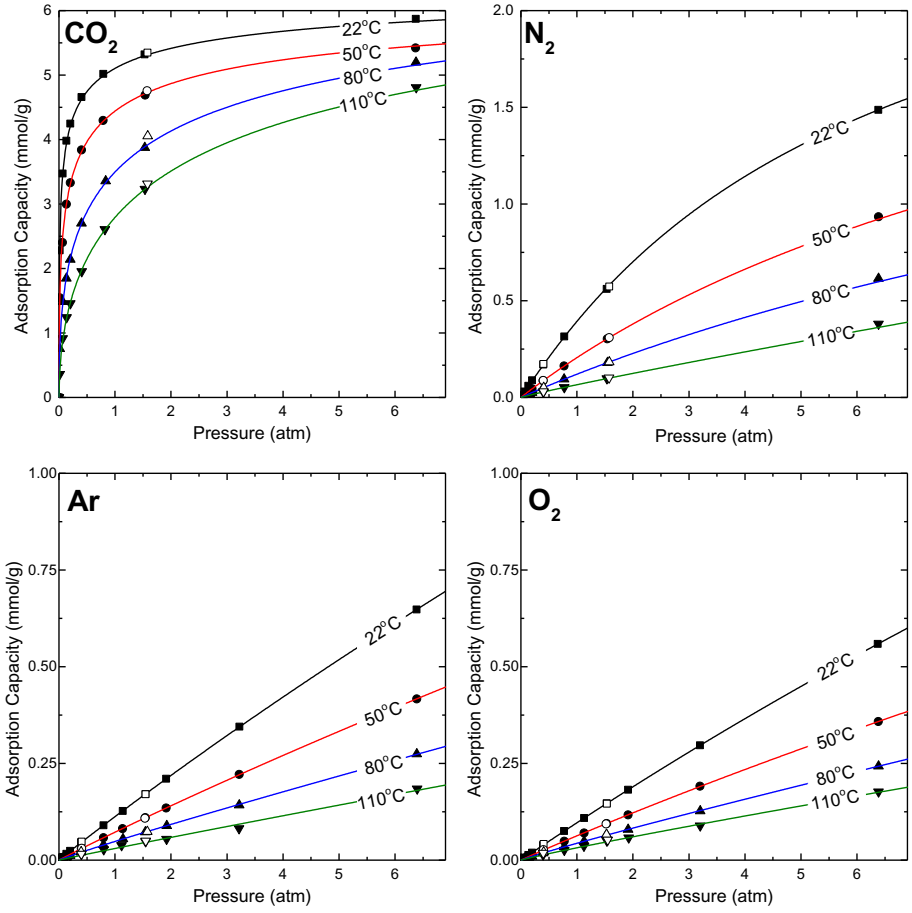

Figure 3.3 – CO_2, N_2, O_2, and Ar pure adsorption isotherms at 22°C, 50°C, 80°C, and 110°C for Na-X with each isotherm being fitted to Langmuir, Freundlich, Sips, and Toth and is represented by the model with the best fit. Filled points = adsorption, hollow points = desorption.

As can be seen from Figure 3.3, at all pressures, CO_2 is significantly more adsorbed, followed by N_2, Ar, and O_2, with last 2 gases having similar adsorption capacities. Similar trends were observed in literature, as well [11,12]. These differences in adsorption capacity were shown in a previous study that CO_2 is selectively adsorbed over the other components in air [7]. This is not surprising since Na-X is marketed for air pre-purification which is an application looking at removing CO_2 from the air before separating N_2 from O_2. This difference in adsorption of CO_2 from the other components in air is highlighted in the van't Hoff

plot in Figure 3.4. This shows the two orders of magnitude difference between the adsorption of CO_2 in the Henry's Law region compared to the adsorption of N_2 and the other gaseous components in the air. This difference in the Henry's Law region is important for the TVSA cycle to produce high purity CO_2. This is because of two reasons. Firstly, that the high Henry's Law constant for CO_2 allows the CO_2 to be adsorbed in significant quantities at very low concentrations. Secondly, that during the blowdown step, when a vacuum is applied, N_2, O_2, and Ar get desorbed but CO_2 remains on the adsorbent's surface.

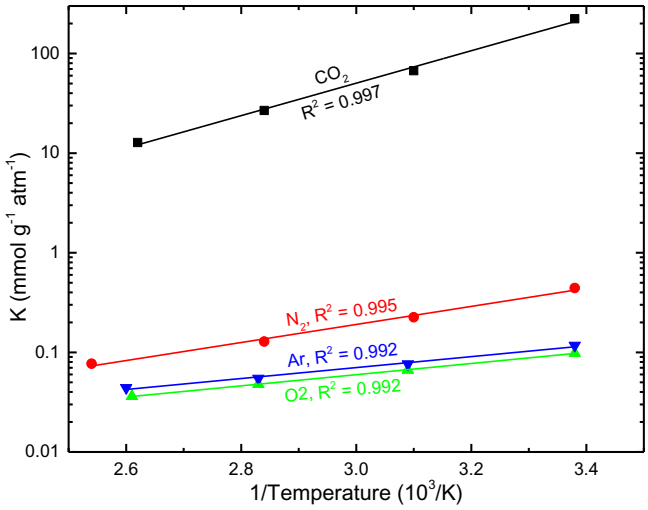

Figure 3.4 – Van't Hoff plot for CO_2, N_2, O_2, and Ar for Na-X using calculated Henry's Law constants at temperatures of 22°C, 50°C, 80°C, and 110°C including their respective line of best fit.

From the van't Hoff plots in Figure 3.4, the limiting heat of adsorption values were calculated from the slopes of the lines of best fit giving 31.0 ± 1.2 kJ/mol, 17.4 ± 0.9 kJ/mol, 10.8 ± 0.2 kJ/mol, and 10.5 ± 0.7 kJ/mol for CO_2, N_2, O_2, and Ar, respectively. The values for O_2 and Ar adsorption are comparable to values from literature [13]. The values for CO_2 and N_2 are slightly on the lower end of values seen from review studies (35 – 50 kJ/mol for CO_2 and 18.4 – 25 kJ/mol for N_2) [14] and individual studies (40 – 55 kJ/mol for CO_2 and 14 – 19.9 kJ/mol for N_2) [3,13] with similar Na^+ type low Si/Al ratio faujasite structured zeolites. This can be explained on the material in this study containing small amounts of K^+, Mg^+, Ca^+, and Fe^+, with a majority of Na^+ as can be seen in the Supporting Information in Appendix II (Table AII.2).

From the isothermal data points at the 4 different temperatures for CO_2, N_2, O_2, and Ar, the TD-Toth parameters were calculated in order to understand the adsorption behaviour between pressures of 0 – 6 atm and temperatures of 20 – 110°C. The parameters for the TD-Toth model are included in the Supporting Information in Appendix II (Table AII.11). These parameters were used to plot Figure 3.5 which shows the adsorption capacity of CO_2, N_2, O_2, and Ar between 20°C – 90°C, and 0 – 1 atm for N_2, O_2, and Ar, and 0 – 0.0004 atm for CO_2, or 400 ppm of CO_2. This shows that the adsorption capacity of CO_2 at lower temperatures at 400 ppm is greater than that of N_2, O_2, or Ar at 1 atm. As temperature increases, the ratio of the adsorption capacity of Na-X for CO_2/air decreases showing the detrimental effect of higher adsorption step temperature on the DAC of CO_2 using low Si/Al ratio faujasite structure zeolites.

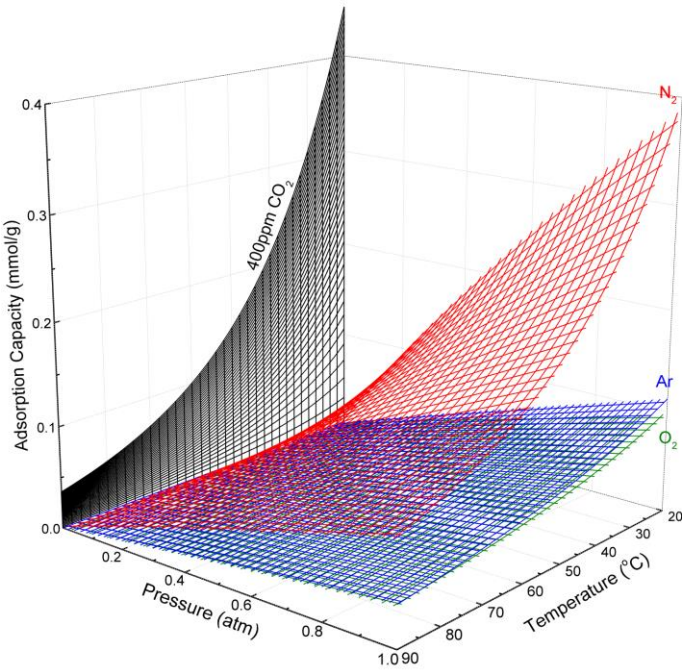

Figure 3.5 – 3D surface plots of the adsorption capacity of CO_2, N_2, O_2, and Ar on Na-X determined using the TD-Toth model. For CO_2 the pressure goes only to 400 ppm or 0.0004 atm.

These surface plots are useful tools in understanding the effect of changing variables such as temperature and pressure during the different parts of the TVSA cycle. For this study, the adsorption step in the TVSA cycle occurs at approximately 1 atmosphere and 20°C composed of 78.09% nitrogen, 20.95% oxygen, 0.93% argon, and 0.04% carbon dioxide. Under these conditions at equilibrium, there is predicted to be 0.45 mmol/g of CO_2, 0.32 mmol/g of N_2, 0.02 mmol/g of O_2, and an insignificant amount of Ar adsorbed onto Na-X according to the TD-Toth model. As can be seen in Figure 3.6, there is 0.45 mmol/g of CO_2 and 0.34 mmol/g of air adsorbed, if the evacuation step were to proceed without a blowdown step, the maximum concentration of the product would be 57% CO_2. However, to increase the purity of CO_2 in the product, it is common practice that a blowdown step is utilized where N_2, O_2, and Ar would be desorbed by reducing the pressure using a vacuum. This is a common step in literature with CO_2 purities of as high as 99.997% reported from simulations [15]. With Na-X and other low Si/Al ratio faujasite structured zeolites, decreasing the pressure would remove the N_2, O_2, and Ar from the column while leaving the CO_2 as long as the pressure is not decreased too much. This can be seen in Figure 3.6 by N_2 and O_2 adsorption capacities significantly changing as the pressure is reduced, but CO_2 still being within the Henry's Law region. After a sufficient reduction in pressure would occur, mostly CO_2 would remain allowing the evacuation step of increasing temperature and reducing pressure further to produce pure CO_2. Another method proposed in this study is to increase the temperature and reduce the pressure during the blowdown step to remove N_2, O_2, and Ar.

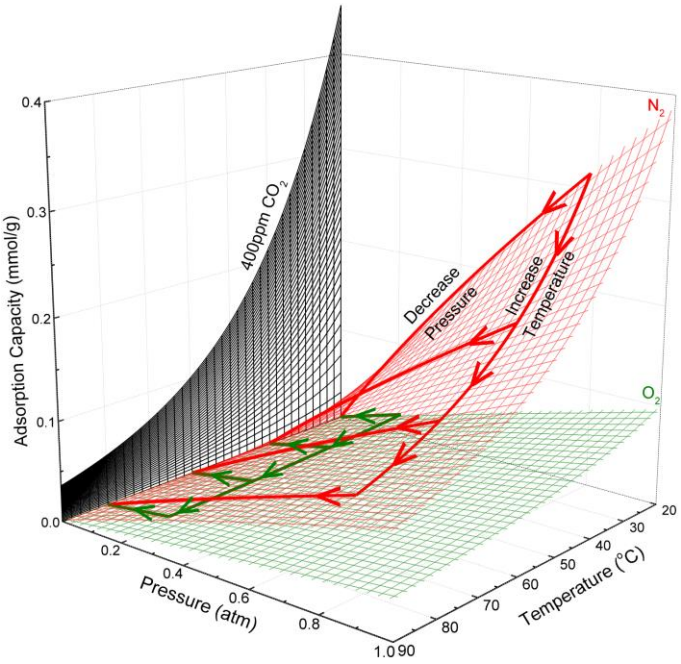

Figure 3.6 – 3D surface plots of the adsorption capacity of CO_2, N_2, and O_2 on Na-X determined using the TD-Toth model along with the TVSA route during the blowdown step for either pressure decrease, or a temperature increase with a pressure decrease.

3.4.2 TVSA Cycle Breakthrough

To determine the multicomponent adsorption behaviour of CO_2, N_2, O_2, and Ar, a fixed bed adsorption breakthrough was done at 20°C with a step change in inlet using Ottawa, Canada ambient air. The adsorption step was carried out isothermally until equilibrium was reached for all runs in this study. After the adsorption step, the blowdown step would occur. In this study, two variables were changed, the blowdown temperature and the blowdown duration. To test these variables 7.5 min, 15 min, 30 min, and 60 min blowdown durations at a blowdown temperature of 20°C, and 30 min blowdown duration at 20°C, 40°C, 60°C, and 80°C blowdown temperatures were selected. Multiple replicates of each run were completed and are presented along with the data. After the blowdown step, each run would have the same evacuation step conditions of 200°C for 120 min. The evacuation temperature was selected from results from a previous study [7]. After evacuation, the column would then be quickly pressurized to 1 atm and the adsorption step would proceed.

The adsorption breakthrough curve at 20°C and 2,500 sccm of air after a full regeneration using 300 sccm of N_2 at 250°C for over 48 hours is compared to the steady state breakthrough curve for the center point conditions of T_B = 20°C, t_B = 30 min, T_E = 200°C, and t_E = 120 min at the same flowrate. Both of these breakthrough curves are presented in Figure 3.7. For these runs, certified air with 383 ± 1 ppm of CO_2 was used. This was done to minimize the error during these runs due to the varying level of CO_2 in the air over the course of the day and throughout the year as mentioned in the literature [16]. The cyclical steady state condition was achieved after the first cycle for these experiments. The adsorption capacity was

calculated from the area between the breakthrough curve and the atmospheric CO_2 concentration, which was determined to be 0.44 ± 0.04 mmol/g for the initial adsorption and 0.35 ± 0.03 mmol/g for the cyclical steady state conditions. This difference of 0.09 mmol/g is due to the vacuum being unable to pull out all of the CO_2 during the evacuation step. When the outlet concentration equates to 95% of the inlet concentration, the capture fraction were found to be 77.0 ± 0.7% and 75.7 ± 0.7% for the initial adsorption and the cyclic steady state conditions, respectively. When the predicted CO_2 adsorption capacity from the TD-Toth model is compared to the adsorption capacity calculated from the breakthrough curve, the values are quite similar at 0.45 mmol/g and 0.44 mmol/g, respectively. One thing to note in Figure 3.7 is the similar shapes presented with both the initial adsorption and the cyclical steady state conditions, indicating similar kinetics.

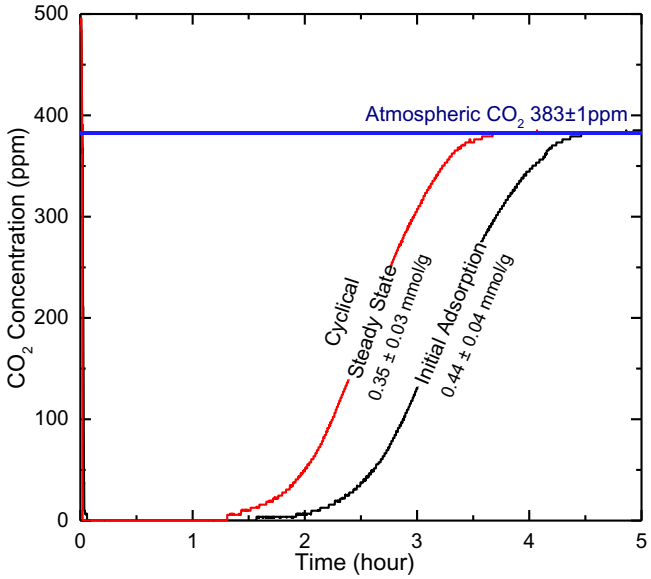

Figure 3.7 – Comparison of breakthrough curves for the initial adsorption after a full regeneration and at cyclical steady state for the conditions of T_B=20°C, t_B=30min, T_E=200°C, and t_E=120min with a column packed with Na-X with a positive CO_2 concentration step of 383 ± 1 ppm of CO_2 (indicated in blue) at 20°C and a flow rate of 2,500 sccm.

3.4.2.1 Effect of Blowdown Duration

After the adsorption step would reach equilibrium, the blowdown step would occur with the goal of reducing the amount of N_2, O_2, and Ar while leaving the CO_2 adsorbed for the evacuation step. By increasing the duration of the blowdown step, the pressure within the column would be reduced, aiding the removal of unwanted gases during this step. In this study, four blowdown durations of 7.5 min, 15 min, 30 min, and 60 min were selected at 20°C with the same evacuation conditions of T_E = 200°C, and t_E = 120 min. The flow rates of N_2, O_2, Ar, and CO_2 exiting the column during these two steps is presented in Figure 3.8. It can be seen from this figure that, N_2, O_2, and Ar gases, which are represented by the dotted line in this figure, exit the column first during the blowdown step with the CO_2 exiting afterwards during the evacuation step. For example, for a blowdown duration of 60 min indicated by the black color, N_2, O_2, and Ar leave the column first, then after 60 minutes, the column is placed into the temperature controlled

oven and the evacuation step begins by heating the column to 200°C. During this step it is observed that the CO_2 is desorbed from Na-X. In order to measure the outlet concentration from the column, a 6 port GC injection valve was used to inject a small sample from the outlet gas into the GC, which would restrict the flow every 3 minutes. This created the ripple patterns in Figure 3.8. This ripple was partially smoothed using a second order Savitzky-Golay technique. Included in Figure 3.8 is the CO_2 flow rate uncertainty, which is represented as the faded coloured bands around the solid lines.

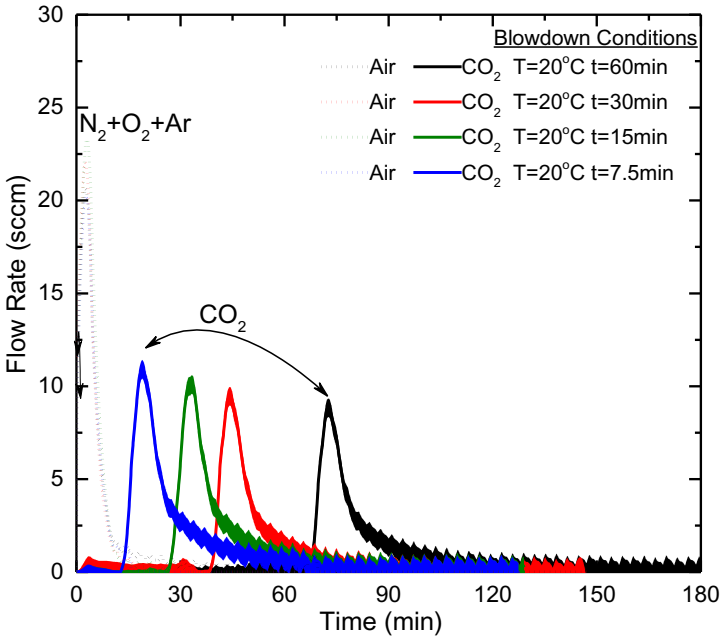

Figure 3.8 – Flow rates of N_2, O_2, Ar, and CO_2 during the blowdown (constant temperature, varying duration) and evacuation (T_E=200°C, and t_E=120min) steps for Na-X.

By increasing the duration of the blowdown step, the pressure in the column was decreased, and the purity of the product was increased. This can be seen in Figure 3.9 with the blowdown duration shown on the x-axis, purity in ppm shown on the y-axis on the left side of the figure, and blowdown pressure on the y-axis on the right side of the figure. The error for the purity is the standard deviation in the replicate runs and the error for the blowdown pressure is the uncertainty in the measurement. From these results, utilizing a blowdown duration of 7.5 min at 20°C, a product purity of 99.54 ± 0.23% CO_2 was acquired meeting the lowest high purity grade of 99.5% CO_2. As the blowdown duration increased from 15 min to 30 min, to 60 min, the purity increased from 99.73 ± 0.14% to 99.83 ± 0.12% to 99.96 ± 0.05%, respectively. This increase in CO_2 purity meets the requirements for anaerobic, laser, and supercritical fluid grade CO_2, while being within the margin of error of research grade CO_2. This is the first reported increase in purity of CO_2 from air using a single adsorption cycle in literature. This increase is due to lower pressures reached during the blowdown step where the N_2, O_2, and Ar are evacuated from the column, leaving the CO_2 adsorbed. However, the amount of CO_2 captured during the evacuation step decreases as the blowdown duration increases. This can be seen in Figure 3.8 by the reduction of the size of peak as the blowdown duration becomes longer. An important design parameter for the production of high purity CO_2 is the empty space

inside and around the column which holds N_2, O_2, and Ar in quantities that are equivalent to that of the blowdown pressure after the blowdown step. By reducing this void space, higher purities can be achieved for similar conditions. This study required evaluating equipment such as thermocouples and pressure gauges which added roughly 7.1 cm^3 of void space, as well as 11.4 cm^3 of void space due to the void fraction of the pellets. This cumulative void space of 18.5 cm^3 would have reduced the measured purity, therefore, for the highest purity CO_2, it is recommended to reduce the void space as much as possible.

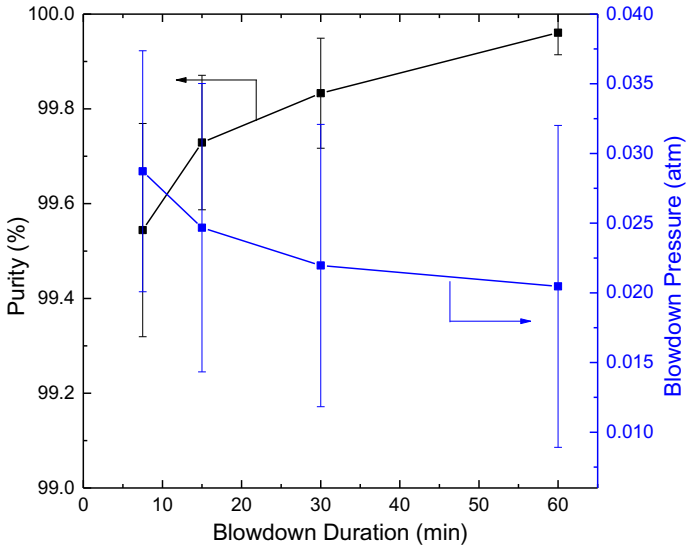

Figure 3.9 – The effect of blowdown duration on the blowdown pressure and the purity of the product.

3.4.2.2 Effect of Blowdown Temperature

Another strategy examined in this study to increase the amount of N_2, O_2, and Ar desorbed from the Na-X during the blowdown step is to use an elevated temperature with a vacuum to remove these impurities. Four blowdown temperatures of 20°C, 40°C, 60°C, and 80°C were investigated at a blowdown duration of 30 min. It was observed that by elevating the temperature of the blowdown step from 20°C to 80°C, the purity of the product increased from 99.83 ± 0.12% to 99.95 ± 0.04%, which can be seen from Figure 3.10. This increase in purity was not due to the decrease in pressure which was observed by changing the blowdown duration, but by elevating the temperature. This can be seen from the near constant blowdown pressure observed from Figure 3.10, with a slight increase in blowdown pressure for a blowdown temperature of 80°C.

This increase in blowdown pressure indicates an undesirable attribute that can be seen in Figure 3.11, where not only the amount of N_2, O_2, and Ar desorb during the blowdown step, but also significant quantities of CO_2 desorb as well. This desorption of CO_2 can be seen by the peaks for the CO_2 during the evacuation portion of the cycle decreasing in size as the temperature of the blowdown step increases. This makes sense and can be observed from the TD-Toth plot in Figure 3.6 with the slope of the Henry's Law region decreasing along with the overall adsorption capacity for CO_2 decreasing at 400 ppm at higher temperatures. This loss of CO_2 by changing the blowdown temperature during the blowdown step is

significantly greater than that observed by changing the blowdown duration. Further studies into utilizing an elevated temperature during the blowdown step at lower duration times should be investigated before ruling out the two main benefits of using an elevated temperature during the blowdown step. Firstly, the reduced vacuum requirement during the blowdown step for the TVSA cycle and secondly, the energy required for the elevated blowdown temperature which will later be utilized for the evacuation step.

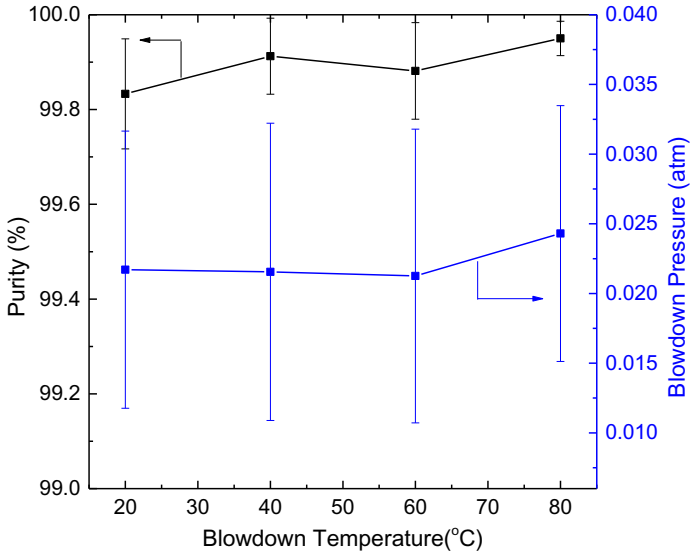

Figure 3.10 – The effect of blowdown temperature on the blowdown pressure and the purity of the product.

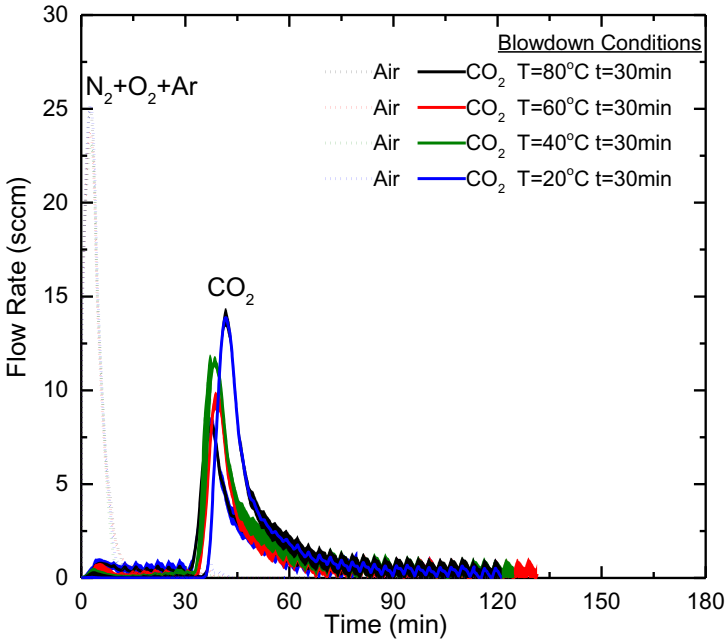

Figure 3.11 – Flow rates of N_2, O_2, Ar, and CO_2 during the blowdown (constant duration, varying temperature) and evacuation (T_E=200°C, and t_E=120min) steps for Na-X.

3.5 Conclusions

The goal of this study was to experimentally produce high purity CO_2 above 99.5% by capturing and concentrating the CO_2 from the air. This study first showed that CO_2 was favourably adsorbed onto Na-X over the other components in the air by determining the pure component isotherms of each gas which confirmed results from literature. These results were then used to create the TD-Toth model which showed the pure component adsorption of CO_2, N_2, O_2, and Ar between 20 – 110°C and 0 – 6 atm. This model was used to evaluate the behaviour during the blowdown step of the TVSA cycle with the goal of desorbing only the N_2, O_2, and Ar while leaving CO_2 adsorbed by the Na-X in order to increase the purity of the product during the evacuation step. Two proposed methods were then hypothesized from the TD-Toth model which were investigated: decrease the pressure (by varying the blowdown duration) with and without an increase in temperature.

Fixed bed adsorption desorption breakthrough curves were used to study the TVSA cycle with the same adsorption, evacuation, and pressurization step conditions and varying blowdown step conditions. The cyclical steady state breakthrough of center point conditions was compared to the initial adsorption after a complete regeneration. The results showed that CO_2 with a purity of 99.5% to 99.96% can be produced by varying the blowdown duration from 7.5 minutes to 60 minutes, and 99.8% to 99.95% purity can be produced by varying the blowdown temperature. However, while varying the blowdown temperature, significantly more CO_2 was lost during the blowdown step in comparison to varying the blowdown duration. This study proved that CO_2 can be produced in high purities which meet the requirements for medical, bone dry, beverage, food, anaerobic, and laser grade from DAC of CO_2.

3.6 Nomenclature

$\boldsymbol{K}$	Henry's Law Constant (mmol g^{-1} atm^{-1})
$\boldsymbol{H_0}$	Limiting Heats of Adsorption (kJ mol^{-1})
$\boldsymbol{P}$	Pressure (atm)
$\boldsymbol{P_A}$	Adsorption Step Pressure (atm)
$\boldsymbol{P_B}$	Blowdown Step Pressure (atm)
$\boldsymbol{P_E}$	Evacuation Step Pressure (atm)
$\boldsymbol{R}$	Ideal Gas Law Constant (m^3 atm K^{-1} mol^{-1})
$\boldsymbol{R^2}$	Coefficient of Determination (-)
$\boldsymbol{t}$	Time (min)
$\boldsymbol{t_B}$	Blowdown Duration (min)
$\boldsymbol{t_E}$	Evacuation Duration (min)
$\boldsymbol{T}$	Temperature (K)
$\boldsymbol{T_A}$	Adsorption Step Temperature (K)
$\boldsymbol{T_B}$	Blowdown Step Temperature (K)
$\boldsymbol{T_E}$	Evacuation Step Temperature (K)
$\boldsymbol{\alpha_A}$	Adsorption Capture Fraction (-)

α_D	Desorption Capture Fraction (-)

3.7 List of Abbreviations

DAC	Direct Air Capture
GC	Gas Chromatograph
IR	Infrared Spectroscopy
LPP	Light Product Pressurization
MFC	Mass Flow Controller
MFM	Mass Flow Meter
MOFs	Metal Organic Frameworks
TD-Toth	Temperature Dependant Toth
TSA	Temperature Swing Adsorption
TVSA	Temperature Vacuum Swing Adsorption
VSA	Vacuum Swing Adsorption

3.8 Bibliography

1. Na, B., Koo, K., Eum, H., Lee, H. & Song, H. K. CO_2 Recovery from Flue Gas by PSA Process using Activated Carbon. *Korean J. Chem. Eng.* **18,** 220–227 (2001).
2. Choi, W., Kwon, T., Yeo, Y., Lee, H., Song, H. K. & Na, B. Optimal Operation of the Pressure Swing Adsorption (PSA) Process for CO2 Recovery. *Korean J. Chem. Eng.* **20,** 617–623 (2003).
3. Stuckert, N. R. & Yang, R. T. CO_2 Capture from the Atmosphere and Simultaneous Concentration Using Zeolites and Amine-Grafted SBA-15. *Environ. Sci. Technol.* **45,** 10257–10264 (2011).
4. Chue, K. T., Kim, J. N., Yoo, J., Cho, S. H. & Yang, R. T. Comparison of Activated Carbon and Zeolite 13X for CO_2 Recovery from Flue Gas by Pressure Swing Adsorption. *Ind. Eng. Chem. Res.* **34,** 591–598 (1995).
5. Shekhah, O., Belmabkhout, Y., Chen, Z., Guillerm, V., Cairns, A., Adil, K. & Eddaoudi, M. Made-to-Order Metal-Organic Frameworks for Trace Carbon Dioxide Removal and Air Capture. *Nat. Commun.* **5,** 4228 (2014).
6. Reza, H., Nilam, R., Rajendran, A., Farooq, S. & Karimi, I. A. Cycle Synthesis and Optimization of a VSA Process for Postcombustion CO_2 Capture. *AIChE J.* **59,** 4735–4748 (2013).
7. Wilson, S. M. W. & Tezel, F. H. Direct Dry Air Capture of CO_2 using VTSA with Faujasite Zeolites. *Ind. Eng. Chem. Res.* (2020). doi:10.1021/acs.iecr.9b04803
8. Cavenati, S., Grande, C. A. & Rodrigues, A. E. Adsorption Equilibrium of Methane, Carbon Dioxide, and Nitrogen on Zeolite 13X at High Pressures. *J. Chem. Eng. Data* **49,** 1095–1101 (2004).
9. Socolow, R., Desmond, M., Aines, R., Blackstock, J., Bolland, O., Kaarsberg, T., Lewis, N., Mazzotti, M., Pfeffer, A., Sawyer, K., Siirola, J., Smit, B. & Wilcox, J. *Direct Air Capture of CO_2 with Chemicals*. *American Physical Society - Panel on Public Affairs* (2011).
10. Wilson, S. M. W., Kennedy, D. A. & Tezel, F. H. Adsorbent Screening for CO2/CO Separation for Applications in Syngas Production. *Sep. Purif. Technol.* **236,** 1–11 (2020).
11. Jayaraman, A., Yang, R. T., Cho, S. H., Bhat, T. S. G. & Choudary, V. N. Adsorption of Nitrogen, Oxygen and Argon on Na-CeX Zeolites. *Adsorption* **8,** 271–278 (2002).
12. Sebastian, J. & Jasra, R. V. Sorption of Nitrogen, Oxygen, and Argon in Silver-Exchanged Zeolites. *Ind. Eng. Chem. Res.* **44,** 8014–8024 (2005).
13. Dunne, J. A., Mariwala, R., Rao, M., Sircar, S., Gorte, R. J. & Myers, A. L. Calorimetric Heats of Adsorption and Adsorption Isotherms. 2. O_2, N_2, Ar, CO_2, CH_4, C_2H_6, and SF_6 on NaX, H-ZSM-5, and Na-ZSM-5 Zeolites. *Langmuir* **12,** 5896–5904 (1996).
14. Harlick, P. J. E. & Tezel, F. H. An Experimental Adsorbent Screening Study for CO_2 Removal from N_2. *Microporous Mesoporous Mater.* **76,** 71–79 (2004).

15. Kikkinides, E. S., Yang, R. T. & Cho, S. H. Concentration and Recovery of $C0_2$ from Flue Gas by Pressure Swing Adsorption. *Ind. Eng. Chem. Res.* **32,** 2714–2720 (1993).

16. Bacastow, R. B., Keeling, C. D. & Whorf, T. P. Seasonal Amplitude Increase in Atmospheric CO_2 Concentration at Mauna Loa, Hawaii, 1959-1982. *J. Geophys. Res.* **90,** 10529–10540 (1985).

Chapter 4

Adsorption Separation of CF_4, O_2, CO_2, and COF_2 from an Excimer Gas Mixture

Sean M.W. Wilson, and F. Handan Tezel

Department of Chemical and Biological Engineering, University of Ottawa, 161 Louis-Pasteur, Ottawa, Ontario K1N 6N5 Canada

To be submitted to: Separation and Purification Technology 2020

4.1 Abstract

The use of adsorbents is explored as an option for the removal of trace impurities of CO_2, CF_4, COF_2, and O_2 from F_2, Kr, and Ne for applications in excimer lasers. Due to the incompatibility of many adsorbents to F_2 and HF, aluminas and polymeric adsorbents were selected as potentially compatible materials. To determine the adsorption potential of these adsorbents in the low concentration region, the concentration pulse chromatographic technique was chosen to determine the Henry's Law constants of CO_2, CF_4, and O_2 gases on three polymeric adsorbents (HayeSep Q, HayeSep B, and Fluorinated DVB) and two aluminas (AA-300, and Alumina A). The results were plotted and compared on van't Hoff plots with the heat of adsorption values being calculated from the lines of best fit for all gases and adsorbents tested in this study. Due to the large energies required to operate the excimer lasers, a cryo-cooler was determined to be feasible to precool the feed stream before separation, which increases the adsorption capacity and the compatibility of the adsorbents to F_2 and HF. The van't Hoff plots were extrapolated to colder temperatures to determine the Henry's Law constants to analyze the potential of using the cryo-cooler. From this study, it was determined that HayeSep Q was the best polymeric adsorbent with significant adsorption of CO_2 at temperatures below -50°C while being the best performing CF_4 adsorbent. AA-300 was the best performing alumina in this study while having significant adsorption of CF_4 at temperatures below -135°C. However, from a compatibility standpoint, both of these materials need to be tested to determine their robustness in the presence of F_2 and HF at room and reduced temperatures.

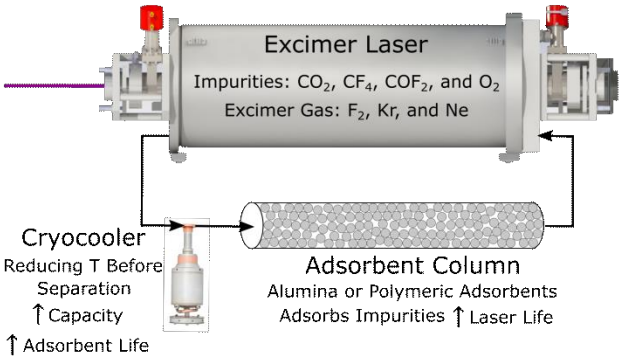

Keywords: Excimer Laser, COF_2, CO_2, CF_4, O_2 Adsorption, Cryocooler Adsorbent Separation

4.2 Introduction

4.2.1 Excimer Lasers

Excimer lasers, also known as exciplex laser, produce a very specific ultraviolet light which is used in the production of semiconductors [1–3] and have allowed semiconductors to get to the size they are today [4]. The use of excimer lasers also extends into other fields including eye surgery [5–8] and micromachining [9,10]. These lasers work by exciting a noble gas (Ar, Kr, or Xe and sometimes Hg) and a reactive gas (F_2, Cl_2, or Br and sometimes I) into an exciplex [11]. The gas mixture in this study of interest is fluorine and krypton, which when excited produces an exciplex krypton fluoride (Equation 1).

$$2Kr + F_2 \xrightarrow{Energy} 2KrF \quad (1)$$

When krypton fluoride is produced it starts in an energized state which shortly afterwards releases energy in the form of a light pulse at a wavelength of 248 nanometers and goes into a metastable, but highly repulsive ground state. This ground state then quickly dissociates into the original gas mixture (Equation 2)[12].

$$2KrF \longrightarrow 2Kr + F_2 \quad (2)$$

In order to produce the exciplex, gases F_2 and Kr are needed at approximate concentrations of 0.1% and 2%, respectively, with a balance of neon within the laser chamber.

This study looks into a specific problem that all Kr-F excimer lasers have, which is the build-up of undesirable by-products from the reaction of fluorine as well as side reactions of hydrofluoric acid. These undesirable by-products, CO_2, COF_2, CF_4, O_2, and HF, are absent at the beginning of the gas lifetime of the laser and their concentrations slowly increase to the concentrations outlined in Table 4.1 [13] at the end of its cycle. These gases are undesirable because they either absorb light in the spectrum of 248 nm or they impede the formation of the exciplex. Therefore, to produce a constant light output, an increase in voltage is required. With the increase in voltage, the life of the laser decreases significantly, making the typical life of these lasers equivalent to 1 billion pulses. Depending on the operating conditions of the laser, its duty cycle, operating energy, etc., its lifetime can be as short as two months. One way to potentially increase the life of these lasers would be to reduce the impurities within the laser chamber.

Table 4.1 – Typical quantity of impurities measured within the 5 atmospheres, 60 litre chamber of a Kr – F excimer laser at the end of its cycle. The quantity of oxygen is unknown [13].

Undesirable	CO_2	HF	CF_4	COF_2	O_2
Concentration	20 ppm	15 ppm	350 ppm	150 ppm	Unknown

Currently, in order to deal with these by-products, a venting and cleaning, followed by injection of new excimer gas into the laser chamber would be done for the laser to run properly. This procedure has always been regarded as quite expensive because of the cost of the excimer gas mixture.

The impurities within an excimer laser affect the laser output with literature showing different impurities having different effect on laser output. For a 10% decrease in laser output HF has the greatest impact followed by CO_2 > SiF_4 > O_2 > N_2 > CF_4 [14]. This impact of the impurities can be seen in Table 4.2. Ar-F excimer laser (wavelength 193 nm) also experiences a similar trend; however, the laser is significantly more sensitive to impurities.

Table 4.2 – Impurities that are present within a KrF laser with a fluorine concentration of 0.18% immediately after gas injection, after resting for 70 hours, and the amount of impurities required for 10% decrease in laser output. This was adapted from Sumitani et al [14].

Impurity	Detection Limit (ppm)	Concentration (ppm) Immediately after gas fill	Concentration (ppm) 70 hours of rest	10% decrease in laser output (KrF)	10% decrease in laser output (ArF)
N_2	0.1	<D.L	0.4	200	25
O_2	0.1	<D.L.	12.7	90	5
CO_2	0.01	0.65	0.49	40	5
CF_4	0.01	0.3	9.87	700	35
SiF_4	0.01	0.06	0.47	60	10
HF	0.1	9.2	31.4	30	10

The impurities from an excimer laser come from reactions with the laser as well as a small amount is injected along with the excimer gas mixture. This was investigated in literature with Sumitani et al. finding that ppm of HF is injected into the laser with the excimer gas [14]. This study showed that even when a Kr-F laser is idling, there is a noticeable increase of HF, CF_4, and O_2 within the laser chamber. However, this increase in impurities is significantly less than when the laser is running, with HF increasing 10 times faster and CF_4 showing a similar trend. Another finding from Sumitani et al. is that when an excimer laser is running for 20 minutes at 1000 Hertz, CO_2 is consumed to below detection limits and COF_2 is produced.

Previous efforts made by the excimer industry have been to use a liquid nitrogen trap to remove CO_2 as well as the other impurities [15]. This effectively separates the components based on the normal boiling points of the species within the laser. The properties of the gases in this system are shown in Table 4.3. Using a liquid nitrogen trap is effective but comes with two compromises; the loss of krypton from the chamber and therefore the need for a topping up of krypton periodically, and the need to manage another consumable within the process, the liquid nitrogen dowers. Liquid nitrogen did not meet the demands of the customers because of these two issues.

Adsorbents can potentially be used to scrub the excimer gas of the impurities which has also been investigated recently by industry [16]. This however is a complicated separation with most traditional adsorbents being unstable in fluorine. Activated carbons are susceptible to violently breaking down to CO_2 and O_2 while scrubbing all the F_2, and preliminary tests using different types of aluminas were not repeatable. This was probably due to the structure of the alumina collapsing as it reacted with the fluorine

to produce non-porous alumina fluoride. This reaction has been seen in literature with HF reacting with alumina at temperatures of 200°C to produce AlF_3 [17]. Fluorine in literature has been shown to react spontaneously with the silica and fluorine etching is common with silicon dioxide [18,19]. Therefore, silica gels would not be able to be used due to the structure being composed of SiO_2. This reactivity has been shown with the zeolites' silica-oxygen bond in the crystal structure with zeolites breaking down in the presence of HF [20]. Two interesting points from this article is that synthetic zeolites were more resilient than their natural counterparts and that the H^+ was said to be more stable than Na^+ as a counterbalancing cation within the crystalline structure. Aluminum Phosphates (AlPO) have also been investigated for their stability to HF and F_2 with studies showing mixed results with decomposition occurring at room temperature for some AlPOs [21] and stability at temperatures above 400°C from others [22–24].

Table 4.3 – Different properties of the gases that are contained within an excimer laser.

Gas		Molar Mass	Normal Freezing Point	Normal Boiling Point	Critical Temp.	Critical Pres.	Liquid Density	Temp. Ref.	Kinetic Diameter	Dipole Moment	Quad-rupole Moment	Polari-zability
IUPAC Name		(g/mol)	(K)	(K)	(K)	(atm)	(g/cm³)	(K)	(Å)	(Debyes)	(Å²)	(Å³)
Neon	Ne	20.18	24.5	27.0	44.4	27.2	1.204	27	0.28	-	-	-
Carbon Dioxide	CO_2	44.01	216.6	194.7	304.2	72.8	0.777	293	0.33†	0†	-4.3†	2.65†
Oxygen	O_2	32.00	54.4	90.2	154.6	49.8	1.149	90	0.34†	0†	-0.39†	1.6†
Krypton	Kr	83.80	115.8	119.8	209.4	54.3	2.42	120	0.36	-	-	2.46×
Carbon Tetrafluoride	CF_4	88.01	86.4	145.2	227.6	36.9			0.47	0†	0†	3.84†
Fluorine	F_2	38.00	53.5	85.0	144.3	51.5	1.51	85	0.37	0	0.88·	1.27¥
Hydrofluoric Acid	HF	20.01	190.0	292.7	461	64				1.736·	2.6·	0.78¥
Carbonyl Fluoride	COF_2	66.01	161	188						0.95		

All gas properties are from R. G. Griskey [25] unless otherwise marked · = D. E. Stogryn & A. P. Stogryn (1966)[26] † = S. Sircar (2006)[27]
× = Granville and Hall (1966)[28] ¥ = Gough et al. (1996)[29]

Porous polymers are industrially available adsorbents and have potential for this separation at ambient conditions (5 atm and 30°C). A list of common polymers is shown in Table 4.4 and a list of adsorbent polymers are included in the Supporting Information in Appendix III. The polymers that show little to no degradation after 30 days of continuous exposure to fluorine and hydrofluoric acid are Fluorinated Ethylene Propylene (FEP), Tetrafluoroethylene (TFE), and Perfluoroalkoxy Alkane (PFA). While there are no polymeric adsorbents marketed under FEP or PFA, Chromosorb T, Kel-F, and Fluoropak 80 are all TFE sorbents. Chormosorb T made from Teflon 6 powder, a long chained TFE, is considered the be the best of the three with a surface area (7 – 8 m^2), a packing density of 0.42 g/mL and high column efficiencies [30].

Table 4.4 – List of different types of polymers and their compatibilities to HF and F_2 at temperatures 20°C/50°C. E - No damage after 30 days of constant exposure. G - Little or no damage after 30 days of constant exposure. F - Some effect after 7 days of constant exposure. N - Immediate damage may occur and therefore not recommended for continuous use. Information is provided by Cornell [31].

Chemical Species	LDPE	HDPE	PP	PPCO	PMP	PETG	FEP	TFE	PFA	ECTFE	ETFE	PC	Ridgid PVC	Flex PVC	PSF	PS	FLPE	RESMER	PMMA	SAN	PEI	XLPE	PVDF
Hydrofluoric Acid	E/E	E/E	E/G	E/E	E/G	N/N	E/E	E/E	E/E	E/E	E/E	F/N	G/F	F/N	F/N	N/N	E/E	N/N	N/N	E/G	G/F	E/E	E/E
Fluorine	F/N	G/N	N/N	F/N	F/N	-/-	E/G	E/G	E/G	E/F	G/N	G/F	E/N	F/N	N/N	N/N	G/N	-/-	-/-	N/N	F/N	N/N	G/N

Due to the large amount of energy required to produce the exciplex (6 kW of power for the excimer laser), it is feasible to cool down the stream before adsorption. This can be done using cryocoolers which are able to drop the temperature down to as low as 40K. This would allow for the possibility to use materials that would otherwise not be able to handle fluorine and hydrofluoric acid at room temperature.

Dropping down the temperature of the gas stream would allow for the possible use of polymers such as High Density Polyethylene (HDPE), Halar Ethylene Chlorotrifluoroethylene (ECTFE), Tefzel Ethylene Tetrafluoroethylene (ETFE), Fluorinated Polyethylene (FLPE), Polyvinyl Chloride (PVC) or polyvinylidene fluoride (PVDF). A fluorinated divinylbenzene chromatography column packing available from Sorbtech is similar structure to that of PVDF with the addition of fluorinated benzene groups. This is another promising sorbent with surface areas measuring in the 700 m^2/g range [32]. Fluorinated styrene-divinylbenzene copolymer with surface areas of 415 m^2 has been demonstrated in literature to be resistant to further fluorination once all alpha and beta hydrogen atoms in the structure have been saturated at temperatures up to 60°C and 1% fluorine gas [33].

At lower temperatures the reaction of the alumina-oxygen bond to fluorinated species decreases significantly [17]. Therefore at lower temperatures aluminas are also prospective sorbents for this separation. Aluminas are interesting adsorbents due to their ability to vary the amount of lewis and bronsted, acid and base sites as well as the overall pH of the alumina. The zero point charge (ZPC) is the pH value that is required to give a zero net surface charge and is an important measurable quantity of activated aluminas [34]. This can be measured by a simple acid-base titration and will help determine whether an alumina will interact stronger with a more anionic molecule or a more cationic molecule relative to the ZPC.

The ideal adsorbent for this separation is one that would adsorb CO_2, CF_4, COF_2, and O_2 while letting F_2, Kr, and Ne pass right through. Typically, CO_2 and COF_2 would have the strongest sorption due to their strong intermolecular forces in comparison to CF_4, O_2, Kr, and F_2 being similar but weaker. Ne with little to no intermolecular forces typically has the weakest adsorption. One of the challenges of this separation is finding an adsorbent that will selectively adsorb CF_4 and O_2 while letting F_2 and Kr through.

4.3 Materials and Methods

4.3.1 Materials

CO_2 and O_2 pure gases were obtained from Linde Canada (Burlington, Ontario, Canada) at purities of 99.99% and 99.994%, respectively. CF_4 and Ne pure gases were obtained from Light Machinery (Ottawa, Ontario, Canada) at purities of 99.999% and 99.999%, respectively. Five adsorbents were selected for this study, including three polymeric adsorbents referred to as HayeSep B, HayeSep Q, and Fluorinated Divinyl Benzene (DVB), and two alumina referred to as AA-300, and Alumina A.

4.3.1.1 HayeSep Q

HayeSep Q is a brand name of a porous polymer composed of DVB which is chemically similar to that of styrene. Styrene however showed immediate effects to the exposure of F_2 and HF at room temperature. In literature, styrene-DVB copolymer was reported to show inertness once all the alpha and beta hydrogens were substituted by fluorines [33]. However, this reaction took a significant amount of time and therefore at lower temperatures might be suitable for this separation. This material was purchased from Sigma Aldrich (St. Louis, Missouri, United States).

4.3.1.2 HayeSep B

HayeSep B is a brand name of a porous co-polymer of DVB and ethylene. As can be seen in Table 4.4, many polymers have good stability in HF and F_2 environments, but many of these materials are non-porous and therefore are not suitable for adsorption. A copolymer between a polymer resistant to HF and F_2 with DVB could potentially increase the stability in comparison to a polymer solely composed of DVB. With polyethylene having decent stability, it was selected as a candidate for this study. HayeSep B was purchased from Sigma Aldrich.

4.3.1.3 Fluorinated DVB

With fluorinated polymers being more resistant to fluorine and hydrofluoric acid, a fluorinated DVB which is an out-dated material for hydrocarbon separation in chromatography was an ideal candidate. This material is composed of DVB which has had the hydrogens substituted for fluorine. Fluorinated DVB was purchased from Jordi Labs (Mansfield, Massachusetts, United States).

4.3.1.4 AA-300

AA-300 is the brand name of activated alumina from Alcan Alumina (now called Axens) located in Brockville, Ontario, Canada. This activated alumina is a prospective material for this separation due to the stability of alumina in the presence of F_2 and CF_4. This particular activated alumina is neutral and was grounded to 20-50 MESH for this study. AA-300 in literature has been shown to have strong electrostatic interactions with adsorbates and one major use of this material is as a desiccant [34]. This strong interaction is due to the hydroxyl group on the activated alumina surface with literature showing its interaction with HF to modify its surface to produce more Lewis acid sites [34].

4.3.1.5 Alumina A

Alumina A is a brand of alumina by Selecto Scientific (Suwanee, Georgia, United States) that is acidic in nature. This alumina was chosen due to its potential to being additionally resilient to HF and F_2.

4.3.2 Concentration Pulse Chromatography

It is possible to determine the Henry's Law constants for an adsorbent at a particular temperature using a packed adsorption column set up within a gas chromatograph, by injecting a very small amount of sample gas into the carrier gas flowing through the adsorption column. This is called the concentration pulse chromatography technique and is done by using the thermal conductivity detector (TCD) placed in the GC.

The injection loop must be small enough to ensure that the concentration of the gas is within the Henry's Law region in the column, yet not so small as to be measurably insignificant by the detector. After injection, the adsorbate sample gas in the carrier gas proceeds to enter the adsorption column where the adsorbate interacts with the adsorbent. The concentration of the gas exiting the column is then measured by the TCD. For this study, a TCD was used due to the difference between the thermal conductivity of the carrier gas (Neon) and the sample gases (CO_2, CF_4, and O_2). Thermal conductivity values of the gases present within the excimer laser are shown in Table 4.5.

Table 4.5 – Thermal conductivity values of gases present in the excimer gas.

Gas		Thermal Conductivities		
IUPAC Name	Formula	200K (W/mK)	300K (W/mK)	400K (W/mK)
Neon	Ne	37.6	49.8	60.3
Carbon Dioxide	CO_2	9.6	16.8	25.1
Oxygen	O_2	18.4	26.3	33.7
Krypton	Kr	6.4	9.5	12.3
Carbon Tetrafluoride	CF_4	-	16	24.1

From the data obtained from the TCD detector (voltage as a function of time), the response peak is analysed for the calculation of the mean residence time (t_u) which is the time when the area underneath the voltage peak is half the total area of the peak (Equation 3).

$$t_\mu = \int Ctdt \Big/ \int Cdt \qquad 3$$

Where C is the measured concentration response from the detector (indicated as the voltage) and t is time. It should be noted that care was taken such that there was not significant dead space before or after the column which would affect the step change or the result. From the mean residence time, the Henry's Law constant as a function of the ratio of concentration in the pellet over concentration in the gas phase (K) can be calculated using Equation 4. The derivation of this is described in detail by Ruthven and Kumar (1980)[35].

$$t_\mu = \frac{L}{v}\left[1 + \frac{1-\varepsilon}{\varepsilon}K\right] \qquad 4$$

Where L is the adsorption column length, v is the interstitial fluid velocity, and ε is the void fraction of the bed which was assumed to be 0.4 for all experiments. The Henry's Law constant is then converted into more common units of mmol g^{-1} atm^{-1} (K_P) using Equation 5.

$$K_P = \frac{K}{R\,T\,\rho_P} \qquad 5$$

Where, R is the gas law constant, T is temperature of the column, and ρ_P is the density of the pellets. The density of the pellets was determined by measuring the bulk density of the adsorbent using a mass balance and a graduated cylinder which was packed with adsorbent. The packing of the graduated cylinder was carried out by placing the adsorbent into the graduated cylinder and placing a small metal weight on top

while applying a vibrational tool to shake the cylinder and compact the adsorbent. The volume and then weight of the cylinder were calculated to determine the bulk density. From the bulk density, assuming the beds void fraction of 0.4, the pellet density was calculated.

The limiting heat of adsorption values were then determined from calculated Henry's Law constants at different temperatures using van't Hoff equation (Equation 6). Each of the five samples have five Henry's Law constants at five different temperatures with the temperatures being selected in order to maximize response size and minimize baseline error from the GC.

$$\frac{\partial lnK_P}{\partial T} = \frac{\Delta H_0}{RT^2} \qquad 6$$

Assuming ΔH_o is not a strong function of T, integrating Equation 6 gives Equation 7.

$$lnK_P = -\frac{\Delta H_0}{R}\frac{1}{T} + lnK_0 \qquad 7$$

By plotting $ln\,K_P$ vs. $1/T$, the slope of this line gives the ratio of the heat of adsorption at zero loading to the gas constant can be calculated. This extrapolation is done in this study to determine the benefit of reducing the temperature on the separation.

4.4 Results and Discussion

The Henry's Law constants for CO_2, CF_4, and O_2 for HayeSep Q, HayeSep B, fluorinated DVB, AA-300, and Alumina A adsorbents were calculated from the concentration pulse chromatography experiments and are presented in Figure 4.1, Figure 4.2, Figure 4.3, Figure 4.4, and Figure 4.5, respectively. These values were calculated using Equation 4 and Equation 5, and the logarithmic plots of the Henry's Law constant vs. 1/T are presented in these figures. The coefficient of determination with relation to Equation 7 is plotted alongside the line of best fit for each data set. Each data point was repeated three times and the standard deviation is plotted. The density of the pellet for HayeSep Q and HayeSep B were found to be the same at 0.66 g/cm^3. The density of the pellet for AA-300 and Alumina A were found to be 1.52 g/cm^3 and 1.57 g/cm^3, respectively. These values are similar to densities reported in literature which are found to be between 0.8 – 1.8 g/cm^3 for aluminas [36]. Due to the very small sample size of fluorinated DVB to accurately measure the density, the pellet density was assumed to be the same as HayeSep Q and HayeSep B.

For all adsorbents tested in this study, CO_2 was adsorbed the most, followed by CF_4 and then O_2. This is not surprising when consulting the van der Waals forces of the adsorbates presented in Table 4.3, it can be seen that CO_2 has the strongest forces followed by CF_4 and then O_2. For the three polymeric adsorbents studied, the difference in adsorption capacities between CO_2 and CF_4 is not as significant as that for the aluminas. This is due to the strong interaction between CO_2 and the aluminas which has been observed in the literature [37,38]. The strength of this interaction between the CO_2 and the aluminas was so strong that it

was only measurable at higher temperatures, with the interaction being so strong at lower temperatures that the CO_2 would "stick" to the alumina.

To see this difference more clearly between the adsorption of CO_2, CF_4, and O_2 in the Henry's Law region for the adsorbents tested in this study, their respective relationships according to Equation 7 are plotted and are shown in Figure 4.6, Figure 4.7, and Figure 4.8, for CO_2, CF_4, and O_2 gases, respectively. This further highlights the difference between the adsorption of CO_2 by the aluminas versus the polymeric adsorbents. The adsorption of CO_2 was found to be the highest for Alumina A at temperatures below 170°C which is an acidic version of alumina compared to AA-300 which is neutral. The adsorption of CO_2 was similar for the three polymeric adsorbents with HayeSep Q being slightly higher than HayeSep B and then fluorinated DVB at lower temperatures close to the ambient conditions.

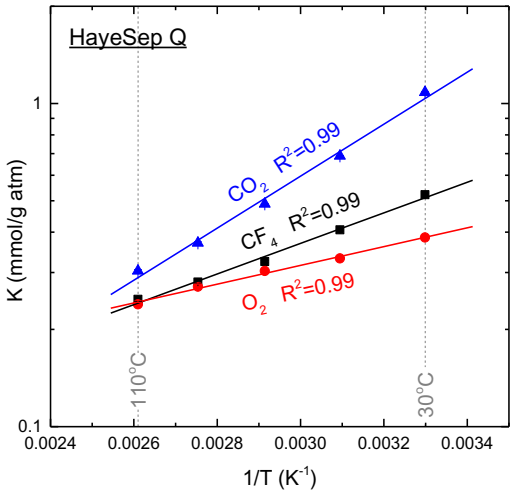

Figure 4.1 – Henry's Law constant values displayed on a van't Hoff plot for the adsorption of CO_2, CF_4, and O_2 on HayeSep Q between temperatures of 30°C and 110°C.

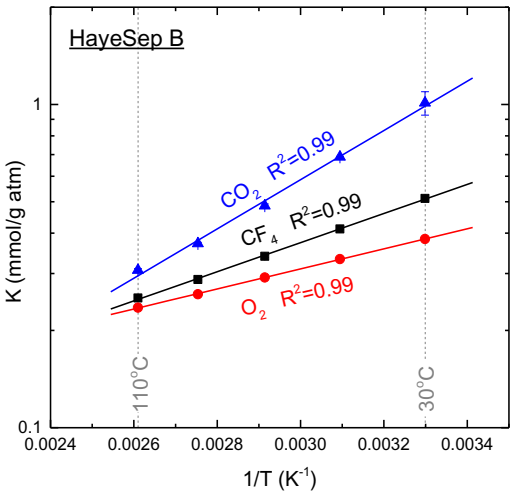

Figure 4.2 – Henry's Law constant values displayed on a van't Hoff plot for the adsorption of CO_2, CF_4, and O_2 on HayeSep B between temperatures of 30°C and 110°C.

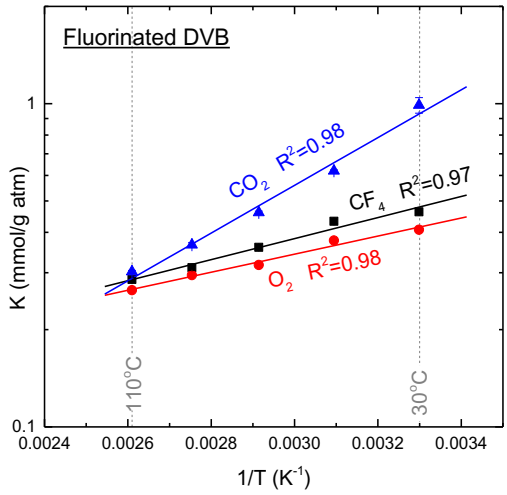

Figure 4.3 – Henry's Law constant values displayed on a van't Hoff plot for the adsorption of CO_2, CF_4, and O_2 on fluorinated DVB between temperatures of 30°C and 110°C.

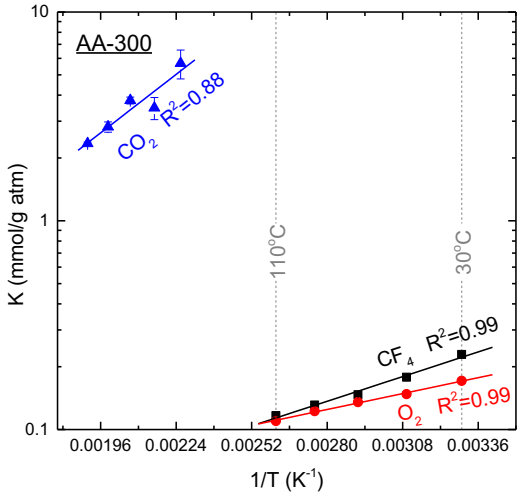

Figure 4.4 – Henry's Law constant values displayed on a van't Hoff plot for the adsorption of CO_2, CF_4, and O_2 on AA-300 between temperatures of 30°C and 250°C.

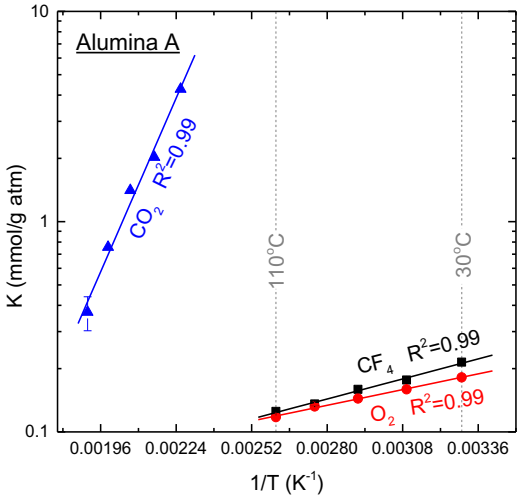

Figure 4.5 – Henry's Law constant values displayed on a van't Hoff plot for the adsorption of CO_2, CF_4, and O_2 on Alumina A between temperatures of 30°C and 250°C.

For the adsorption of CF_4, the polymeric adsorbents have a higher Henry's Law constant values than that of the aluminas. However, if the Henry's Law constants were calculated in terms of the volume of the adsorbent and not the mass, then they would have similar Henry's Law constants. HayeSep Q and HayeSep B have similar Henry's Law constants with fluorinated DVB being higher at temperatures above 50°C. For the aluminas, AA-300 has a higher Henry's Law constant at above 60°C compared to Alumina A. Comparing the Henry's Law constants in this study with zeolite ZSM-5 from literature, the adsorption of CF_4 is significantly more on zeolite ZSM-5 with Henry's Law constant of 2 mmol g^{-1} atm^{-1} at 30°C [39].

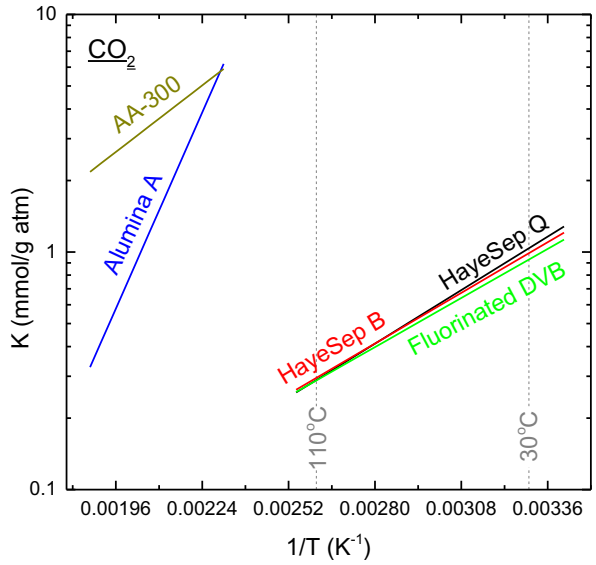

Figure 4.6 – CO_2 Henry's Law constants for HayeSep Q, HayeSep B, fluorinated DVB, AA-300, and Alumina A displayed on a van't Hoff plot.

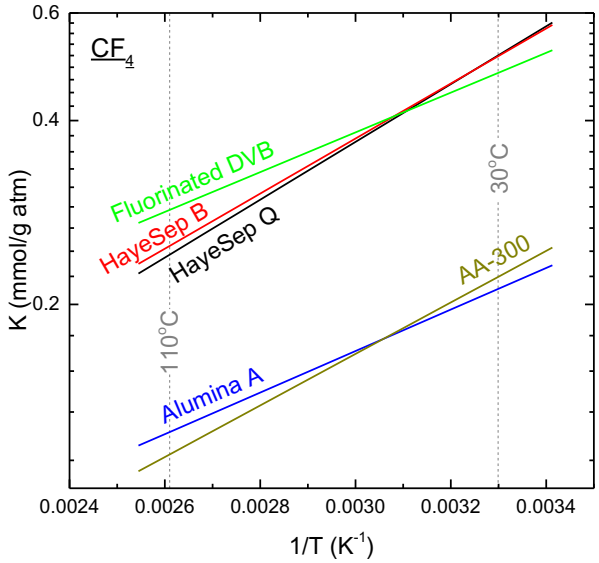

Figure 4.7 – CF_4 Henry's Law constants for HayeSep Q, HayeSep B, fluorinated DVB, AA-300, and Alumina A displayed on a van't Hoff plot.

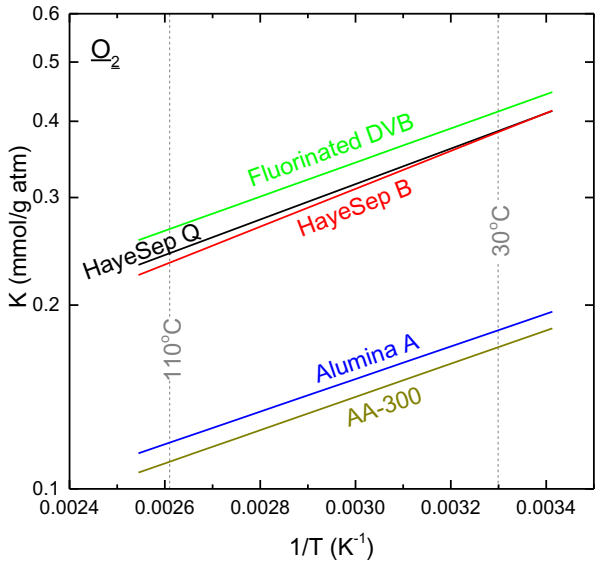

Figure 4.8 – O_2 Henry's Law constants for HayeSep Q, HayeSep B, fluorinated DVB, AA-300, and Alumina A displayed on a van't Hoff plot.

For the adsorption of O_2, all five adsorbents have a similar trend with the adsorption of the polymeric adsorbents having higher Henry's Law constants than the aluminas. However, as discussed before, they would be similar if compared on a per volume basis. It was found that fluorinated DVB has the highest Henry's law constant followed by HayeSep Q, HayeSep B, Alumina A, and AA-300, in that order. Fluorinated DVB probably had a higher interaction with O_2 than the other polymeric adsorbents due to the fluorine interacting strongly with the polarizability of the O_2. Further investigation would be required to confirm. It can be observed from Figure 4.8 that the trend lines for the adsorption of O_2 are parallel to each other, indicating similar heat of adsorption values for all the adsorbents.

From Equation 7, the slope of the line in the van't Hoff plot is related to the heat of adsorption, with higher slopes indicating higher heats of adsorption. From the van't Hoff plots the limiting heats of adsorption were calculated and are presented in Table 4.6 for the gases and adsorbents tested in this study. The adsorption is the strongest for CO_2, followed by CF_4, and then O_2 for all adsorbents in this study. For CO_2 adsorption, the aluminas have the strongest adsorption compared to the polymeric adsorbents.

The limiting heat of adsorption for CO_2 varied between AA-300 and Alumina A by 37 kJ/mol. This difference in heat of adsorption of CO_2 on aluminas was seen in literature with reported values as low as 15.5 kJ/mol to 130 kJ/mol which is based on the heterogeneity of the alumina's surface and the surface's functional groups [38,40,41]. For oxygen adsorption on aluminas, one study reported a heat of adsorption around 10 kJ/mol which is slightly more than the values reported in this study [38]. No literature was found to report on the heat of adsorption of CF_4 on aluminas or for any of the gases with the polymeric adsorbents. For all the adsorbents, the heat of adsorption values for O_2 were similar, since the plots for this gas are all parallel to each other. With CF_4 however, HayeSep Q and HayeSep B have the highest heat of adsorption values compared to the other adsorbents.

Table 4.6 – Limiting heat of adsorption for CO_2, CF_4, and O_2 for the adsorbents tested in this report.

Adsorbent	Limiting Heat of Adsorption		
	CO_2 (kJ/mol)	CF_4 (kJ/mol)	O_2 (kJ/mol)
HayeSep Q	15.40 ± 0.75	9.06 ± 0.45	5.56 ± 0.27
HayeSep B	14.58 ± 0.55	8.63 ± 0.14	5.94 ± 0.05
Fluorinated DVB	14.14 ± 0.97	6.23 ± 0.58	5.34 ± 0.42
AA-300	19.14 ± 4.00	8.07 ± 0.53	5.21 ± 0.20
Alumina A	56.42 ± 3.96	6.51 ± 0.34	5.11 ± 0.19

Due to the amount of energy required to produce the exciplex for the laser, it is feasible to cool down the stream before the separation. Cooling down the feed stream before separation of the impurities from Kr, F_2, and Ne is beneficial in two ways. Firstly, the adsorbents that were tested in this study would be more resilient to F_2 and HF in colder environments with relation to the activation energy in the Maxwell-Boltzmann distribution of molecular energies. Secondly, as temperature decreases, the adsorption capacity which is dictated by the Henry's Law constant for purification increases logarithmically according to Equation 7.

The effect of decreasing temperature on an increase in the Henry's Law constant can be seen in Figure 4.9, Figure 4.10, and Figure 4.11 for CO_2, CF_4, and O_2, respectively. These trends were extrapolated past 30°C for colder temperatures, so care should be taken as the error would be larger the colder the temperature. The boiling points of the gases that are present in a Kr-F excimer laser are included in the figures.

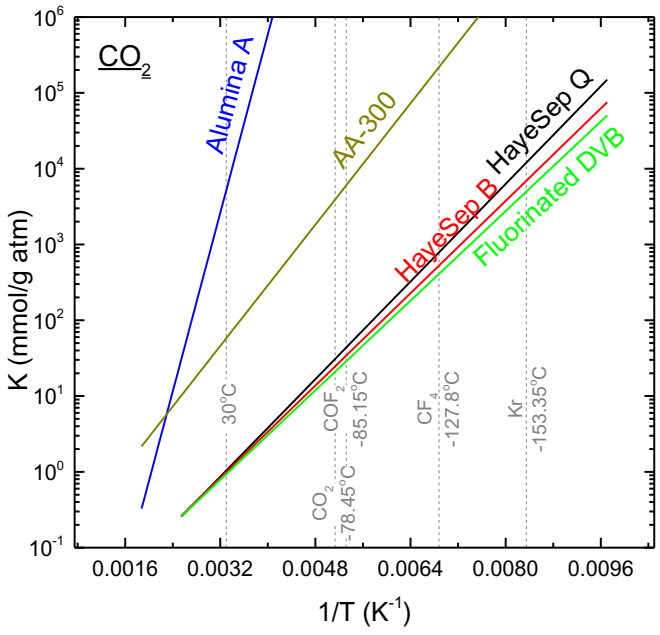

Figure 4.9 – CO_2 Henry's Law constants for adsorbents in this study extrapolated to colder temperatures. The boiling points of CO_2, COF_2, CF_4, and Kr are included.

For the adsorption of all gases, as the temperature decreases, the Henry's Law constant values of all the adsorbents increases since adsorption is an exothermic process. This increase is significant, for example, adsorbents which are commonly used to scrub CO_2 in air prepurification have Henry's Law constants around 10 - 100 mmol g^{-1} atm^{-1} [37]. This value for CO_2 adsorption occurs at 30°C for AA-300, but only at -50 to -100°C for the polymeric adsorbents.

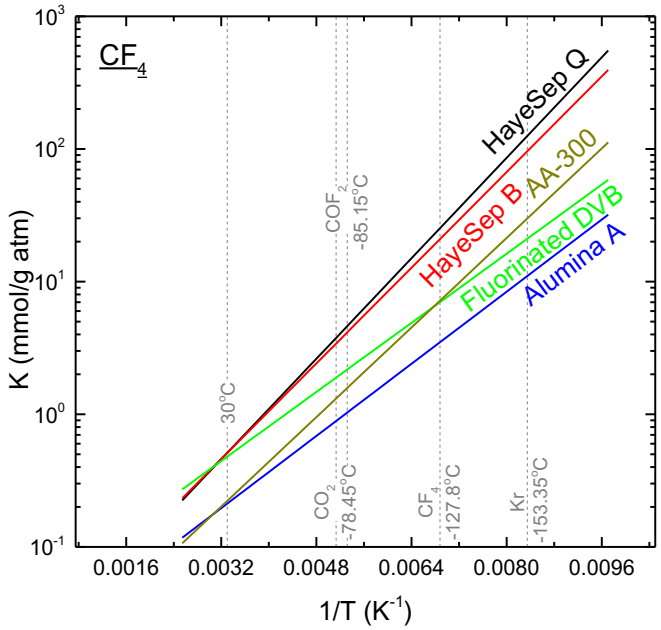

Figure 4.10 – CF_4 Henry's Law constants for adsorbents in this study extrapolated to colder temperatures. The boiling points of CO_2, COF_2, CF_4, and Kr are included.

For the adsorption of CF_4, HayeSep Q and HayeSep B polymeric adsorbents had significant Henry's Law constants above 10 mmol g^{-1} atm^{-1} occurring below -110°C. AA-300 from the aluminas was the best adsorbents for CF_4 with Henry's Law constants above 10 mmol g^{-1} atm^{-1} below temperatures of -135°C.

For O_2 adsorption, significant adsorption only occurs at temperatures below -145°C for the best performing material, HayeSep B. This temperature however is close to the condensing point of krypton which could potentially condense out of the gas onto the adsorbent which is undesirable.

For the adsorption of COF_2, with the molecule having a larger distribution of electronegativities with the fluorines on one side of the carbon and the oxygen on the other, carbonyl fluoride will have stronger electrostatic forces than CO_2. This increase in strength of electrostatic forces is good and it would be expected that the any adsorbent that adsorbs CO_2 effectively, would adsorb COF_2 better. In this study, utilizing aluminas at room temperature or polymeric adsorbents below -50°C should provide effective removal of COF_2 from the stream.

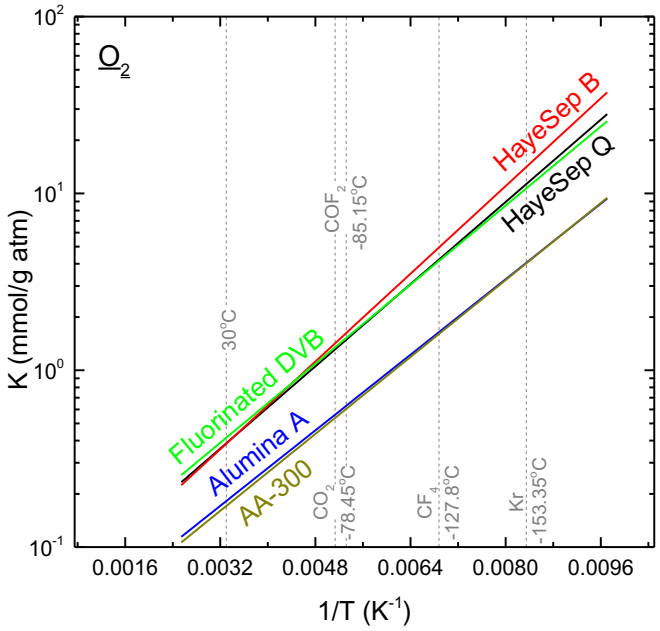

Figure 4.11 – O_2 Henry's Law constants for adsorbents in this study extrapolated to colder temperatures. The boiling points of CO_2, COF_2, CF_4, and Kr are included.

4.5 Conclusions

Due to an environment that contains F_2 and HF, potential compatible materials HayeSep Q, HayeSep B, fluorinated DVB, AA-300, and Alumina A were selected as adsorbents for this separation. These materials were tested for the adsorption capacity in the Henry's Law region for CO_2, CF_4, and O_2 with adsorption being significant at room temperature for the aluminas for the adsorption of CO_2. For CO_2 on the polymeric adsorbents as well as CF_4 and O_2 on all the adsorbents, the Henry's Law constant values were below 10 mmol g^{-1} atm^{-1}.

To increase the adsorption of these impurities as well as increase the life of these adsorbents in F_2 and HF, a decrease in the separation temperature was proposed. By decreasing the temperature, all adsorbents would have significant adsorption of CO_2 above 10 mmol g^{-1} atm^{-1} even at moderately cool temperatures of -50°C, with few materials having decent adsorption of CF_4 at temperatures as high as -100°C. O_2 adsorption was only significant at temperatures as high as -145°C which is close to the condensation point of krypton.

Two adsorbents are recommended from an adsorption standpoint above the other ones as potential materials to be used for this separation. They are HayeSep Q and AA-300. HayeSep Q has significant adsorption of CO_2 at temperatures below -50°C while being the best performing CF_4 adsorbent in this study. AA-300 is already an adsorbent used for CO_2 adsorption while having significant adsorption of CF_4 at temperatures below -135°C. However, from a compatibility standpoint, both of these materials need to be tested to determine their robustness in the presence of F_2 and HF that are present in this system.

4.6 Nomenclature

C	Concentration (mol m^{-3})
H_0	Heat of Adsorption at Zero Loading (kJ mol^{-1})
K	Henry's Law Constant (mol m^{-3}/mol m^{-3})
K_P	Henry's Law Constant (mmol g^{-1} atm^{-1})
L	Adsorbent Column Length (m)
R	Ideal Gas Law Constant (m^3 Pa K^{-1} mol^{-1})
t	Time (s)
t_u	Mean Residence Time (s)
T	Temperature (K)
v	Interstitial Fluid Velocity (m s^{-1})
ε	Void Fraction of the Bed (-)
ρ	Density (kg m^{-3})

4.7 List of Abbreviations

AlPO	Aluminum Phosphate
BET	Brunauer-Emmett-Tellor
DVB	Divinyl Benzene
FEP	Fluorinated Ethylene Propylene
FLPE	Fluorinated polyethylene
ECTFE	Halar Ethylene Chlorotrifluoroethylene
ETFE	Tefzel Ethylene Tetrafluoroethylene
GC	Gas Chromatograph
HDPE	High Density Polyethylene
PFA	Perfluoroalkoxy Alkane
PVC	Polyvinyl Chloride
PVDF	Polyvinylidene fluoride
TFE	Tetrafluoroethylene
ZPC	Zero Point Charge

4.8 Bibliography

1. Aoki, T., Hatanaka, Y. & Look, D. C. ZnO Diode Fabricated by Excimer-Laser Doping. *Appl. Phys. Lett.* **76,** 3257–3258 (2000).
2. Tsukazaki, A., Ohtomo, A., Onuma, T., Ohtani, M., Makino, T., Sumiya, M., Ohtani, K., Chichibu, S. F., Fuke, S., Segawa, Y., Ohno, H., Koinuma, H. & Kawasaki, M. Repeated Temperature Modulation Epitaxy for P-Type Doping and Light-Emitting Diode Based on ZnO. *Nat Mater* **4,** 42–46 (2005).
3. Nomura, K., Ohta, H., Takagi, A., Kamiya, T., Hirano, M. & Hosono, H. Room-Temperature Fabrication of Transparent Flexible Thin-Film Transistors using Amorphous Oxide Semiconductors. *Nature* **432,** 488–492 (2004).
4. La Fontaine, B. Lasers and Moore's Law. *SPIE Prof. Oct.* 20 (2010).
5. Trokel, S. L., Srinivasan, R. & Braren, B. Excimer Laser Surgery of the Cornea. *Am. J. Ophthalmol.* **96,** 710–715 (1983).
6. Puliafito, C. A., Steinert, R. F., Deutsch, T. F., Hillenkamp, F., Dehm, E. J. & Adler, C. M. Excimer Laser Ablation of the Cornea and Lens. *Ophthalmology* **92,** 741–748 (1985).
7. Sakimoto, T., Rosenblatt, M. I. & Azar, D. T. Laser Eye Surgery for Refractive Errors. *Lancet* **367,** 1432–1447 (2006).
8. Munnerlyn, C. R., Koons, S. J. & Marshall, J. Photorefractive Keratectomy: A Technique for Laser Refractive Surgery. *J. Cataract Refract. Surg.* **14,** 46–52 (1988).

9. Pedraza, A. J., Fowlkes, J. D. & Lowndes, D. H. Silicon Microcolumn Arrays Grown by Nanosecond Pulsed-Excimer Laser Irradiation. *Appl. Phys. Lett.* **74,** 2322–2324 (1999).
10. Dongre, S., Gujrathi, A. & Nandan, H. A Review of Laser Micromachining. *Int. J. Eng. Sci.* **6,** 2416–2420 (2016).
11. Lakoba, I. S. & Yakovlenko, S. I. Active Media of Exciplex Lasers (Review Article). *Kvantovaya Elektron.* **7,** 677–719 (1980).
12. Ong, D. S., Tou, T. Y. & Low, K. S. Kinetics Modelling of a Self-Sustained Discharge KrF Laser. *J. Phys. D. Appl. Phys.* **29,** 2586–2594 (1996).
13. Williams, E. Personal Correspondence to Light Machinery. 1–2 (2017).
14. Sumitani, A., Andoua, S., Watanabea, T., Konishi, M., Egawa, S., Ohta, T., Terashimab, K., Suzukib, N., Enamib, T. & Mizoguchi, H. Output Stabilization Technology with Chemical Impurity Control on ArF Excimer Laser. *Analyzer* **4000,** 1424–1434 (2000).
15. Basting, D. *Excimer Laser Technology*. (Springer Science & Business Media, 2005).
16. Vininski, J. & Scott, D. US20170063016A1 - System for Reclaiming, Rebalancing and Recirculating Laser Gas Mixtures used in a High Energy Laser System. (2016).
17. Scokart, P. O., Selim, S. A., Damon, J. P. & Rouxhet, P. G. The Chemistry and Surface Chemistry of Fluorinated Alumina. *J. Colloid Interface Sci.* **70,** 209–222 (1979).
18. Flamm, D. L., Donnelly, V. M. & Mucha, J. A. The Reaction of Fluorine Atoms with Silicon. *J. Appl. Phys.* **52,** 3633–3639 (1981).
19. Standaert, T. E. F. M., Hedlund, C., Joseph, E. a., Oehrlein, G. S. & Dalton, T. J. Role of Fluorocarbon Film Formation in the Etching of Silicon, Silicon Dioxide, Silicon Nitride, and Amorphous Hydrogenated Silicon Carbide. *J. Vac. Sci. Technol. A Vacuum, Surfaces, Film.* **22,** 53 (2004).
20. Kirsch, W. B. & Laurent, S. M. US:4557921 Purification of Halide. (1985).
21. Rampersadh, P. Removal of Hydrogen Fluoride from Gas Streams. (Faculty of Science, University of Witwatersrand, Johannesburg, 2005).
22. Takita, Y., Ninomiya, M., Miyake, H., Wakamatsu, H., Yoshinaga, Y. & Ishihara, T. Catalytic Decomposition of Perfluorocarbons Part II. Decomposition of CF_4 over $AlPO_4$ Rare Earth Phosphate Catalysts. *Phys. Chem. Chem. Phys.* **1,** 4501–4504 (1999).
23. Takita, Y., Ninomiya, M., Matsuzaki, R., Wakamatsu, H., Nishiguchi, H. & Ishihara, T. Decomposition of Chlorofluorocarbons over Metal Phosphate Catalysts Part I. Decomposition of CCl_2F_2 over Metal Phosphate Catalysts. *Phys. Chem. Chem. Phys.* **1,** 2367–2372 (1999).
24. Takita, Y., Wakamatsu, H., Li, G. L., Moro-Oka, Y., Nishiguchi, H. & Ishihara, T. Decomposition of Chlorofluorocarbons over Metal Phosphate Catalysis. II. Origin of the Stability of $AlPO_4$ and the Location of CE as a Promoter. *J. Mol. Catal. A Chem.* **155,** 111–119 (2000).
25. Griskey, R. G. *Transport Phenomena and Unit Operations: A Combined Approach*. (John Wiley & Sons, 2005).
26. Stogryn, D. E. & Stogryn, A. P. Molecular Multipole Moments. *Mol. Phys.* **11,** 371–393 (1966).
27. Sircar, S. Basic Research Needs for Design of Adsorptive Gas Separation Processes. *Ind. Eng. Chem. Res.* **45,** 5435–5448 (2006).
28. Granville, A. & Hall, P. G. Adsorption of Krypton and Nitric Oxide on Alkali Metal Chloride Films. *Trans. Faraday Soc.* **63,** 701–707 (1967).
29. Gough, K. M., Yacowar, M. M., Cleve, R. H. & Dwyer, J. R. Analysis of Molecular Polarizabilities and Polarizability Derivatives in H_2, N_2, F_2, CO, and HF, with the Theory of Atoms in Molecules. *Can. J. Chem.* **74,** 1139–1144 (1996).
30. Barry, E. F. & Grob, R. L. *Columns for Gas Chromatography: Performance and Selection*. (John Wiley & Sons, 2007).
31. Cornell. Chemical Compatibility Guide. Available at: http://sevierlab.vet.cornell.edu/resources/Chemical-Resistance-Chart-Detail.pdf.
32. Sorbtech. Jordi Fluorinated Polymeric Resins. (2017). Available at: https://www.sorbtech.com/chromatography/adsorbents/polymeric-resins/jordi-resins/fluorinated/. (Accessed: 18th April 2017)
33. Wu, J. J., Fu, L. & Chuang, K. T. Fluorinated Styrene Divinylbenzene Copolymer as Catalyst Support. *Appl. Catal.* **72,** 71–80 (1991).
34. Yang, R. T. *Adsorbents: Fundamentals and Applications*. (John Wiley & Sons, 2003).
35. Ruthven, D. M. & Kumar, R. An Experimental Study of Single-Component and Binary Adsorption Equilibria by a Chromatographic Method. *Ind. Eng. Chem. Fundam.* **19,** 27–32 (1980).
36. Suzuki, M. *Adsorption Engineering*. (Kondansha LTD and Elsevier Science Publishers B.V., 1990).
37. Wilson, S. M. W., Kennedy, D. A. & Tezel, F. H. Adsorbent Screening for CO2/CO Separation for Applications in Syngas

Production. *Sep. Purif. Technol.* **236,** 1–11 (2020).

38. Manchado, M. C., Guil, J. M., Masia, A. P., Paniego, A. R. & Menayo, J. M. T. Adsorption of H_2, O_2, CO, and CO_2 on a Gamma-Alumina: Volumetric and Calorimetric Studies. *Langmuir* **10,** 685–691 (1994).
39. Singh, S., Tezel, F. H. & Harlick, P. J. E. Adsorption of Tetrafluoromethane and Nitrogen on Various Adsorbents. *Sep. Sci. Technol.* **37,** 2763–2784 (2002).
40. Cao, D. V & Sircar, S. Heats of Adsorption of Pure SF_6 and CO_2 on Silicalite Pellets With Alumina Binder. *Ind. Eng. Chem. Res.* **40,** 156–162 (2001).
41. Rosynek, M. P. Isotherms and Energetics of Carbon Dioxide Adsorption on Gamma-Alumina at 100-300 Degrees. *J. Phys. Chem.* **79,** 1280–1284 (1975).

Chapter 5

Adsorption of Components from Air on Silica Aerogels

Sean M.W. Wilson, Vida A. Gabriel, and F. Handan Tezel

Department of Chemical and Biological Engineering, University of Ottawa, 161 Louis-Pasteur, Ottawa, Ontario K1N 6N5 Canada

Accepted: Microporous and Mesoporous Materials 2020

5.1 Abstract

Aerogels are porous media that have large internal surface areas causing them to have significant gas adsorption. The adsorption isotherms of carbon dioxide, nitrogen, oxygen, and argon with a tetramethoxysilane (TMOS) silica aerogel, a [trimethylsilyl]oxy (TMS)-modified silica aerogel, and a silica gel were measured in the pressure range of 0 to 6.5 atm at 10°C, 30°C, 50°C, 70°C, and 90°C. These isotherms were fitted to Langmuir, Freundlich, Sips, and Toth isotherms, as well as the temperature dependent Toth model and their cumulative adsorption of the components of air were discussed. Isosteric heats of adsorption were quantified. With this data, we can see the impact of the surface groups on adsorption as well as the pore size, with a significant increase in the quantity and strength of adsorption of CO_2 reported between silanol and TMS groups. The relationship between adsorption capacity and the thermal properties of silica aerogels were also discussed in this study.

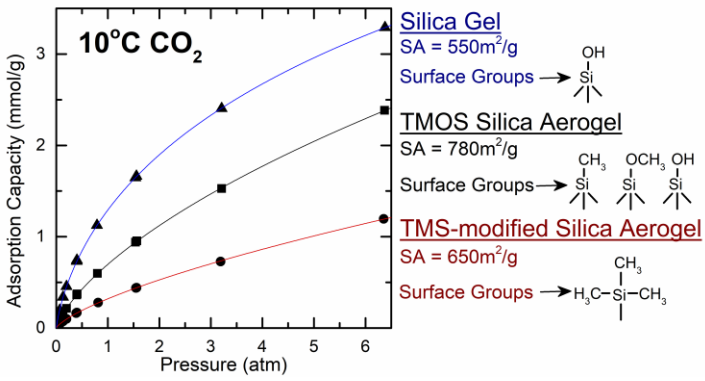

Keywords: Silica Aerogel, Silica Gel, Adsorption, Air, Gas Thermal Conductivity in the Pores, TMS Modification

5.2 Introduction

Aerogels are synthetic porous materials that are derived from replacing the liquid component of a gel with a gas while maintaining its structure. These structures were first invented by S. Kistler using supercritical dehydration of sol-gel materials that can be composed of organic, inorganic, or hybrid molecular precursors [1,2]. The beauty of aerogels are their unique properties such as low density (~0.003 to 0.5 g cm^{-3}), high surface area (~500 to 1200 m^2g^{-1}), and high porosity (~80 to 99.8%) [3]. This has made them attractive for many possible applications [4] including, thermal insulation [5–9], adsorption gas separation [10–12], CO_2 capture from air using amine impregnated aerogels [13–17], wastewater treatment [18], and hydrogen fuel cells [19], just to name a few.

Aerogels are synthesised using three common steps; sol-gel process, aging, and then drying. These three steps during the manufacturing of silica aerogel are what differentiate them from producing silica gel, which is significantly denser, with similar surface areas (300 to 850 m^2 g^{-1}). Similarly to the surface of silica gel, the surface of the silica aerogel contains hydroxyl groups (also known as silanols) which make the surface of the silica aerogel hydrophilic. This hydrophilicity however is a detriment to the silica aerogels due to water from the air being adsorbed onto their surface [20]. This adsorbed water can lead to capillary stress which will cause fracture within the silica aerogel. To prevent this degradation, it is common that silica aerogels are modified and made hydrophobic by substituting the silanol groups with hydrophobic compounds. A list of possible compounds are included in the literature [21].

Little is published on the adsorption properties of aerogels apart from carbon aerogel [10,19,22–24] and the use of adsorption for characterization at cryogenic temperatures [25–29]. This study investigates the adsorption properties of two silica aerogel samples and their adsorption behaviour for CO_2, N_2, O_2, and Ar gases. This knowledge will be important for applications in insulation, where these gas species present in the air can make up the majority of the contribution to the thermal conductivity of the aerogels [5–9]. The total thermal conductivity of the aerogel is broken down into the conduction through the solid lattice, the radiative heat transfer across and through the material, and the gas conduction in the pores which has been thoroughly discussed in literature [30,31]. The conduction through the lattice and the radiative heat conduction are generally considered independent of the pressure and whose contribution to the total thermal conductivity can be measured in vacuum conditions. As gas is introduced and the pressure increases, the thermal conductivity of the gas in the pore contributes more to the majority of the total thermal conductivity. For materials such as aerogels that have pore sizes in the mesopore range, the gas molecules are restricted and therefore, typically have gas conduction values far below that of gases in free space. The gas thermal conductivity can be calculated from the Knudsen number (Kn) which is the ratio of the mean free path of the gas molecules (l_g) to the effective pore diameter (D_e) [30,31].

$$Kn = \frac{l_g}{D_e} \quad (1)$$

For $Kn >> 1$, the effective pore diameter is significantly smaller than the mean free path of the gas molecules. Therefore, the gas molecules predominantly collide with the surface of the lattice structure than with each other, leading to the thermal conductivity being proportional to the number of gas molecules. This molecular heat transfer is pressure dependent. For $Kn << 1$, the effective pore diameter is much greater than the mean free path of the gas molecules. Therefore, the gas molecules predominantly collide with themselves than with the lattice structure, leading to the thermal conductivity being independent of the number of molecules. This diffusive heat transfer is independent of pressure.

This is depicted graphically in Figure 5.1 with the gas pressure of the air plotted logarithmically against calculated gas thermal conductivity in the pores at 20°C. Further details of the calculation are presented in the Supporting Information in Appendix IV. Two things of interest can be seen from Figure 5.1: First that as the effective pore diameter (D_e) becomes larger, the pressure at which there is equivalence between the gas thermal conductivity in free air and in the gas thermal conductivity in pores is lower. Secondly, that for a particular effective pore size, the thermal conductivity is dominated at lower pressures by molecular heat transfer, and transitions to diffusive heat transfer at high pressures. For an effective pore diameter of 10 nm which is around the diameter of the pore of silica aerogels in this study, molecular heat transfer dominates under 1 atm, transitions between 1 – 500 atm, and is diffusive heat transfer dominate above 500 atm.

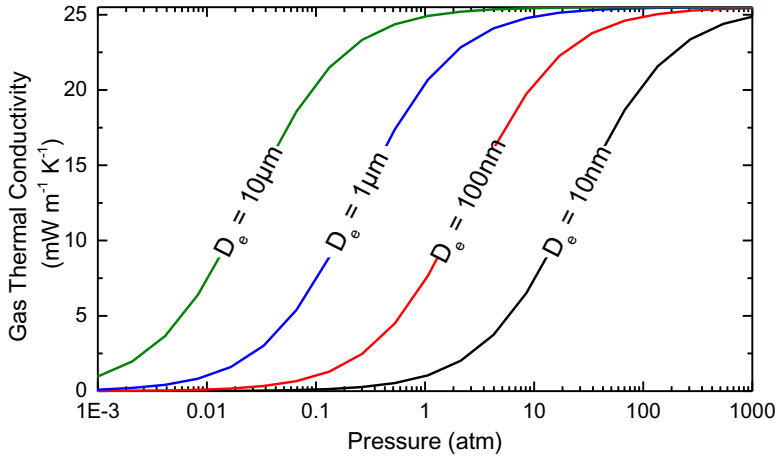

Figure 5.1 – Calculated gas thermal conductivity in the pores for air as a function of gas pressure for different pore sizes at 20°C. The conductivity of air in free space is 25.5 mW m^{-1} K^{-1}.

Seeing as adsorption is a surface based phenomenon where there is an increased gas concentration on the surface and therefore within the pores, adsorption would undoubtedly affect the thermal conductivity of aerogels. Some modeling work has been investigated in literature into the effect of adsorption on the thermal conductivity of MOF-5 materials for applications in gas storage of CH_4 and H_2 [32–34]. These modeling works looked at the high pressures of gas storage (therefore in the diffusive heat transfer region) and shown opposite trends between H_2 which had increasing thermal conductivity with increasing pressure [34], and CH_4 which had decreasing or no change in thermal conductivity with increasing pressure [32,33].

In the low pressure region where molecular heat transfer and the transition between the two modes occur, adsorption would potentially make a large impact on the thermal conductivity of the material. This can be abstractly depicted on Figure 5.1 with adsorption shifting and warping the S-curve to the left depending on the degree of adsorption if the x-axis was the gas pressure in free space. No studies have been found in literature to date equating the effect of an increase in gas concentration on the surface (adsorption capacity) and therefore within the pores, to the thermal conductivity of a material. Some circumstantial evidence to the effect of adsorption on thermal conductivity can be seen in work measuring the thermal conductivity of Linde Type A (LTA) zeolites for He, H_2, N_2, and Ar [35]. This paper noted two things of interest: 1) Hydrated potassium LTA zeolite had a higher thermal conductivity of the solid by up to 30% for pressures above 1 bar compared to the dehydrated form, 2) At pressures below 0.01 bar, sodium LTA zeolite in a nitrogen environment has a lower thermal conductivity than one in an Ar environment, even though N_2 has a higher thermal conductivity in free air than Ar.

Before investigating the effect of adsorption on the thermal conductivity of super insulating materials such as silica aerogel, investigation and quantification into the adsorption of CO_2, N_2, O_2, and Ar on silica aerogel needs to be done first. In this study two silica aerogels, one produced from tetramethoxysilane (TMOS), and another [trimethylsilyl]oxy (TMS) modified silica aerogel, as well as a silica gel were investigated by analysing their pure gas adsorption isotherms of CO_2, N_2, O_2, and Ar between 10°C and 90°C. This gave insights into the effect of surface groups on the adsorption, as well as pore size on the adsorption capacity and heat of adsorption values for these silicas. This research could also be useful for separation applications looking at similar materials. An example includes applications such as Direct Air Capture (DAC), which looks into separating and concentrating CO_2 from ambient air. Aerogels have been of interest for this as a support material for DAC which has been studied extensively [36–39].

5.3 Materials and Methods

5.3.1 Materials

Table 5.1 – Manufacturer, trademark name, and manufacturer supplied surface area for silica aerogel samples studied.

Source	Name	Surface Area	Pellet Info	Comments
Cabot Aerogel	LA1000	700m^2/g	0.7 – 4 mm	TMS-modified silica aerogel
Aerogel Technologies	Silica Aerogel	700m^2/g	Cut up monolith	TMOS silica aerogel
Strem Chemicals	Silica Gel	835m^2/g	100 – 200 MESH	GC grade silica gel

CO_2, N_2, O_2, and Ar pure gases were obtained from Linde Canada (Burlington, ON, Canada) at purities of 99.99%, 99.998%, 99.995%, and 99.9993%, respectively. Silica gel was purchased from Stream Chemicals (Newburyport, MA, USA). A type of TMS-modified silica aerogel brand name Lumira Translucent

Aerogel LA1000 was purchased from Cabot Corporation (Boston, MA, USA). A TMOS base catalyzed brand name Classic Silica Aerogel was purchased from Aerogel Technologies (Boston, MA, USA). The details of these silicas are given in Table 5.1.

5.3.2 Methods

5.3.2.1 Adsorption Isotherms

Adsorption equilibrium of CO_2, N_2, O_2, and Ar pure gases were determined in a VTI Scientific Instruments (Irvine, CA, USA) GHP gravimetric analyzer for temperatures of 10°C, 30°C, 50°C, 70°C, and 90°C for all samples for pressures between 0 to 6.5 atm. This pressure range was selected to analyse the adsorption of these components above and below atmospheric pressures. The average temperatures for each isotherm are included in Tables AIV.1 – AIV.15 in the Supporting Information in Appendix IV together with the adsorption isotherm data. The schematic diagram of the set-up used is shown in Figure AIV.1 in the Supporting Information in Appendix IV. Experiments were conducted by first weighing then regenerating the samples at 110°C under a vacuum pressure of approximately 10^{-8} atm until there was a negligible weight change. Each samples' desorption temperature was determined to be under the point at which minimum weight change occurred using the thermogravimetric analysis (TGA) which is explained in the Supporting Information in Appendix IV. After the regeneration, helium adsorption measurements were performed for up to 6 atm at similar temperatures used for the isotherm. All samples tested had a constant negative slope of the curve which is indicative of helium not being adsorbed [40] and from these values, the solid volume of the adsorbent was calculated. This solid volume of the adsorbent was used to distinguish between absolute adsorption and excess adsorption with all reported isotherms showing absolute adsorption. After the helium adsorption measurements, the samples were regenerated at vacuum pressure. The isotherms would then begin by determining the weight gains of the samples at increasing pressures of up to 6.5 atm. Two desorption data points were then performed by decreasing the pressure to determine any hysteresis. The accuracy of the microbalance within the gravimetric analyser is about $\pm 5 \times 10^{-7}$ g. Two pressure transducers were used, one from 0 to 1000 Torr pressure range with an accuracy of ± 0.25% of the reading, and another from 0 to 900 psi pressure range with an accuracy of ± 0.36 psi.

The Langmuir, Freundlich, Sips, and Toth isotherm models were used to evaluate the adsorption isotherm over the full range of pressures tested in this study. The models were fitted using the sum of least squares method and the isotherm with the highest coefficient of determination (R^2) was used to represent the isotherm. These models are included in Table 5.2.

Table 5.2 – Langmuir, Freundlich, Sips, and Toth adsorption isotherm models.

Langmuir Model	Freundlich Model	Sips Model	Toth Model
$\frac{q_e}{q_s} = \frac{\beta P}{1+\beta P}$	$q_e = k\,P^{\,1/n}$	$\frac{q_e}{q_s} = \frac{(\beta P)^n}{1+(\beta P)^n}$	$\frac{q_e}{q_s} = \frac{\beta P}{(1+(\beta P)^t)^{1/t}}$

In order to determine the adsorption equilibrium capacity at different temperatures from 10°C to 90°C and from 0 to 6.5 atm, the empirical temperature dependant Toth (TD-Toth) model was used. This converts the Toth parameters q_s, β, and t into temperature dependant variables. These equations are included in Table 5.3.

Table 5.3 – The empirical TD-Toth model equation parameters. These parameters are substituted into the Toth model included in Table 5.2.

$$q_s = q_{s0} exp\left[X(1-\frac{T}{T_0})\right] \qquad \beta = \beta_0 \exp\left[\frac{Q}{RT_0}(\frac{T_0}{T}-1)\right] \qquad t = t_0 + \alpha\left(1-\frac{T_0}{T}\right)$$

The limiting heats of adsorption (H_0) values were calculated using the van't Hoff plot (Henry's Law constant vs. 1/T) with the slope of the line of best fit giving the ratio of the heat of adsorption at zero loading to the gas constant. This procedure used the Henry's law constant (K) calculated from the linear section of the isotherms for CO_2, N_2, O_2, and Ar gases.

5.3.2.2 Characterization

To determine the surface characterization of the silica samples, nuclear magnetic resonance (NMR) and Fourier-Transform Infrared Spectroscopy (FTIR). To characterize the pores of the silicas BET analysis was done. The ^{29}Si solid-state NMR experiments were performed at 4.7 T on a Bruker Avance III 200 MHz NMR spectrometer at $\nu_i(^{29}Si)$ = 39.75 MHz using a Bruker 7 mm ^{1}H/X/Y MAS probe. A $^1H \rightarrow ^{29}Si$ cross-polarization magic-angle spinning (CP-MAS) pulse sequence was used with a 3.8 μs proton π/2 pulse, a 5 ms contact time, and proton decoupling. A recycle delay of 2 s was used for all samples, acquiring between 4000 and 16000 scans at a spinning frequency of 4.5 kHz. The chemical shifts were referenced to tetrakis(trimethylsilyl)silane at -9.9 ppm. Samples were ground using a mortar and pestle prior to the analysis. Note that the TMOS silica aerogel was packed in a smaller volume rotor due to lack of sample.

The FTIR analysis of the silica samples were conducted using a Cary 630 FTIR with an Attenuated Total Reflectance (ATR) diamond accessory (Agilent Technologies, Canada). The silica materials were each crushed in a mortor and pestle and then analysed as fine powder. The N_2 BET data was collected at liquid nitrogen temperatures using an ASAP 2020 Physisorption Micrometrics (Norcross, Georgia, USA) with care to ensure sufficient equilibration time.

5.4 Results and Discussion

5.4.1 Characterization

5.4.1.1 NMR

Figure 5.2 shows the spectra obtained from the solid state NMR obtained using ^{29}Si-^{1}H CP-MAS for the TMS-modified silica aerogel, TMOS silica aerogel, and silica gel. The three overlapping peaks at $\delta(^{29}Si)$ = -

110 ppm, -101 ppm and -92 ppm which have been assigned to $(SiO)_4 - Si$, $(SiO)_3 - Si - OX$, and $(SiO)_2 - Si - (OX)_2$ surface molecules, respectively, where X represents either CH_3 or H [41]. For the bottom spectrum of silica gel and the top spectrum of TMS-modified silica aerogel in Figure 5.2, the X represents H due to the lack of Si-OCH_3 observed in the FTIR data. These silanol surface groups of the silica gel are depicted in Figure 5.3. For the TMOS silica aerogel, X is an amalgam of H and CH_3 due to the presence of both Si-OCH_3 and Si-OH peaks in the FTIR data. Similarly for the TMOS silica aerogel, the peaks at δ = -56 ppm and δ = -63.5 ppm are assigned to $(SiO)_2 - Si - OXCH_3$ and $(SiO)_3 - Si - CH_3$ shifts, respectively, with X being an amalgam of H or CH_3 [42,43]. For the ^{29}Si spectrum of the TMS-modified silica aerogel in Figure 5.2, the peak at δ = 12.9 ppm has been assigned to the TMS group, $SiO - Si - (CH_3)_3$ [44,45]. Note that Figure 5.2 intends to qualitatively identify the surface groups present in each of the samples. This is because relaxation studies have shown that the peak breadth of each of the ^{29}Si signals in a spectra are functions of cross polarization contact time [41,44,46]. For example, the cross-polarization contact time is the largest for $(SiO)_4 - Si$ surface atoms, which are removed by at least four bonds from the nearest hydroxyl proton. As such, the ^{29}Si-^{1}H CP techniques helps the ^{29}Si nucleus detection based on their proximity to protons and therefore discriminate in favor of surface ^{29}Si atoms making this technique better suited for qualitative surface characterization for these types of systems [41,47].

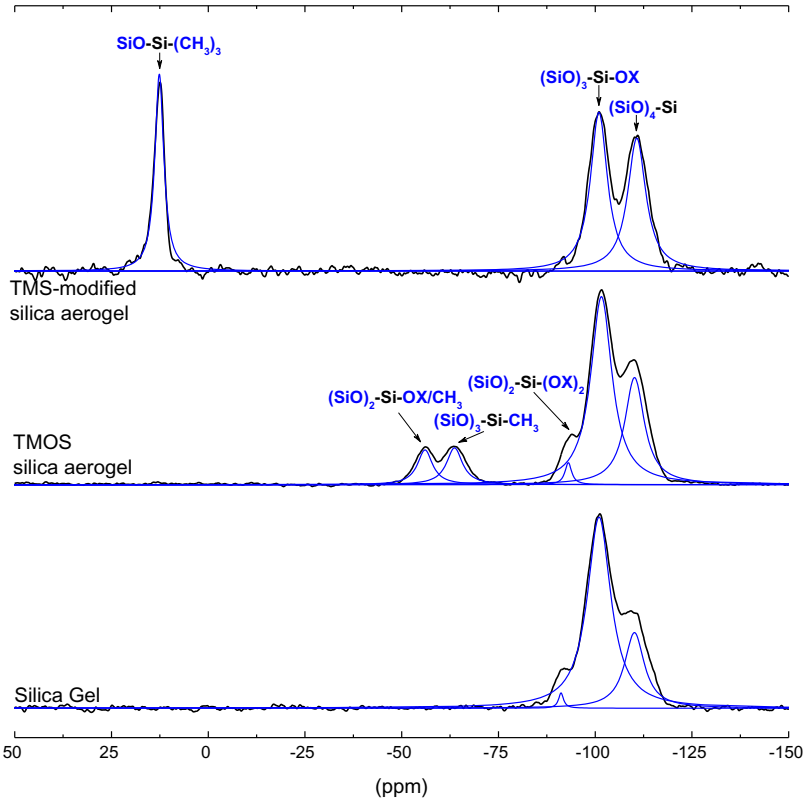

Figure 5.2 – Solid state 29Si-NMR spectra of TMS-modified silica aerogel, TMOS silica aerogel, and silica gel acquired under CP-MAS conditions on a Bruker Avance III 200 NMR spectrometer. Black lines are the experimental data and the blue lines are the Lorentzian distribution fits for the specific species. X in the chemical structure denotes either CH3 or H.

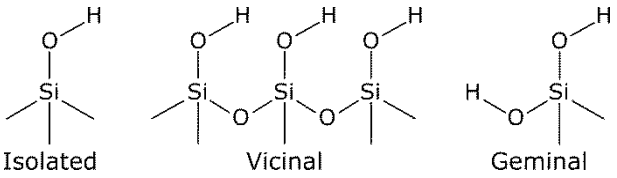

Figure 5.3 – Structural representation of isolated silanol, vicinal silanol, and geminal silanol groups.

5.4.1.2 FTIR

Figure 5.4 shows the results from the FTIR analysis of the three silica samples. Si-OH peaks are shown from the broad stretching vibration peaks at 3400-3200 cm^{-1} and 950-810 cm^{-1} [43,48] which is the strongest for the silica gel sample with distinct peaks at around 950 cm^{-1} region for all samples. A peak at 1635 cm^{-1} corresponds to Si–H_2O flexion [43] which is most noticeable for the silica gel sample. Sharp peaks produced from asymmetric and symmetric bending of Si-CH_3 are located at 2975, 1270, and 780-760 cm^{-1} [43,48]. There is no observation of the peaks at 2975 and 1270 cm^{-1} for the silica gel sample but these peaks are prominent for TMOS silica aerogel and for TMS-modified silica aerogel. The 2975 cm^{-1} peak for TMS-modified aerogel is due to the TMS being composed of three Si-CH_3 bonds for which there is a peak shift for Si-$(CH_3)_3$ at 1250 cm^{-1} compared to Si-CH_3 [43] which can be seen in Figure 5.4. For the TMOS silica aerogel, there is a sharp signal at 2840 which correlates to Si-O-CH_3 [43,48]. Si–O–Si, Si–O and O–Si–O vibration bands appeared at 1080, 800, 561 and 455 cm^{-1} for all samples [43,48].

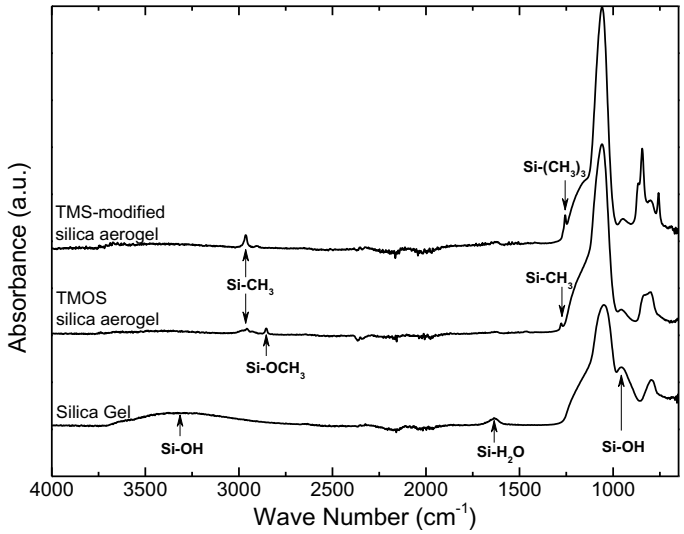

Figure 5.4 – FTIR spectra for TMS-modified silica aerogel, TMOS silica aerogel, and silica gel conducted using a Cary 630 FTIR-ATR.

5.4.1.3 BET Analysis

Table 5.4 presents the Brunauer-Emmett-Teller (BET) surface areas, the average Barrett-Joyner-Halenda desorption pore width (4V/A), as well as the cumulative pore volume in the micropore range (<2 nm), and mesopore range (2 – 50 nm) using the 2D Non-Local Density-Functional-Theory for Heterogeneous-Surfaces

(2D-NLDFT-HS) for the adsorbent samples in this study. This 2D-NLDFT-HS allows for the meaningful pore size distribution in the microporous and mesoporous range compared to other methods [49,50] with the pore size distribution in terms of surface area and volume being presented in Figure 5.5. The measured surface areas of the aerogels are similar to that of industry with there being a deviation between the industrially reported values for silica gel.

Table 5.4 – Surface area, average pore width, and pore volume for carbon samples in this study.

Name	Surface Area (m^2/g)	Average Pore Width (nm)	Micropore Volume (cm^3/g)	Mesopore Volume (cm^3/g)
TMOS Silica Aerogel	780	15.6	0.110	3.268
TMS-Modified Silica Aerogel	650	12.0	0	3.439
Silica Gel	550	2.65	0.193	0.270

The TMOS silica aerogel has the largest surface area and average pore width followed by TMS-modified silica aerogel, and then silica gel. In terms of pore size distribution, TMS-modified silica aerogel was found to have no microporosity with the majority of the surface area being found in the mesopores. TMOS silica aerogel has some microporosity making up 27% of its measured surface area but has most of its pores in the mesopore range. Silica gel has most of its pores in the micropore range making up 88% of its surface area compared to the mesoporous region. This pore size distribution can be seen in Figure 5.5 with silica gel being mostly microporous, TMOS silica aerogel having peaks in both, and TMS-modified silica aerogel being mostly mesoporous.

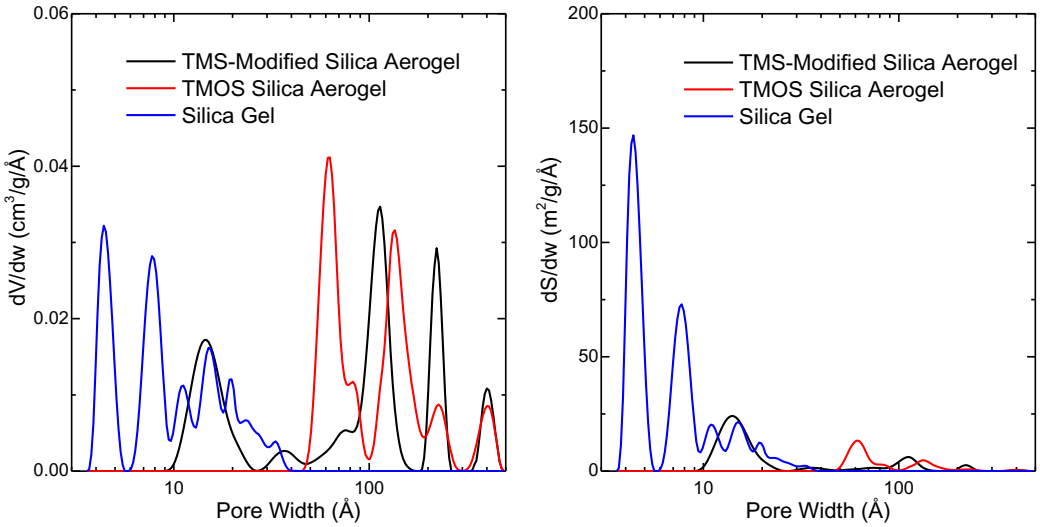

Figure 5.5 – Surface area and pore volume distribution relative to pore width using 2D-NLDFT-HS analysis for the silicas tested in this study.

5.4.2 Pure Component Isotherms

Figure 5.6, Figure 5.7, and Figure 5.8 show the experimental adsorption equilibrium isotherms of CO_2, N_2, O_2, and Ar at temperatures of 10°C, 30°C, 50°C, 70°C, and 90°C for TMOS silica aerogel, TMS-modified silica aerogel, and silica gel, respectively, as adsorption capacity as a function of pressure. All adsorption isotherms had two desorption points with no significantly noticeable hysteresis which is indicative of physisorption. All isotherm data points are given in Tables AIV.1 – AIV.12 in the Supporting Information in Appendix IV along with the coefficients for the Langmuir, Freundlich, Sips, and Toth adsorption isotherm models (Tables AIV.13 – AIV.15 in the Supporting Information). The increase in adsorption capacity with decreasing temperature indicates that the adsorption is exothermic which is expected for physical adsorption. All adsorption isotherms in this study follow Type I classification of isotherms. Comparative adsorption capacity data for silica aerogels has yet to be published. However, silica gel has been investigated for quite some time and for similar temperatures for CO_2 adsorption isotherms, over the range 1 atm, only a 8 % difference in adsorption capacity was observed from literature which could be due to the differences in the silica gel samples [51,52] .

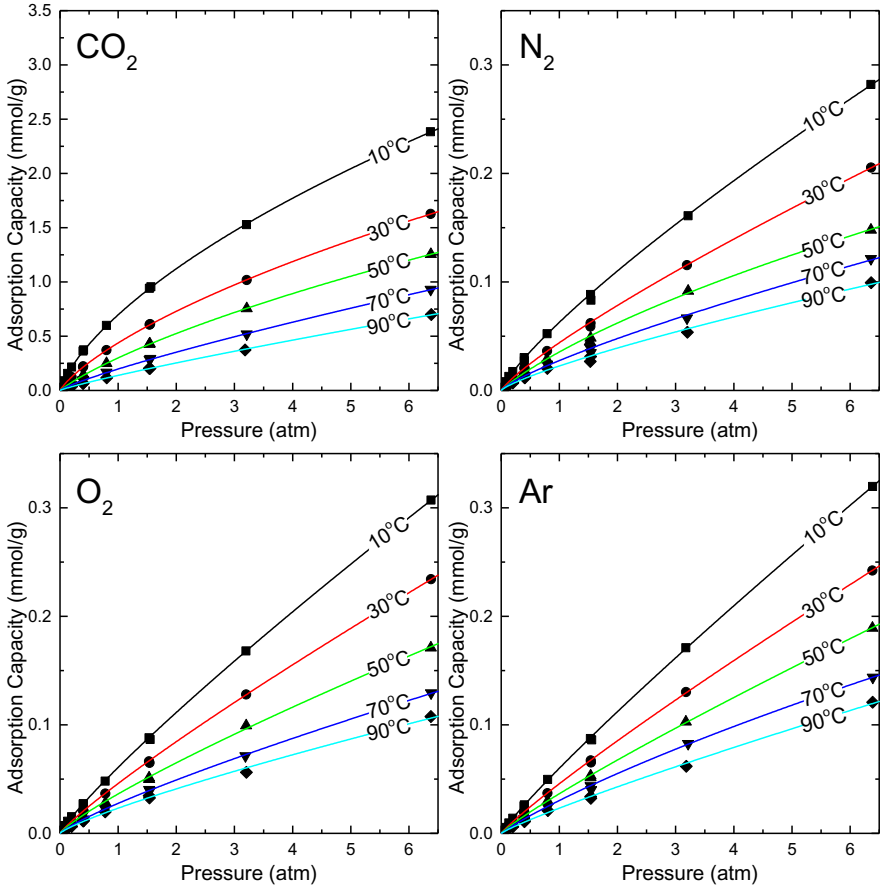

Figure 5.6 – Experimentally determined CO_2, N_2, O_2, and Ar pure adsorption isotherms at 10°C, 30°C, 50°C, 70°C, and 90°C for TMOS silica aerogel.

For all adsorbents tested, CO_2 has the highest adsorption capacity in comparison to the other gases studied. For the adsorption of CO_2, silica gel has the highest adsorption, followed by TMOS silica aerogel, then TMS-modified silica aerogel. This difference is more significant for CO_2 than the difference between the three samples for the other gases examined. Silica gel on average has roughly 1.75 times the CO_2 capacity over the pressure range than TMOS silica aerogel which has roughly double the capacity over the pressure range than TMS-modified silica aerogel. This difference in the adsorption of CO_2 between silica gel and TMOS silica aerogel is explained by the difference of surface functional groups which are defined in Figure 5.3 and the pore size distribution as seen in Figure 5.5. With silica gel, the surface is mainly composed of isolated or vicinal silanol groups with a small amount of geminal silanol groups when compared to TMOS silica aerogels surface being composed of a mixture of silanol, methoxy, and methyl groups on a mixture of isolated, vicinal, or geminal sites. With the electronegativity of oxygen being greater than that of carbon, the electrostatic forces of silanol groups have a stronger interaction than that of methyl or methoxy groups leading to more significant adsorption of CO_2. This correlation of the strength of adsorption of CO_2 to the presence of silanol groups on the surface has been seen in literature with other silica aerogel and silica samples [12].

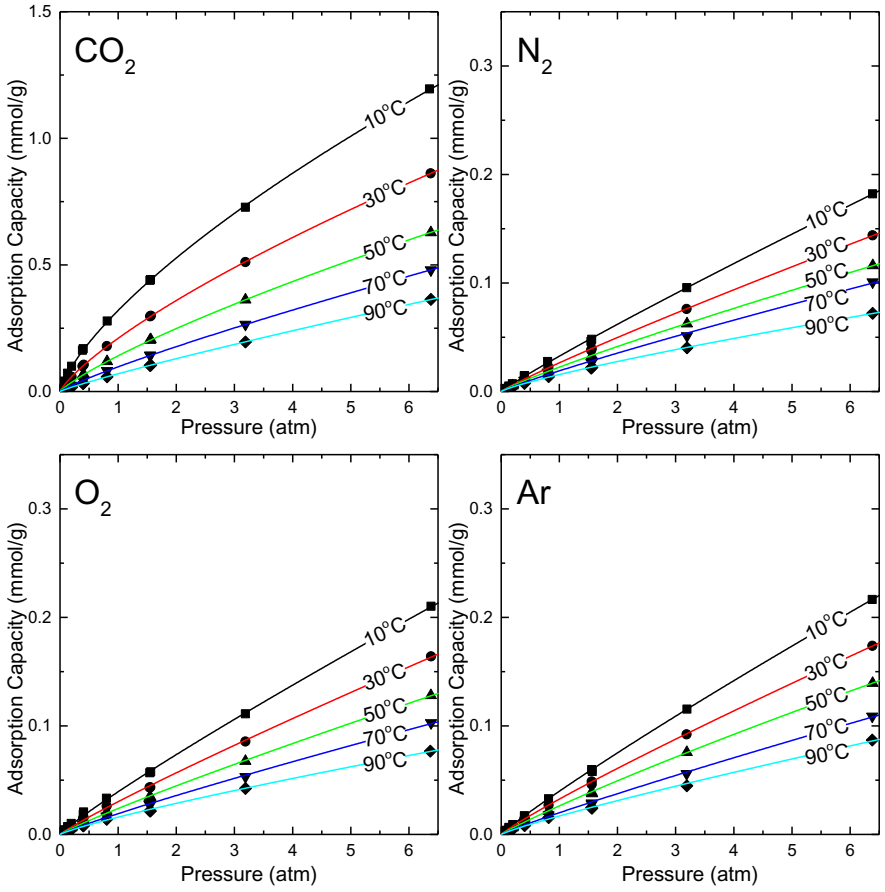

Figure 5.7 – Experimentally determined CO_2, N_2, O_2, and Ar pure adsorption isotherms at 10°C, 30°C, 50°C, 70°C, and 90°C for TMS-modified silica aerogel (LA1000).

The pore size also affects difference in the CO_2 adsorption between the silica gel and the TMOS silica aerogel, with smaller pores typically having stronger interactions than larger pores. This is due to the increased energy well between the two surfaces which is described well by the Dubinin-Radushkevich equation [53]. For TMS-modified silica aerogel, the TMS substitution with silanol groups on the surface removed any geminal sites and left only vicinal and isolated silanols (group types are shown in Figure 5.2).

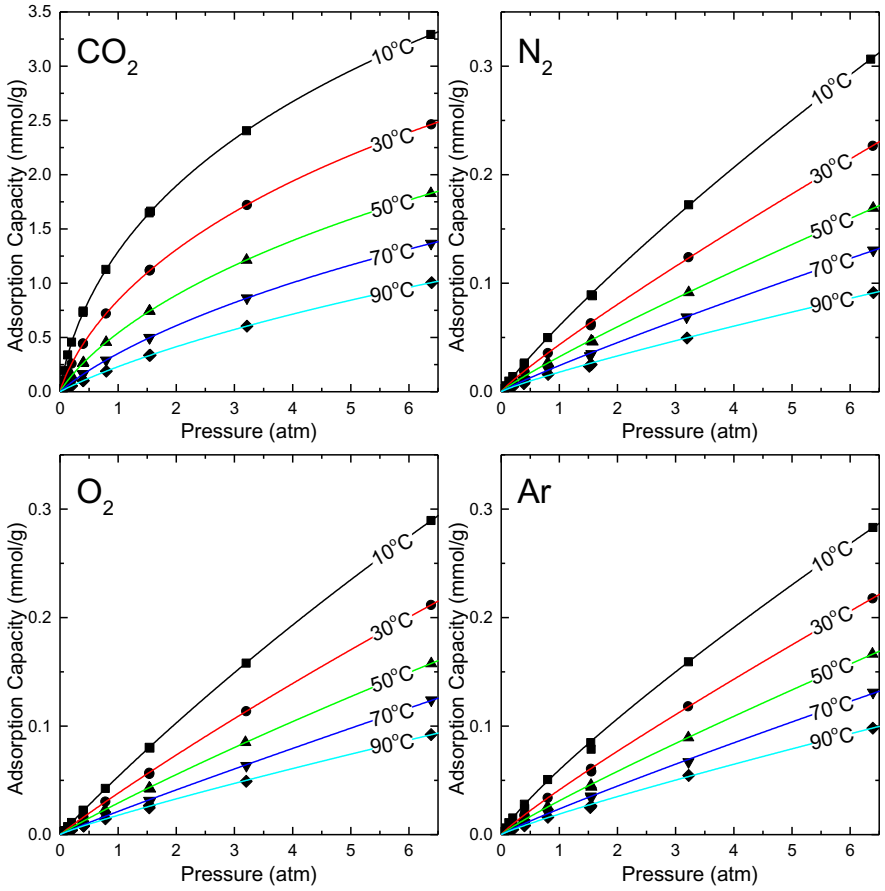

Figure 5.8 – Experimentally determined CO_2, N_2, O_2, and Ar pure adsorption isotherms at 10°C, 30°C, 50°C, 70°C, and 90°C for silica gel.

Comparing TMOS silica aerogel (Figure 5.6) to TMS-modified silica aerogel (Figure 5.7), both the majority of the surface area of the silicas are in the mesoporous range, but the CO_2 adsorption capacity is roughly 70% higher for TMOS silica aerogel than TMS-modified silica aerogel. This highlights the effect of the difference in surface groups on the CO_2 adsorption capacity. Comparing TMS-modified silica aerogel (Figure 5.7) to silica gel (Figure 5.8), the TMS modification of silica aerogel has roughly a third of the CO_2 adsorption capacity over the pressure range in comparison to silica gel which highlights the compound effect of a surface group that does not interact strongly with CO_2 and larger pore size.

For all three adsorbent samples, the shape of the isotherms for CO_2 is significantly less linear than isotherms for N_2, Ar, and O_2. This higher adsorption capacity for CO_2 and the less linear nature of the CO_2 isotherms in comparison to N_2, O_2, and Ar are not surprising because of the stronger intermolecular forces of CO_2

compared to the other gases. The strength of these intermolecular forces is due to their polarizability and quadrupole moment and is presented in Table 5.5 for the gases in this study. Even though CO_2 has a stronger adsorption interaction, the adsorption of CO_2 on silica and its silanol groups only forms a physical bond with the CO_2 which has been seen in the literature [12,54,55]. This has also been seen in literature with polydimethylsiloxane's methyl groups which are similarly present in the TMS-modified silica aerogels producing a reversible sorption [55]. The adsorption isotherms for CO_2 at 10°C for all three adsorbent samples are more non-linear and become more linear as temperature increases.

Table 5.5 – Properties of adsorbate gases used in this study.

Gas		Kinetic Diameter	Liquid Molar Vol.	Polariza-bility	Dipole Moment	Quadrupole Moment
IUPAC Name	Formula	(Å)	(cm^3/mol)	($Å^3$)	(Debye)	($Å^2$)
Carbon Dioxide	CO_2	3.3-3.9	37.4	2.65	0	4.3
Nitrogen	N_2	3.64-3.8	34.7	1.76	0	1.52
Oxygen	O_2	3.467	27.9	1.60	0	0.39
Argon	Ar	3.54	28.7	1.64	0	0

All gas properties are from S. Sircar (2006) [19]

For the adsorption of N_2, TMOS silica aerogel has the most adsorption at lower pressures under 1 atm followed by silica gel then TMS-modified silica aerogel. Above 1 atm, silica gel adsorption capacity is slightly larger than that of TMOS silica aerogel. For all pressures and temperatures for N_2 adsorption, TMS-modified silica aerogel adsorbs the least amount of N_2. Also, the TMS-modified silica aerogel N_2 isotherms are more linear than the isotherms for silica gel and the TMOS silica aerogel.

For O_2 adsorption, TMOS silica aerogel has the largest adsorption capacity at all temperatures and pressures. This is followed by TMS-modified silica aerogel which has larger adsorption capacities at pressures approximately below 0.2 atm (see the data points in Tables AIV.7 and AIV.11 in the Supporting Information in Appendix IV) and silica gel having larger capacities above 0.2 atm. The difference in adsorption capacity changed with pressure with TMOS silica aerogel adsorbing more than double that of silica gel at lower pressures and plateauing to 110% the value of silica gel at 6 atm.

The shape of the Ar adsorption isotherms compared to the adsorption isotherms of other gases studied are significantly more linear. The Ar adsorption isotherms compared between the three different adsorbents all had very similar shapes with TMOS silica aerogel adsorbing roughly 13% more Ar than silica gel which adsorbed roughly 22% more Ar than TMS-modified silica aerogel over similar temperatures and pressures.

5.4.3 Heat of Adsorption

Van't Hoff plots were created for the adsorbents studied using the Henry's law constants which were obtained from the low pressure section of the isotherm for CO_2, N_2, O_2, and Ar and are presented in Figure 5.9. For TMOS silica aerogel, CO_2 has the highest Henry's Law constant value (K) followed by N_2 which has similar but slightly larger K values than O_2 which has similar but slightly larger K values than Ar. This

trend was consistent with the adsorption capacities observed from the isotherms in Figure 5.6. All linear fits for TMOS silica aerogel showed good agreement for the lines of best fit for the van't Hoff equation. TMS-modified silica aerogel also has the highest K value for CO_2 followed by Ar which is similar to O_2 which is larger than the K values for N_2. These trends for TMS-modified silica aerogel agree with the adsorption isotherm data seen in Figure 5.7. Figure 5.9 shows an excellent agreement for the lines of best fit with the van't Hoff equation for CO_2, N_2 and O_2 for TMS-modified silica aerogel with only a mediocre agreement with the values for Ar. For silica gel, like other adsorbents studied, CO_2 has the highest K values followed by N_2 and Ar which had similar values which were both larger than O_2. All four gases have a good agreement with the lines of best fit for van't Hoff equation for silica gel in Figure 5.9.

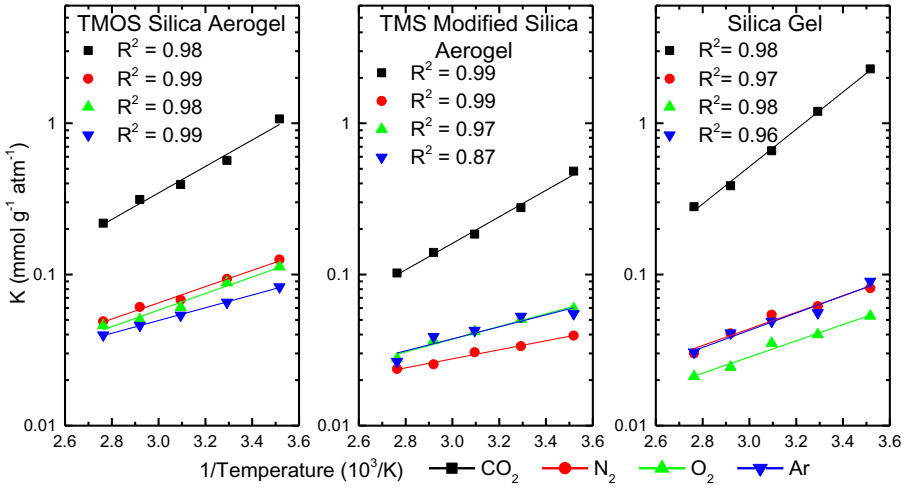

Figure 5.9 – Vant Hoff plot for CO_2, N_2, O_2, and Ar for TMOS silica aerogel, TMS-modified silica aerogel, and silica gel using calculated Henry's Law constants at temperatures of 10°C, 30°C, 50°C, 70°C, and 90°C including their respective line of best fit.

The limiting heat of adsorption values for CO_2, N_2, O_2, and Ar were calculated from the slopes of the van't Hoff plots for TMOS silica aerogel, TMS-modified silica aerogel, and silica gel. These heat of adsorption values are presented in Table 5.6. For CO_2, they are larger ranging from 16.77 to 23.63 kJ/mol. For all three adsorbent samples used for N_2, O_2, and Ar gases, heat of adsorption values are similar, ranging from 5.71 to 10.9 kJ/mol. The higher values for CO_2 and similar values for N_2, O_2, and Ar gases for heat of adsorption have also been reported in the literature [56].

Table 5.6 – Limiting heats of adsorption for CO_2, N_2, O_2, and Ar for silica aerogel, TMS-modified silica aerogel, and silica gel.

Gas	TMOS Silica Aerogel kJ/mol		TMS-modified silica aerogel kJ/mol		Silica Gel kJ/mol		Silica Gel [56] kJ/mol
CO_2	16.77	±1.53	16.78	±0.95	23.63	±0.95	20.91
N_2	10.27	±0.82	5.71	±0.45	10.50	±1.30	8.89
O_2	10.49	±1.19	8.05	±0.99	10.26	±1.09	9.30
Ar	8.07	±0.19	7.60	±2.06	10.90	±1.50	8.99

For CO_2 adsorption, the heat of adsorption value observed for silica gel is similar to that seen in literature with similar silica gel samples ranging from 20.91 kJ/mol[56] to 26.32 kJ/mol[57], as well as other silica species such as MCM-41 (23.2 to 25.1 kJ/mol[58]), and others (20 to 38 kJ/mol[12]). However for TMOS silica aerogel, the heat of adsorption for CO_2 was determined to be 16.77 kJ/mol which is significantly less than that of silica gel for 23.63 kJ/mol. This is the lowest known heat of adsorption for CO_2 reported in literature for silica and is due to the surface being an amalgam of silanol, methoxy and methyl groups on the surface in isolated, vicinal, and geminal locations. One thing to note is that the heat of adsorption values for CO_2 for TMOS silica aerogel and TMS-modified silica aerogel are very similar. This is interesting with the adsorption capacity of TMOS silica aerogel being much higher than that for TMS-modified silica aerogel with respectively similar surface areas. This indicates that having TMS-modification, reduces the number of adsorption sites to gas molecules while not affecting the strength of adsorption in comparison to methyl or methoxy groups.

5.4.4 TD-Toth Model

Table 5.7 – The fitted parameters for the empirical TD-Toth model for TMOS silica aerogel, TMS-modified silica aerogel, and silica gel for CO_2, N_2, O_2, and Ar adsorption. T_0 is equal to 284 K.

		q_{so} (mmol/g)	b_o (atm-1)	Q/RT_0	t_o	α	χ
TMOS Silica Aerogel	CO_2	2.817E+02	1.402E-02	1.964E+01	2.024E-01	6.318E-02	-5.961E+00
	N_2	3.088E+04	7.858E-06	9.533E+00	1.359E-01	-1.533E-01	-6.470E+00
	O_2	1.227E+05	1.086E-06	3.004E+00	1.511E-01	-1.434E-01	-7.272E-01
	Ar	2.119E+03	5.675E-05	9.103E+00	1.943E-01	2.207E-01	-1.024E+00
TMS-modified silica aerogel	CO_2	8.525E+03	4.105E-04	2.659E+01	1.297E-01	1.100E-01	-9.530E+00
	N_2	1.939E+04	1.176E-05	9.970E+00	1.414E-01	-1.684E-01	-6.893E+00
	O_2	9.409E+03	5.460E-06	8.772E+00	2.216E-01	-4.052E-01	-6.428E+00
	Ar	2.385E+03	2.235E-05	-1.538E+00	2.431E-01	-8.958E-02	3.997E+00
Silica Gel	CO_2	1.416E+01	3.897E-01	1.444E+01	3.687E-01	9.415E-02	-1.635E+00
	N_2	2.757E+03	3.633E-05	2.050E+00	2.128E-01	7.999E-02	3.435E+00
	O_2	2.359E+01	2.596E-03	3.520E+00	4.643E-01	-1.074E-01	1.540E+00
	Ar	3.289E+04	4.588E-06	1.040E+01	1.519E-01	1.662E-01	-1.620E+00

The TD-Toth model was used to predict the adsorption capacities of CO_2, N_2, O_2, and Ar on adsorbents studied at different temperatures from 283 K to 363 K and for pressures from 0 to 6.5 atm. The fitted coefficients are given in Table 5.7. These coefficients were fitted to equations found in Table 5.3, together with the Toth model given in Table 5.2. These pure component TD-Toth fitted coefficients were then used to calculate the cumulative adsorption capacities of the components of air by TMOS silica aerogel and TMS-modified silica aerogel, which are shown in Figure 5.10. This figure shows the adsorption capacities of CO_2, N_2, O_2, and Ar at 400, 780840, 209460, and 9300 ppm with the colors blue, green, red, and black, respectively. For the adsorption of air, N_2 is the most adsorbed species followed by O_2, Ar, and CO_2 for both aerogels which follows the order of the prevalence in the air. The adsorption of Ar and CO_2

is significantly less than the adsorption of N_2 and O_2, since their concentrations of these components in the air are the lowest.

The cumulative adsorption values of the components of air by TMOS silica aerogel are greater than that of TMS-modified silica aerogel at all temperatures and pressures as shown in Figure 5.10. This difference is due to the greater adsorption of O_2 on TMOS silica aerogel than TMS-modified silica aerogel with the adsorption of N_2 being similar for both aerogels. Since the compositions of N_2 and O_2 are the largest in the air, their capacity would have the largest effect on the cumulative adsorption capacities.

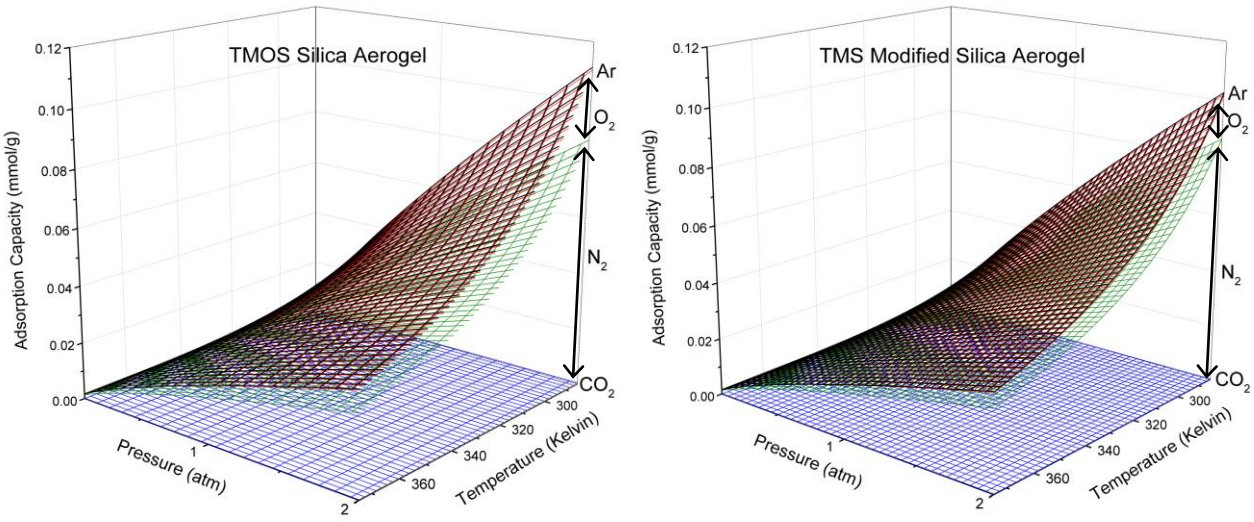

Figure 5.10 – Cumulative adsorption capacities for TMOS silica aerogel and TMS-modified silica aerogel of CO_2, N_2, O_2, and Ar at 400, 780840, 209460, and 9300 ppm, respectively, from temperatures of 285K to 375K and pressures of 0 to 2 atm.

5.4.5 Adsorption and Thermal Conductivity

In the literature, no significant body of work has investigated and quantified the effect of adsorption capacity on the gas thermal conductivity in the pores for porous materials. This is particularly important for materials with high surface areas because they would experience large capacities of adsorption such as the materials examined in this study. This adsorption could theoretically increase the thermal conductivity of the gas in the pores in two ways. 1) Increase excess of molecules of the gas within the pores leading to additional collisions with the walls and/or other gas molecules which would increase the thermal conductivity of the material. 2) The adsorbed species on the surface of the material would be in a pseudo gas-liquid adsorbed phase, and with liquids generally having higher thermal conductivities than their gaseous counterparts, this would lead to increase in the thermal conductivity in the material.

For materials such as aerogels, this is particularly important because the majority of the thermal conductivity of the material is due to the presence of gas within the pores rather than the skeletal structure or the intramaterial radiative heat transfer at ambient temperatures and pressures [8,30,59,60]. This can be seen from

the S-shaped curve that is created in a semi-log plot (Figure 5.1) when you measure the effective thermal conductivity of silica aerogels in relation to the pressure of the gas with low pressures (< 0.1 atm) being dominated by solid and radiative conduction and higher pressures being dominated by gas conduction within the pores [30,60–62].

In literature, there is a body of evidence that adsorption of water increases the effective thermal conductivity of 4A zeolite [35,63], as well as the modified [64] and unmodified silica gels [65,66]. They showed that having water present in the pores of these materials significantly increased their effective thermal conductivity by up to 30% compared to their dehydrated forms [35], and that larger loadings of water in the pores showed a trend of increasing thermal conductivities [63]. In the present study, the surface of TMS-modified silica aerogel was modified with TMS with the purpose of reducing water sorption to prevent degradation. This modification has also been found to reduce the cumulative adsorption of the components in air. Since it is hypothesised that an increase in adsorption increases the shift from molecular heat transfer towards diffusive heat transfer and therefore increases the thermal conductivity of the material, this TMS modification would expected to reduce thermal conductivity of the silica aerogel due to there being less adsorption in the pores.

5.5 Conclusions

The adsorption isotherms of CO_2, N_2, O_2, and Ar on TMOS silica aerogel, TMS-modified silica aerogel, and silica gel were determined at different temperatures along with their heat of adsorption values. With this aim, we can see the impact of changing the surface of the silica and the pore size on the adsorption of the different components in the air. This particularly impacted the adsorption of CO_2, with silanol groups showing significantly higher and stronger adsorption on silica gel than the TMS, methoxy, or methyl groups on TMOS silica aerogel or TMS silica aerogel. The adsorption isotherms examined in this study were fitted to the TD-Toth model and the cumulative adsorption of the components of air were analysed at different temperatures and pressures. It was found that N_2 and O_2 made up the majority of the adsorption from air onto the aerogel samples, with TMS-modified silica aerogel having the overall lowest cumulative adsorption. These models can be used to predict the adsorption of CO_2, N_2, O_2, and Ar between the temperatures of 10°C to 90°C and pressures of 0 to 6.5 atm. The quantification of this adsorption is important for applications in insulation where adsorption potentially affects the thermal conductivities of these super materials, which were discussed. Future studies will be pursued to quantify and model the effect of adsorption on the thermal conductivity of materials.

5.6 Nomenclature

$\boldsymbol{H_0}$	Heat of adsorption (kJ mol^{-1})
$\boldsymbol{k}$	Freundlich parameter (mmol g^{-1} atm^{-1})
$\boldsymbol{K}$	Henry's law constant (mmol g^{-1} atm^{-1})
$\boldsymbol{n}$	Freundlich parameter (-)

P	Pressure (atm)
q_e	Equilibrium adsorption capacity (mmol g^{-1})
q_s	Monolayer or saturation adsorption capacity (mmol g^{-1})
q_{s0}	Empirical TD-Toth parameter (mmol g^{-1})
Q	Empirical TD-Toth heat of adsorption (kJ mol^{-1})
R	Gas constant (m^3 atm K^{-1} mol^{-1})
R^2	Coefficient of determination (-)
t	Toth parameter (-)
t_0	Empirical TD-Toth parameter (-)
T	Temperature (K)
T_0	Empirical TD-Toth reference temperature (K)
α	Empirical TD-Toth parameter (-)
β	Langmuir parameter (atm^{-1})
β_0	Empirical TD-Toth reference parameter (atm^{-1})
χ	Empirical TD-Toth constant (-)

5.7 List of Abbreviations

2D-NLDFT-HS	2D Non-Local Density-Functional-Theory for Heterogeneous-Surfaces
ATR	Attenuated Total Reflectance
BET	Brunaur, Emmett, and Teller
CP-MAS	Cross-Polarization Magic-Angle Spinning
DAC	Direct Air Capture
FTIR	Fourier-Transform Infrared Spectroscopy
GC	Gas Chromatography
LTA	Linde Type A
NMR	Nuclear Magnetic Resonance
TD-Toth	Temperature Dependant Toth
TGA	Thermogravimetric Analysis
TMOS	Tetramethoxysilane
TMS	(Trimethylsilyl)oxy

5.8 Bibliography

1. Kistler, S. S. Coherent Expanded Aerogels. *Nature* **127,** 741 (1931).
2. Kistler, S. S. Coherent Expanded-Aerogels. *J. Phys. Chem.* **36,** 52–64 (1931).
3. Maleki, H. Recent Advances in Aerogels for Environmental Remediation Applications : A Review. *Chem. Eng. J.* **300,** 98–118 (2016).
4. Hrubesh, L. W. Aerogel Applications. *J. Non. Cryst. Solids* **225,** 335–342 (1998).
5. Herrmann, G., Iden, R., Mielke, M., Teich, F., Ziegler, B., Ag, B., Str, C. B. & Ludwigshafen, D.-. On the Way to Commercial Production of Silica Aerogel. **186,** 380–387 (1995).
6. Fricke, J., Lu, X., Wang, P., Buttner, D. & Heinemann, U. Optimization of Monolithic Silica Aerogel Insulants. *Int. J. Mass Transf.* **35,** 2305–2309 (1992).
7. Lu, X., Caps, R., Fricke, J., Alviso, C. T. & Pekala, R. W. Correlation between Structure and Thermal Conductivity of Organic Aerogels. *J. Non. Cryst. Solids* **188,** 226–234 (1995).
8. Hrubesh, L. W. & Pekala, R. W. Thermal Properties of Organic and Inorganic Aerogels. *J. Mater. Res.* **9,** 731–738 (1994).
9. Lee, O. J., Lee, K. H., Jin Yim, T., Young Kim, S. & Yoo, K. P. Determination of Mesopore Size of Aerogels from Thermal

Conductivity Measurements. *J. Non. Cryst. Solids* **298,** 287–292 (2002).

10. Fairen-Jimenez, D., Carrasco-Marin, F. & Moreno-Castilla, C. Adsorption of Benzene, Toluene, and Xylenes on Monolithic Carbon Aerogels from Dry Air Flows. *Langmuir* **23,** 10095–10101 (2007).
11. Ahmed, M. S. & Attia, Y. A. Multi-Metal Oxide Aerogel for Capture of Pollution Gases from Air. *Appl. Therm. Eng.* **18,** 787–797 (1998).
12. Roque-Malherbe, R., Polanco-Estrella, R. & Marquez-Linares, F. Study of the Interaction Between Silica Surfaces and the Carbon Dioxide Molecule. *J. Phys. Chem. C* **114,** 17773–17787 (2010).
13. Fan, H., Wu, Z., Xu, Q. & Sun, T. Flexible, Amine-Modified Silica Aerogel with Enhanced Carbon Dioxide Capture Performance. *J. Porous Mater.* **23,** 131–137 (2016).
14. Wörmeyer, K., Alnaief, M. & Smirnova, I. Amino functionalised Silica-Aerogels for CO_2 Adsorption at Low Partial Pressure. *Adsorption* **18,** 163–171 (2012).
15. Linneen, N., Pfeffer, R. & Lin, Y. S. CO_2 Capture using Particulate Silica Aerogel Immobilized with Tetraethylenepentamine. *Microporous Mesoporous Mater.* **176,** 123–131 (2013).
16. Cui, S., Cheng, W., Shen, X., Fan, M. & Russell, T. Mesoporous Amine-Modified SiO_2 Aerogel: A Potential CO_2 Sorbent. *Energy Environ. Sci.* **4,** 2070–2074 (2011).
17. Begag, R., Krutka, H., Dong, W., Mihalcik, D., Rhine, W., Gould, G., Baldic, J. & Nahass, P. Superhydrophobic Amine Functionalized Aerogels as Sorbents for CO_2 Capture. *Greenh. Gases Sci. Technol.* **3,** 30–39 (2013).
18. Ahmed, M. S. & Attia, Y. A. Aerogel Materials for Photocatalytic Detoxification of Cyanide Wastes in Water. *J. Non. Cryst. Solids* **186,** 402–407 (1995).
19. Tian, H. Y., Buckley, C. E., Wang, S. B. & Zhou, M. F. Enhanced Hydrogen Storage Capacity in Carbon Aerogels Treated with KOH. *Carbon N. Y.* **47,** 2128–2130 (2009).
20. Knez, Z. & Novak, Z. Adsorption of Water Vapor on Silica, Alumina, and Their Mixed Oxide Aerogels. *J. Chem. Eng. Data* **46,** 858–860 (2001).
21. Venkateswara Rao, A., Kulkarni, M. M., Amalnerkar, D. P. & Seth, T. Surface Chemical Modification of Silica Aerogels using Various Alkyl-Alkoxy/Chloro Silanes. *Appl. Surf. Sci.* **206,** 262–270 (2003).
22. Alhwaige, A. A., Ishida, H. & Qutubuddin, S. Carbon Aerogels with Excellent CO_2 Adsorption Capacity Synthesized from Clay-Reinforced Biobased Chitosan-Polybenzoxazine Nanocomposites. *ACS Sustain. Chem. Eng.* **4,** 1286–1295 (2016).
23. Gavalda, S., Gubbins, K. E., Kaneko, K. & Thomson, K. T. Nitrogen Adsorption in Carbon Aerogels: A Molecular Simulation Study. *Langmuir* **18,** 2141–2151 (2002).
24. Jeon, D.-H., Min, B.-G., Oh, J. G., Nah, C. & Park, S.-J. Influence of Nitrogen Moieties on CO_2 Capture of Carbon Aerogel. *Carbon Lett.* **16,** 57–61 (2015).
25. Reichenauer, G. & Scherer, G. W. Nitrogen Sorption in Aerogels. *J. Non. Cryst. Solids* **285,** 167–174 (2001).
26. Bhagat, S. D., Kim, Y. H., Suh, K. H., Ahn, Y. S., Yeo, J. G. & Han, J. H. Superhydrophobic Silica Aerogel Powders with Simultaneous Surface Modification, Solvent Exchange and Sodium Ion Removal from Hydrogels. *Microporous Mesoporous Mater.* **112,** 504–509 (2008).
27. Aravind, P. R., Mukundan, P., Krishna Pillai, P. & Warrier, K. G. K. Mesoporous Silica-Alumina Aerogels with High Thermal Pore Stability through Hybrid Sol-Gel Route followed by Subcritical Drying. *Microporous Mesoporous Mater.* **96,** 14–20 (2006).
28. Wong, J. C. H., Kaymak, H., Tingaut, P., Brunner, S. & Koebel, M. M. Mechanical and Thermal Properties of Nanofibrillated Cellulose Reinforced Silica Aerogel Composites. *Microporous Mesoporous Mater.* **217,** 150–158 (2015).
29. Bhagat, S. D., Kim, Y. H., Ahn, Y. S. & Yeo, J. G. Textural Properties of Ambient Pressure Dried Water-Glass based Silica Aerogel Beads: One Day Synthesis. *Microporous Mesoporous Mater.* **96,** 237–244 (2006).
30. Reichenauer, G., Heinemann, U. & Ebert, H. P. Relationship Between Pore Size and the Gas Pressure Dependence of the Gaseous Thermal Conductivity. *Colloids Surfaces A Physicochem. Eng. Asp.* **300,** 204–210 (2007).
31. Ebert, H. P. Thermal Properties of Aerogels. in *Aerogels Handbook* 537–564 (Springer US, 2011).
32. Babaei, H., McGaughey, A. J. H. & Wilmer, C. E. Effect of Pore Size and Shape on the thermal Conductivity of Metal-Organic Frameworks. *Chem. Sci.* **8,** 583–589 (2017).
33. Babaei, H. & Wilmer, C. E. Mechanisms of Heat Transfer in Porous Crystals Containing Adsorbed Gases: Applications to Metal-Organic Frameworks. *Phys. Rev. Lett.* **116,** 1–6 (2016).
34. Han, L., Budge, M. & Alex Greaney, P. Relationship between Thermal Conductivity and Framework Architecture in MOF-5. *Comput. Mater. Sci.* **94,** 292–297 (2014).
35. Griesinger, A., Spindler, K. & Hahne, E. Measurements and Theoretical Modelling of the Effective Thermal Conductivity of Zeolites. *Int. J. Heat Mass Transf.* **42,** 4363–4374 (1999).

36. Choi, S., Drese, J. H., Chance, R. R., Eisenberger, P. M. & Jones, C. W. US 8491705 B2 - Application of Amine Tethered Solid Sorbent to CO_2 Fixation from Air. 1–7 (2013). doi:10.1126/science.Liquids

37. Kong, Y., Shen, X., Fan, M., Yang, M. & Cui, S. Dynamic Capture of Low-Concentration CO_2 on Amine Hybrid Silsesquioxane Aerogel. *Chem. Eng. J.* **283,** 1059–1068 (2016).

38. Kong, Y., Jiang, G., Wu, Y., Cui, S. & Shen, X. Amine Hybrid Aerogel for High-Efficiency CO2 Capture: Effect of Amine Loading and CO2 Concentration. *Chem. Eng. J.* **306,** 362–368 (2016).

39. Sayari, A., Liu, Q. & Mishra, P. Enhanced Adsorption Efficiency through Materials Design for Direct Air Capture over Supported Polyethylenimine. *ChemSusChem* **9,** 2796–2803 (2016).

40. Hyun, S. H. & Danner, R. P. Equilibrium Adsorption of Ethane, Ethylene, Isobutane, Carbon Dioxide, and Their Binary Mixtures on 13X Molecular Sieves. *J. Chem. Eng. Data* **27,** 196–200 (1982).

41. Maciel, G. E. & Sindorf, D. W. Silicon-29 Nuclear Magnetic Resonance Study of the Surface of Silica Gel by Cross Polarization and Magic-Angle Spinning. *J. Am. Chem. Soc.* **102,** 7606–7607 (1980).

42. Brinker, J. C. & Scherer, G. W. Sol-gel Science : The Physics and Chemistry of Sol-Gel Processing. (1990).

43. El Rassy, H. & Pierre, A. C. NMR and IR spectroscopy of silica aerogels with different hydrophobic characteristics. *J. Non. Cryst. Solids* **351,** 1603–1610 (2005).

44. V, E. S. P. B., Miller, M. L., Linton, R. W., Hill, C., Maciel, G. E., Hawkins, B. L. & Collins, F. Characterization of Silanol Reactivity and Acidity on Octadecyl-Bonded Chromatographic Supports by 29Si Solid-State Nuclear Magnetic Resonance Spectroscopy and Surface Titration. **319,** 9–21 (1985).

45. Sindorf, D. W. & Maciel, G. E. 29Si CP/MAS NMR Studies of Methylchlorosilane Reactions on Silica Gel. *J. Am. Chem. Soc.* **103,** 4263–4265 (1981).

46. Wynberg, H. & Marsman, B. Synthesis of Optically Active 2, 3-Epoxycyclohexanone and the Determination of its Absolute Configuration. *J. Org. Chem.* **45,** 158–161 (1980).

47. Sindorf, D. W. & Maciel, G. E. Cross-polarization/magic-angle-spinning silicon-29 nuclear magnetic resonance study of silica gel using trimethylsilane bonding as a probe of surface geometry and reactivity. *J. Phys. Chem.* **86,** 5208–5219 (1982).

48. Launer, P. J. & Arkles, B. Infrared Analysis of Organosilicon Compounds: Spectra-Structure Correlations. *Silicon Compd. Silanes Silicones* 175–178 (2013).

49. Reichenauer, G. Structural Characterization of Aerogels. in *Aerogels Handbook* 449–498 (Springer US, 2011). doi:10.1007/978-1-4614-1957-0

50. Thommes, M., Kaneko, K., Neimark, A. V., Olivier, J. P., Rodriguez-Reinoso, F., Rouquerol, J. & Sing, K. S. W. Physisorption of Gases, with Special Reference to the Evaluation of Surface Area and Pore Size Distribution (IUPAC Technical Report). *Pure Appl. Chem.* **87,** 1051–1069 (2015).

51. Wang, Y. & LeVan, M. D. Adsorption Equilibrium of Binary Mixtures of Carbon Dioxide and Water Vapor on Zeolites 5A and 13X. *J. Chem. Eng. Data* **55,** 3189–3195 (2010).

52. Ferreira, D., Magalhães, R., Taveira, P. & Mendes, A. Effective Adsorption Equilibrium Isotherms and Breakthroughs of Water Vapor and Carbon Dioxide on Different Adsorbents. *Ind. Eng. Chem. Res.* **50,** 10201–10210 (2011).

53. Dubinin, M. M. Fundamentals of the Theory of Adsorption in Micropores of Carbon Adsorbents: Characteristics of their Adsorption Properties and Microporous Structures. *Pure Appl. Chem.* **61,** 1841–1843 (1989).

54. Di Giovanni, O., Dörfler, W., Mazzotti, M. & Morbidelli, M. Adsorption of Supercritical Carbon Dioxide on Silica. *Langmuir* **17,** 4316–4321 (2001).

55. Goodman, A. L. A Comparison Study of Carbon Dioxide Adsorption on Polydimethylsiloxane, Silica Gel, and Illinois No. 6 Coal Using in Situ Infrared Spectroscopy. *Energy & Fuels* **23,** 1101–1106 (2009).

56. Brunauer, S., Emmett, P. H. & Teller, E. Adsorption of Gases in Multimolecular Layers. *J. Am. Chem. Soc.* **60,** 309–319 (1938).

57. Greene, S. A. & Pust, H. The Determination of Heats of Adsorption by Gas-Solid Chromatography. *J. Phys. Chem.* **62,** 55–58 (1958).

58. He, Y. & Seaton, N. A. Heats of Adsorption and Adsorption Heterogeneity for Methane, Ethane, and Carbon Dioxide in MCM-41. *Langmuir* **22,** 1150–1155 (2006).

59. Lu, X., Arduini-Schuster, M. C., Kuhn, J., Nilsson, O., J., F. & Pekala, R. W. Thermal Conductivity of Monolithic Organic Aerogels. *Science (80-.).* **255,** 971–972 (1992).

60. Swimm, K., Reichenauer, G., Vidi, S. & Ebert, H. P. Gas Pressure Dependence of the Heat Transport in Porous Solids with Pores Smaller than 10μm. *Int. J. Thermophys.* **30,** 1329–1342 (2009).

61. Zeng, S. Q., Hunt, A. J., Cao, W. & Greif, R. Pore Size Distribution and Apparent Gas Thermal Conductivity of Silica Aerogel. *J. Heat Transfer* **116,** 756 (1994).

62. Bi, C., Tang, G. H. & Tao, W. Q. Prediction of the Gaseous Thermal Conductivity in Aerogels with Non-Uniform Pore-Size Distribution. *J. Non. Cryst. Solids* **358,** 3124–3128 (2012).

63. Dawoud, B., Sohel, M. I., Freni, A., Vasta, S. & Restuccia, G. On the Effective Thermal Conductivity of Wetted Zeolite under the Working Conditions of an Adsorption Chiller. *Appl. Therm. Eng.* **31,** 2241–2246 (2011).

64. Tanashev, Y. Y. & Aristov, Y. I. Thermal Conductivity of a Silica Gel and Calcium Chloride System: The Effect of Adsorbed Water. *J. Eng. Phys. Thermophys.* **73,** 876–883 (2000).

65. Bjurström, H., Karawacki, E. & Carlsson, B. Thermal Conductivity of a Microporous Particulate Medium: Moist Silica Gel. *Int. J. Heat Mass Transf.* **27,** 2025–2036 (1984).

66. Coquard, R. & Quenard, D. Modeling of Heat Transfer in Nanoporous Silica - Influence of Moisture. in *8th International Vacuum Insulation Symposium 2007* 1–13 (2007).

Chapter 6

Effect of Pore Size and Heterogeneous Surface on the Adsorption of CO_2, N_2, O_2, and Ar on Carbon Aerogel, RF Aerogel, and Activated Carbons

Sean M.W. Wilson, Fatma Al-Enzi, Vida A. Gabriel, F. Handan Tezel

Department of Chemical and Biological Engineering, University of Ottawa, 161 Louis-Pasteur, Ottawa, Ontario K1N 6N5 Canada

Submitted to: Microporous and Mesoporous Materials 2020

6.1 Abstract

Aerogels are porous super materials that have many desirable properties including high surface areas which cause them to have significant gas adsorption. In this study, carbon aerogel and resorcinol-formaldehyde (RF) aerogel are compared with six commercial activated carbons (Derived from wood, coconut shells, polymers, and bituminous coal). This study investigates many intrinsic properties of these carbons including surface area, pore size, presence and type of surface groups, as well as ash content and determines their influence on the adsorption of CO_2, N_2, O_2, and Ar using pure gas adsorption isotherms. This study noted that there was no trend for ash content but a strong correlation existed between the adsorption capacity and the pore size in the higher pressure region according to Dubinin's micropore volume filling theory. In the lower pressure range, the heterogeneous nature of the surface dominates the adsorption particularly for CO_2 which has the strongest polarizability and quadrupole moment of the probe molecules investigated. The two aerogel samples were then further investigated by determining their adsorption in the presence of air using the temperature dependant Toth model with N_2 and O_2 being adsorbed significantly more than CO_2 and Ar at ambient conditions.

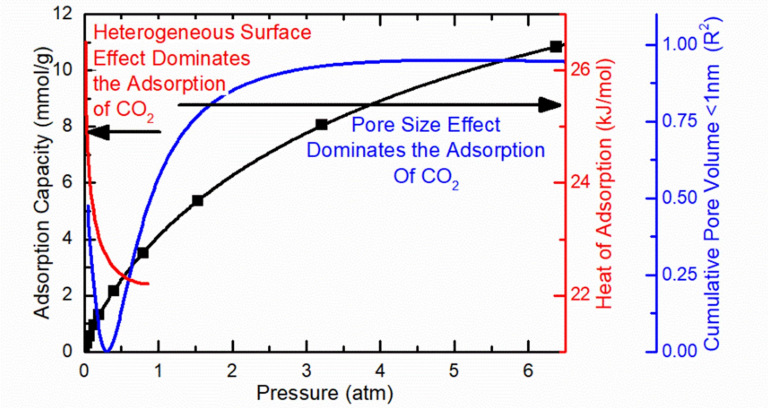

Key Words: Carbon Aerogel, Adsorption, CO_2, RF Aerogel, Carbons, Thermal Conductivity, Activated Carbon, Air Separation, Pore Size, Heterogeneous Surface

6.2 Introduction

Aerogels are a class of exceptional materials with properties making them the best insulating medium, the lightest synthetic solids, having the lowest sound speed, as well as having the lowest dielectric constant [1]. Aerogels also have a lot of potential in the field of adsorption with their structures having high surface areas (~500 to 3500 m^2g^{-1}) that are very porous (~80 to 99.8%) [2,3]. This, along with the fact that aerogels can be made from a wide range of materials (which will affect their surface adsorption properties), makes aerogels materials of interest for the field of adsorption. For instance, aerogels can be made from metal oxides (including most transition, lanthanide, and actinide metal oxide with several main group metal oxides such as tin oxide), organic polymeric (such as resorcinol-formaldehyde, phenol-formaldehyde, polyurethanes, polyacrylates, polystyrenes, and epoxies), biological polymers (such as agar-agar, pectin, and gelatin), pure metals (such as copper and gold), and carbon (carbon nanotubes, and pyrolyzed biological or organic polymeric aerogels). Carbon aerogels, the subject of this study, are of particular interest due to their stability as well as their similar surfaces to activated carbons with ability for a wide range of tuneable pore sizes. These are most commonly produced from pyrolyzed resorcinol-formaldehyde (RF) aerogels which has a tuneable pore size that is maintained after pyrolysis [4,5].

Even though aerogels have gas adsorption potential, little work has been published in the field. Carbon aerogels are the most published aerogel in the gas adsorption field with studies investigating adsorption of air pollutants (such as benzene, toluene, and xylene) [6], use in hydrogen storage [7], using carbon aerogels for CO_2 capture or modifying them to maximize CO_2 capture [8–11], adsorption of ethane & ethylene [4], and adsorption for surface characterization (nitrogen) [12].

The present study investigates the adsorption properties for CO_2, N_2, O_2, and Ar gases on RF aerogel and carbon aerogel which was pyrolyzed from RF aerogel. These gases have similar kinetic diameters but different polarizabilities and quadrapole moments, which can be seen in Table 6.1. This work will be useful for applications where RF or carbon aerogel are in the presence of air such as in Direct Air Capture (DAC) of CO_2 or in applications in insulation. This knowledge will be particularly important for applications in insulation where these gas species will likely impact the heat transfer properties of the aerogels [13–17] which was discussed in a previous article for silica aerogel [18].

Table 6.1 – Properties of adsorbate gases used in this study.

Gas		Kinetic Diameter	Liquid Molar Vol	Polarizability	Dipole Moment	Quadrupole Moment
IUPAC Name	Formula	(Å)	(cm^3/mol)	($Å^3$)	(Debye)	($Å^2$)
Carbon Dioxide	CO_2	3.3-3.9	37.4	2.65	0	4.3
Nitrogen	N_2	3.64-3.8	34.7	1.76	0	1.52
Oxygen	O_2	3.467	27.9	1.60	0	0.39
Argon	Ar	3.54	28.7	1.64	0	0

All gas properties are from S. Sircar (2006) [19]

In this study, two aerogels (carbon aerogel and RF aerogel), along with two polymeric based activated carbons (fiber and powder), and four natural based activated carbons (two bituminous-coal, a coconut shell, and a wood) were investigated and compared to each other. Since there is little comparison in the literature for the adsorption of the components of air on carbon aerogels, selecting multiple activated carbons, which have similar carbonous turbostratic structure, will allow this comparison to previous activated carbon research for the adsorption of CO_2, N_2, O_2, and Ar gases. Activated carbons have been studied extensively for these gases within the field including but not limited to air separation (CO_2, N_2, O_2, and Ar) [20–23], adipic acid production (N_2, and O_2) [23,24], post combustion CO_2 capture (CO_2, N_2, and Ar) [25,26], and syngas separation (CO_2, and N_2) [27–29]. The observations from these previous studies on activated carbons will be shown later to have similar trends for carbon aerogel. Unlike activated carbons which go through an activation process with a mild oxidant to develop microporosity and therefore high surface area [30,31], carbon aerogels typically do not go through an activation process and have porous structures with a high surface area after carbonization in an inert atmosphere.

Activated carbons are relatively complex materials with adsorption being a function of many intrinsic parameters of the activated carbon including surface area, pore size, presence and type of surface groups, as well as the ash content. Surface area impacts the magnitude but not the strength of adsorption due to adsorption being a surface based phenomenon. This surface area exists in pores which according to the volume filling of micropores theory of M. M. Dubinin, will first fill up the smaller pores before larger pores with the saturation of smaller pores before larger ones [32]. This theory is somewhat coherent to literature for the adsorption of CO_2 onto activated carbons [33,34]. Presser et al. (2011)[34] showed for CO_2 data at 0°C between 0.1 to 1 atm, that there is a linear correlation between CO_2 adsorption capacity and the cumulative pore volume up to a particular pore size, with the correlation being stronger for larger pores as the pressure increases. Casco et al. (2014)[33] expanded further upon this work by investigating CO_2 adsorption for pressures up to 45 atm at 25°C, finding a similar trend particularly at higher pressures. However, when comparing correlation between adsorption capacities and cumulative pore volume up to a particular pore size at a pressure of 1 atm, significant deviations with this trend between the two works are noticed. This, along with each paper not presenting correlations in the low pressure portion of the isotherm fails to identify a key aspect that influences the adsorption onto activated carbons; the unique surface chemistry of activated carbons which is energetically heterogeneous. This complex surface is composed of adsorption sites of different energies with the higher energy sites being preferentially occupied at lower pressures and lower energy sites being progressively occupied at higher gas pressures [35]. In literature, this effect of the heterogeneous surface of activated carbon can be seen from plots of the isosteric heats of adsorption as a function of surface coverage with the lowest coverages having the highest heats of adsorption with a drop and then a plateau at higher coverages [21,25,26,35]. This heterogeneous surface consists of saturated basal plane sites which make up the bulk of the surface, edge sites with heteroatom-containing functional groups, unsaturated edge sites, and π-electrons delocalized on the turbostratic structure. A comprehensive review of the surface chemistry of activated carbons can be found in the literature [36–38]. Ash, composed of silica, alumina, iron, alkaline and alkaline earth metals are remnants of

the raw carbon material, and adds to the heterogeneous nature of the activated carbons. However, the function of these ashes have yet to be thoroughly quantified [39]. Current research has found that the ash content has little to no influence in the gas adsorption properties of the activated carbon, particularly after being exposed to atmospheric oxygen which reacts with any unoxidized metals of the ash [40].

In this study, the effect of pore size and by extension surface area, as well as the effect of oxygen species on the surface and ash content have been investigated to determine their influence on the adsorption of CO_2, N_2, O_2, and Ar up to 6.5 atm and between 10°C – 90°C. This was first done by characterizing and determining the pore size, surface area, type and quantity of oxygen species, and ash content percentages of the carbons. This was then compared to the adsorption capacity of the four gases which was determined using gravimetrically measured pure gas adsorption isotherms. Heat of adsorption values were determined from the isotherms at different temperatures and they were used to discuss the effect of the heterogeneous surface of the carbons on their adsorption capacity for the gases. Investigating both the effect of a heterogeneous surface and pore size of the activated carbon allowed insights into maximizing or minimizing the adsorption capacity across all pressures of the isotherms.

6.3 Materials and Methods

6.3.1 Materials

Table 6.2 – Manufacturer, trademark name, and shape information for carbon samples used in this study.

Name	Manufacturer	Shape Info	Carbon Source
Carbon Aerogel	Aerogel Technologies	Cut up monolith	RF-Aerogel
RF Aerogel	Aerogel Technologies	Cut up monolith	Resorcinol-Formaldehyde
ACC	Spectracorp	Fabric (D=15μm)*	Polymer weave based
BPL	Calgon Carbon	4x10 MESH	Bituminous coal based
F-600	Calgon Carbon	12x30 MESH	Bituminous coal based
M-30	Spectracorp	Powder (30μm)*	Polymer based
NZ-AC	Activated Carbon NZ LTD	12x60MESH	Wood Based
OLC	Calgon Carbon	12x30MESH	Coconut Husk Based

*Determined size from SEM images

CO_2, N_2, O_2, and Ar pure gases were obtained from Linde Canada (Burlington, ON, Canada) at purities of 99.99%, 99.998%, 99.995%, and 99.9993%, respectively. RF aerogel and carbon aerogel were acquired from Aerogel Technologies (Boston, Massachusetts, USA). They produced the carbon aerogel from carbonizing the RF-aerogel. Two polymeric based activated carbons, Activated Carbon Cloth (ACC) which is in fabric form, and M-30 which is in powdered form were acquired from Spectracorp (Lawrence, Kansas, USA). Four activated carbons from natural materials were also selected for this study. They include BPL and F-600 which are both bituminous coal based activated carbons made for gas and liquid based separations due to their small and large pores, respectively. OLC which is an activated carbon produced from coconut

shells, and NZ-AC which is a wood based activated carbon were also used. BPL, F-600, and OLC were purchased from Calgon Carbon (Pittsburgh, Pennsylvania, USA) and NZ-AC was acquired from Activated Carbon NZ LTD (Taupo, New Zealand). The details of these carbons are given in Table 6.2.

6.3.2 Methods

6.3.2.1 Adsorption Isotherms

Pure gas adsorption equilibrium isotherms of CO_2, N_2, O_2, and Ar were determined by using a VTI Scientific Instruments (Irvine, CA, USA) GHP gravimetric analyzer for temperatures of 10°C, 30°C, 50°C, 70°C, and 90°C for all adsorbent samples. The average temperatures for each isotherm along with the adsorption isotherm data (Tables AV.1 – AV.32), as well as the schematic diagram of the setup used (Figure AV.1) are included in the Supplementary Information in Appendix V. Experiments were conducted by weighing, then regenerating the adsorbent samples at 300°C under a vacuum pressure of approximately 10^{-8} atm until there was negligible weight change. After the regeneration, helium adsorption measurements were performed at similar temperatures and pressures used for the isotherm. All samples tested had a constant slope of the curve for helium, which indicated that it is not adsorbed [41]. From these values, the solid volume of the adsorbent was calculated. This value was used to distinguish between absolute adsorption and excess adsorption with all reported isotherms showing absolute adsorption. After the helium adsorption measurements, the samples were regenerated again before measuring the isotherm. The measurement would then begin by evaluating the adsorbent weight at different increasing adsorbate equilibrium pressures up to 6.5 atm. To determine hysteresis, two desorption data points were then performed by decreasing the equilibrium pressure. The accuracy of the microbalance within the gravimetric analyser is about $\pm 5 \times 10^{-7}$ g. Two pressure transducers were used, one from 0 to 1.32 atm with an accuracy of ± 0.25% of the reading, and another from 0 to 61 atm with an accuracy of ± 0.025 atm.

In order to model the adsorption isotherm over the full range of pressures, the Langmuir, Freundlich, Sips, and Toth isotherm equations were used. These models were fitted using the sum of least squares method and the isotherm with the highest coefficient of determination (R^2) was used to represent the isotherm. These models are included in Table 6.3.

Table 6.3 – Langmuir, Freundlich, Sips, and Toth adsorption isotherm models.

Langmuir Model	Freundlich Model	Sips Model	Toth Model
$\frac{q_e}{q_s} = \frac{\beta P}{1+\beta P}$	$q_e = k\,P^{\,1/n}$	$\frac{q_e}{q_s} = \frac{(\beta P)^n}{1+(\beta P)^n}$	$\frac{q_e}{q_s} = \frac{\beta P}{(1+(\beta P)^t)^{1/t}}$

To determine the heterogeneity of the adsorbents the Clausius-Clapeyron equation was used to determine the isosteric heat of adsorption values as a function of surface coverage. This was calculated from the isotherm models at 10°C to 90°C and pressures between 0 and 6.5 atm. The Clausius-Clapeyron equation is shown in Equation 1, where $(-\Delta H_{ads})$ is the isosteric heat of adsorption at a specific loading, q_e.

$$\frac{(-\Delta H_{ads})}{RT^2} = \left[\frac{\partial lnP}{\partial T}\right]_{q_e} \quad 1$$

In order to determine the adsorption equilibrium capacity between temperatures of 10°C to 90°C and between pressures of 0 atm to 6.5 atm, the empirical temperature dependant Toth (TD-Toth) model was used. This turns the Toth parameters q_s, β, and t into temperature dependant variables with these equations being included in Table 6.4.

Table 6.4 – The empirical TD-Toth model equation parameters as functions of temperature. These parameters are substituted into the Toth model included in Table 6.3.

$q_s = q_{s0} exp\left[X(1-\frac{T}{T_0})\right]$	$\beta = \beta_0 \exp\left[\frac{Q}{RT_0}(\frac{T_0}{T}-1)\right]$	$t = t_0 + \alpha\left(1-\frac{T_0}{T}\right)$

6.3.2.2 Characterization

To determine the elemental analysis of the carbon samples from beryllium to uranium, as well as for high resolution images while under high vacuum a Jeol 6610LV scanning electron microscopy – energy dispersive X-ray spectroscopy (SEM-EDS) equipped with an Oxford INCA large area silicon drift detector was used as an analytical technique. To determine the type of surface groups on the carbon structure a Cary 630 FTIR with an Attenuated Total Reflectance (ATR) diamond accessory from Agilent Technologies (Mississauga, ON, Canada) was used. These samples were ground using a mortar and pestle prior to FTIR and analysed under atmospheric conditions. The BET data for this study was collected using nitrogen at 77 K on a 3Flex Physisorption Micrometrics (Norcross, Georgia, USA) at University of Ottawa.

6.4 Results and Discussion

6.4.1 Characterization

6.4.1.1 SEM-EDS

Images of the activated carbons are presented in Figure 6.1, which were all found to be quite conductive. RF aerogel was found to be insulating material which did not produce a good image. These SEM images are representative of the surface and micrometer structure of the materials. Carbon aerogel has a noticeably porous surface due to its three-dimensional network of interconnected structure of carbon particles with large holes observed in this sample into the bulk of the material. This structure of the carbon aerogels is described well in the literature with these carbon particles being roughly 5 – 10 nm in size which can be seen clearly from a transmission electron micrograph [5,6,12]. ACC's fibers were determined to be around 15 µm in diameter. The crystal size of M-30 was determined to be 30 µm in size. BPL and F-600 had very similar structures which are both bituminous coal based activated carbons. NZ-AC, a wood based activated carbon, have clear xylem or phloem structures which are maintained after activation creating a

very 1D macroporous structure. OLC, a coconut based activated carbon, also had a macroporous structure but in no discernable direction.

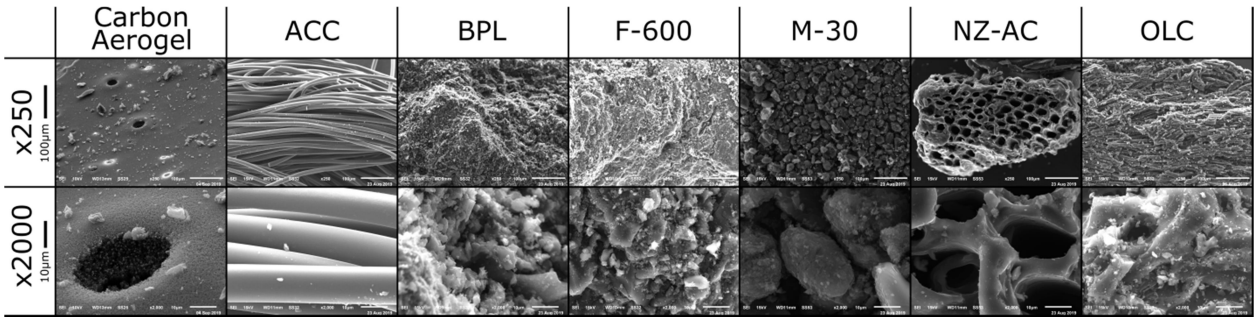

Figure 6.1 – SEM images at x250 and x2000 resolution for carbon aerogel and the activated carbons in this study.

The results from the elemental analysis are shown in Table 6.5 for carbon samples without any ash content and Table 6.6 for carbon samples with ash content. Carbon aerogel was manufactured from the carbonization of RF aerogel which is a porous form of a resorcinol-formaldehyde polymer. This co-polymer contains many hydroxyl and ester groups which are accounted for in the SEM-EDS data by the stoichiometric ratio of carbon to oxygen, which after pyrolysis has significantly less oxygen in its structure. Since RF aerogel was made from pure monomer, the material does not contain any elements that would be characterized as ash content according to the literature such as silica, alumina, iron or alkaline and alkaline earth metals [39]. Since a pure source carbonous material is used to produce carbon aerogel, it does not contain any ash content as can be seen in Table 6.5. This is also true of ACC and M-30 which are also polymer derived activated carbons. It is important to note that carbon aerogel was only carbonized in an inert environment unlike the other polymeric carbons in this study which were activated using either steam or carbon dioxide as mild oxidants. This can be seen from the chemical composition with carbon aerogel having significantly less oxygen in its structure than the polymeric activated carbons.

Table 6.5 – SEM-EDS analysis of the elemental composition of carbon aerogel, RF aerogel, ACC, and M-30.

	Carbon Aerogel (atomic %)	RF Aerogel (atomic %)	ACC (atomic %)	M-30 (atomic %)
C	97.62 ±0.40	77.74 ±3.05	93.46 ±2.06	94.59 ±0.84
O	2.39 ±0.40	22.26 ±3.05	6.53 ±2.06	5.41 ±0.84

The carbon samples in Table 6.6 are all derived from natural carbonous materials such as bituminous coal for BPL and F-600, wood for NZ-AC, and coconut shells for OLC. Since these activated carbons are derived from natural materials, after carbonization and activation, significant ash contents can be found in their structure. BPL and F-600 were found to have an ash content which is mainly composed of silica, alumina, and sulphur. Observations utilizing the SEM-EDS identified sizable chunks composed of silica and alumina on BPL and F-600 of the order of size of 3 µm and 5 µm, respectively. NZ-AC was produced from saw dust which was chemically activated using phosphoric acid as a catalyst. From the SEM-EDS data, it was

observed that a small amount of phosphorus from the catalyst is still within the structure of the NZ-AC as well as calcium, and iron which was probably deposited from the processing equipment such as saws. It is assumed that the phosphorus is most likely in phosphate form on the surface of the NZ-AC.

Table 6.6 – SEM-EDS analysis of the elemental composition of BPL, F-600, NZ-AC, and OLC from Be to U.

	BPL (atomic %)		F-600 (atomic %)		NZ-AC (atomic %)		OLC (atomic %)	
C	96.45	±3.99	91.43	±8.53	84.43	±1.97	91.97	±6.56
O	2.48	±4.32	6.57	±8.70	14.04	±2.52	7.77	±6.49
Mg	-	-	0.03	±0.08	0.05	±0.05	0.14	±0.18
Al	0.28	±0.22	0.61	±0.35	-	-	0.04	±0.14
Si	0.33	±0.17	0.73	±0.43	-	-	-	-
P	-	-	-	-	0.67	±0.27	-	-
S	0.36	±0.24	0.54	±0.13	-	-	-	-
K	-	-	0.01	±0.03	-	-	0.07	±0.13
Ca	0.03	±0.12	-	-	0.37	±0.31	0.01	±0.05
Fe	0.01	±0.05	0.03	±0.08	0.44	±0.40	-	-

These ash contents form complexes with oxygen such as silicon and aluminum being more stable as silica and alumina. Therefore, they would decrease the amount of oxygen from these measurements which could be present on the surface as oxygen containing groups. Assuming this and following the calculations described in the Supplementary Information in Appendix V, the oxygen contents that are within the ash were determined to be 1.15 ± 0.9%, 2.44 ± 1.60%, 2.75 ± 1.64%, and 0.25 ± 0.50% for BPL, F-600, NZ-AC, and OLC, respectively. Using this value for the oxygen content of the ash, the %mass ash content of the samples were calculated to be 3.99 ± 3.05%, 7.62 ± 4.13%, 4.54 ± 3.72%, and 0.95 ± 1.82% for BPL, F-600, NZ-AC, and OLC, respectively. These ash contents include sulphur which if analyzed via thermo gravimetric analysis with air or oxygen would produce volatile oxides which would be negated in the measurement.

6.4.1.2 FTIR

The remaining oxygen that does not make up the ash content either persists in the bulk of the carbon or on the surface where it can interact and has been reported to significantly affect the adsorption properties [31,42–45]. These surface oxygens effect the surface chemistry of the activated carbon and can either add to the surface basicity as with pyrones and chromenes, or acidicity as with carboxyls, hydroxyls, lactones (or lactols), and carboxylic anhydrides. Some groups such as quinones, and carbonyls have had mixed reporting on the acidic or basic nature of the group [31,45]. These groups are shown in Figure 6.2.

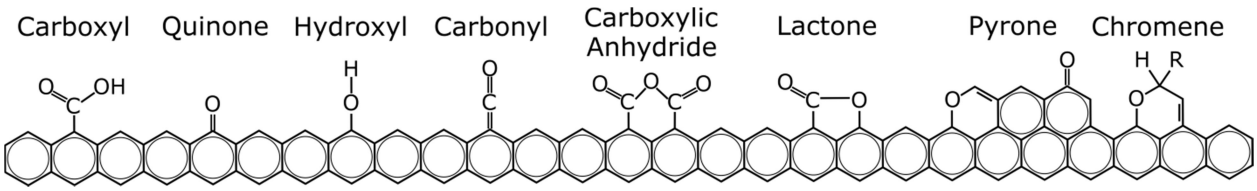

Figure 6.2 – Different surface oxygen groups that are present in activated carbons. The bottom row of benzenes represents the bulk of the activated carbon.

Figure 6.3 shows the Fourier-Transform Infrared Spectroscopy (FTIR) spectrum for the carbons in this study. For the six activated carbons, the spectrums are all similar to those found in literature for activated carbons activated at high temperatures with unmodified surfaces [11,46–49] with spectrums that have only small and broad peaks. This is because of the carbonous turbostratic structure of the carbons which increase the difficulty of identifying surface group peaks because of their structural complexity. RF aerogel spectrum was similar to those found in literature [49,50].

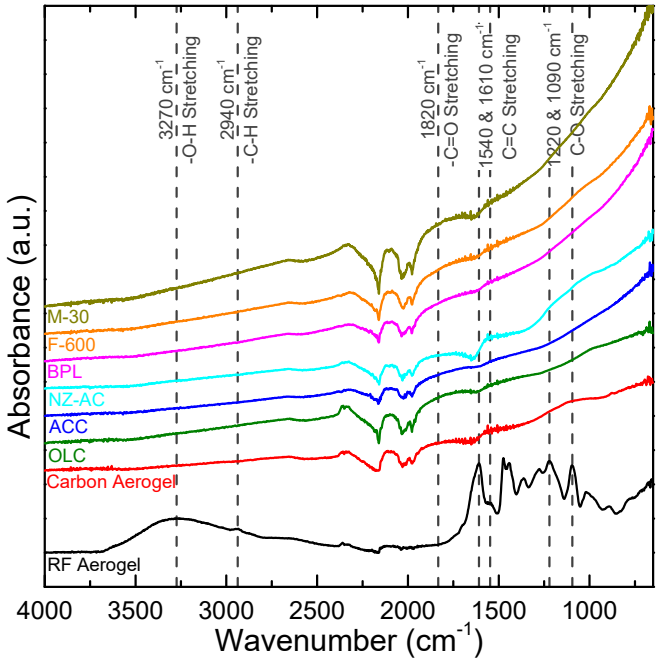

Figure 6.3 – FTIR spectra for the adsorbents tested in this study conducted using a Cary 630 FTIP- ATR.

In the functional group region between 1500 and 4000 cm^{-1} of the FTIR spectrum, the aromatic carbon-carbon stretching peak can be observed between 1540 and 1680 cm^{-1} [45,47,49–53] which is present for all of the carbonous samples which is the bulk of the activated carbons. This is most apparent for the RF aerogel which has two distinct aromatic carbon-carbon stretching peaks which is associated with the benzene ring found in the resorcinol portion of the copolymer. The RF aerogel was the only material that had an observable broad peak between 3000 and 3500 cm^{-1} which is most associated with a hydroxyl group stretch in literature [45–47,51–55] which is expected from the structure of the co-polymer. This absence of hydroxyl group stretching indicates the lack of carboxyl, hydroxyl, or lactol groups on the surface of the activated carbons. RF aerogel was also the only material to have a peak at between 2840 and 3000 cm^{-1} at 2940 cm^{-1} which is indicative of carbon-hydrogen alkane stretching. Carbon-hydrogen aromatic stretching between 3000 and 3100 cm^{-1} was also not observed for any of the samples. This lack of carbon-hydrogen peaks is not due to these groups not being present but due to the turbostratic structure of the carbons and the overall small presence within the carbons. Between 1650 and 1850 cm^{-1} in literature is a C=O bond [45,47,51–54] which is present for all activated carbon samples and not the RF aerogel. This broad peak is a combination of the carboxylic anhydride, quinone, carbonyl, lactone, and pyrone groups that can be present on the surface.

In the fingerprint region of the FTIR spectrum between 400 and 1500 cm^{-1}, it is harder to identify peaks due to many overlying signals. Carbon-oxygen stretching between 1040 and 1310 cm^{-1} is most likely attributable to the peaks for RF aerogel which are very prominent as well as for carbon aerogel, NZ-AC, and F-600 which are subtle [45,46,48,49,51–53,55]. This carbon-oxygen stretching is most likely due to carboxylic anhydride, lactone, or pyrone in the structure and less likely due to chromene, carboxyl, or hydroxyl groups due to lack of other indicating peaks. For NZ-AC, due to the presence of phosphorous in the structure, bands between 990 and 1220 cm^{-1} can be due to P-O-P, P-O-C, P=O, and POOH [55–57] which overlaps with the carbon-oxygen stretching in the FTIR spectrum.

Another prominent peak observed in Figure 6.3 is the CO_2 peak at 2350cm^{-1} for all samples indicating the excess surface concentration of CO_2 on the carbons compared to the correction curve using air of the FTIR.

6.4.1.3 BET Analysis

Table 6.7 – Surface area, BJH average pore width, and pore volume for carbon samples used in this study.

Name	Surface Area (m^2/g)	Average Pore Width (nm)	Total Pore Volume (cm^3/g)	<1nm (cm^3/g)	<2nm (cm^3/g)	<3nm (cm^3/g)
Carbon Aerogel	640	25	2.442	0.149	0.174	0.174
RF Aerogel	445	22	2.389	0.002	0.071	0.074
ACC	1590	2.4	0.700	0.483	0.700	0.700
BPL	1160	3.8	0.727	0.254	0.409	0.481
F-600	680	5.5	0.364	0.235	0.285	0.292
M-30	3430	1.7	1.815	0.501	0.953	1.618
NZ-AC	1930	2.3	0.863	0.439	0.781	0.859
OLC[T]	1080	3.2	0.404	0.169	0.295	0.310

[T] Data from Kose (2010) [58]

Table 6.7 presents the Brunauer-Emmett-Teller (BET) surface areas, the average Barrett-Joyner-Halenda (BJH) pore width (4V/A), as well as the total (between 0.3–50 nm) and cumulative pore volumes for under 1 nm, 2 nm, 3 nm pores using the Two-Dimensional Non-Local Density-Functional-Theory for Heterogeneous-Surfaces (2D-NLDFT-HS) for the carbon samples used in this study. This 2D-NLDFT-HS was demonstrated in literature to provide improved accuracy of the pore size distribution in comparison to older models [59]. This, along with the model accounting for surface heterogeneity, significantly improves the accuracy of the pore size analysis of heterogeneous nanoporous carbons [60]. The original BET data is given in Table AV.33 in Supplementary Information in Appendix V. The surface areas in order of the largest to the smallest are M-30 > NZ-AC > ACC > BPL and OLC > F-600 and carbon aerogel > RF aerogel. Carbon aerogel, NZ-AC, and OLC have noticeable porous structure from the SEM images in the µm range. In the unobservable range for the SEM, with the data determined from nitrogen adsorption at 77K, it can be seen that the aerogels have the largest average pore width which is an order of magnitude larger than the other activated carbons. Of the polymeric based carbons, ACC has a slightly larger average pore width than M-30 according to BJH 4V/A but have similar pore size distributions up to 500Å. ACC however has a narrow and uniform pore size distribution in comparison to the adsorbents tested in this study which can be

seen in the pore size distribution in the Supplementary Information in Appendix V (Figures AV.2 and AV.3). This narrow and uniform pore size has been noted in literature [31]. BPL and F-600 which are both bituminous coal based activated carbons, have different pore sizes which is indicative of the different activation conditions, with average BJH pore widths at 3.8 and 5.5 nm, respectively.

6.4.2 Adsorption Capacity

Figure 6.4, Figure 6.5, Figure 6.6, and Figure 6.7 show the experimental adsorption equilibrium isotherms of CO_2, N_2, O_2, and Ar at temperatures of 10°C, 30°C, 50°C, 70°C, and 90°C for the carbons in this study. The data points for the isotherms are included in Tables AV.1 – AV.32 along with the respective different isotherm model parameters for the curve fits in Tables AV.34 – AV.41 in the Supplementary Information in Appendix V. All adsorbents have two desorption points with no significantly noticeable hysteresis which is indicative of physisorption. For all carbons, the adsorption capacity increased with decrease in temperature indicating the adsorption is exothermic in behaviour which is expected for physical adsorption. All isotherms follow a Type I isotherm according to the IUPAC (2015) classification of isotherms [60].

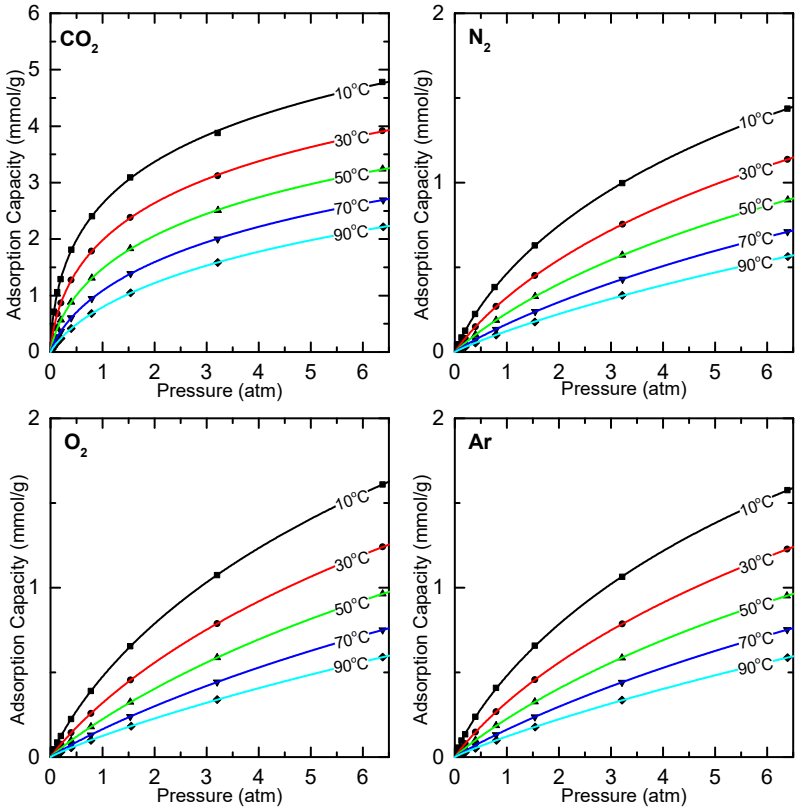

Figure 6.4 – Experimentally determined CO_2, N_2, O_2, and Ar pure adsorption isotherms at 10°C, 30°C, 50°C, 70°C, and 90°C for carbon aerogel.

Adsorption isotherms of BPL for CO_2 and N_2 are within range of previously published data which is present in Figure 6.6 with data from Sircar and Golden (2000)[27] at 30°C over the full range of pressures and

McEwen et al. (2013)[61] at 25°C up to 1.25 atm. This data was taken from the figures in these articles and fitted to the Sips isotherm model (Values located in Table AV.42 in Supplementary Information in Appendix V) then plotted against experimental data.

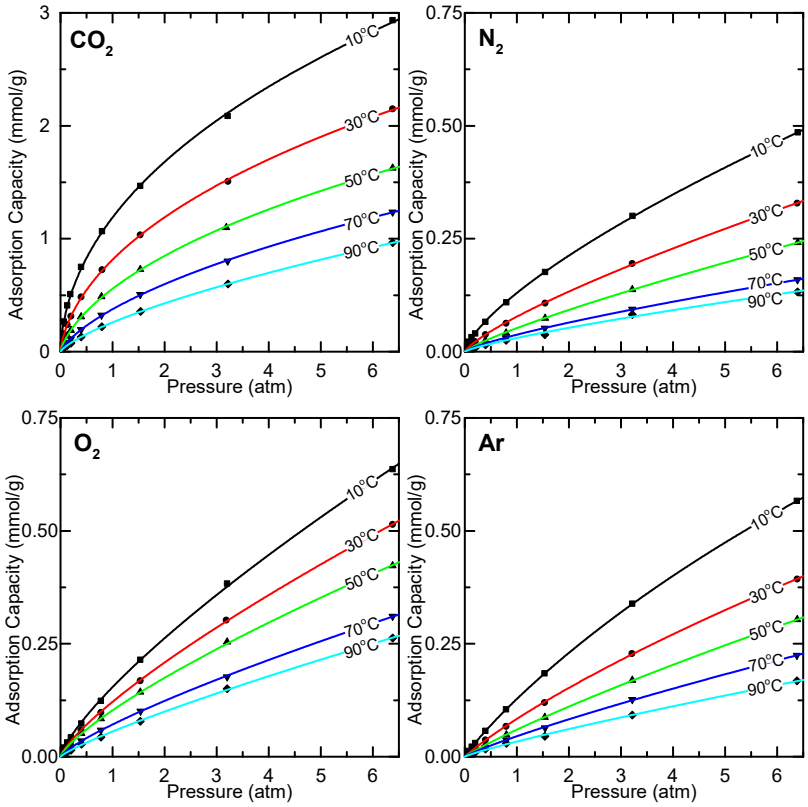

Figure 6.5 – Experimentally determined CO_2, N_2, O_2, and Ar pure adsorption isotherms at 10°C, 30°C, 50°C, 70°C, and 90°C for RF aerogel.

A trend that was observed for all carbons at all temperatures is the significantly higher adsorption capacity of CO_2 >> N_2 ≈ O_2 ≈ Ar. This correlates to the adsorbates strength of the intermolecular forces (polarizability, and quadrupole moment) which can be seen in Table 6.1 where CO_2 has significantly stronger forces than the other molecules. This trend can also be seen in experimental data from literature [21,26,27]. This difference in adsorption capacity is significant in both the low pressure region and in the high pressure region getting closer to the saturation portion of the isotherm. To compare the adsorption capacity of CO_2 over N_2, the selectivity is defined as the ratio of adsorption capacities (capacity for CO_2/capacity of N_2) for the carbons studied and is presented graphically in the Supplementary Information in Appendix V (Figure AV.4). In the high pressure region, this CO_2 selectivity would change from around 3.5 for carbon aerogel to 7 for RF aerogel. Among the activated carbons, NZ-AC was found to have the highest selectivity values for CO_2 at higher pressures (between 5 and 5.5). M-30 and ACC selectivity values at high pressures were 4 – 5.3 and 4.5 – 5, respectively. OLC, BPL, and F-600 had similar selectivity values at high pressures for CO_2 over N_2 (between 3.6 and 4.2 at 6.5 atm).

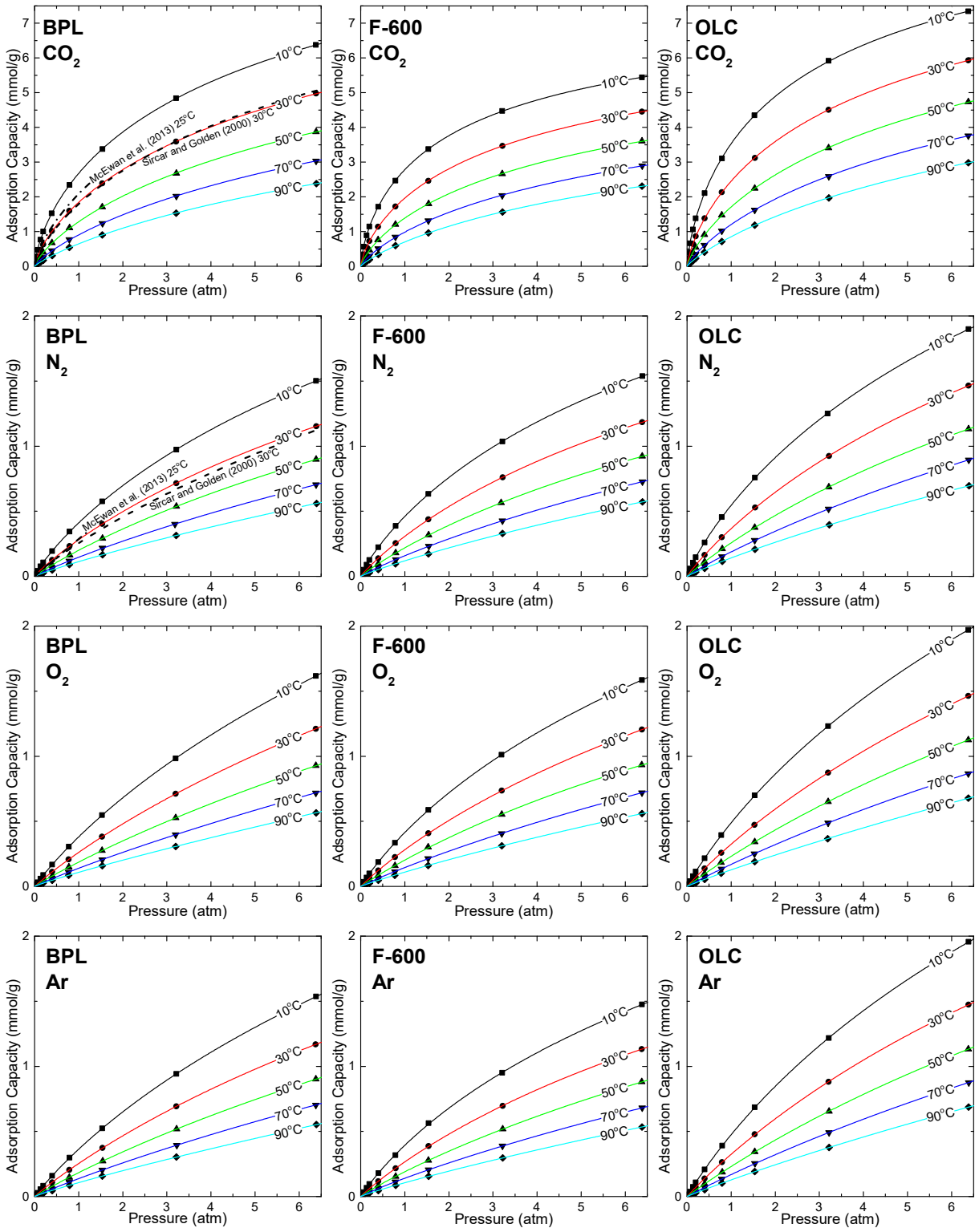

Figure 6.6 – Experimentally determined CO_2, N_2, O_2, and Ar pure adsorption isotherms at 10°C, 30°C, 50°C, 70°C, and 90°C for BPL on the left, F-600 in the middle, and OLC on the right. Comparison data for BPL from Sircar and Golden (2000)[27] at 30°C and McEwen et al. (2013)[61] at 25°C are also shown.

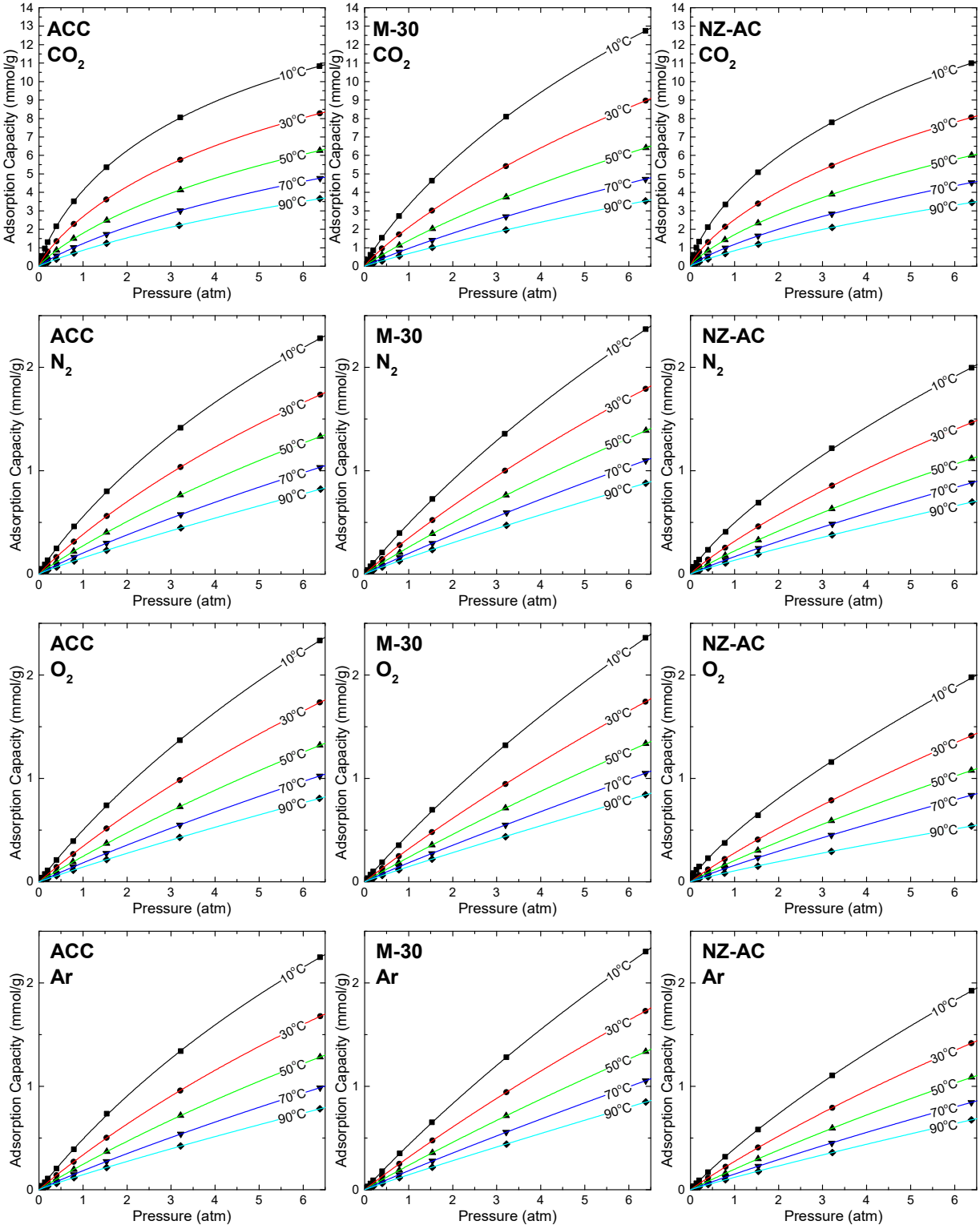

Figure 6.7 – Experimentally determined CO_2, N_2, O_2, and Ar pure adsorption isotherms at 10°C, 30°C, 50°C, 70°C, and 90°C for ACC on the left, M-30 in the middle, and NZ-AC on the right.

In the low pressure region, the selectivity values for CO_2 over N_2 are much greater than those in the high pressure region for all the adsorbents studied. This is due to the more rectangular shape of the CO_2

adsorption isotherms in comparison to the more linear shape of the N_2 isotherm. In this region the selectivity trend is carbon aerogel ≥ RF aerogel ≥ OLC ≈ BPL ≈ F-600 ≈ NZ-AC ≥ ACC ≥ M-30. One thing to note is that M-30 selectivity has a noticeable trend with temperature, with increase selectivity for CO_2 over N_2 as temperature lowers over the whole pressure range in this study. This is also observable for ACC in the lower pressures with the selectivity converging in the higher pressure range.

For the adsorption of N_2, O_2, and Ar, the adsorption isotherms would roughly overlay each other for each adsorbent, except for RF aerogel. Minor deviations between the isotherms were noticed in the low pressure region with N_2 isotherm having a larger capacity and showing less linearity than O_2 and Ar. This is not surprising as N_2 has the largest polarizability and quadrupole moment out of the three gases. Outside this region, the adsorption of these components was found to be within 10% of each other with the O_2 and Ar differing by only 5%. This difference between low pressure region adsorbing more N_2 than O_2 and Ar compared to higher pressure region is indicative of the heterogeneous nature of the surface with N_2 having stronger polarizability and its quadrupole interacting stronger with field effects of the adsorption sites.

6.4.3 Pore Size, Surface Area, %Oxidation, %Ash Content

The adsorption by activated carbons is a function of many intrinsic parameters including surface area and pore size which were measured using BET analysis (results in Table 6.7), as well as the presence and type of surface groups, and ash content which were measured using SEM-EDS and FTIR. From the SEM-EDS results, the quantity of oxygen on the surface was measured (referred to as %oxidized) which was determined in the FTIR data to be mostly in the form of either carboxylic anhydride, quinone, carbonyl, lactone, or pyrone groups on the surface. To determine the effect of these intrinsic parameters of the activated carbon on the adsorption of CO_2, N_2, O_2, and Ar, the coefficient of determination (R^2) was used and calculated for different pressures, as displayed in Equation 2.

$$R^2 = 1 - \frac{\sum_{i=1}^{n}(y_i - f(x_i))^2}{\sum_{i=1}^{n}(y_i - \overline{y})^2} \quad 2$$

This assumes a linear relationship between the intrinsic parameter (y_i) and the adsorption capacity at a particular pressure $f(x_i)$ for each i^{th} adsorbent to a total of n adsorbents). This method has been used in literature before to determine the correlation between the total pore volume, pore volume up to a particular pore size, average pore size, and surface area of an activated carbon with respect to adsorption of CO_2 [33,34]. In those studies, only a finite pressure range was examined (excluded low pressures) at one temperature for CO_2. In this study, a wide range of pressures are examined between 0.03 atm and 6.5 atm at 10°C, 30°C, 50°C, 70°C, and 90°C for CO_2, N_2, O_2 and Ar for carbon aerogel along with the activated carbons. This study correlated the adsorption capacity calculated from the isotherm model at a particular pressure to five intrinsic parameters: cumulative pore size <1 nm, <2nm, and <3nm, surface area, and %oxidation. The results for 10°C for CO_2, N_2, O_2, and Ar are presented in Figure 6.8 along with the effect of temperature for CO_2 in Figure 6.9. The results for 90°C for CO_2, N_2, O_2, and Ar as well as the effect of temperature for N_2, O_2, and Ar are presented in the Supplementary Information in Appendix

V (Figure AV.5 – AV.8). %Ash content, total pore volume, and average pore size were found to have insignificant effect on the adsorption capacity of CO_2, N_2, O_2, and Ar. This agrees with previous literature for total pore volume and average pore size and its effect on CO_2 adsorption capacity [33,34].

In Figure 6.8 the effect by which an intrinsic parameter correlates with adsorption capacity can be observed to change with respect to pressure. For cumulative pore volume <1 nm, <2 nm, and <3 nm, it can be observed that other than at low pressures, as the pressure increases the effect increases, with the effect of <1 nm being greater than <2 nm, being greater than <3 nm, as indicated by higher R^2 values. This for CO_2 at 10°C continues until the pores of the <1 nm are saturated and the effect of <2 nm is greater than that of the <1 nm ones. This trend agrees with the theory of volume filling micropores by M. M. Dubinin by which first the smaller pores will fill up before the larger pores with the saturation of smaller pores before larger ones [32]. This trend of smaller micropores having a stronger effect has also been seen before in literature by Presser et al. (2011)[34] between 0.1 and 1 atm. Extending Presser et al. (2011)'s results with Casco et al. (2014) to between 10 and 45 atm, the effect of pores between 0.5 and 1.2 nm decreases from $R^2 > 0.95$ to less than $R^2 < 0.08$, which shows agreement with M. M. Dubinin theory. However, the Dubinin theory does not hold true in the low pressure region. This is due to the Dubinin theory assuming a homogeneous surface which is not true for activated carbons with few exceptions.

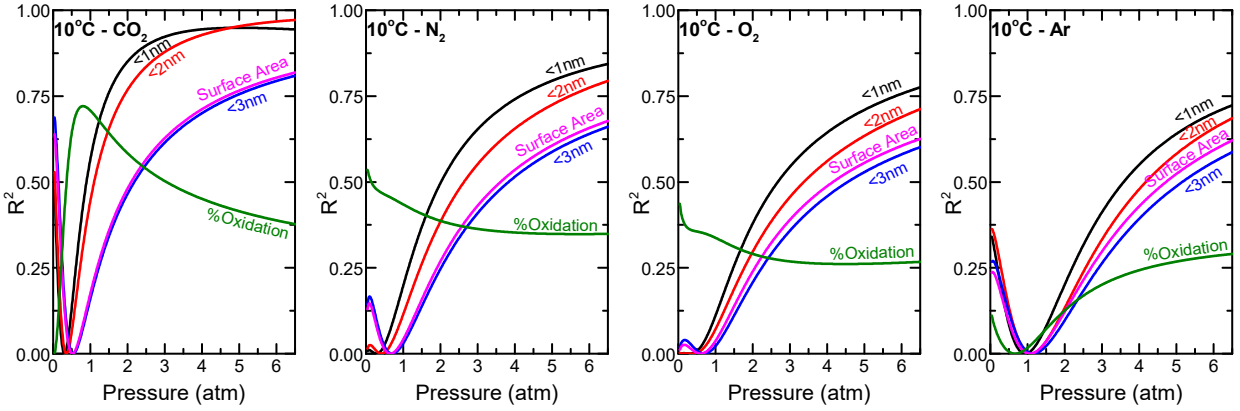

Figure 6.8 – Coefficient of determination with respect to pressure between adsorption capacity (CO_2, N_2, O_2, and Ar) at 10°C and five parameters: cumulative pore size <1nm, <2nm, and <3nm, surface area, and %oxidation.

In this study, every activated carbon and the carbon aerogel had measurable oxygen present on its surface in the form of C=O groups. These groups offered a different type of site by which the gases could interact with on the surface. For CO_2 at 10°C this effect was found to be the strongest in the region between 0.5 and 1.5 atm which can be seen by the %oxidization line in Figure 6.8. This effect of the %oxidization of the surface for CO_2 was stronger than that of $N_2 > O_2 >$ Ar at 10°C. This trend follows the strength of the quadrupole moment with $CO_2 > N_2 > O_2$, with Ar having no quadrupole moment. This trend for N_2, O_2, and Ar should be taken with a caution as the R^2 correlation value is relatively weak (below 0.5).

For CO_2 at 10°C in the low pressure region, the effect of cumulative pore size <3 nm is the strongest followed closely by surface area. This interaction is probably due to the unsaturated edge sites and π-

electrons delocalized on the turbostratic structure interacting with the CO_2. With CO_2 being a weak Lewis acid and these sites being a Lewis base [36] would explain why CO_2 was the only molecule observed with this trend. With field and linear point quadrupole interactions being r^3 distance away compared to dispersion interaction being r^6 interaction [31], would explain why larger pores potential well is favourable than smaller pores. This explanation would need further studies to measure and verify this effect.

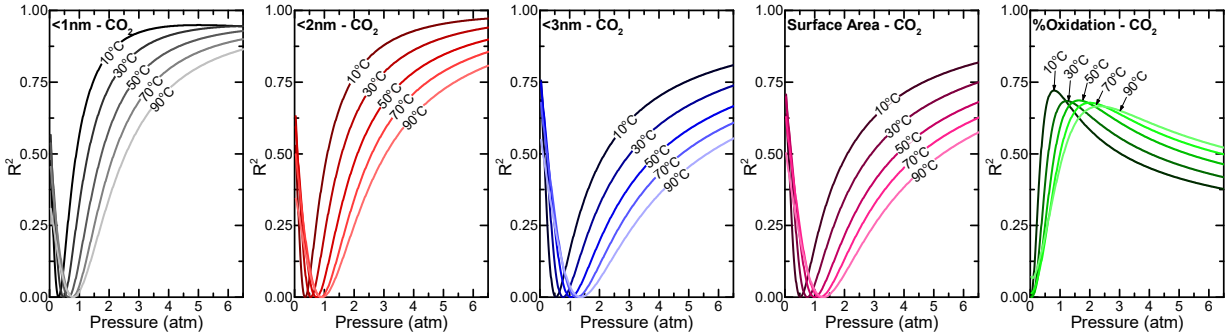

Figure 6.9 – Effect of temperature on the coefficient of determination with respect to pressure between adsorption capacity of CO_2 and five parameters: cumulative pore volume <1nm, <2nm, and <3nm, surface area, and %oxidation.

The effect of surface area on the adsorption capacity was found to be very similar to that of <3 nm for all conditions and adsorbates. This effect, like all effects, in order of strength is $CO_2 > N_2 > O_2 >$ Ar. The effect of temperature on the coefficient of determination between the adsorption capacity of CO_2 and five intrinsic parameters of the carbon aerogel and the activated carbons are included in Figure 6.9. By increasing the adsorption temperature the effect of cumulative pore volume <1 nm, <2 nm, and <3 nm as well as surface area decreases and moves to the right (towards higher pressures) with little to no change occurring with respect to temperature on the effect at the lowest pressures. This decrease in effect is due to lower adsorption capacities occurring at higher temperatures decreasing the amount of CO_2 adsorbed. However, for changing temperature on the effect for N_2, O_2 and Ar adsorption by the intrinsic parameters (Figure AV.6 – AV.8), this trend is not present. The R^2 value for these trends are relatively low, so it is hard to predict how strong the trends are. The %oxidation has the strongest effect for CO_2 which decreases and shifts to the right as temperature increase. This is explained similarly to the trend for <1 nm, <2 nm, and <3 nm, and is likely due to the lower adsorption capacities at higher temperatures at a particular pressure.

6.4.4 Energetically Heterogeneous Surface

Activated carbons have complex surfaces which are composed of different energy sites consisting of saturated basal plane sites, edge sites with heteroatom-containing functional groups, unsaturated edge sites, and π-electrons delocalized on the turbostratic structure which have been discussed extensively in literature [36–38,45]. Saturated basal plane sites makes up the majority of the adsorption sites on the surface of the activated carbon which interact weaker with adsorbates than the heteroatom-containing functional groups, unsaturated edge sites, and π delocalized electron sites which all impose a field effect. In this study, C=O groups is the only heteroatom functional group for the majority of carbons along with some phosphate

groups on NZ-AC and hydroxyl groups on RF aerogel. With carbon being less electronegative than oxygen, oxygen imposes a field which interacts with an induced dipole which is typically stronger than just dispersion interactions. This field also interacts with the quadrupole moment which is present for CO_2, N_2, and O_2 in order of strongest to weakest. Unsaturated edge sites and π-electrons delocalized on the turbostratic structure have been poorly studied in literature with regards to its adsorption of CO_2, N_2, O_2, and Ar but have been investigated more thoroughly for H_2O based systems using the aid of indirect methods such as electrophoresis and mass titration [36]. These sites, which were not measured in this study, would interact similarly to heteroatom functional groups by producing a field due to the presence of the unpaired electrons.

To determine the heterogeneous nature of the carbon surfaces, the Clausius-Clapeyron equation was used to look at the effect of adsorption capacity on the heat of adsorption. These results are presented in Figure 6.10 for CO_2, N_2, O_2, and Ar for all the carbon adsorbents used in this study along with values from literature which were found to be similar [24–26]. The heat of adsorption values for CO_2 were found to be significantly higher than those for N_2, O_2, and Ar for all adsorbents which agree with similar trends observed in the literature [25,26]. This is due to the stronger polarizability and quadrupole moment of CO_2 in comparison to N_2, O_2, and Ar. For the latter three gases in general, the heat of adsorption values in order of strength were $N_2 > O_2 \geq Ar$ for the carbons tested in this study. This followed the combined trend presented in Table 6.1 for polarizability $CO_2 > N_2 > Ar \geq O_2$ and quadrupole moment $CO_2 > N_2 > O_2$ with Ar having no moment. The exception of the heat of adsorption trend of $N_2 > O_2 \geq Ar$ is NZ-AC and the aerogel samples. This could be correlated to the unique surface chemistry of the NZ-AC which had the highest C=O groups and phosphate groups, as well as the unique surface chemistry of RF aerogel which had many hydroxyl groups and ester groups. This was also spotted in literature by Park et al (2019)[24] with $O_2 > N_2$ heat of adsorption, however no explanation was provided.

The heterogeneous nature of the carbons surface can be noted from Figure 6.10 for the adsorption of CO_2 by the greater heat of adsorption at low adsorption capacities which decrease and plateau at higher loadings. This demonstrates that CO_2 first adsorbs to the most energetically favourable sites before the lower energetic sites. RF aerogel was found to have the strongest adsorption at very low loadings due to the presence of hydroxyl groups found on its surface. Similar trends were observed for silicas in the literature [18]. The second strongest adsorption of CO_2 was with carbon aerogel which has the lowest oxygen content as seen in Table 6.5. Therefore, the strong interactions are not due to heteroatom containing functional groups but likely due to the presence of unsaturated edge sites, and π delocalized electron sites on the surface of the carbon aerogel. These sites are created during the carbonization of the raw material which is discussed in literature [45] which are probably in abundance compared to the other carbons due to tighter controls during the manufacture and transportation to the exposure of oxygen. This exposure to oxygen reacts with the highest energy sites producing oxygen groups which happens either at elevated temperatures rapidly or ambient temperature over long times (aging)[62,63] . To reduce this effect to the exposure of oxygen, hydrogen can be used to react with these strongest sites, passivating the active sites and thus resulting in a more stable activated carbon [64]. The heterogeneous nature of the carbons is less

pronounced with the adsorption of N_2 with the polymeric based carbons (carbon aerogel, ACC, and M-30) having almost a constant heat of adsorption with respect to adsorption capacity. This trend is less noticeable with O_2 and even more so with Ar which concurs with the quadrupole and polarizability of the adsorbates mentioned earlier.

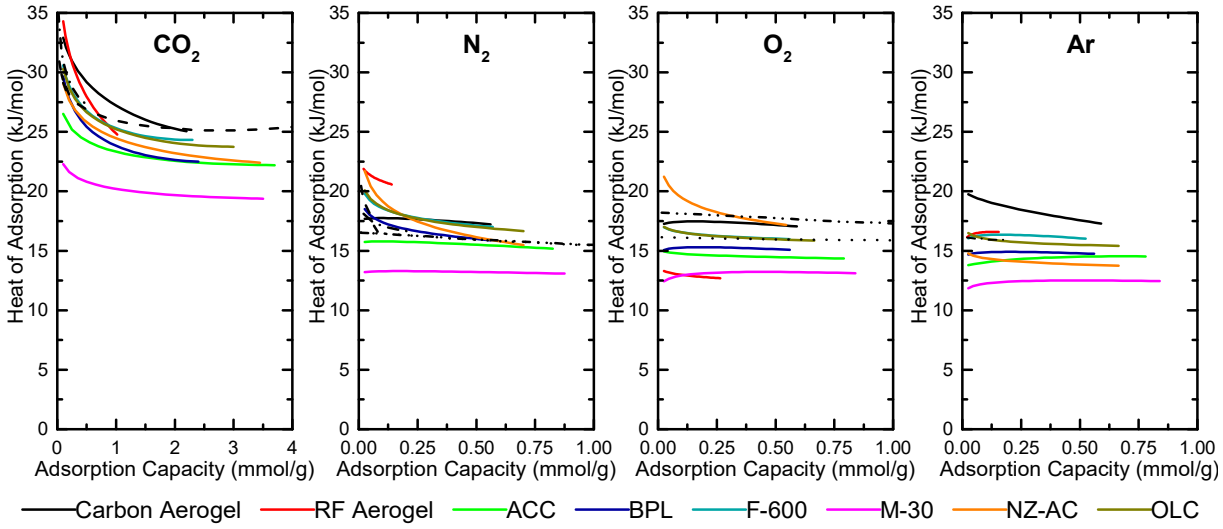

Figure 6.10 – Heat of adsorption values for CO_2, N_2, O_2, and Ar with respect to adsorption capacity using the Clausius-Clapeyron equation for the carbon adsorbents used in this study and literature being represented by dash and dot Park et al (2014)[26], dash Shen et al (2010)[25], dot Park et al (2019)[24], and double dot dash Park et al (2019)[24].

Figure 6.11 shows an isotherm of ACC which can be broken down into two regions that overlap: effect due to the heterogeneous surface (can be seen from the heat of adsorption in red), and effect due to the size of the pores (can be seen from the R^2 coefficient for the cumulative pore size <1nm in blue). The heterogeneous surface effect is due to the higher energy adsorption sites being occupied before the lower energy adsorption sites. For activated carbon, these high energy sites from oxygen containing groups, unsaturated edge sites, and π delocalized electron sites dominate the adsorption in the lowest pressures and are saturated as pressure increases until only weaker energy basal plane sites are left. In this figure, you can see the heat of adsorption beginning to plateau (experimental pressure not high enough for analysis past this point). As this happens, the effect of the pore size begins to dominate the adsorption isotherm. The pore size effect is due to smaller pores filling up before larger pores with the saturation of smaller pores before larger ones. This effect is the strongest with almost no influence by the heterogeneous surface at the highest pressures.

Utilizing these two effects can tailor the activated carbon to an application. For example, to create a more rectangular adsorption isotherm of CO_2, increasing the heterogeneity of the surface by increasing the amount of high energy sites and utilizing a smaller pore size would create an adsorption isotherm more similar to the shape of zeolites CO_2 isotherm.

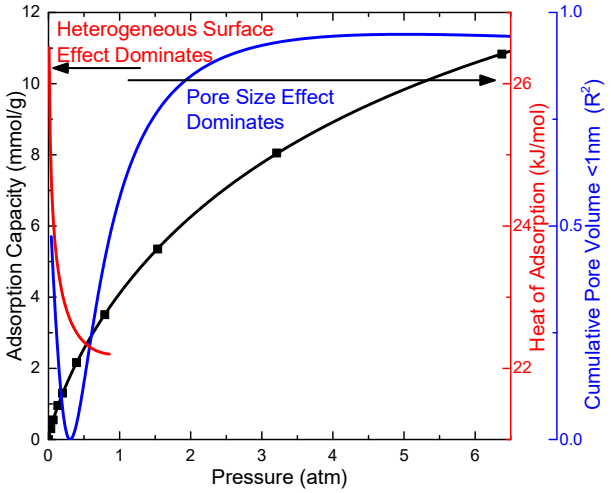

Figure 6.11 – The effect of the heterogeneous surface which can be seen by the heat of adsorption (red) and the effect of the pore size which can be seen by the cumulative pore volume <1 nm (blue) on the adsorption capacity. This example shows the data for CO_2 adsorption on ACC at 10°C.

6.4.5 Carbon Aerogel and RF Aerogel

In order to determine the adsorption capacities of CO_2, N_2, O_2, and Ar between temperatures of 10°C and 90°C for pressures from 0 to 6.5 atm on the carbons studied, where there is no experimental data obtained, the TD-Toth model was used. The coefficients for the TD-Toth model are given in Table 6.4 which fit into the Toth model in Table 6.3 at different temperatures. The fitted coefficients for all the carbons are presented in Table AV.43 in the Supplementary Information in Appendix V. These pure component TD-Toth fitted coefficients were then used to determine the cumulative adsorption capacities for carbon aerogel and RF aerogel in air between air pressures of 0 to 2 atm and temperatures of 10°C to 90°C with concentrations of CO_2, N_2, O_2, and Ar at 400, 780840, 209460, and 9300 ppm, respectively. These surface plots are presented in Figure 6.12 with the blue surface indicating the CO_2 adsorption capacity, the difference between the blue and green surface indicating N_2 adsorption capacity, the difference between the green and red indicating O_2 adsorption capacity, and the difference between the red and black indicating Ar adsorption capacity. For the adsorption of air, the adsorption capacity in order of the highest to the smallest was $N_2 > O_2 >> Ar > CO_2$. This follows the order of the prevalence of the components in air, with air being mostly composed of N_2 and O_2 with some Ar and CO_2.

The black surface indicates the cumulative adsorption of the components of air with carbon aerogel, cumulative adsorption being roughly three times that of RF aerogel. This difference in adsorption capacity would affect the thermal conductivity of the materials when in the presence of air or other gases that would be significantly adsorbed which has been discussed in a previous article [18]. This is due to the thermal conductivity of the gas in the pores in the molecular heat transfer region being dependant on concentration (pressure), and with higher adsorption capacity increasing the concentration of the gas on the surface, which would increase the thermal conductivity of the gas in the pores. Therefore, carbon aerogel would

have increased thermal conductivity of the gas in the pores compared to RF aerogel due to having significantly stronger adsorption.

To reduce this adsorption capacity for high surface area insulating materials to decrease the gas thermal conductivity in the pores, some steps have been highlighted from the previously discussed topics in this article including producing a material without micropores, and having a surface with less higher energy sites. Different techniques can be used in the production of RF aerogel which can be controlled to reduce the amount of micropores which is maintained after the carbonization to carbon aerogel [4,5]. This however, would also affect the Knudsen number, so the reduction of the micropores should be done by creating a tighter pore size distribution and not an overall larger pore size. Also, high energy edge sites with heteroatom-containing functional groups, unsaturated edge sites, and π-electrons delocalized on the turbostratic structure can be reduced using techniques such as exposure to hydrogen gas after carbonization at elevated temperature which has been shown to reduce these high energy sites in literature [42,43].

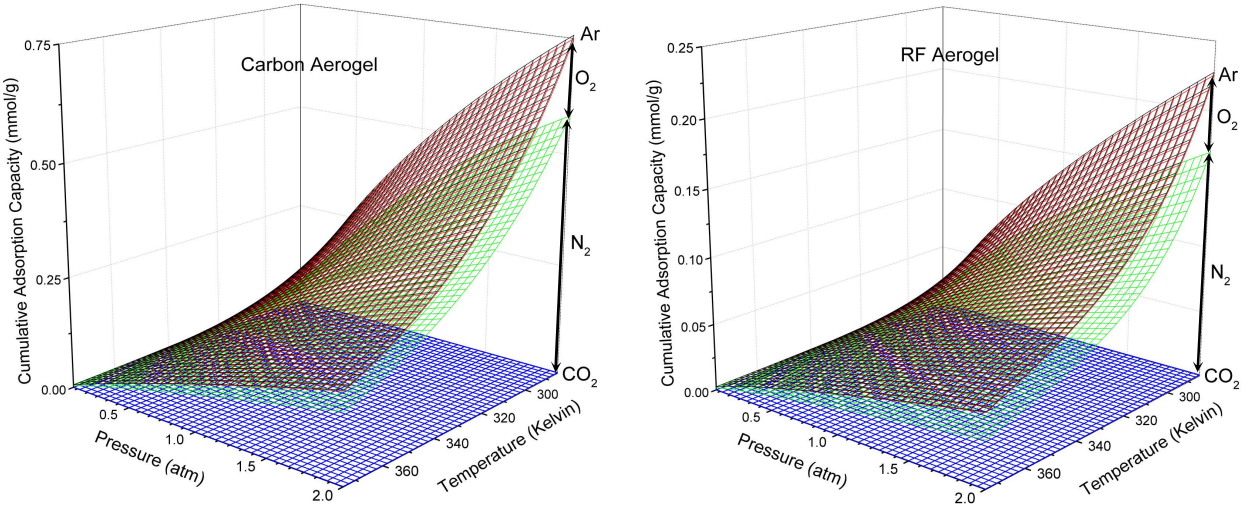

Figure 6.12 – Cumulative adsorption capacities for carbon aerogel and RF aerogel of CO_2, N_2, O_2, and Ar at 400, 780840, 209460, and 9300 ppm, respectively, from temperatures of 285K to 375K and pressures of 0 to 2 atm.

6.5 Conclusions

In this study, carbons including two aerogels and six commercial activated carbons were investigated to determine the influence of pore size and by extension surface area as well as their heterogeneous surface on their adsorption of the components of air. This was done by first characterizing the surface and comparing it to the pure gas adsorption capacities of CO_2, N_2, O_2, and Ar between 10°C – 90°C and 0 – 6.5 atm. From the pure gas adsorption capacities, it was found that CO_2 was adsorbed the most and the strongest out of the four probe gases. This adsorption of CO_2 was the highest for ACC, NZ-AC, and M-30 which all had CO_2 adsorption capacities at 6.5 atm above 11 mmol/g. Of these three, NZ-AC had the highest CO_2/N_2 selectivity while being in a pelletized form. From the comparison between the

characterization and pure gas adsorption capacities, there was a strong correlation between the cumulative pore volume up to a particular pore size of the carbons and the adsorption capacity, with the strength of the correlation being stronger at higher pressures. At the lower pressures, the adsorption capacity was found to be dominated by the heterogeneous nature of the surface particularly for CO_2, with unsaturated edge sites, and π-electrons delocalized on the turbostratic structure having the strongest adsorption at the lowest pressures and oxygen species on the surface following. This data can be used to help tailor the carbon for a particular adsorption application. For example, this study looks into carbon aerogels for insulation applications where techniques could be used to reduce the adsorption of the components of air to make these materials better insulators.

6.6 Nomenclature

H_{ads}	Heat of adsorption (kJ/mol)
k	Freundlich parameter (mmol g^{-1} atm^{-1})
n	Freundlich parameter (-)
P	Pressure (atm)
q_e	Equilibrium adsorption capacity (mmol/g)
q_s	Monolayer or saturation adsorption capacity (mmol/g)
q_{s0}	Empirical TD-Toth parameter (mmol/g)
Q	Empirical TD-Toth heat of adsorption (kJ/mol)
R	Gas constant (m^3 atm K^{-1} mol^{-1})
R^2	Coefficient of determination (-)
t	Toth parameter (-)
t_0	Empirical TD-Toth parameter (-)
T	Temperature (K)
T_0	Empirical TD-Toth reference temperature (K)
α	Empirical TD-Toth parameter (-)
β	Langmuir parameter (atm^{-1})
β_0	Empirical TD-Toth reference parameter (atm^{-1})
χ	Empirical TD-Toth constant (-)

6.7 List of Abbreviations

2D-NLDFT-HS	Two-Dimensional Non-Local Density-Functional-Theory for Heterogeneous-Surfaces
ACC	Activated Carbon Cloth
ATR	Attenuated Total Reflectance
BET	Brunaur, Emmett, and Teller
BJH	Barrett-Joyner-Halenda
DAC	Direct Air Capture
FTIR	Fourier-Transform Infrared Spectroscopy
RF	Resorcinol-Formaldehyde
SEM-EDS	Scanning Electron Microscopy – Energy Dispersive X-ray Spectroscopy
TD-Toth	Temperature Dependant Toth

6.8 Bibliography

1. Hrubesh, L. W. Aerogel Applications. *J. Non. Cryst. Solids* **225**, 335–342 (1998).
2. Maleki, H. Recent Advances in Aerogels for Environmental Remediation Applications□: A Review. *Chem. Eng. J.* **300**, 98–118 (2016).
3. Kabbour, H., Baumann, T. F., Satcher, J. H., Saulnier, A. & Ahn, C. C. Toward New Candidates for Hydrogen Storage: High-Surface-Area Carbon Aerogels. *Chem. Mater.* **18**, 6085–6087 (2006).
4. Tamon, H., Ishizaka, H., Araki, T. & Okazaki, M. Control of Mesoporous Structure of Organic and Carbon Aerogels. *Carbon N. Y.* **36**, 1257–1262 (1998).
5. Horikawa, T., Hayashi, J. & Muroyama, K. Controllability of Pore Characteristics of Resorcinol-Formaldehyde Carbon Aerogel. *Carbon N. Y.* **42**, 1625–1633 (2004).
6. Fairen-Jimenez, D., Carrasco-Marin, F. & Moreno-Castilla, C. Adsorption of Benzene, Toluene, and Xylenes on Monolithic Carbon Aerogels from Dry Air Flows. *Langmuir* **23**, 10095–10101 (2007).
7. Tian, H. Y., Buckley, C. E., Wang, S. B. & Zhou, M. F. Enhanced Hydrogen Storage Capacity in Carbon Aerogels Treated with KOH. *Carbon N. Y.* **47**, 2128–2130 (2009).
8. Alhwaige, A. A., Ishida, H. & Qutubuddin, S. Carbon Aerogels with Excellent CO_2 Adsorption Capacity Synthesized from Clay-Reinforced Biobased Chitosan-Polybenzoxazine Nanocomposites. *ACS Sustain. Chem. Eng.* **4**, 1286–1295 (2016).
9. Jeon, D.-H., Min, B.-G., Oh, J. G., Nah, C. & Park, S.-J. Influence of Nitrogen Moieties on CO_2 Capture of Carbon Aerogel. *Carbon Lett.* **16**, 57–61 (2015).
10. Marques, L. M., Carrott, P. J. M. & Carrott, M. M. L. R. Carbon Aerogels used in Carbon Dioxide Capture. *Bol. Grup. Español Carbón* **40**, 9–12 (2016).
11. Hao, G. P., Li, W. C., Qian, D. & Lu, A. H. Rapid Synthesis of Nitrogen-Doped Porous Carbon Monolith for CO_2 Capture. *Adv. Mater.* **22**, 853–857 (2010).
12. Gavalda, S., Gubbins, K. E., Kaneko, K. & Thomson, K. T. Nitrogen Adsorption in Carbon Aerogels: A Molecular Simulation Study. *Langmuir* **18**, 2141–2151 (2002).
13. Fricke, J., Lu, X., Wang, P., Buttner, D. & Heinemann, U. Optimization of Monolithic Silica Aerogel Insulants. *Int. J. Mass Transf.* **35**, 2305–2309 (1992).
14. Herrmann, G. *et al.* On the Way to Commercial Production of Silica Aerogel. **186**, 380–387 (1995).
15. Lee, O. J., Lee, K. H., Jin Yim, T., Young Kim, S. & Yoo, K. P. Determination of Mesopore Size of Aerogels from Thermal Conductivity Measurements. *J. Non. Cryst. Solids* **298**, 287–292 (2002).
16. Hrubesh, L. W. & Pekala, R. W. Thermal Properties of Organic and Inorganic Aerogels. *J. Mater. Res.* **9**, 731–738 (1994).
17. Lu, X., Caps, R., Fricke, J., Alviso, C. T. & Pekala, R. W. Correlation between Structure and Thermal Conductivity of Organic Aerogels. *J. Non. Cryst. Solids* **188**, 226–234 (1995).
18. Wilson, S. M. W., Gabriel, V. A. & Tezel, F. H. Adsorption of Components from Air on Silica Aerogel. *Microporous Mesoporous Mater.* (2020).
19. Sircar, S. Basic Research Needs for Design of Adsorptive Gas Separation Processes. *Ind. Eng. Chem. Res.* **45**, 5435–5448 (2006).
20. Reid, C. R., Okoye, I. P. & Thomas, K. M. Adsorption of Gases on a Carbon Molecular Sieve used for Air Separation: Linear Adsorptives as Probes for Kinetic Selectivity. *Langmuir* **15**, 2415–2425 (1998).
21. Bae, Y. S. & Lee, C. H. Sorption Kinetics of Eight Gases on a Carbon Molecular Sieve at Elevated Pressure. *Carbon N. Y.* **43**, 95–107 (2005).
22. Verma, S. K. & Walker, P. L. Preparation of Carbon Molecular Sieves by Propylene Pyrolysis over Microporous Carbons. *Carbon N. Y.* **30**, 829–836 (1992).
23. Bazan, R. E., Bastos-Neto, M., Moeller, A., Dreisbach, F. & Staudt, R. Adsorption Equilibria of O_2, Ar, Kr and Xe on Activated Carbon and Zeolites: Single Component and Mixture Data. *Adsorption* **17**, 371–383 (2011).
24. Park, D., Ju, Y., Kim, J. H., Ahn, H. & Lee, C. H. Equilibrium and Kinetics of Nitrous Oxide, Oxygen, and Nitrogen Adsorption on Activated Carbon and Carbon Molecular Sieve. *Sep. Purif. Technol.* **223**, 63–80 (2019).
25. Shen, C., Grande, C. A., Li, P., Yu, J. & Rodrigues, A. E. Adsorption Equilibria and Kinetics of CO_2 and N_2 on Activated Carbon Beads. *Chem. Eng. J.* **160**, 398–407 (2010).
26. Park, Y., Moon, D. K., Kim, Y. H., Ahn, H. & Lee, C. H. Adsorption Isotherms of CO_2, CO, N_2, CH_4, Ar and H_2 on Activated Carbon and Zeolite LiX up to 1.0 MPa. *Adsorption* **20**, 631–647 (2014).
27. Sircar, S. & Golden, T. C. Purification of Hydrogen by Pressure Swing Adsorption. *Sep. Sci. Technol.* **35**, 667–687 (2000).
28. Wilson, S. M. W., Kennedy, D. A. & Tezel, F. H. Adsorbent Screening for CO_2/CO Separation for Applications in Syngas Production. *Sep. Purif. Technol.* **236**, 1–11 (2020).
29. Drage, T. C., Blackman, J. M., Pevida, C. & Snape, C. E. Evaluation of Activated Carbon Adsorbents for CO_2 Capture in Gasification. *Energy and Fuels* **23**, 2790–2796 (2009).
30. Barton, T. J. *et al.* Tailored Porous Materials. *Chem. Mater.* **11**, 2633–2656 (1999).
31. Yang, R. T. *Adsorbents: Fundamentals and Applications*. (John Wiley & Sons, 2003).
32. Dubinin, M. M. Generalization of the Theory of Volume Filling of Micropores to Nonhomogeneous Microporous Structures. *Carbon N. Y.* **23**, 373–380 (1985).

33. Casco, M. E., Martínez-Escandell, M., Silvestre-Albero, J. & Rodríguez-Reinoso, F. Effect of the Porous Structure in Carbon Materials for CO_2 Capture at Atmospheric and High-Pressure. *Carbon N. Y.* **67**, 230–235 (2014).
34. Presser, V., McDonough, J., Yeon, S. H. & Gogotsi, Y. Effect of Pore Size on Carbon Dioxide Sorption by Carbide Derived Carbon. *Energy Environ. Sci.* **4**, 3059–3066 (2011).
35. Sircar, S. & Rao, M. Chapter 19: Heat of Adsorption of Pure Gas and Multi-Component Gas Mixtures on Microporous Adsorbents. in *Surfaces of Nanoparticles and Porous Materials* 501–528 (1999).
36. Radovic, L. R. Chapter 20: Surface Chemistry of Activated Carbon Materials: State of the Art and Implications for Adsorption. in *Surfaces of Nanoparticles and Porous Materials* 529–566 (1999).
37. Boehm, H. P. Some Aspects of the Surface Chemistry of Carbon Blacks and Other Carbons. *Carbon N. Y.* **32**, 759–769 (1994).
38. Leon Y Leon, C. A. & Radovic, L. R. Interfacial Chemistry and Electrochemistry of Carbon Surfaces. *Chem. Phys. Carbon* **24**, 213–310 (1994).
39. Suzuki, M. *Adsorption Engineering*. (Kondansha LTD and Elsevier Science Publishers B.V., 1990).
40. Uranowski, L. J., Tessmer, C. H. & Vidic, R. D. The Effect of Surface Metal Oxides on Activated Carbon Adsorption of Phenolics. *Water Res.* **32**, 1841–1851 (1998).
41. Hyun, S. H. & Danner, R. P. Equilibrium Adsorption of Ethane, Ethylene, Isobutane, Carbon Dioxide, and Their Binary Mixtures on 13X Molecular Sieves. *J. Chem. Eng. Data* **27**, 196–200 (1982).
42. Bansal, R. C., Vastola, F. J. & Walker, P. L. Influence of Hydrogen Chemisorption on the Subsequent Chemisorption of Oxygen on Activated Carbon. *Carbon N. Y.* **12**, 355–357 (1973).
43. Menendez, J. A., Phillips, J., Xia, B. & Radovic, L. R. On the Modification and Characterization of Chemical Surface Properties of Activated Carbon: In the Search of Carbons with Stable Basic Properties. *Langmuir* **12**, 4404–4410 (1996).
44. Karpinski, Z. & Szymanski, G. S. The Effect of the Gradual Thermal Decomposition of Surface Oxygen Species on the Chemical and Catalytic Properties of Oxidized Activated Carbon. *Carbon N. Y.* **40**, 2627–2639 (2002).
45. Shafeeyan, M. S., Mohd, W., Wan, A., Houshmand, A. & Shamiri, A. A Review on Surface Modification of Activated Carbon for Carbon Dioxide Adsorption. *J. Anal. Appl. Pyrolysis* **89**, 143–151 (2010).
46. Islam, S., Ang, B. C., Gharehkhani, S. & Afifi, M. Adsorption Capability of Activated Carbon Synthesized from Coconut Shell. *Carbon Lett.* **20**, 1–9 (2016).
47. Meng, Y., Young, T. M. & Liu, P. Ultralight Carbon Aerogel from Nanocellulose as a Highly Selective Oil Absorption Material. *Cellulose* **22**, 435–447 (2015).
48. Tanaka, S., Yasuda, T., Katayama, Y. & Miyake, Y. Pervaporation Dehydration Performance of Microporous Carbon Membranes prepared from Resorcinol/Formaldehyde Polymer. *J. Memb. Sci.* **379**, 52–59 (2011).
49. Wang, Y., Chang, B., Guan, D. & Dong, X. Mesoporous Activated Carbon Spheres derived from Resorcinol-Formaldehyde Resin with High Performance for Supercapacitors. *J. Solid State Electrochem.* **19**, 1783–1791 (2015).
50. Zhou, H. *et al.* Facile Preparation and Ultra-Microporous Structure of Melamine-Resorcinol- Formaldehyde Polymeric Microspheres. *Chem. Commun.* **49**, 3763–3765 (2013).
51. Shin, S., Jang, J., Yoon, S. H. & Mochida, I. A Study on the Effect of Heat Treatment on Functional Groups of Pitch Based Activated Carbon Fiber using FTIR. *Carbon N. Y.* **35**, 1739–1743 (1997).
52. Ţucureanu, V., Matei, A. & Avram, A. M. FTIR Spectroscopy for Carbon Family Study. *Crit. Rev. Anal. Chem.* **46**, 502–520 (2016).
53. Grzyb, B. *et al.* Functionalisation and Chemical Characterisation of Cellulose-Derived Carbon Aerogels. *Carbon N. Y.* **48**, 2297–2307 (2010).
54. Chingombe, P., Saha, B. & Wakeman, R. J. Surface Modification and Characterisation of a Coal-Based Activated Carbon. *Carbon N. Y.* **43**, 3132–3143 (2005).
55. Guo, Y. & Rockstraw, D. A. Physical and Chemical Properties of Carbons Synthesized from Xylan , Cellulose, and Kraft Lignin by H_3PO_4 Activation. *Carbon N. Y.* **44**, 1464–1475 (2006).
56. Solum, M. S., Pugmire, R. J., Jagtoyen, M. & Derbyshire, F. Evolution of Carbon Structure in Chemically Activated Wood. *Carbon N. Y.* **33**, 1247–1254 (1995).
57. Puziy, A. M. & Poddubnaya, O. I. Synthetic Carbons Activated with Phosphoric Acid I. Surface Chemistry and Ion Binding Properties. *Carbon N. Y.* **40**, 1493–1505 (2002).
58. Kose, H. The Effects of Physical Factors on the Adsorption of Synthetic Organic Compounds By Activated Carbons and Activated Carbon Fibers. (Clemson University, 2010). doi:10.1111/j.1600-0714.2011.01008.x
59. Jagiello, J., Ania, C., Parra, J. B. & Cook, C. Dual Gas Analysis of Microporous Carbons using 2D-NLDFT Heterogeneous Surface Model and Combined Adsorption Data of N_2 and CO_2. *Carbon N. Y.* **91**, 330–337 (2015).
60. Thommes, M. *et al.* Physisorption of Gases, with Special Reference to the Evaluation of Surface Area and Pore Size Distribution (IUPAC Technical Report). *Pure Appl. Chem.* **87**, 1051–1069 (2015).
61. McEwen, J., Hayman, J. & Yazaydin, A. O. A Comparative Study of CO_2 , CH_4 and N_2 Adsorption in ZIF-8 , Zeolite-13X and BPL Activated Carbon. *Chem. Phys.* **412**, 72–76 (2013).
62. Carrasco-Marín, F., Rivera-Utrilla, J., Joly, J. P. & Moreno-Castilla, C. Effects of Ageing on the Oxygen Surface Complexes of an Oxidized Activated Carbon. *J. Chem. Soc. - Faraday Trans.* **92**, 2779–2782 (1996).
63. Boehm, H. P. Surface Oxides on Carbon and Their Analysis: A Critical Assessment. *Carbon N. Y.* **40**, 145–149 (2002).
64. Verma, S. K. & Walker, P. L. Carbon Molecular Sieves with Stable Hydrophobic Surfaces. *Carbon N. Y.* **30**, 837–844

(1992).

Chapter 7

Conclusions, Contributions, and Recommendations

7.1. CONCLUSIONS

The main objectives of this thesis were to use adsorption technology and apply existing adsorbents for the removal of CO_2 in low concentration for applications in DAC of CO_2 and excimer gas purification as well as to discover new adsorbents that could be used for those applications. In the pursuit of these objectives, over the course of this thesis many conclusions were drawn.

To reduce the \$/tonCO_2 for DAC the sorbent needs to have large CO_2 adsorption capacity, fast kinetics, selective for CO_2 over N_2, O_2, and Ar, easy regeneration, long working life, and low cost. (Chapter 1) Implementing DAC of CO_2 requires costs to be broken down to the capital cost and operating cost with the operating cost being a function of the mechanical energies and the thermal energies. To lower the required thermal energies for DAC, the sorbent benefits from having an easy regeneration (low regeneration temperature, low heat of adsorption) as well as a large CO_2 adsorption capacity which reduces sensible heat loss from heating the sorbent. It was also found that a large CO_2 adsorption capacity also reduces the capital cost of the system by capturing more CO_2 per cycle. For the capital costs, they can be further reduced by utilizing an adsorbent that is inexpensive, that will function for a long time, and with fast cycles. These fast cycles are only possible with fast kinetics which also reduces the mechanical energy required for flow. These sorbent parameters along with CO_2 being selective over N_2, O_2, and Ar, will allow the sorbent to economically capture CO_2 then concentrate it to 95% and beyond.

Low Si/Al ratio faujasite structured zeolites are potential adsorbents for DAC of CO_2. (Chapter 1) A literature review conducted showed that low Si/Al ratio faujasite structured zeolites have a competitive advantage compared to other technologies that are currently in literature and on the market for DAC. This advantage lies in the large CO_2 adsorption capacities, fast kinetics, selectivity for CO_2, long working life, and their low costs. These materials were not thoroughly investigated before this thesis due to their hydrophilic nature but utilizing a desiccant bed can allow their use. Chapter 3 repeats these finding from literature with seven zeolites and shows the large adsorption capacities for CO_2, fast kinetics, and their selectivity for CO_2 which are desirable for DAC.

Utilizing the 4-step TVSA cycle, low Si/Al ratio faujasite structured zeolites can be used to produce 95% pure CO_2 from air. (Chapter 2) From the results for the pure component isotherms for these zeolites, it was noted that the maximum purity that could be produced from a 3-step TVSA cycle without blowdown would be insufficient to meet the 95% required purity. However, utilizing a blowdown step would allow the rectangular nature of the CO_2 isotherm to keep the CO_2 adsorbed with the application of a vacuum relative to the linear nature of the N_2, O_2, and Ar isotherms. This was confirmed with breakthrough experiments and

CO_2 was concentrated from 0.04% in air to 95% using the 4-step TVSA cycle for greenhouse gas reduction.

There is an optimum regeneration temperature for a TVSA cycle for DAC of CO_2. (Chapter 2) Meeting the requirement for 95% pure CO_2 using the 4-step TVSA cycle, different regeneration temperatures were tested to determine their influence on the \$/tonCO_2. The regeneration temperature has its largest influence on the working capacity of the adsorbent, as well as the capture fraction of the process. This creates the effect that lower regeneration temperatures have lower thermal energies and higher mechanical energies, and vice versa for larger regeneration temperature with an optimum in-between.

Energy for flow is significantly reduced with slower flow rates. (Chapter 2) By testing four flow rates during the adsorption step, it was noted that the breakthrough was sharp for the fastest flow rates. These fast flow rates were sharp but they also allowed more CO_2 to escape the bed before the bed was at 95% saturation. Because of this, these fast flow rates had lower capture fractions compared to their slower counterparts increasing the energy required for flow. This increased energy for flow was amplified by the fact that faster flow rates have larger pressure drops increasing the MJ/tonCO_2 even more.

DAC of CO_2 using zeolites requires low humidity environments. (Chapter 2) Due to zeolitic materials being hydrophilic, water competitively adsorbs over CO_2. Therefore, the feed air stream must be dehumidified before CO_2 separation, potentially with desiccants. Assessing the required energies for a feed stream it was noted that even removing CO_2 from air at 12°C and 100% humidity or 24°C and 20% humidity would require an equivalent energy to remove H_2O as CO_2. Therefore, the successful implementation of this technology for green-house gas separation would need to be placed in low humidity desert areas of the planet such as the Atacama Desert or McMurdo Dry Valley.

Value added high purity CO_2 was produced from air up to 99.96% by modifying blowdown conditions. (Chapter 3) Increasing CO_2 to the point where the CO_2 is intrinsically more valuable increases the viability of DAC seeing as there is a desirable product being produced. To achieve this, an in-depth analysis of the pure gas isotherms showed the benefit of reducing the pressure or pressure & temperature during the blowdown step to remove N_2, O_2, and Ar while leaving the CO_2. This modeling prediction was then validated with 4-step TVSA breakthrough experiments using a low Si/Al ratio faujasite structured zeolite which showed the N_2, O_2, and Ar leaving the column during the blowdown step, and CO_2 leaving the column during the evacuation step. At the end of the experiments, high purity CO_2 was produced between a concentration of 99.5% and 99.96% by lowering the blowdown pressure. By controlling the blowdown temperature, the concentration of the product was increased from 99.8% to 99.95%, however with a significant loss of CO_2.

Aluminas and polymeric adsorbents are potential adsorbents for excimer gas purification. (Chapter 4) Excimer gas contains F_2 and HF which react violently with many commercial adsorbents. It was determined that aluminas and polymeric adsorbents are the most likely to be resilient to these two gases. To determine their potential for purification of CO_2, CF_4, COF_2, and O_2 from F_2, Kr, and Ne, a preliminary study using

concentration pulse chromatography technique was chosen to analyse their Henry's Law constants. These results also allowed the analysis of limiting heat of adsorption of CO_2, CF_4, and O_2 on the five tested adsorbents. From these results, AA-300 was found to be the most promising alumina and HayeSep Q was found to be the most promising polymeric adsorbent for the purification of excimer gas.

Reducing adsorption temperature increases the adsorption capacity and compatibility of the material to F_2 and HF. (Chapter 4) Reducing the temperature of the excimer gas separation would increase the adsorbent materials' working lifetime with relation to the activation energy in the Maxwell-Boltzmann distribution of molecular energies. Reducing temperature also benefits the adsorption capacity, with the adsorption capacity increase logarithmically with relation to the inverse temperature. This increase was shown using van't Hoff plots with the best performing polymer having significant adsorption of CO_2 and CF_4 of 10 mmol g^{-1} atm^{-1} occurring at -50°C and -100°C, and the best performing alumina having significant adsorption of CO_2 at room temperatures and CF_4 at 10 mmol g^{-1} atm^{-1} occurring at -135°C.

The surface groups on silica aerogels heavily influence CO_2 adsorption. (Chapter 5) By analyzing pure gas adsorption isotherms of CO_2, N_2, O_2, and Ar at multiple temperatures for three silica samples and characterizing their surfaces using FTIR and NMR, it was shown that the surface groups heavily influenced CO_2 adsorption capacity. This difference was roughly 3.75 times more if the surface was composed of a majority of silanol groups compared to trimethylsilyl groups. This influence of surface groups on CO_2 adsorption and not N_2, O_2, and Ar highlights the order of size difference between CO_2's polarizability and quadrupole moment compared to the other gases.

Adsorption onto the surface of aerogels would affect the gas thermal conductivity in the pores within the molecular heat transfer and transitional domains. (Chapter 5) Aerogels are the best known insulating materials with their total thermal conductivity being a function of conduction through the solid lattice, the radiative heat transfer across and through the material, and the gas conduction in the pores. This gas thermal conduction in the pores makes up the majority of the total thermal conductivity of these materials and is dependent on the Knudsen number. This Knudsen number is pressure dependant, and seeing as adsorption is a surface based phenomenon where there is an increased gas concentration on the surface and therefore within the pores, adsorption would undoubtedly affect the thermal conductivity of aerogels with emphasis to the molecular heat transfer and transitional domains. This study was a preliminary study into the effect of adsorption on thermal conductivity which quantified the adsorption of CO_2, N_2, O_2, and Ar on two silica aerogel samples. This will allow further experiments to then quantify the effect of adsorption on the gas thermal conductivity within the pores.

Adsorption onto porous carbons including carbon aerogel is dominated by the heterogeneous nature of the surface more at lower pressures and by the pore size more at higher pressure. (Chapter 6) This chapter investigates two carbonous aerogels and six commercial activated carbons to determine the influence of pore size and by extension surface area as well as their heterogeneous surface on their adsorption of the components from air. This was done by first characterizing the surface and comparing it to the pure gas adsorption capacities of CO_2, N_2, O_2, and Ar in the range of 10°C – 90°C and 0 – 6.5 atm. From this

data it was observed that there was a strong correlation between the cumulative pore volume up to a particular pore size of the carbons and the adsorption capacity, with the strength of the correlation being stronger at higher pressures which concurs with Dubinin's micropore volume filling theory. At the lower pressures, the adsorption capacity was found to be dominated by the heterogeneous nature of the surface particularly for CO_2, with unsaturated edge sites, and π-electrons delocalized on the turbostratic structure having the strongest adsorption at the lowest pressures followed by the effect of oxygen species on the surface. This data can be used to help tailor a porous carbon for a particular adsorption application.

7.2. CONTRIBUTIONS

The overall scientific contributions of the work presented in this thesis are summarized as follows:

- A novel process was developed utilizing low Si/Al ratio faujasite structured zeolite to capture CO_2 from dry air and concentrate it to 95% purity for greenhouse gas reduction in a single 4-step TVSA cycle with process conditions to reduce the overall energy requirement.
- Pioneered a novel process utilizing low Si/Al ratio faujasite structured zeolite to capture CO_2 from dry air and concentrate CO_2 up to 99.96% for the production of high purity CO_2 in a single 4-step TVSA cycle. This is the first time in literature that a study has experimentally shown that CO_2 being concentrated up to 99.96% using a single adsorption cycle from a low CO_2 concentration source.
- For the first time a study has been carried out to investigate using adsorption to purify excimer gas to increase the life of the laser. This preliminary study identified and tested potential adsorbents along with strategies to do the separation such as reducing the temperature which will increase the life of the adsorbents in the presence of F_2 and HF.
- Original research has been carried out into our understanding of the adsorption of CO_2, N_2, O_2, and Ar onto silica aerogel, carbon aerogel, and RF aerogel. This thesis discussed the potential of utilizing aerogels as adsorbent materials and went in-depth into the adsorption of the components from air.
- This thesis introduced the concept of the influence of adsorption on the thermal conductivity of insulative materials such as aerogels. This was a preliminary work with the quantity and strength of adsorption being measured on three aerogel species.
- This thesis amalgamated the influence of the heterogeneous surface and pore size on the adsorption of CO_2, N_2, O_2, and Ar by porous carbons such as carbon aerogels or activated carbons. This will allow the ability to tailor these carbon adsorbents better for applications involving adsorption.

7.3. RECOMMENDATIONS

In spite of the success of the research presented in this thesis, there is a significant amount of both experimental and theoretical work remaining that can be done. These recommendations for future work are presented but not limited to the following:

- A novel process to capture then concentrate CO_2 was done in Chapters 2 & 3 utilizing a small quantity of adsorbent at the bench top scale. Therefore, it should naturally follow that the next step would be the application of these technologies in a much larger scale. This will encounter many challenges where these technologies will need to be developed and optimized for their particular applications. This scaled solution can be easily tested using indoor or outdoor air in the Ottawa region.
    - Green-house gas mitigation requires the lowest \$/tonCO_2 which needs to be further optimized. This can be done by testing ways to reduce the pressure drop across the adsorbent bed such as low L/D bed or structured beds. Testing the effect of using a stronger vacuum and less heat during the regeneration of the adsorbent can be done to reduce the thermal energy requirements to increase the desorption capture fraction.
    - High purity CO_2 from this process was limited by the void space due to the testing equipment. Future experiments can be done to reduce this void space to increase purity. The reduction of void space can also be done on the working material in the bed by using structured zeolites so that pressure drop through the bed is not compromised.
- In Chapter 4 the use of adsorbents was tested for excimer lasers as a means to reduce the amount of impurities and increase the life of these lasers. The next step is to determine the degradation of these materials in the presence of F_2 and HF at room and reduced temperatures. This research can be done in tandem with testing these materials utilizing real excimer gas at reduced temperatures.
- With there being numerous types of aerogel materials, further investigation into the adsorption potential of these materials can be done. This should focus on using aerogels in a way that current adsorbents cannot be used or in a situation where current adsorbents are incompatible for a separation. Examples include Cu(I) aerogel for π-bond adsorption of CO from syngas or Ni(II) aerogel for room temperature adsorption of COF_2, and CO_2 from excimer gas.
- The influence of adsorption onto the thermal conductivity of aerogels was postulated in Chapter 5. This can be validated using the hot-wire method in a pressurized vessel. This can be done using the adsorption data for the aerogels tested in this thesis or for faujasite type zeolites with varying Si/Al ratios and/or alkali metal cation for CO_2, N_2, and Ar which will change the adsorption significantly for the same structure.

Appendix I

Supporting Information

for

"Direct Dry Air Capture of CO_2 using VTSA with Faujasite Zeolites"

Sean M.W. Wilson, and F. Handan Tezel

Department of Chemical and Biological Engineering, University of Ottawa, 161 Louis-Pasteur, Ottawa, Ontario K1N 6N5 Canada

Accepted by: Industrial & Engineering Chemistry Research 2020

Contents

AI.1. Schematic Diagram of the Gravimetric System

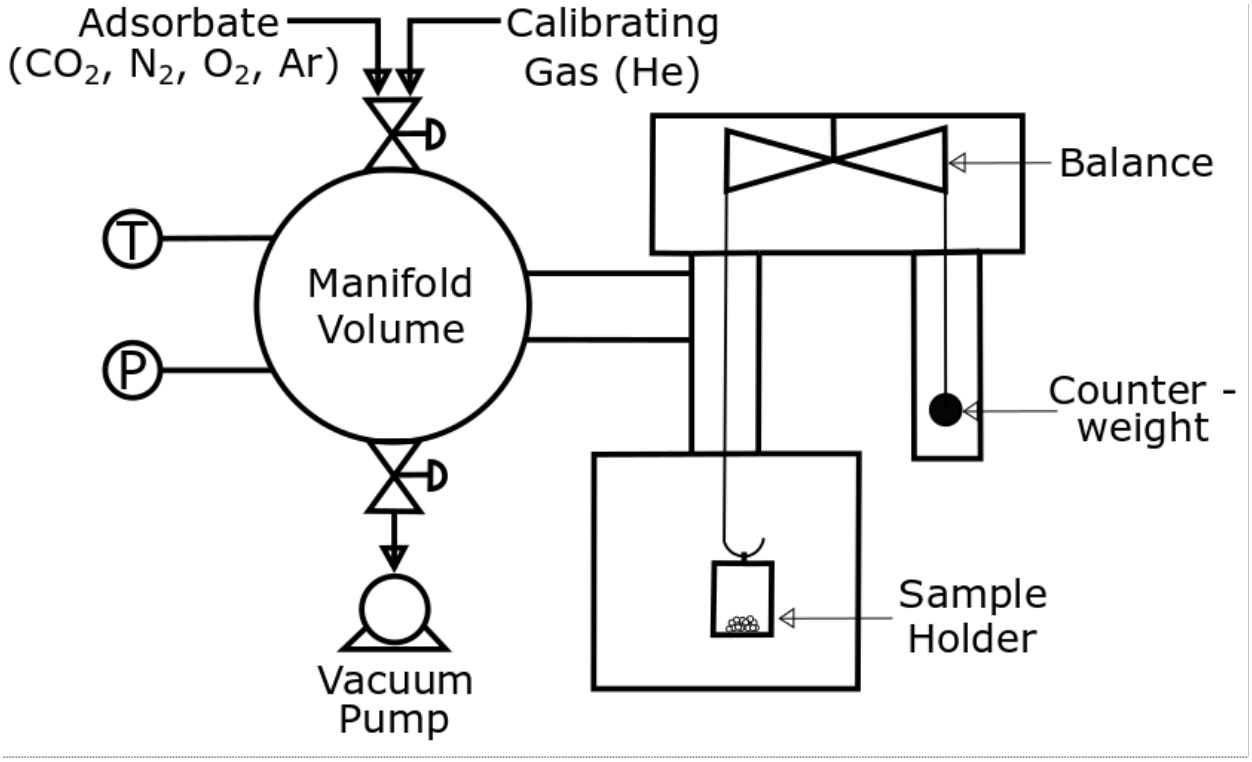

Figure AI.1 – Process flow diagram of the VTI Scientific Instruments GHP gravimetric system that is used in this study.

AI.2. Equations for the Langmuir, Freundlich, Sips, Toth, and TD-Toth models and Ideal Selectivities

The isotherms can be fitted to the Langmuir, Freundlich, Sips, and Toth models using the sum of least squares method. The isotherm model with the highest coefficient of determination (R^2) can then be used to reflect the isotherm. These models can then be used to analyse the ideal selectivity (A) between the different adsorbates.

The ideal selectivity for an adsorbent is the pure gas adsorption capacity of one species (q_A) over the other (q_B) (Equation AI.1). However, for air having 780840 ppm of N_2, 20960 ppm of O_2, and 9300 ppm of Ar to 400 ppm of CO_2, the selectivity is modeled as the quotient of CO_2 pure gas adsorption capacity with a relative partital pressure of 400 ppm over the summation of the pure gas adsorption capacity for N_2, O_2, and Ar with their relative partial pressures (Equation AI.2).

$$\boldsymbol{Ideal\ Selectivity} = {}^{\boldsymbol{q_A}}/_{\boldsymbol{q_B}} \quad \text{[AI.1]}$$

$$\boldsymbol{CO_2\ Selectivity} = {}^{\boldsymbol{q_{CO2}}}/_{\boldsymbol{q_{N2} + q_{O2} + q_{Ar}}} \quad \text{[AI.2]}$$

Table AI.1 – Langmuir, Freundlich, Sips, and Toth adsorption isotherm models.

Langmuir Model	Freundlich Model	Sips Model	Toth Model
$\frac{q_e}{q_s} = \frac{\beta P}{1+\beta P}$	$q_e = k\,P^{\,1/n}$	$\frac{q_e}{q_s} = \frac{(\beta P)^n}{1+(\beta P)^n}$	$\frac{q_e}{q_s} = \frac{\beta P}{(1+(\beta P)^t)^{1/t}}$

In order to determine the adsorption equilibrium capacity over a wide range of temperatures, the empirical temperature dependent Toth (TD-Toth) model relates temperature dependence to the individual parameters q_S (Equation AI.3), β (Equation AI.4), and t (Equation AI.5). This model correlates the q_S, β, and t to q_{S0}, X, β_0 Q, t_0 and a. All these parameters are fitted to the adsorption equilibrium data at different temperatures for a reference temperature of T_O.

$$\boldsymbol{q_s = q_{s0} exp\left[X(1-\frac{T}{T_0})\right]} \quad \text{[AI.3]}$$

$$\boldsymbol{\beta = \beta_0 \exp\left[\frac{Q}{RT_0}(\frac{T_0}{T}-1)\right]} \quad \text{[AI.4]}$$

$$\boldsymbol{\tau = \tau_0 + a\left(1-\frac{T_0}{T}\right)} \quad \text{[AI.5]}$$

AI.3. Linear Driving Force

The rate of adsorption into an adsorbent particle of a single adsorbate for the Linear Driving Force model is given in Equation AI.6 where $\bar{q}(t)$ is the average concentration of the adsorbate in the adsorbent particle at time t, $\bar{q}^*(t)$ is the concentration of the adsorbate in the adsorbent particle at equilibrium with the gas phase partial pressure, and k_L is the effective Linear Driving Force mass transfer coefficient at a particular adsorbent loading and temperature.

$$\boldsymbol{\frac{d\bar{q}(t)}{dt} = k_L[\bar{q}^*(t) - \bar{q}(t)]} \quad \text{[AI.6]}$$

For a constant pressure experiment such as those done with gravimetric adsorption systems, this can be simplified to Equation AI.7 with $\bar{q}^0$ and q^∞being the equilibrium concentration in the adsorbent at the start and finish of the concentration change, respectively. The derivation from Equation AI.6 to Equation AI.7 is explained in detail in the literature [1].

$$\boldsymbol{\frac{\bar{q}(t) - \bar{q}^0}{\bar{q}^\infty - \bar{q}^0} = 1 - e^{-k_L t}} \quad \text{[AI.7]}$$

AI.4. Schematic Diagram of the Breakthrough Setup

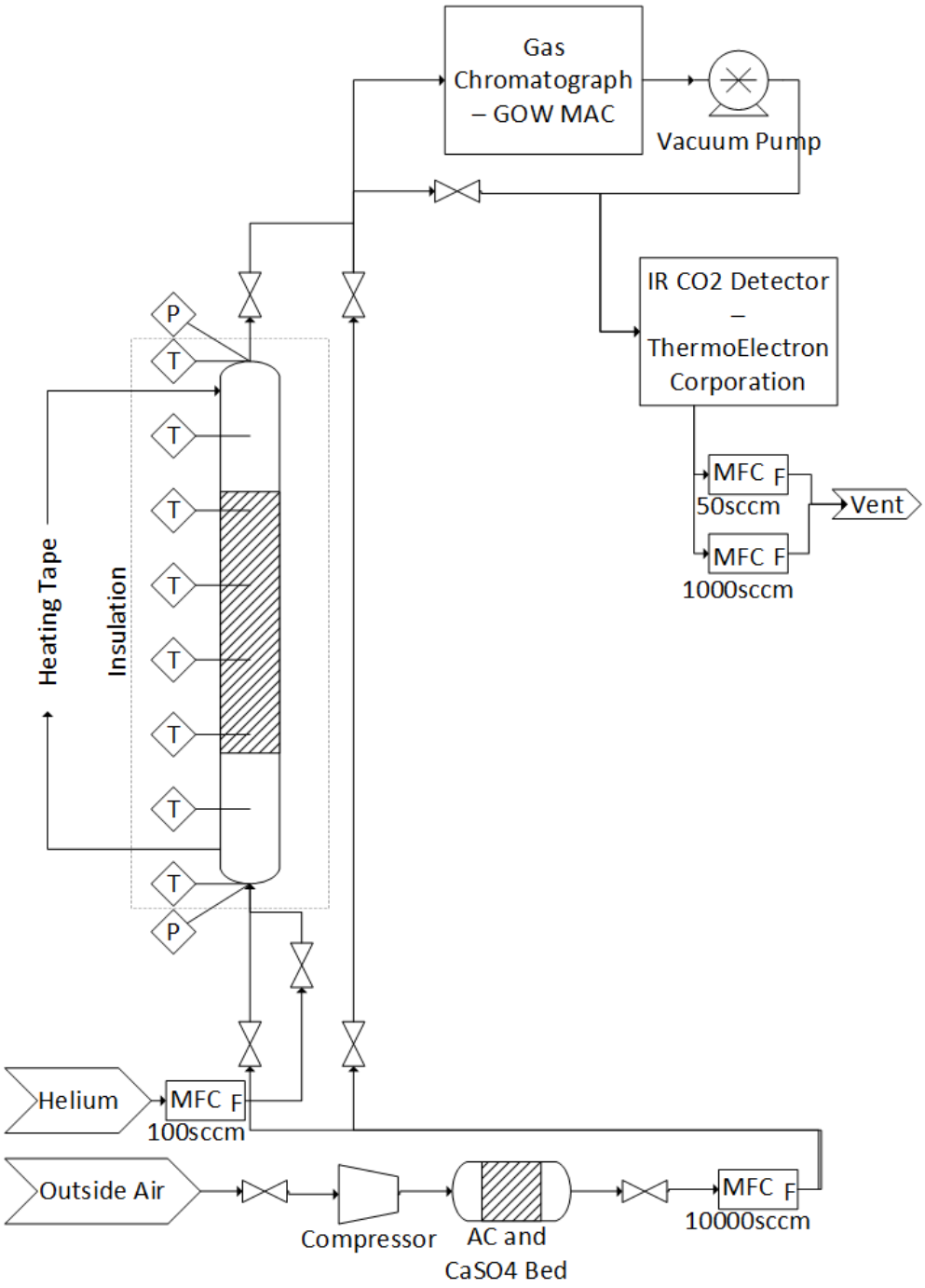

Figure AI.2 - A schematic diagram of the breakthrough setup.

AI.5. Isotherm Data Points

Table AI.2 – Isotherm data points for G5CO2M for CO_2, N_2, O_2, and Ar at 22°C.

Carbon Dioxide		Nitrogen		Oxygen		Argon	
Pressure	q	Pressure	q	Pressure	q	Pressure	q
Atm	mmol/g	Atm	mmol/g	Atm	mmol/g	Atm	mmol/g
0.0000	0.0000	0.0000	0.0000	0.0000	0.0000	0.0000	0.0000
0.0666	3.1292	0.0640	0.0925	0.0136	0.0020	0.0135	0.0062
0.1348	3.7144	0.1345	0.1303	0.0676	0.0081	0.0676	0.0142
0.2022	4.0178	0.2026	0.1617	0.1351	0.0156	0.1350	0.0223
0.4011	4.4697	0.4030	0.2403	0.2026	0.0232	0.2021	0.0294
0.7933	4.8569	0.7937	0.3749	0.3938	0.0443	0.4029	0.0493
1.5312	5.1675	1.5346	0.5880	0.7717	0.0850	0.7886	0.0856
6.3710	5.7249	6.3839	1.4289	1.5313	0.1647	1.5333	0.1526
1.5806	5.2016	1.5686	0.5984	6.3752	0.6221	6.3814	0.5898
0.3996	4.4977	0.4009	0.2515	1.5752	0.1709	1.5759	0.1557
				0.4047	0.0469	0.4027	0.0519

Table AI.3 – Isotherm data points for Z10-01 for CO_2, N_2, O_2, and Ar at 22°C.

Carbon Dioxide		Nitrogen		Oxygen		Argon	
Pressure	q	Pressure	q	Pressure	q	Pressure	q
Atm	mmol/g	Atm	mmol/g	Atm	mmol/g	Atm	mmol/g
0.0000	0.0000	0.0000	0.0000	0.0000	0.0000	0.0000	0.0000
0.0660	3.0542	0.0638	0.0817	0.0136	0.0028	0.0136	0.0033
0.1348	3.4986	0.1352	0.1209	0.0676	0.0092	0.0676	0.0105
0.2021	3.7402	0.2025	0.1530	0.1350	0.0171	0.1352	0.0186
0.4014	4.1194	0.4028	0.2346	0.2026	0.0251	0.2028	0.0260
0.7910	4.4577	0.7892	0.3724	0.3933	0.0471	0.4023	0.0469
1.5315	4.7447	1.5352	0.5946	0.7724	0.0894	0.7866	0.0852
6.3775	5.2800	6.3809	1.4441	1.5328	0.1720	1.5326	0.1572
1.5731	4.7682	1.5676	0.6057	6.3751	0.6428	6.3853	0.5941
0.3987	4.1374	0.4085	0.2492	1.5773	0.1788	1.5748	0.1612
				0.4034	0.0496	0.4079	0.0499

Table AI.4 – Isotherm data points for APG-III for CO_2, N_2, O_2, and Ar at 22°C.

Carbon Dioxide		Nitrogen		Oxygen		Argon	
Pressure	q	Pressure	q	Pressure	q	Pressure	q
Atm	mmol/g	Atm	mmol/g	Atm	mmol/g	Atm	mmol/g
0.0000	0.0000	0.0000	0.0000	0.0000	0.0000	0.0000	0.0000
0.0663	3.4423	0.0649	0.0354	0.0136	0.0037	0.0136	0.0027
0.1348	3.9493	0.1350	0.0691	0.0676	0.0109	0.0676	0.0090
0.2016	4.2113	0.2024	0.1001	0.1349	0.0191	0.1350	0.0164
0.4024	4.6250	0.4033	0.1860	0.2024	0.0279	0.2027	0.0237
0.7879	4.9835	0.7943	0.3365	0.3954	0.0507	0.4033	0.0446
1.5328	5.2889	1.5346	0.5773	0.7741	0.0932	0.7899	0.0841
6.3731	5.8399	6.3837	1.5240	1.5323	0.1763	1.5316	0.1583
1.5787	5.3120	1.5692	0.5839	6.3747	0.6671	6.3893	0.6149
0.4055	4.6391	0.4082	0.1893	1.5798	0.1793	1.5820	0.1588
				0.4054	0.0538	0.4075	0.0459

Table AI.5 – Isotherm data points for Ca-X for CO_2, N_2, O_2, and Ar at 22°C.

Carbon Dioxide		Nitrogen		Oxygen		Argon	
Pressure	q	Pressure	q	Pressure	q	Pressure	q
Atm	mmol/g	Atm	mmol/g	Atm	mmol/g	Atm	mmol/g
0.0000	0.0000	0.0000	0.0000	0.0000	0.0000	0.0000	0.0000
0.0667	3.0163	0.0676	0.2138	0.0136	0.0036	0.0135	0.0055
0.1348	3.7049	0.1350	0.3515	0.0676	0.0193	0.0676	0.0169
0.2022	4.0948	0.2025	0.4515	0.1351	0.0375	0.1350	0.0307
0.4025	4.6916	0.4033	0.6435	0.2025	0.0555	0.2019	0.0434
0.7953	5.1830	0.7865	0.8445	0.3944	0.1034	0.4033	0.0798
1.5330	5.5590	1.5358	1.0572	0.7748	0.1900	0.7893	0.1447
6.3808	6.1827	6.3827	1.6870	1.5301	0.3386	1.5356	0.2610
1.5753	5.5818	1.5700	1.0607	6.3766	0.9929	6.3785	0.8609
0.3995	4.7013	0.4068	0.6452	1.5767	0.3450	1.5730	0.2649
				0.4054	0.1080	0.4013	0.0803

Table AI.6 – Isotherm data points for NaLSX for CO_2, N_2, O_2, and Ar at 22°C.

Carbon Dioxide		Nitrogen		Oxygen		Argon	
Pressure	q	Pressure	q	Pressure	q	Pressure	q
Atm	mmol/g	Atm	mmol/g	Atm	mmol/g	Atm	mmol/g
0.0000	0.0000	0.0000	0.0000	0.0000	0.0000	0.0000	0.0000
0.0663	3.3757	0.0639	0.0513	0.0136	0.0027	0.0136	0.0037
0.1349	3.8454	0.1351	0.0854	0.0676	0.0090	0.0676	0.0101
0.2017	4.0889	0.2023	0.1153	0.1350	0.0163	0.1352	0.0176
0.4022	4.4738	0.4033	0.1937	0.2026	0.0236	0.2025	0.0243
0.7893	4.8094	0.7858	0.3269	0.3933	0.0440	0.4024	0.0437
1.5327	5.0929	1.5368	0.5497	0.7722	0.0832	0.7908	0.0801
6.3741	5.6067	6.3830	1.4193	1.5314	0.1605	1.5408	0.1494
1.5800	5.1147	1.5672	0.5593	6.3748	0.6131	6.3871	0.5796
0.3993	4.4809	0.4012	0.2022	1.5785	0.1656	1.5779	0.1518
				0.4042	0.0461	0.4024	0.0454

Table AI.7 – Isotherm data points for Z10-02ND for CO_2, N_2, O_2, and Ar at 22°C.

Carbon Dioxide		Nitrogen		Oxygen		Argon	
Pressure	q	Pressure	q	Pressure	q	Pressure	q
Atm	mmol/g	Atm	mmol/g	Atm	mmol/g	Atm	mmol/g
0.0000	0.0000	0.0000	0.0000	0.0000	0.0000	0.0000	0.0000
0.0665	3.6218	0.0675	0.0332	0.0136	0.0053	0.0136	0.0047
0.1348	4.1454	0.1350	0.0658	0.0676	0.0132	0.0676	0.0119
0.2024	4.4276	0.1929	0.0929	0.1351	0.0222	0.1350	0.0198
0.4024	4.8636	0.4036	0.1871	0.2025	0.0308	0.2026	0.0272
0.7954	5.2454	0.7925	0.3436	0.3943	0.0546	0.3889	0.0467
1.5331	5.5588	1.5349	0.5960	0.7763	0.1004	0.7875	0.0861
6.3747	6.1302	6.3842	1.5765	1.5305	0.1886	1.5405	0.1601
1.5812	5.5813	1.5733	0.6041	6.3739	0.7090	6.3821	0.6402
0.3990	4.8679	0.4070	0.1885	1.5756	0.1925	1.5772	0.1618
				0.3980	0.0577	0.4084	0.0505

Table AI.8 – Isotherm data points for Na-X Hengye HP for CO_2, N_2, O_2, and Ar at 22°C.

Carbon Dioxide		Nitrogen		Oxygen		Argon	
Pressure	q	Pressure	q	Pressure	q	Pressure	q
Atm	mmol/g	Atm	mmol/g	Atm	mmol/g	Atm	mmol/g
0.0000	0.0000	0.0000	0.0000	0.0000	0.0000	0.0000	0.0000
0.0667	3.2584	0.0640	0.0480	0.0136	0.0027	0.0136	0.0036
0.1348	3.8476	0.1350	0.0854	0.0676	0.0093	0.0676	0.0107
0.2023	4.1673	0.2025	0.1185	0.1352	0.0179	0.1352	0.0188
0.4028	4.6516	0.4018	0.2040	0.2024	0.0263	0.2026	0.0267
0.7920	5.0585	0.7879	0.3501	0.3935	0.0500	0.3896	0.0475
1.5330	5.3875	1.5331	0.5849	0.7713	0.0956	0.7848	0.0903
6.3720	5.9739	6.3830	1.4888	1.5325	0.1852	1.5354	0.1683
1.5798	5.4240	1.5662	0.5938	6.3758	0.6957	6.3910	0.6503
0.4061	4.6923	0.4008	0.2109	1.5769	0.1906	1.5721	0.1708
				0.4056	0.0523	0.4023	0.0504

AI.6. Adsorption Isotherm Model Parameters

Table AI.9 – Adsorption isotherm model parameters for the adsorbents tested in this study at 22°C. Associated equations are given in **Table AI.1 and Equations AI.3-AI.5.**

		Langmuir		Freundlich		Sips			Toth		
		q_m mmol/g	B Atm^{-1}	k mmol/g•atm	a	q_m mmol/g	B Atm^{-1}	a	q_m mmol/g	B Atm^{-1}	t
G5CO2M	CO_2	5.39	16.90	4.78	8.43	6.32	14.93	0.490	6.48	201.82	0.410
	N_2	2.34	0.24	0.444	1.58	209.67	6.01E-05	0.633	1398647	2.16E-04	0.068
	O_2	4.90	0.023	0.109	1.06	7.16	0.014	0.979	13.05	8.7E-03	0.731
	Ar	4.11	0.026	0.107	1.09	96.57	6.28E-04	0.923	34969	4.17E-06	0.215
Z10-01	CO_2	4.92	19.43	4.43	8.98	6.15	14.83	0.393	6.42	1202	0.310
	N_2	2.40	0.234	0.440	1.56	14.13	6.36E-03	0.678	4581	3.56E-03	0.116
	O_2	4.52	0.026	0.115	1.07	10.87	8.72E-03	0.958	51.77	2.4E-03	0.513
	Ar	4.02	0.027	0.107	1.08	216.59	2.68E-04	0.926	34969	4.17E-06	0.215
APG-III	CO_2	4.98	44.83	5.20	6.42	6.30	23.01	0.473	6.72	636	0.356
	N_2	2.90	0.157	0.386	1.12	2.83	0.162	1.003	2.54	0.178	1.07
	O_2	4.82	0.025	0.119	1.07	74.30	1.02E-03	0.934	79172	1.99E-06	0.212
	Ar	4.43	0.025	0.108	1.07	5.29	0.020	0.988	10.76	0.011	0.743
Ca-X	CO_2	5.88	12.78	5.03	7.25	6.73	10.57	0.570	6.88	64.68	0.486
	N_2	1.80	1.270	0.856	2.64	2.79	0.309	0.606	4.18	3.65	0.331
	O_2	2.45	0.106	0.231	1.27	3.11	0.070	0.941	6.15	0.049	0.605
	Ar	2.95	0.064	0.178	1.18	7.84	0.015	0.898	2149.45	1.57E-04	0.218
Na-LSX	CO_2	5.25	21.70	4.77	9.70	6.39	20.36	0.402	6.60	1166.34	0.325
	N_2	2.68	0.176	0.389	1.43	5.31	0.045	0.813	49.82	0.024	0.278
	O_2	5.18	0.021	0.107	1.06	23.09	3.60E-03	0.954	86.05	1.34E-03	0.494
	Ar	5.35	0.019	0.101	1.06	440.19	1.39E-04	0.944	235.16	4.67E-04	0.424
Z10-02ND	CO_2	5.74	20.46	5.19	9.37	6.96	18.61	0.416	7.19	803.27	0.338
	N_2	3.24	0.148	0.403	1.35	3.49	0.128	0.971	4.12	0.124	0.827
	O_2	4.73	0.028	0.128	1.08	324.40	2.08E-04	0.925	5159	3.15E-05	0.264
	Ar	8.22	0.013	0.109	1.04	329.88	2.30E-04	0.957	101262	1.23E-06	0.247
Na-X HP	CO_2	5.62	16.63	4.98	8.34	6.63	14.32	0.484	6.81	211.7571	0.403
	N_2	2.76	0.183	0.411	1.44	4.40	0.071	0.847	14.85	0.059	0.393
	O_2	5.21	0.024	0.123	1.07	8.69	0.013	0.972	34.08	3.86E-03	0.583
	Ar	5.59	0.021	0.114	1.06	71.10	1.10E-03	0.945	212.37	5.86E-04	0.430

AI.7. Heat of Adsorption

In order to determine the isosteric heat of adsorption value for CO_2 on APG-III, multiple isotherms were measured at 22C, 50C, 80C, and 110C and each fitted to the Langmuir model. The isosteric heat of adsorption was calculated using the van't Hoff plot from the results of multiple isotherms at different temperatures. Using the Langmuir isotherm model, when pressure approaches zero, the denominator of the Langmuir equation approaches unity and the Henry's Law constant, K, is given by the product of q_m and β. These Langmuir coefficients for CO_2 are shown in Table AI.10 for APG-III.

Table AI.10 – Langmuir Isotherm parameters for APG-III

		Langmuir	
		q_m mmol/g	β Atm^{-1}
APG-III	22°C	4.98	44.83
	50°C	4.50	18.92
	80°C	4.01	6.69
	110°C	3.64	3.51

After the calculation of Henry's Law constant at different temperatures, heat of adsorption was calculated from the slope of ln(K) versus (1/T) plot according to Equation AI.8.

$$\boldsymbol{lnK = -\frac{\Delta H_0}{R}\frac{1}{T} + lnK_0} \qquad \text{[AI.8]}$$

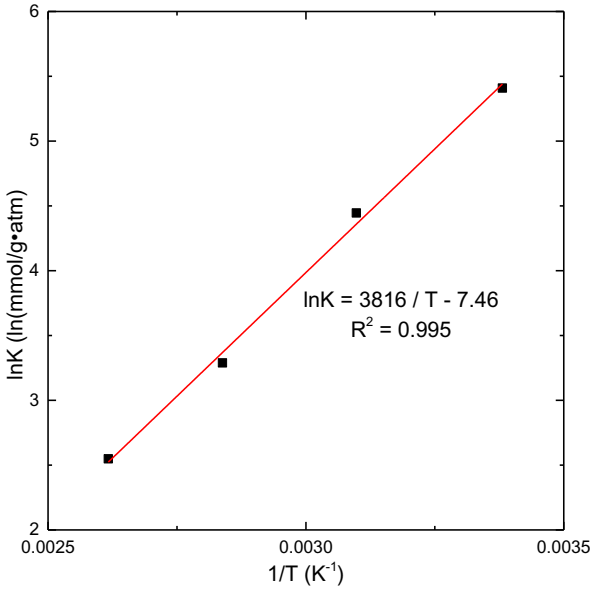

Figure AI.3 – van't Hoff plot for APG-III using Langmuir coefficients to determine the Henry's Law constant at temperatures 22°C, 50°C, 80°C, and 110°C.

From the slope of the van't Hoff plot given in Figure AI.3, the calculated CO_2 limited heat of adsorption is determined to be - 31.7 ± 1.3 kJ/mol according to Equation AI.8. This heat of adsorption was used in the calculation of the energy required for desorption. It was kept constant but due to the adsorption occurring at very low concentrations.

AI.8. Uptake Rate Graphs

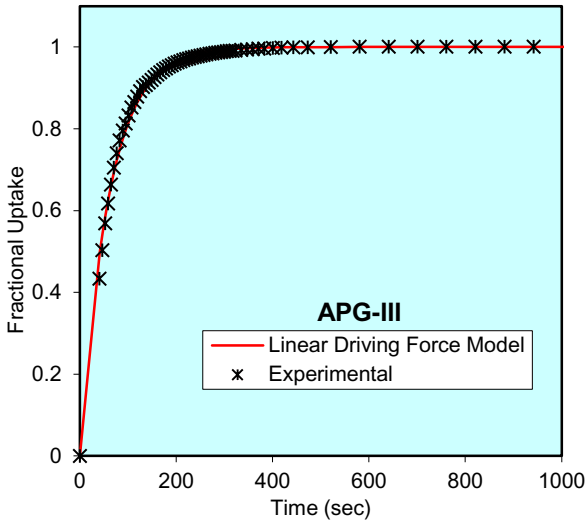

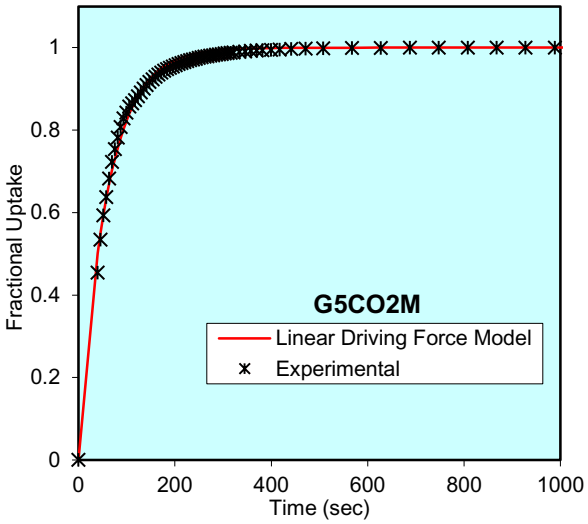

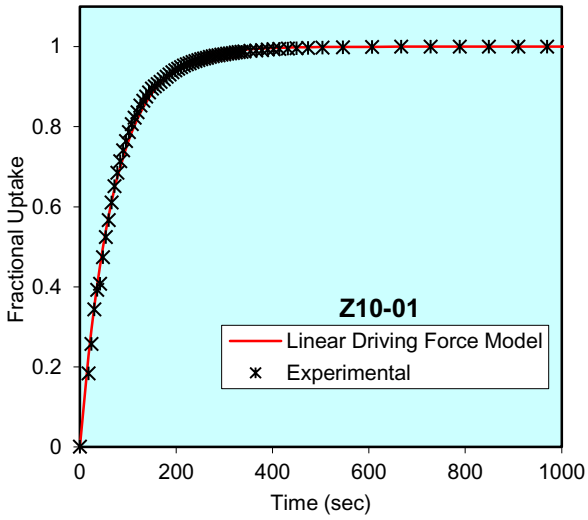

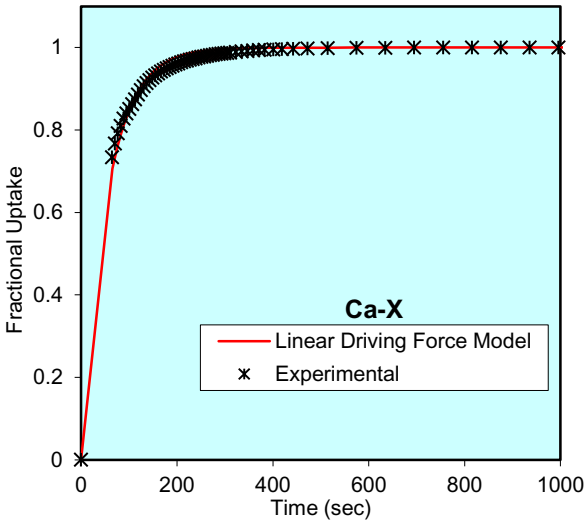

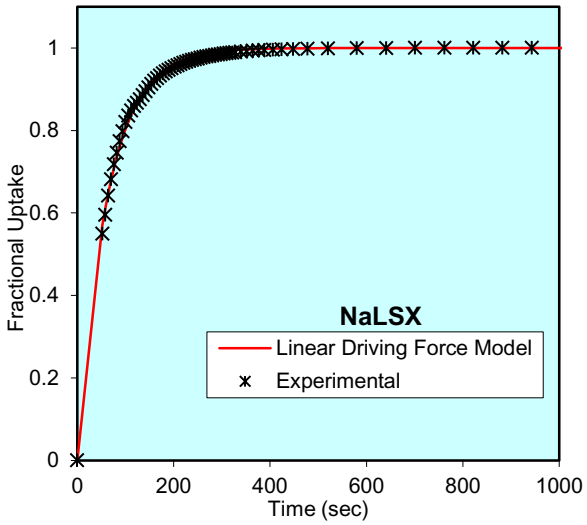

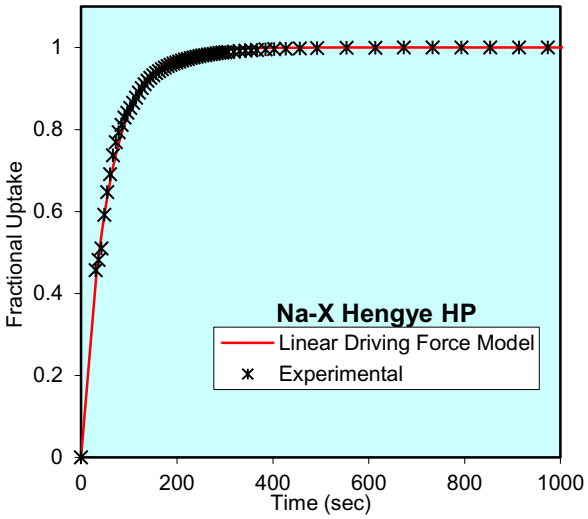

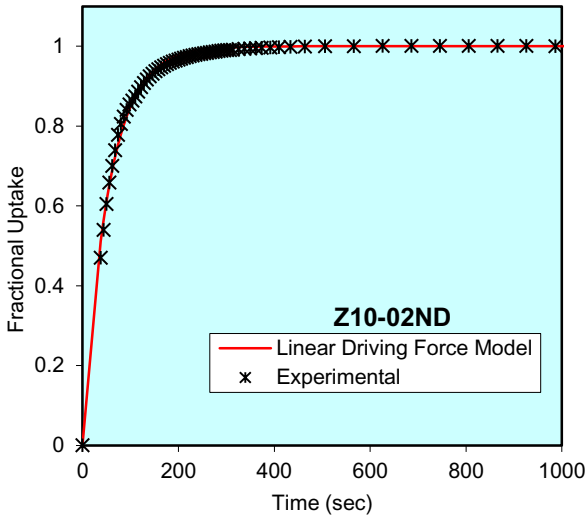

Figure AI.4 - Adsorption rates for zeolites for the adsorbents tested in this study using pure CO_2, upon a step change in CO_2 pressure from vacuum to 0.067 atm at 22°C. Due to pressure shock, only stable pressure points were used. The LDF model was used to model the fractional uptake rates.

AI.9. Equation For Gas Hourly Space Velocities (GHSV)

The gas hourly space velocities (GHVS's) is a measure of the flow of air during the adsorption portion of the cycle and were calculated using Equation AI.9. $\dot{V}$ is the standard volumetric flow rate, ε_B is the bed void fraction, and V is the volume of the column.

$$GHSV = \frac{\dot{V}}{\varepsilon_B V} \qquad [AI.9]$$

AI.10. Adsorption and Desorption Temperature Profiles

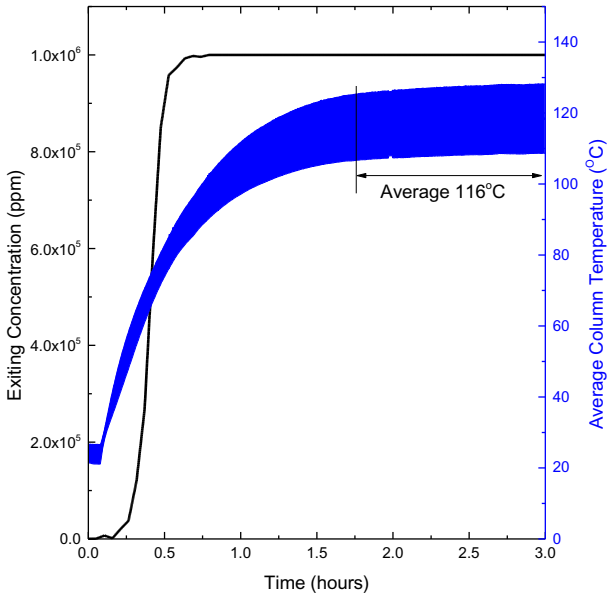

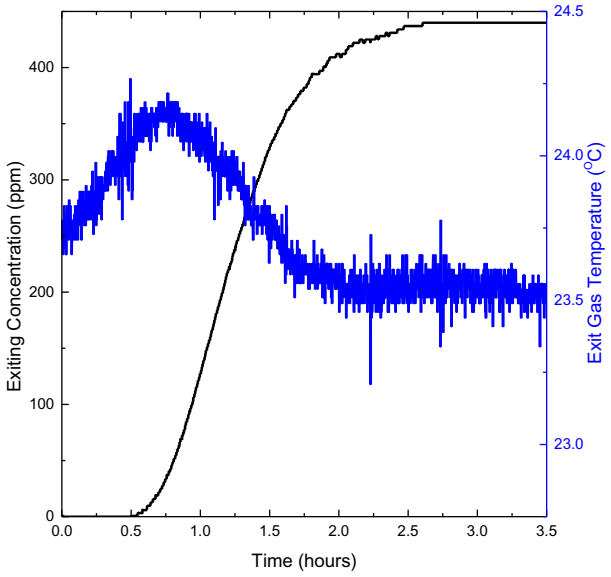

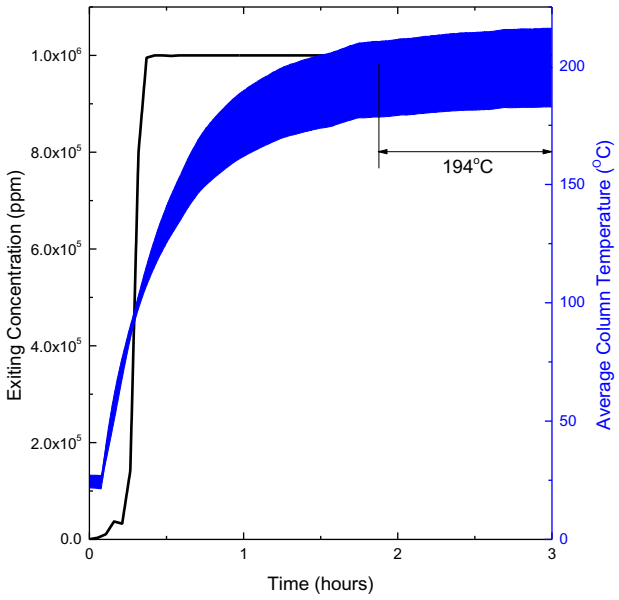

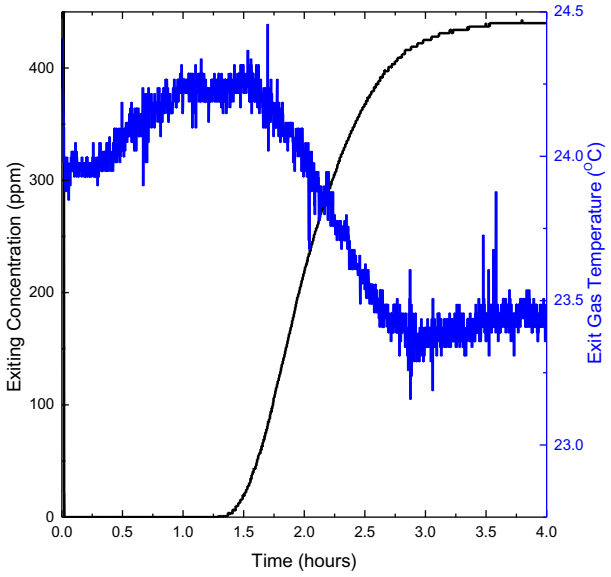

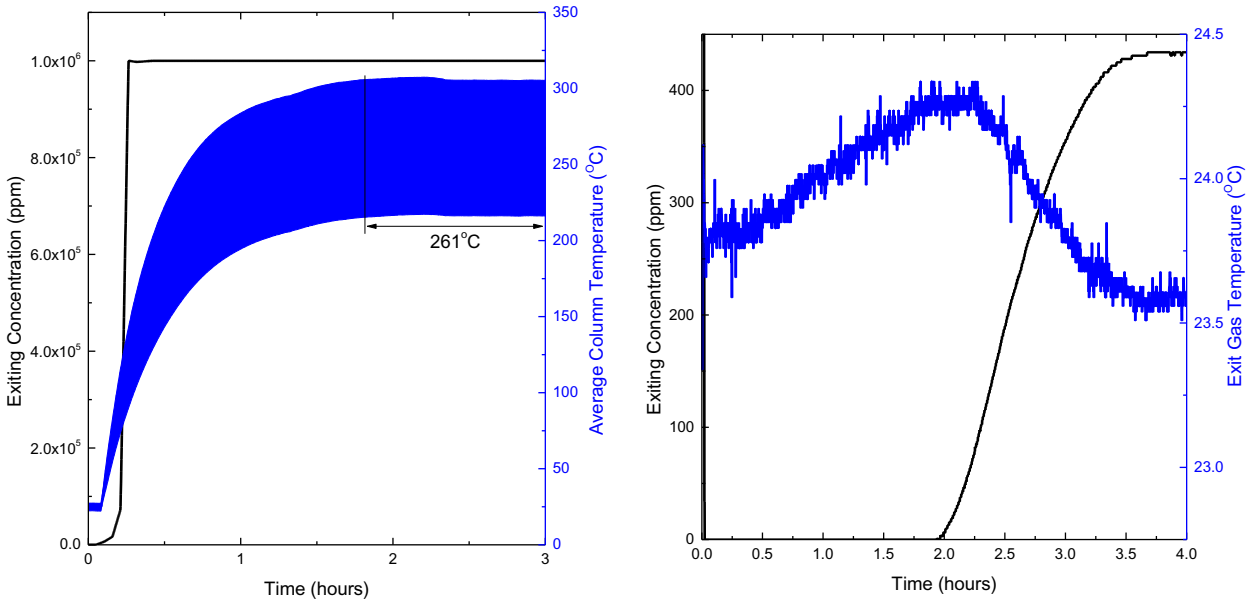

Figure AI.5 – Exit concentration and temperatures as a function of time for the 116°C, 194°C, and the 261°C regeneration runs along with the coupled following adsorption showing the exit gas temperature and the exiting concentrations as a function of time.

AI.11. Breakthrough Adsorption and Desorption Capacities

For the adsorption capacity, the area underneath the input concentration of CO_2 and above the exiting concentration of CO_2 was integrated using Simpson's 3/8ths rule. The cumulative amount of CO_2 calculated using the input flow rate was then divided using the mass of the sample within the adsorption column. For the desorption capacity, knowing the exiting flow rate and concentration, the cumulative amount of CO_2 was calculated and was then divided by the mass of the sample within the adsorption column.

AI.12. Water Energy Requirements Calculation

In order to calculate the MJ/ton of CO_2 captured at varying temperatures and humidities, one experimental CO_2 adsorption run was used at 23.5°C and 431ppm of CO_2 in the air, flow of 13400 h^{-1},with a regeneration temperature of 194°C, an adsorption capacity of 0.33mmol/g, an a_A of 72%, and an a_Δ of 97%. The amount of water in the air was calculated using an empirical formula by Buck (1981) which has a significantly accurate calculation for the amount of water in the air for temperatures between -80°C and 50°C [2]. This formula is shown in Equation AI.10. After calculating the quantity of water in the air, water adsorption capacities for 3A and silica gel were calculated at different temperatures and partial pressures using the TD-Toth equations presented in Equations AI.3, AI.4, and AI.5. The TD-Toth parameters for 3A and silica gel for the temperature range of -45°C to 175°C were acquired from literature [3]. No multi-temperature water adsorption capacity data was found for 3A for temperature ranges of -20°C to 35°C, so data for 5A was used instead which has been shown to have very similar water adsorption properties [4].

This information along with using the properties listed within the article was then used to calculate the energy required per ton of CO_2 captured.

$$e'_w = \left(\mathbf{1.0007} + (\mathbf{3.46} \times \mathbf{10^{-6}} P)\right) \times \mathbf{6.1121} \exp\left(\frac{\mathbf{17.502} T}{\mathbf{240.97} + T}\right) \quad \text{[AI.10]}$$

AI.13. References

1. Sircar, S. & Hufton, J. R. Why Does the Linear Driving Force Model for Adsorption Kinetics Work? *Adsorption* **6,** 137–147 (2000).

2. Buck, A. L. New Equations for Computing Vapor Pressure and Enhancement Factor. *Journal of Applied Meteorology* **20,** 1527–1532 (1981).

3. Wang, Y. & LeVan, M. D. Adsorption Equilibrium of Binary Mixtures of Carbon Dioxide and Water Vapor on Zeolites 5A and 13X. *J. Chem. Eng. Data* **55,** 3189–3195 (2010).

4. Lalik, E., Mirek, R., Rakoczy, J. & Groszek, A. Microcalorimetric Study of Sorption of Water and Ethanol in Zeolites 3A and 5A. *Catal. Today* **114,** 242–247 (2006).

Appendix II

Supporting Information

for

"High Purity CO_2 from Direct Air Capture using a Single Cycle TVSA with Na-X Zeolites"

Sean M.W. Wilson, and F. Handan Tezel

Department of Chemical and Biological Engineering, University of Ottawa, 161 Louis-Pasteur, Ottawa, Ontario K1N 6N5 Canada

To be submitted: Industrial & Engineering Chemistry Research 2020

Contents

AII.1. Adsorbent Material Information

Table AII.1 – Commercially available faujasite structured zeolite sample used in this study with its respective manufacturer, trademark name, structure and cation.

Manufacturer	Name	Structure	Ion*	SiO_2/Al_2O_3†	US MESH Size	Comments
Honeywell UOP	APG-III	Type X	Na	2.74	8×12	Air prepurification

*Major cation component in the crystalline structure (full data included in Table SI.2)
†SiO_2/Al_2O_3 ratios were calculated from data included in Table SI.2

Table AII.2 – Chemical composition of faujasite structured zeolites used in this study in atomic percentages for cations within the lattice structure of the zeolite. The balance would be oxygen.

	Cation					Lattice Structure	
Adsorbent	Na^+	K^+	Mg^{2+}	Ca^{2+}	Fe^{2+}	Si^{4-}	Al^{3-}
APG-III	11.12	0.083	1.005	0.360	0.275	16.55	12.07

AII.2. Schematic Diagram of the Gravimetric System

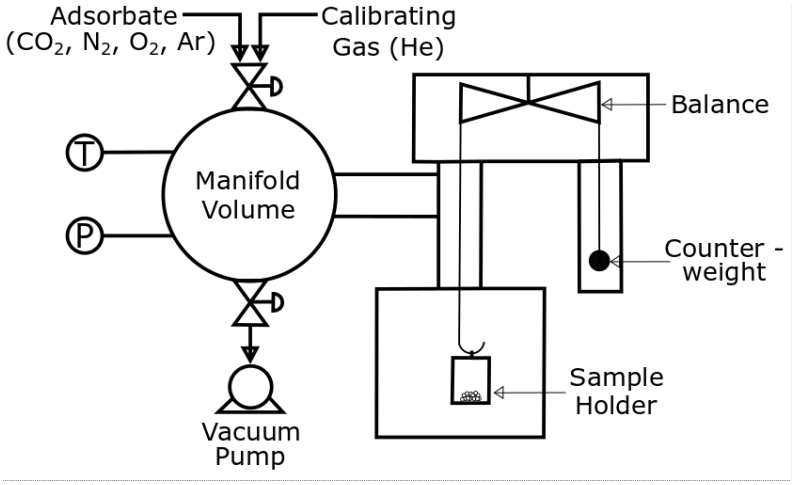

Figure AII.1 – Process flow diagram of the VTI Scientific Instruments GHP micro-gravimetric system that is used in this study.

AII.3. Langmuir, Freundlich, Sips, Toth, and TD-Toth models

Table AII.3 – Langmuir, Freundlich, Sips, and Toth adsorption isotherm models.

Langmuir Model	Freundlich Model	Sips Model	Toth Model
$\frac{q_e}{q_s} = \frac{\beta P}{1+\beta P}$	$q_e = k\,P^{\,1/n}$	$\frac{q_e}{q_s} = \frac{(\beta P)^n}{1+(\beta P)^n}$	$\frac{q_e}{q_s} = \frac{\beta P}{(1+(\beta P)^t)^{1/t}}$

In order to determine the adsorption capacity between isothermal data points and temperatures, the empirical temperature dependant Toth (TD-Toth) model was used. This turns the Toth parameters q_s, β, and t into temperature dependant variables using the relations given in Table AII.4. In this study, the TD-Toth

model allowed the determination of the adsorption equilibrium capacity at different temperatures from 10°C to 90°C and at different pressures from 0 atm to 6.5 atm.

Table AII.4 – The empirical TD-Toth model equation parameters. These parameters are substituted into the Toth model included in Table AII.3.

$$q_s = q_{s0} exp\left[X\left(1 - \frac{T}{T_0}\right)\right] \qquad \beta = \beta_0 \exp\left[\frac{Q}{RT_0}\left(\frac{T_0}{T} - 1\right)\right] \qquad t = t_0 + \alpha\left(1 - \frac{T_0}{T}\right)$$

AII.4. Schematic Diagram of the Breakthrough Setup

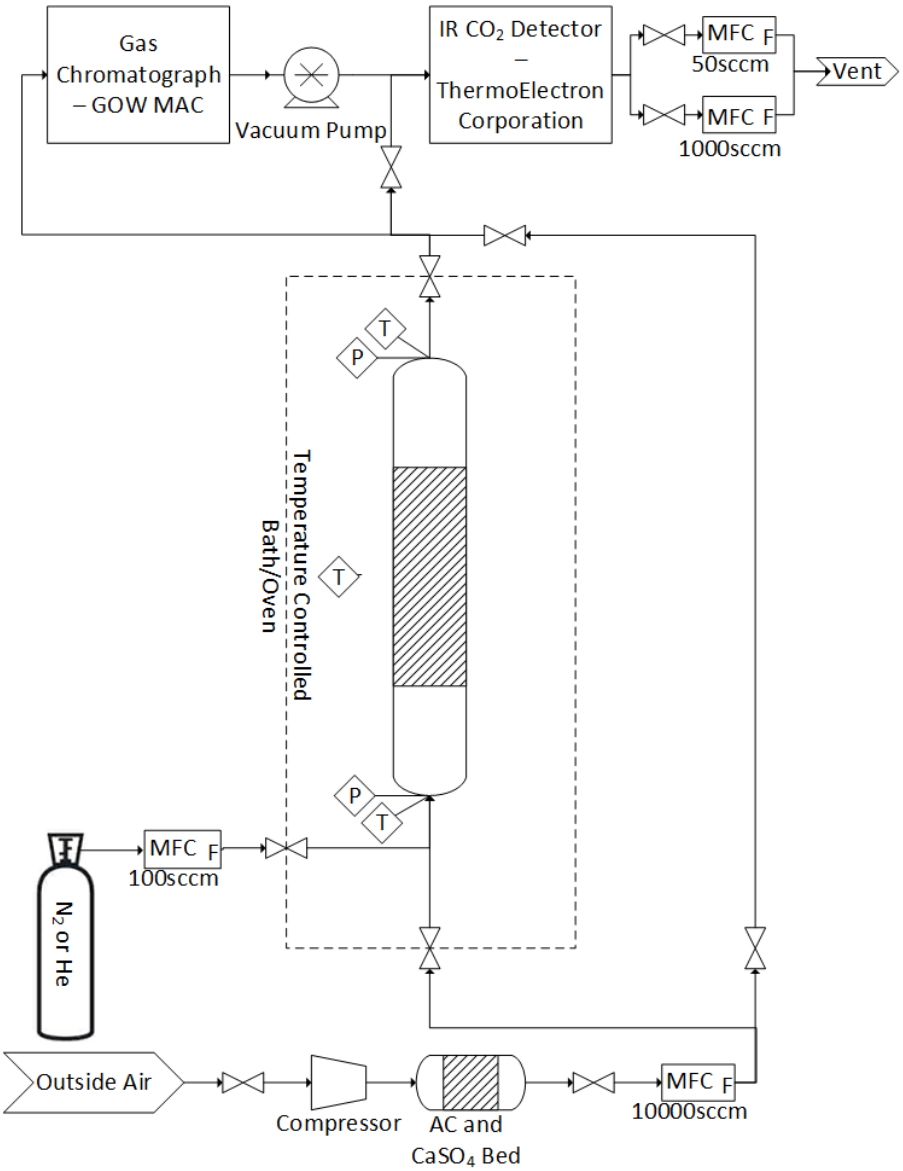

Figure AII.2 – The schematic diagram of the breakthrough setup used in this study. The column was either placed within a temperature controlled oven or a temperature controlled bath to keep the temperature constant.

Table AII.5 - Column properties and operating conditions for adsorption-desorption breakthrough curves used in this study.

Parameter	Value
Column Properties	
Column length, L	30 cm
Inner column diameter, D_{in}	1.09 cm
Outer column diameter, D_{out}	1.27 cm
Volume of column, V_c	28.1 cm^3
Void fraction, ε	0.4
Adsorption Step Conditions for Case Study	
Total feed volumetric flow rate, Q	10000 sccm
Average column pressure, P	1.25 atm
Average temperature, T	20.0°C
Feed Concentration	
CO_2 feed concentration, y_{CO2}	409 – 441 ppm
N_2 feed concentration, y_{N2}	78.1%
O_2 feed concentration, y_{O2}	20.9%
Ar feed concentration, y_{Ar}	0.93%
Evacuation Step Conditions	
Duration, t_E	120 minutes
Temperature, T_E	200°C

AII.5. Isotherm Data Points

Table AII.6 – Isotherm data points for APG-III for CO_2 at 22°C, 50°C, 80°C, and 110°C.

22.6 ± 0.1°C		49.7 ± 0.1°C		79.2 ± 2.8°C		109.0 ± 3.5°C	
Pressure	**q**	**Pressure**	**q**	**Pressure**	**q**	**Pressure**	**q**
Atm	**mmol/g**	**Atm**	**mmol/g**	**Atm**	**mmol/g**	**Atm**	**mmol/g**
0	0	0	0	0	0	0	0
0.0132	2.2805	0.0133	1.5451	0.0139	0.7564	0.0136	0.3592
0.0673	3.4727	0.0636	2.4013	0.0674	1.4833	0.0672	0.9139
0.1349	3.9827	0.1348	2.9959	0.1346	1.8468	0.1357	1.2416
0.2021	4.2455	0.2022	3.3288	0.2020	2.1407	0.2026	1.4588
0.4021	4.6577	0.4027	3.8372	0.4034	2.6999	0.4064	1.9541
0.7928	5.0180	0.7893	4.2966	0.8334	3.3553	0.8193	2.6061
1.5303	5.3199	1.5387	4.6905	1.5335	3.8764	1.5351	3.2314
6.3715	5.8705	6.3657	5.4213	6.3750	5.1969	6.3768	4.8083
1.5805	5.3469	1.5754	4.7551	1.5831	4.0563	1.5817	3.3128

Table AII.7 – Isotherm data points for APG-III for N_2 at 22°C, 50°C, 80°C, and 110°C.

22.4 ± 0.2°C		49.7 ± 0.2°C		78.7 ± 0.4°C		119.8 ± 3.4°C	
Pressure	**q**	**Pressure**	**q**	**Pressure**	**q**	**Pressure**	**q**
Atm	**mmol/g**	**Atm**	**mmol/g**	**Atm**	**mmol/g**	**Atm**	**mmol/g**
0	0	0	0	0	0	0	0
0.0135	0.0065	0.0135	0.0035	0.0135	0.0016	0.0136	0.0017
0.0674	0.0305	0.0672	0.0157	0.0674	0.0088	0.0674	0.0060
0.1345	0.0598	0.1341	0.0304	0.1346	0.0173	0.1346	0.0105
0.2010	0.0885	0.2014	0.0450	0.2014	0.0257	0.2017	0.0150
0.3994	0.1702	0.3964	0.0861	0.3983	0.0497	0.3995	0.0279
0.7747	0.3146	0.7721	0.1625	0.7729	0.0943	0.7760	0.0518
1.5310	0.5611	1.5418	0.3033	1.5476	0.1802	1.5368	0.0977
6.3809	1.4867	6.3850	0.9341	6.3840	0.6144	6.3834	0.3798
1.5792	0.5734	1.5776	0.3085	1.5780	0.1825	1.5755	0.1013
0.4036	0.1726	0.4007	0.0874	0.4069	0.0505	0.4044	0.0303

Table AII.8 – Isotherm data points for APG-III for O_2 at 22°C, 50°C, 80°C, and 110°C.

22.7 ± 0.2°C		50.2 ± 0.2°C		79.6 ± 0.3°C		109.6 ± 3.0°C	
Pressure	**q**	**Pressure**	**q**	**Pressure**	**q**	**Pressure**	**q**
Atm	**mmol/g**	**Atm**	**mmol/g**	**Atm**	**mmol/g**	**Atm**	**mmol/g**
0	0	0	0	0	0	0	0
0.0665	0.0064	0.0665	0.0049	0.0665	0.0039	0.0663	0.0032
0.1329	0.0130	0.1327	0.0093	0.1329	0.0069	0.1329	0.0054
0.1990	0.0195	0.1987	0.0135	0.1989	0.0098	0.1990	0.0075
0.3950	0.0388	0.3982	0.0260	0.3951	0.0184	0.3954	0.0138
0.7727	0.0750	0.7735	0.0489	0.7752	0.0342	0.7736	0.0259
1.1297	0.1086	1.1294	0.0703	1.1297	0.0487	1.1242	0.0366
1.5326	0.1465	1.5311	0.0944	1.5299	0.0656	1.5346	0.0498
1.9152	0.1819	1.9128	0.1168	1.9140	0.0792	1.9252	0.0576
3.1992	0.2968	3.1979	0.1909	3.2004	0.1271	3.2015	0.0887
6.3712	0.5587	6.3825	0.3583	6.3841	0.2430	6.3835	0.1767
1.5339	0.1460	1.5202	0.0932	1.5298	0.0662	1.5498	0.0523
0.4057	0.0416	0.4036	0.0269	0.4058	0.0207	0.3986	0.0181

Table AII.9 – Isotherm data points for APG-III for Ar at 22°C, 50°C, 80°C, and 110°C.

22.7 ± 0.2°C		50.2 ± 0.2°C		80.5 ± 0.3°C		111.8 ± 7.2°C	
Pressure	q	Pressure	q	Pressure	q	Pressure	q
Atm	mmol/g	Atm	mmol/g	Atm	mmol/g	Atm	mmol/g
0	0	0	0	0	0	0	0
0.0665	0.0080	0.0665	0.0056	0.0665	0.0045	0.0663	0.0050
0.1329	0.0160	0.1329	0.0106	0.1329	0.0081	0.1333	0.0076
0.1993	0.0240	0.1996	0.0155	0.1995	0.0115	0.1989	0.0100
0.3978	0.0461	0.3991	0.0300	0.3977	0.0209	0.3985	0.0159
0.7955	0.0899	0.7953	0.0577	0.7947	0.0393	0.7994	0.0273
1.1383	0.1270	1.1368	0.0813	1.1414	0.0549	1.1182	0.0381
1.5456	0.1709	1.5430	0.1095	1.5414	0.0726	1.5459	0.0483
1.9154	0.2101	1.9159	0.1344	1.9242	0.0890	1.9203	0.0541
3.2236	0.3449	3.2198	0.2214	3.2181	0.1423	3.2148	0.0817
6.3842	0.6478	6.3874	0.4168	6.3889	0.2742	6.3936	0.1845
1.5464	0.1703	1.5349	0.1081	1.5767	0.0734	1.5485	0.0498
0.4056	0.0479	0.4054	0.0306	0.3951	0.0211	0.3985	0.0159

AII.6. Adsorption Isotherm Model Parameters

Table AII.10 – Adsorption isotherm model parameters for the adsorbents tested in this study. Associated equations are located in Table AII.3. Highlighted grey cells indicate model with highest R^2 used to represent the isotherm.

		Langmuir		Freundlich		Sips			Toth		
	°C	q_m mmol/g	B Atm^{-1}	k mmol/g•atm	a	q_m mmol/g	B Atm^{-1}	a	q_m mmol/g	B Atm^{-1}	t
CO_2	22	4.9824	44.831	5.2005	6.4242	6.2972	23.007	0.4730	6.7201	636.60	0.3556
	50	4.8752	13.790	4.0758	6.4041	6.5450	5.1276	0.4515	7.6009	551.15	0.2821
	80	4.0064	6.6889	3.4785	3.1678	7.8245	0.6352	0.4705	17.130	171.50	0.1957
	110	3.6436	3.5089	2.7648	2.4521	8.0282	0.3145	0.5435	26.236	17.780	0.1992
N_2	22	2.9877	0.1552	0.3758	1.3476	2.9263	0.1617	1.0224	2.6714	0.1665	1.1258
	50	2.3922	0.1003	0.2033	1.2157	2.8096	0.0776	0.9931	3.9352	0.0577	0.8261
	80	2.0240	0.0683	0.1167	1.1157	2.5497	0.0496	0.9975	3.1929	0.0415	0.8635
	110	0.9535	0.1037	0.0689	1.0854	17.533	0.0024	0.9143	0.8855	0.0988	1.1847
O_2	22	5.0942	0.0193	0.0980	1.0622	5.0943	0.0193	1.0000	5.0941	0.0193	1.0001
	50	2.9776	0.0214	0.0636	1.0704	4.1196	0.0142	0.9797	10.144	0.0065	0.6800
	80	1.9264	0.0226	0.0436	1.0790	31.276	0.0009	0.9305	123.69	0.0004	0.3785
	110	1.3922	0.0226	0.0319	1.0877	427.50	3.2E-05	0.9194	4383.9	9.5E-06	0.2337
Ar	22	5.9142	0.0193	0.1136	1.0636	8.3266	0.0126	0.9809	23.847	0.0049	0.6596
	50	3.9170	0.0186	0.0729	1.0620	6.3652	0.0103	0.9756	157.30	5.0E-04	0.4279
	80	2.5145	0.0191	0.0483	1.0700	118.04	2.4E-04	0.9356	15309	3.9E-06	0.2351
	110	18.597	0.0015	0.0301	1.0366	151.43	1.5E-04	0.9648	2857.5	1.1E-05	0.3600

AII.7. TD-Toth Model Parameters

Table AII.11 – The fitted parameters for the empirical TD-Toth model for APG-III for CO_2, N_2, O_2, and Ar adsorption.

		T_o (K)	q_{so} (mmol/g)	b_o (atm^{-1})	Q/RT_0	t_o	α	χ
APG-III	CO_2	295.77	6.760E+00	6.672E+02	1.869E+01	3.515E-01	-1.277E-01	-1.054E+00
	N_2	295.57	6.157E+00	8.444E-02	1.415E+01	6.411E-01	-7.103E-01	-4.959E+00
	O_2	295.86	1.751E+03	6.378E-05	7.146E+00	3.219E-01	-3.744E-01	-2.237E+00
	Ar	295.88	8.334E+03	1.604E-05	3.709E+00	2.761E-01	-1.425E-02	1.480E+00

Appendix III

Supporting Information

for

"Adsorption Separation of CF_4, O_2, CO_2, and COF_2 from an Excimer Gas Mixture"

Sean M.W. Wilson, and F. Handan Tezel

Department of Chemical and Biological Engineering, University of Ottawa, 161 Louis-Pasteur, Ottawa, Ontario K1N 6N5 Canada

To be submitted to: Separation and Purification Technology 2020

Contents

AIII.1. POROUS POLYMERS:

There are three main separate product lines of commercially available porous polymers including HayeSep (Hayes Separation), Chromosorb (Johns-Manville), Porapaks (Millpore Crop). Each one of these product lines contains different compositions within it. Even though they are different brands, Porapak Q and HayeSep Q are both similar styrene-divinylbenzene copolymers, and HayeSep C and Chromosorb 104 are both acrylonitrile-divinylbenzene copolymers. Common acroynms for porous polymers are Ethylvinyl benzene (EVB), acrylonitrile (ACN), polyethyleneimine (PEI), ethylene glycol dimehtacrylate (EGDMA), and divinylbenzene (DVB).

Table AIII.1 – Table of commercially available polymeric sorbents.

Polymeric Composition or Polar Monomer	Adsorbent	Properties	Maximum Temperature (°C)	Applications
High Purity DVB	HayeSep D (diff from website to website)		290	Separation of CO and CO_2 from room air at ambient temperature; elutes acetylene before other c2 hydrocarbons; analyses of water and hydrogen sulfide
DVB - Styrene	Porapak P HayeSep P Chromosorb 102	250 to 350 m^2/g, average pore diameter of 0.0091µm	250 (102, 275)	Separation of a wide variety of alcohols, glycols, and carbonyl analytes. (102, Separation of volatile organics and permanent gases; no peak tailing for water and alcohols)
DVB - Styrene	Chromosorb 101	50m^2/g, average pore diameter of 0.3 to 0.4µm	275	Separation of fatty acids, alcohols, glycols, esters, ketones, aldehydes, ethers, and hydrocarbons.
DVB-EVB	Porapak Q HayeSep Q Super Q	500 to 600m^2/g, average pore diameter of 0.0075µm	250	Most widely used; separation of hydrocarbons, organic analytes in water, oxides of nitrogen
DVB-EGDMA	HayeSep A		165	Permanent gases including hydrogen, nitrogen, oxygen, argon, CO, NO at ambient T. can separate c2 hydrocarbons, hydrogen sulphide, and water at elevated t
DVB-EVB-EGDMA	Porapak N		190	Separation of ammonia, carbon dioxide, water, and separation of acetylene from other C2 hydrocarbons
DVB-PEI	HayeSep B*		190	c1 and c2 amines; trace amounts of ammonia and water
DVB-ACN	HayeSep C		250	Analysis of polar gases (HCN, ammonia, hydrogen sulphide) and water
DVB-ACN	Chromosorb 104		250	Nitriles, nitroparaffins, hydrogen sulphide, ammonia, sulphur dioxide, carbon dioxide, vinylidene chloride, vinyl chloride, and trace water content in solvents
DVB-4-vinyl pyridine	HayeSep S	These are the same	250	
Vinyl Pyridine	Porapak S		250	Separation of normal and branched alcohols
EGDMA (copolymer)	HayeSep N		190	

EGDMA (PM)	Porapak T		190	Highest polarity Porapak; offers greatest water retention; determination of formaldehyde in water
EGDMA polymer	HayeSep T		165	
Vinyl pyrollidone (styrene-DVB copolymer with aromatic –O and –N groups)	Porapak R HayeSep R	400-600m^2/g, average pore diameter of 0.0076μm	250	Separation of ethers and esters; seprartion of water rom chlorine and HCl
Cross-linked PS	Chromosorb 103		275	Separation of basic compounds such as amines and ammonia; useful for separation of amides, hydrazines, alcohols, aldehydes, and ketones
Cross Linked PS	Chromosorb 106		225	Separation of C2 to C5 alcohols; separation of c2 to c5 fatty acids from corresponding alcohols
Crosslinked Polyaromatic	Chromosorb 105		250	Separation of aqueous solutions of formaldehyde; separation of acetylene from lower hydrocarbons and various classes of organic with boiling points up to 200C
Cross-linked acrylic ester	Chromosorb 107		225	Analysis of formaldehyde, sulphur gases, and various classes of compounds
Cross-Linked Acrylic	Chromosorb 108		225	Separation of gases
PTFE	Chromosorb T	7-8m^2/g, packing density 0.42g/mL	250	Application involving water, acids, amines, HF, HCl, Chlorosilanes, sulphur dioxide, and hydrazine
2,6-diphenyl-p-phenylene oxide	Tenax TA			

Appendix IV

Supporting Information

for

"Adsorption of Components from Air on Silica Aerogels"

Sean M.W. Wilson, Vida A. Gabriel, and F. Handan Tezel

Department of Chemical and Biological Engineering, University of Ottawa, 161 Louis-Pasteur, Ottawa, Ontario K1N 6N5 Canada

Accepted by: Microporous and Mesoporous Materials 2020

Contents

AIV.1. Gas Thermal Conductivity in the Pores

The gas thermal conductivity in a confined space is less than that of a gas in a free space. This is called the Knudsen effect where the gas thermal conductivity in the confined space (λ_g), is related to the Knudsen number (K_n) (Equation 2), by Equation 1.

$$\lambda_g = \frac{\lambda_{g0}}{1 + 2\beta K_n} \quad (1)$$

$$K_n = \frac{l_g}{D_e} \quad (2)$$

Where λ_{g0} is the conductivity of the gas in free space (25.5 mW m^{-1} K^{-1} for air), D_e is the effective pore diameter, β is a constant for the effectiveness of the energy transfer between gas molecules and the solid pore wall (values are commonly between 1.5 and 2), and l_g is the mean free path of the gas. The pressure (P) and temperature (T) dependence of the thermal conductivity comes from the relation for the mean free path for the gas (Equation 3).

$$l_g = \frac{k_B T}{\sqrt{2}\,\sigma P} \quad (3)$$

Where k_B is the Boltzmann constant, and σ is the molecular cross-section of the gas which for oxygen and nitrogen is around 0.4 nm^2.

AIV.2. Schematic Diagram of the Gravimetric System

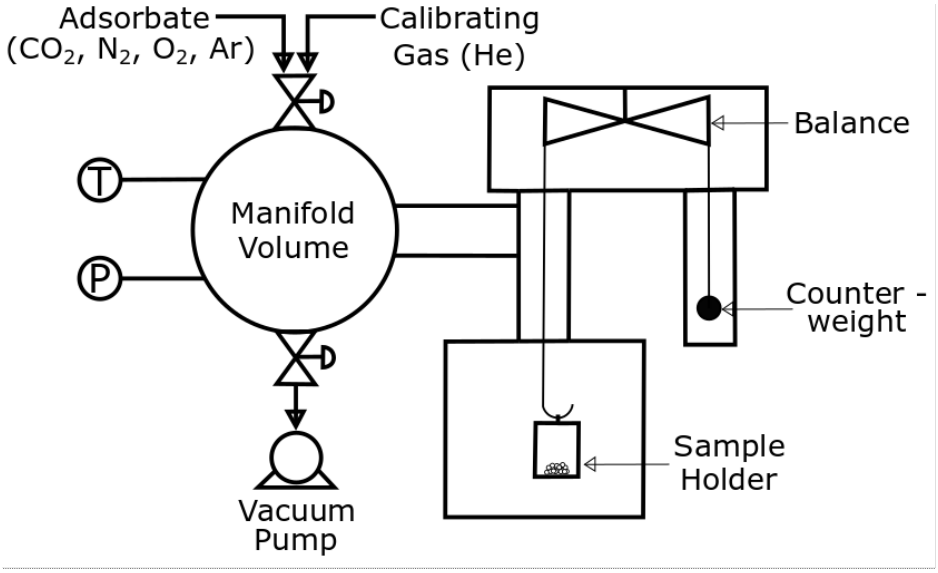

Figure AIV.1 - Process flow diagram of the VTI Scientific Instruments GHP Gravimetric system that is used in this study.

AIV.3. Thermogravimetric Analysis (TGA)

In order to study the thermal stability of TMOS silica aerogel, and TMS modified silica aerogel, a controlled heating rate of 2 °C min^{-1} was applied under a vacuum of up to 10^{-8} atm on aerogel samples of approximately 40 mg in weight from 50 °C to 500 – 550 °C using the VTI Scientific Instruments GHP Gravimetric Analyzer. The samples were first evacuated out under vacuum until satisfactory low pressure was achieved, and then flushed with helium for up to 6 atm. This was repeated twice before TGA began. The main purpose of the TGA was to determine a suitable regeneration temperature for the aerogel samples such that it would not affect its chemical or surface properties.

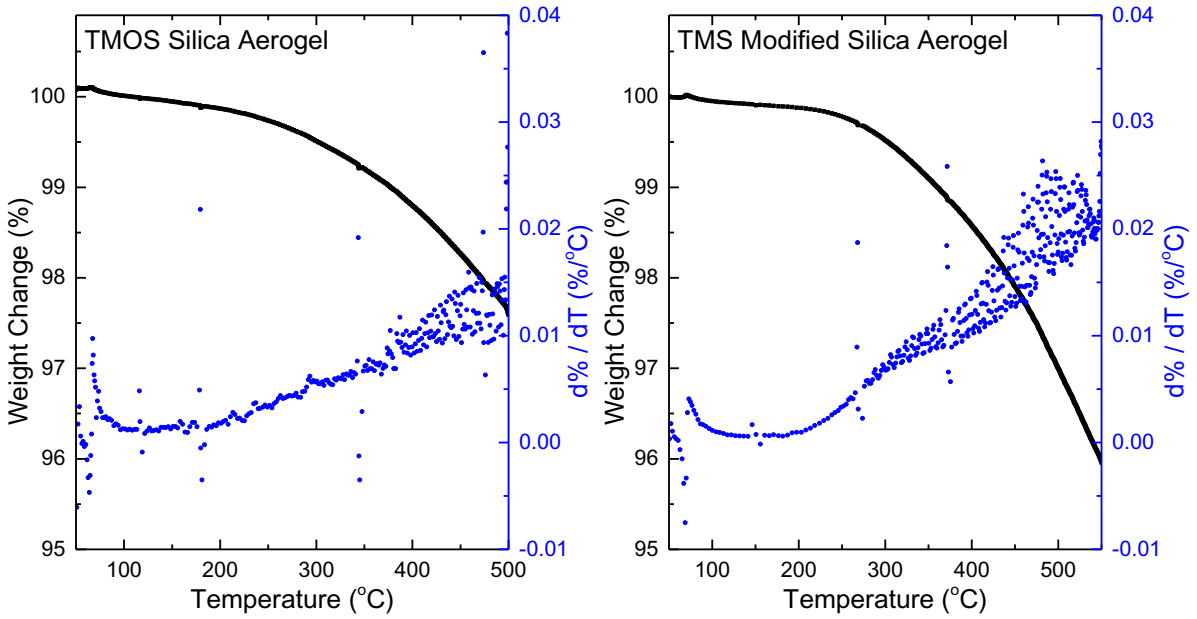

Figure AIV.2 – TGA under vacuum results showing the weight loss as a function of temperature including its derivative for TMOS silica aerogel on the left and TMS modified silica aerogel on the right.

The results from the TGA are included in Figure AIV.2 for the TMOS silica aerogel and the TMS modified silica aerogel. The TMOS silica aerogel sample was found to have minimum weight loss at 120 °C until 175 °C which shows a continuous increase in the rate of weight loss within the sample. The TMS modified silica aerogel was found to have minimum weight change at 140 °C until 200 °C which shows a continuous increase in the rate of weight loss within the sample. This increase in rate of weight loss is due to the possible trapped water or ethanol within the pores of the aerogel or the liberation of functional groups on the surface of the silica aerogel and hydrophobic silica aerogel which has been seen in literature for similar temperatures[1–4].

AIV.4. Isotherm Data Points

Table AIV.1 – Carbon dioxide equilibrium adsorption capacities for TMOS silica aerogel. Exact temperatures for the isotherms are included above the isotherm data.

11.23 °C		30.55 °C		49.97 °C		69.32 °C		88.66 °C	
Pressure Atm	q_e mmol/g	Pressure Atm	q_e mmol/g	Pressure Atm	q_e mmol/g	Pressure Atm	q_e mmol/g	Pressure Atm	q_e mmol/g
0.0000	0.0000	0.0000	0.0000	0.0000	0.0000	0.0000	0.0000	0.0000	0.0000
0.0334	0.0489	0.0334	0.0269	0.0333	0.0137	0.0334	0.0129	0.0334	0.0102
0.0666	0.0885	0.0666	0.0482	0.0666	0.0267	0.0666	0.0212	0.0666	0.0161
0.1329	0.1561	0.1329	0.0873	0.1330	0.0510	0.1331	0.0363	0.1329	0.0260
0.1996	0.2159	0.1993	0.1225	0.1996	0.0742	0.1993	0.0508	0.1991	0.0356
0.3972	0.3631	0.3975	0.2156	0.3976	0.1375	0.3968	0.0919	0.3977	0.0637
0.7982	0.5990	0.7987	0.3712	0.7985	0.2503	0.8008	0.1671	0.8039	0.1161
1.5380	0.9408	1.5400	0.6052	1.5384	0.4274	1.5396	0.2846	1.5355	0.2034
3.2090	1.5275	3.2124	1.0178	3.2103	0.7551	3.2118	0.5196	3.1824	0.3738
6.3706	2.3837	6.3755	1.6269	6.3787	1.2554	6.3758	0.9302	6.3838	0.6989
1.5628	0.9544	1.5517	0.6118	1.5449	0.4310	1.5551	0.2926	1.5466	0.2031
0.4056	0.3733	0.4007	0.2218	0.4067	0.1426	0.4001	0.0967	0.3965	0.0673

Table AIV.2 – Nitrogen equilibrium adsorption capacities for TMOS silica aerogel. Exact temperatures for the isotherms are included above the isotherm data.

11.16 °C		30.57 °C		49.98 °C		69.42 °C		88.79 °C	
Pressure Atm	q_e mmol/g	Pressure Atm	q_e mmol/g	Pressure Atm	q_e mmol/g	Pressure Atm	q_e mmol/g	Pressure Atm	q_e mmol/g
0.0000	0.0000	0.0000	0.0000	0.0000	0.0000	0.0000	0.0000	0.0000	0.0000
0.0333	0.0053	0.0333	0.0042	0.0333	0.0030	0.0333	0.0025	0.0333	0.0019
0.0666	0.0080	0.0666	0.0059	0.0666	0.0042	0.0665	0.0040	0.0665	0.0032
0.1331	0.0128	0.1330	0.0086	0.1330	0.0069	0.1330	0.0062	0.1331	0.0054
0.1993	0.0173	0.1998	0.0118	0.1994	0.0091	0.1994	0.0079	0.1993	0.0069
0.3977	0.0302	0.3988	0.0208	0.3965	0.0165	0.3985	0.0139	0.3978	0.0124
0.7907	0.0523	0.7886	0.0363	0.7877	0.0285	0.7886	0.0242	0.7934	0.0202
1.5379	0.0883	1.5389	0.0620	1.5376	0.0484	1.5363	0.0389	1.5379	0.0313
3.2137	0.1610	3.1948	0.1155	3.2131	0.0917	3.1943	0.0666	3.2016	0.0536
6.3597	0.2820	6.3602	0.2055	6.3580	0.1480	6.3579	0.1214	6.3608	0.0993
1.5438	0.0831	1.5356	0.0589	1.5258	0.0449	1.5419	0.0347	1.5321	0.0268
0.4004	0.0273	0.4017	0.0198	0.4066	0.0153	0.4062	0.0126	0.4073	0.0116

Table AIV.3 – Oxygen equilibrium adsorption capacities for TMOS silica aerogel. Exact temperatures for the isotherms are included above the isotherm data.

11.19 °C		30.57 °C		50.00 °C		69.39 °C		88.77 °C	
Pressure Atm	q_e mmol/g	Pressure Atm	q_e mmol/g	Pressure Atm	q_e mmol/g	Pressure Atm	q_e mmol/g	Pressure Atm	q_e mmol/g
0.0000	0.0000	0.0000	0.0000	0.0000	0.0000	0.0000	0.0000	0.0000	0.0000
0.0333	0.0049	0.0333	0.0039	0.0333	0.0025	0.0333	0.0022	0.0333	0.0019
0.0666	0.0072	0.0665	0.0055	0.0666	0.0038	0.0665	0.0031	0.0665	0.0030
0.1328	0.0111	0.1331	0.0086	0.1330	0.0065	0.1329	0.0052	0.1329	0.0048
0.1993	0.0153	0.1996	0.0113	0.1995	0.0087	0.1994	0.0067	0.1991	0.0065
0.3997	0.0272	0.4001	0.0206	0.4002	0.0160	0.4009	0.0131	0.4014	0.0118
0.7783	0.0480	0.7814	0.0365	0.7829	0.0282	0.7764	0.0226	0.7786	0.0199
1.5330	0.0880	1.5326	0.0664	1.5329	0.0513	1.5350	0.0403	1.5315	0.0348
3.1991	0.1681	3.2014	0.1279	3.2002	0.0994	3.1895	0.0714	3.2054	0.0563
6.3810	0.3071	6.3815	0.2342	6.3785	0.1710	6.3798	0.1293	6.3779	0.1076
1.5505	0.0865	1.5425	0.0650	1.5336	0.0499	1.5449	0.0392	1.5367	0.0326
0.4017	0.0267	0.4054	0.0204	0.3945	0.0153	0.4081	0.0122	0.3989	0.0113

Table AIV.4 – Argon equilibrium adsorption capacities for TMOS silica aerogel. Exact temperatures for the isotherms are included above the isotherm data.

11.22 °C		30.61 °C		50.00 °C		69.29 °C		88.71 °C	
Pressure Atm	q_e mmol/g	Pressure Atm	q_e mmol/g	Pressure Atm	q_e mmol/g	Pressure Atm	q_e mmol/g	Pressure Atm	q_e mmol/g
0.0000	0.0000	0.0000	0.0000	0.0000	0.0000	0.0000	0.0000	0.0000	0.0000
0.0333	0.0032	0.0333	0.0024	0.0333	0.0021	0.0333	0.0017	0.0333	0.0015
0.0665	0.0053	0.0665	0.0043	0.0666	0.0035	0.0666	0.0031	0.0666	0.0026
0.1329	0.0095	0.1330	0.0077	0.1330	0.0060	0.1329	0.0051	0.1329	0.0045
0.1992	0.0139	0.1995	0.0105	0.1992	0.0084	0.1992	0.0072	0.1995	0.0062
0.3991	0.0263	0.3978	0.0197	0.3989	0.0160	0.3981	0.0133	0.3984	0.0114
0.7995	0.0496	0.7971	0.0370	0.7993	0.0297	0.7989	0.0245	0.8018	0.0210
1.5360	0.0873	1.5416	0.0671	1.5385	0.0531	1.5390	0.0437	1.5395	0.0339
3.1770	0.1710	3.1800	0.1303	3.1743	0.1027	3.2153	0.0826	3.1815	0.0617
6.3869	0.3197	6.3851	0.2422	6.3827	0.1893	6.3901	0.1438	6.3870	0.1208
1.5560	0.0861	1.5434	0.0652	1.5367	0.0513	1.5492	0.0401	1.5398	0.0323
0.3934	0.0252	0.3969	0.0190	0.3984	0.0155	0.3944	0.0118	0.3984	0.0108

Table AIV.5 - Carbon Dioxide equilibrium adsorption capacities for TMS modified silica aerogel. Exact temperatures for the isotherms are included above the isotherm data.

11.18 °C		30.55 °C		49.95 °C		69.35 °C		88.71 °C	
Pressure Atm	q_e mmol/g	Pressure Atm	q_e mmol/g	Pressure Atm	q_e mmol/g	Pressure Atm	q_e mmol/g	Pressure Atm	q_e mmol/g
0.0000	0.0000	0.0000	0.0000	0.0000	0.0000	0.0000	0.0000	0.0000	0.0000
0.0333	0.0224	0.0333	0.0115	0.0333	0.0074	0.0333	0.0055	0.0333	0.0047
0.0665	0.0411	0.0666	0.0220	0.0666	0.0135	0.0665	0.0093	0.0665	0.0074
0.1330	0.0724	0.1330	0.0406	0.1329	0.0246	0.1330	0.0165	0.1330	0.0125
0.1995	0.0994	0.1994	0.0577	0.1995	0.0353	0.1994	0.0236	0.1994	0.0174
0.3868	0.1629	0.3877	0.1000	0.3981	0.0649	0.3979	0.0437	0.3980	0.0314
0.8135	0.2786	0.8072	0.1793	0.8089	0.1189	0.8098	0.0818	0.8084	0.0582
1.5477	0.4392	1.5499	0.2968	1.5483	0.2030	1.5518	0.1427	1.5488	0.1029
3.1885	0.7279	3.1889	0.5112	3.1894	0.3622	3.1885	0.2651	3.1886	0.1957
6.3548	1.1950	6.3743	0.8620	6.3759	0.6282	6.3768	0.4803	6.3775	0.3635
1.5586	0.4417	1.5648	0.2991	1.5621	0.2056	1.5524	0.1430	1.5614	0.1040
0.4000	0.1687	0.4079	0.1054	0.4073	0.0684	0.4072	0.0456	0.3995	0.0327

Table AIV.6 – Nitrogen equilibrium adsorption capacities for TMS modified silica aerogel. Exact temperatures for the isotherms are included above the isotherm data.

11.01 °C		30.53 °C		49.97 °C		69.36 °C		88.80 °C	
Pressure Atm	q_e mmol/g	Pressure Atm	q_e mmol/g	Pressure Atm	q_e mmol/g	Pressure Atm	q_e mmol/g	Pressure Atm	q_e mmol/g
0.0000	0.0000	0.0000	0.0000	0.0000	0.0000	0.0000	0.0000	0.0000	0.0000
0.0335	0.0014	0.0333	0.0012	0.0333	0.0011	0.0333	0.0009	0.0333	0.0009
0.0652	0.0026	0.0666	0.0022	0.0666	0.0020	0.0666	0.0017	0.0666	0.0016
0.1331	0.0050	0.1331	0.0042	0.1331	0.0038	0.1331	0.0031	0.1332	0.0029
0.1937	0.0071	0.1997	0.0061	0.1996	0.0054	0.1996	0.0045	0.1996	0.0041
0.3987	0.0145	0.3990	0.0118	0.3989	0.0106	0.3991	0.0103	0.3991	0.0075
0.7998	0.0276	0.8140	0.0224	0.8154	0.0191	0.8003	0.0177	0.8157	0.0137
1.5584	0.0480	1.5571	0.0393	1.5602	0.0329	1.5565	0.0279	1.5611	0.0224
3.1923	0.0957	3.1903	0.0760	3.1968	0.0626	3.1940	0.0512	3.1959	0.0403
6.3875	0.1821	6.3875	0.1439	6.3906	0.1161	6.3864	0.1009	6.3876	0.0720
1.5453	0.0461	1.5470	0.0378	1.5528	0.0321	1.5526	0.0266	1.5488	0.0216
0.3995	0.0144	0.4017	0.0115	0.4044	0.0108	0.4036	0.0098	0.4020	0.0099

Table AIV.7 – Oxygen equilibrium adsorption capacities for TMS modified silica aerogel. Exact temperatures for the isotherms are included above the isotherm data.

11.07 °C		30.51 °C		49.95 °C		69.38 °C		88.78 °C	
Pressure Atm	q_e mmol/g	Pressure Atm	q_e mmol/g	Pressure Atm	q_e mmol/g	Pressure Atm	q_e mmol/g	Pressure Atm	q_e mmol/g
0.0000	0.0000	0.0000	0.0000	0.0000	0.0000	0.0000	0.0000	0.0000	0.0000
0.0334	0.0021	0.0334	0.0019	0.0334	0.0017	0.0334	0.0016	0.0334	0.0008
0.0667	0.0042	0.0667	0.0034	0.0667	0.0027	0.0667	0.0023	0.0667	0.0021
0.1332	0.0072	0.1332	0.0059	0.1332	0.0045	0.1332	0.0037	0.1332	0.0036
0.1930	0.0100	0.1997	0.0081	0.1997	0.0063	0.1996	0.0050	0.1997	0.0046
0.3985	0.0184	0.3988	0.0144	0.3986	0.0111	0.3986	0.0092	0.3987	0.0078
0.8009	0.0333	0.8014	0.0260	0.8020	0.0204	0.8010	0.0168	0.8034	0.0139
1.5431	0.0567	1.5420	0.0432	1.5398	0.0344	1.5393	0.0277	1.5455	0.0218
3.1874	0.1110	3.1886	0.0856	3.1897	0.0675	3.1883	0.0532	3.1880	0.0423
6.3814	0.2103	6.3793	0.1640	6.3785	0.1282	6.3801	0.1027	6.3689	0.0768
1.5611	0.0577	1.5537	0.0435	1.5584	0.0344	1.5508	0.0272	1.5542	0.0216
0.4068	0.0206	0.4078	0.0156	0.4014	0.0111	0.4042	0.0086	0.4036	0.0081

Table AIV.8 – Argon equilibrium adsorption capacities for TMS modified silica aerogel. Exact temperatures for the isotherms are included above the isotherm data.

11.10 °C		30.50 °C		49.92 °C		69.36 °C		88.70 °C	
Pressure Atm	q_e mmol/g	Pressure Atm	q_e mmol/g	Pressure Atm	q_e mmol/g	Pressure Atm	q_e mmol/g	Pressure Atm	q_e mmol/g
0.0000	0.0000	0.0000	0.0000	0.0000	0.0000	0.0000	0.0000	0.0000	0.0000
0.0334	0.0020	0.0334	0.0022	0.0333	0.0018	0.0334	0.0016	0.0334	0.0008
0.0667	0.0037	0.0666	0.0033	0.0666	0.0028	0.0666	0.0025	0.0667	0.0020
0.1332	0.0063	0.1332	0.0056	0.1333	0.0045	0.1306	0.0040	0.1332	0.0035
0.1998	0.0090	0.1998	0.0078	0.1998	0.0062	0.1947	0.0054	0.1998	0.0049
0.3995	0.0172	0.3990	0.0144	0.3996	0.0113	0.3987	0.0097	0.3992	0.0086
0.8160	0.0329	0.8157	0.0270	0.8154	0.0215	0.8151	0.0179	0.8143	0.0154
1.5570	0.0597	1.5586	0.0487	1.5579	0.0389	1.5568	0.0288	1.5552	0.0247
3.1951	0.1154	3.1886	0.0922	3.1915	0.0757	3.1884	0.0559	3.1926	0.0449
6.3799	0.2165	6.3826	0.1738	6.3887	0.1394	6.3815	0.1089	6.3805	0.0870
1.5667	0.0579	1.5558	0.0461	1.5622	0.0376	1.5583	0.0279	1.5598	0.0241
0.4067	0.0165	0.4084	0.0138	0.3986	0.0108	0.3999	0.0093	0.4043	0.0082

Table AIV.9 – Carbon dioxide equilibrium adsorption capacities for silica gel. Exact temperatures for the isotherms are included above the isotherm data.

11.32 °C		30.61 °C		49.97 °C		69.36 °C		88.69 °C	
Pressure Atm	q_e mmol/g	Pressure Atm	q_e mmol/g	Pressure Atm	q_e mmol/g	Pressure Atm	q_e mmol/g	Pressure Atm	q_e mmol/g
0.0000	0.0000	0.0000	0.0000	0.0000	0.0000	0.0000	0.0000	0.0000	0.0000
0.0333	0.1083	0.0333	0.0545	0.0333	0.0286	0.0333	0.0164	0.0333	0.0099
0.0666	0.1959	0.0665	0.1022	0.0665	0.0547	0.0665	0.0315	0.0665	0.0191
0.1329	0.3382	0.1330	0.1855	0.1328	0.1028	0.1329	0.0599	0.1329	0.0366
0.1995	0.4562	0.1996	0.2588	0.1993	0.1470	0.1994	0.0868	0.1995	0.0535
0.3979	0.7316	0.3972	0.4403	0.3967	0.2629	0.3970	0.1607	0.3966	0.1008
0.7911	1.1262	0.7908	0.7206	0.7934	0.4562	0.7934	0.2907	0.7966	0.1888
1.5357	1.6471	1.5417	1.1165	1.5407	0.7433	1.5379	0.4978	1.5369	0.3344
3.2092	2.4039	3.2131	1.7197	3.2095	1.2138	3.2135	0.8622	3.2150	0.6043
6.3791	3.2915	6.3853	2.4639	6.3766	1.8279	6.3794	1.3661	6.3891	1.0059
1.5566	1.6635	1.5482	1.1224	1.5375	0.7446	1.5401	0.4991	1.5500	0.3375
0.4005	0.7433	0.3957	0.4442	0.4029	0.2700	0.4005	0.1644	0.3987	0.1033

Table AIV.10 – Nitrogen equilibrium adsorption capacities for silica gel. Exact temperatures for the isotherms are included above the isotherm data.

11.09 °C		30.50 °C		49.95 °C		69.37 °C		88.76 °C	
Pressure Atm	q_e mmol/g	Pressure Atm	q_e mmol/g	Pressure Atm	q_e mmol/g	Pressure Atm	q_e mmol/g	Pressure Atm	q_e mmol/g
0.0000	0.0000	0.0000	0.0000	0.0000	0.0000	0.0000	0.0000	0.0000	0.0000
0.0333	0.0030	0.0333	0.0024	0.0333	0.0023	0.0333	0.0017	0.0333	0.0012
0.0666	0.0053	0.0665	0.0040	0.0666	0.0034	0.0666	0.0026	0.0666	0.0020
0.1332	0.0097	0.1327	0.0071	0.1330	0.0057	0.1329	0.0043	0.1329	0.0033
0.1994	0.0139	0.1996	0.0101	0.1993	0.0079	0.1995	0.0058	0.1993	0.0047
0.3985	0.0264	0.3981	0.0189	0.3984	0.0145	0.3984	0.0110	0.3980	0.0087
0.8003	0.0498	0.8015	0.0356	0.8033	0.0269	0.8048	0.0206	0.8047	0.0160
1.5475	0.0892	1.5407	0.0629	1.5480	0.0469	1.5500	0.0350	1.5469	0.0250
3.2249	0.1722	3.2197	0.1240	3.2256	0.0916	3.1880	0.0687	3.1961	0.0495
6.3543	0.3064	6.3902	0.2266	6.3965	0.1692	6.3976	0.1304	6.3987	0.0913
1.5711	0.0884	1.5402	0.0611	1.5741	0.0461	1.5291	0.0330	1.5165	0.0235
0.3976	0.0256	0.4015	0.0181	0.4021	0.0141	0.3926	0.0101	0.3913	0.0075

Table AIV.11 – Oxygen equilibrium adsorption capacities for silica gel. Exact temperatures for the isotherms are included above the isotherm data.

11.20 °C		30.58 °C		50.02 °C		69.44 °C		88.79 °C	
Pressure Atm	q_e mmol/g	Pressure Atm	q_e mmol/g	Pressure Atm	q_e mmol/g	Pressure Atm	q_e mmol/g	Pressure Atm	q_e mmol/g
0.0000	0.0000	0.0000	0.0000	0.0000	0.0000	0.0000	0.0000	0.0000	0.0000
0.0333	0.0017	0.0333	0.0013	0.0333	0.0013	0.0333	0.0008	0.0333	0.0007
0.0666	0.0036	0.0666	0.0028	0.0665	0.0022	0.0665	0.0016	0.0666	0.0015
0.1330	0.0074	0.1330	0.0054	0.1331	0.0044	0.1331	0.0033	0.1328	0.0028
0.1992	0.0112	0.1993	0.0080	0.1995	0.0064	0.1995	0.0048	0.1995	0.0041
0.3995	0.0224	0.4011	0.0162	0.4003	0.0125	0.4014	0.0098	0.4023	0.0081
0.7797	0.0425	0.7799	0.0304	0.7784	0.0232	0.7774	0.0181	0.7797	0.0146
1.5340	0.0804	1.5353	0.0570	1.5357	0.0430	1.5346	0.0315	1.5343	0.0268
3.2015	0.1580	3.2022	0.1137	3.1882	0.0850	3.2041	0.0635	3.2022	0.0492
6.3794	0.2894	6.3792	0.2116	6.3825	0.1577	6.3831	0.1240	6.3807	0.0922
1.5482	0.0797	1.5390	0.0559	1.5497	0.0422	1.5487	0.0303	1.5358	0.0246
0.4022	0.0221	0.4041	0.0160	0.4075	0.0122	0.3970	0.0090	0.4056	0.0077

Table AIV.12 – Argon equilibrium adsorption capacities for silica gel. Exact temperatures for the isotherms are included above the isotherm data.

11.14 °C		30.52 °C		49.93 °C		69.33 °C		88.70 °C	
Pressure Atm	q_e mmol/g	Pressure Atm	q_e mmol/g	Pressure Atm	q_e mmol/g	Pressure Atm	q_e mmol/g	Pressure Atm	q_e mmol/g
0.0000	0.0000	0.0000	0.0000	0.0000	0.0000	0.0000	0.0000	0.0000	0.0000
0.0334	0.0032	0.0333	0.0021	0.0333	0.0019	0.0333	0.0017	0.0333	0.0012
0.0667	0.0061	0.0666	0.0037	0.0666	0.0032	0.0666	0.0026	0.0666	0.0020
0.1332	0.0110	0.1331	0.0066	0.1331	0.0054	0.1331	0.0044	0.1328	0.0034
0.1995	0.0153	0.1995	0.0096	0.1997	0.0075	0.1995	0.0061	0.1992	0.0046
0.3983	0.0280	0.3988	0.0180	0.3981	0.0138	0.3983	0.0111	0.3983	0.0086
0.7993	0.0507	0.7990	0.0338	0.7994	0.0258	0.8011	0.0205	0.8019	0.0160
1.5412	0.0846	1.5433	0.0606	1.5447	0.0457	1.5411	0.0354	1.5431	0.0263
3.2200	0.1593	3.2161	0.1182	3.2170	0.0894	3.2210	0.0670	3.2233	0.0545
6.3922	0.2829	6.3876	0.2177	6.3854	0.1664	6.3926	0.1310	6.3909	0.0981
1.5478	0.0787	1.5497	0.0582	1.5515	0.0438	1.5467	0.0339	1.5309	0.0250
0.4051	0.0240	0.4034	0.0170	0.3965	0.0129	0.3938	0.0103	0.3996	0.0081

Table AIV.13 - Adsorption isotherm model parameters for TMOS silica aerogel for CO_2, N_2, O_2, and Ar at 10°C, 30°C, 50°C, 70°C, and 90°C. Associated equations are located in Methods section.

		Langmuir		Freundlich		Sips			Toth		
	T	q_s	β	k	n	q_s	β	n	q_s	β	t
	(°C)	mmol/g	Atm^{-1}	$\frac{mmol}{g\ atm}$		mmol/g	Atm^{-1}		mmol/g	Atm^{-1}	
CO_2	**11.23**	4.3494	0.1836	0.6886	1.4840	6.54E+02	3.89E-05	6.75E-01	5.47E+02	9.20E-03	1.81E-01
	30.55	3.3764	0.1428	0.4340	1.3947	6.29E+02	3.95E-05	7.18E-01	1.69E+02	8.83E-03	2.34E-01
	49.97	3.2389	0.0983	0.2993	1.2864	7.04E+02	4.64E-05	7.78E-01	4.75E+01	1.11E-02	3.44E-01
	69.32	3.3857	0.0589	0.1977	1.1975	5.57E+02	7.44E-05	8.35E-01	1.58E+05	3.89E-06	1.41E-01
	88.66	3.3038	0.0418	0.1389	1.1497	9.85E+01	5.43E-04	8.73E-01	6.23E+04	4.50E-06	1.68E-01
N_2	**11.16**	0.9038	0.0706	0.0628	1.2336	2.13E+02	4.44E-05	8.11E-01	4.62E+02	3.18E-04	2.05E-01
	30.57	0.7429	0.0597	0.0440	1.2018	2.17E+02	3.66E-05	8.32E-01	4.82E+02	1.85E-04	2.12E-01
	49.98	0.3859	0.0975	0.0355	1.2862	1.01E+02	3.64E-05	7.78E-01	4.73E+00	1.26E-02	3.60E-01
	69.42	0.3791	0.0727	0.0275	1.2555	7.83E+01	4.65E-05	7.97E-01	1.05E+05	1.72E-06	1.10E-01
	88.79	0.3158	0.0706	0.0226	1.2609	6.86E+01	4.08E-05	7.94E-01	6.42E+02	1.12E-04	1.68E-01
O_2	**11.19**	1.4465	0.0421	0.0608	1.1447	2.38E+02	7.75E-05	8.74E-01	4.00E+03	2.62E-05	2.03E-01
	30.57	1.1490	0.0400	0.0460	1.1386	2.08E+02	6.93E-05	8.79E-01	1.23E+05	7.82E-07	1.52E-01
	50.00	0.6042	0.0618	0.0363	1.1916	1.03E+00	2.74E-02	9.21E-01	5.44E+00	8.65E-03	4.40E-01
	69.39	0.4592	0.0608	0.0277	1.2037	1.07E+01	8.01E-04	8.36E-01	1.07E+02	4.85E-04	2.38E-01
	88.77	0.3896	0.0587	0.0232	1.2190	1.04E+02	3.54E-05	8.21E-01	7.76E+04	1.30E-06	1.21E-01
Ar	**11.22**	1.9096	0.0314	0.0600	1.1084	3.97E+02	5.85E-05	9.03E-01	2.13E+03	3.91E-05	2.44E-01
	30.61	1.3999	0.0327	0.0457	1.1115	3.32E+02	5.12E-05	9.00E-01	7.55E+01	7.40E-04	3.56E-01
	50.00	0.9814	0.0374	0.0365	1.1257	2.78E+02	4.29E-05	8.89E-01	8.05E+01	5.89E-04	3.24E-01
	69.29	0.5148	0.0604	0.0304	1.1901	1.92E+02	3.01E-05	8.41E-01	2.04E+01	2.23E-03	3.23E-01
	88.71	0.7111	0.0318	0.0232	1.1312	2.95E+02	2.28E-05	8.84E-01	1.71E+05	3.95E-07	1.32E-01

Table AIV.14 - Adsorption isotherm model parameters for TMS modified silica aerogel for CO_2, N_2, O_2, and Ar at 10°C, 30°C, 50°C, 70°C, and 90°C. Associated equations are located in Methods section.

		Langmuir		Freundlich		Sips			Toth		
	T	q_s	β	k	n	q_s	β	n	q_s	β	t
	(°C)	mmol/g	Atm^{-1}	$\frac{mmol}{g\ atm}$		mmol/g	Atm^{-1}		mmol/g	Atm^{-1}	
CO_2	**11.18**	2.5205	0.1380	0.3190	1.4001	5.09E+02	3.32E-05	7.15E-01	5.67E+06	3.58E-06	7.74E-02
	30.55	2.1616	0.1025	0.2097	1.3084	5.25E+02	3.61E-05	7.65E-01	1.12E+05	1.63E-05	1.15E-01
	49.95	1.9096	0.0762	0.1409	1.2373	5.30E+02	3.79E-05	8.09E-01	1.11E+05	5.71E-06	1.28E-01
	69.35	2.0180	0.0487	0.0976	1.1624	5.53E+02	4.35E-05	8.61E-01	8.74E+04	2.63E-06	1.53E-01
	88.71	1.9377	0.0361	0.0702	1.1270	4.10E+01	7.89E-04	8.91E-01	2.69E+05	5.10E-07	1.53E-01
N_2	**11.01**	1.5070	0.0215	0.0326	1.0782	2.13E+01	9.52E-04	9.31E-01	1.33E+02	2.80E-04	3.62E-01
	30.53	1.0037	0.0261	0.0264	1.0955	1.27E+01	1.20E-03	9.18E-01	6.86E+01	4.56E-04	3.56E-01
	49.97	0.6097	0.0367	0.0225	1.1301	1.82E+01	5.30E-04	8.88E-01	9.63E+01	3.18E-04	2.91E-01
	69.36	0.6662	0.0277	0.0191	1.1192	2.17E+02	2.88E-05	8.93E-01	2.15E+04	1.50E-06	1.74E-01
	88.80	0.2457	0.0643	0.0156	1.2148	1.26E+01	3.01E-04	8.26E-01	1.82E+02	1.94E-04	2.02E-01
O_2	**11.07**	1.3636	0.0285	0.0393	1.1075	5.71E+02	2.46E-05	9.03E-01	1.25E+06	5.44E-08	1.47E-01
	30.51	1.2178	0.0243	0.0302	1.0976	2.74E+02	4.54E-05	9.11E-01	1.38E+04	3.14E-06	2.02E-01
	49.95	0.8560	0.0275	0.0239	1.1059	2.32E+01	5.09E-04	9.07E-01	1.27E+02	2.33E-04	3.12E-01
	69.38	0.7082	0.0264	0.0192	1.1084	1.42E+02	5.15E-05	9.02E-01	5.76E+04	8.52E-07	1.44E-01
	88.78	0.3171	0.0498	0.0159	1.1800	1.39E+02	2.24E-05	8.48E-01	3.01E+04	1.01E-06	1.56E-01
Ar	**11.10**	1.4504	0.0274	0.0399	1.0952	1.25E+01	1.96E-03	9.21E-01	6.49E+01	7.15E-04	3.82E-01
	30.50	1.0807	0.0299	0.0325	1.1073	2.41E+01	6.84E-04	9.06E-01	1.57E+02	2.61E-04	3.11E-01
	49.92	0.7864	0.0337	0.0264	1.1137	2.79E+00	6.42E-03	9.22E-01	3.30E+01	9.69E-04	3.71E-01
	69.36	0.8672	0.0224	0.0200	1.0970	2.23E+02	3.61E-05	9.11E-01	1.72E+04	1.65E-06	1.96E-01
	88.70	0.4822	0.0342	0.0170	1.1411	1.64E+02	2.83E-05	8.76E-01	3.01E+04	1.14E-06	1.56E-01

Table AIV.15 - Adsorption isotherm model parameters for silica gel for CO_2, N_2, O_2, and Ar at 10°C, 30°C, 50°C, 70°C, and 90°C. Associated equations are located in Methods section.

		Langmuir		Freundlich		Sips			Toth		
	T	q_s	β	k	n	q_s	β	n	q_s	β	t
	(°C)	mmol/g	Atm^{-1}	$\frac{mmol}{g\ atm}$		mmol/g	Atm^{-1}		mmol/g	Atm^{-1}	
CO_2	**11.32**	4.370	0.428	1.230	1.837	7.29E+00	1.19E-01	7.26E-01	1.63E+01	3.76E-01	3.46E-01
	30.61	3.745	0.286	0.812	1.639	5.89E+00	1.03E-01	7.91E-01	1.29E+01	1.79E-01	4.03E-01
	49.97	3.287	0.192	0.531	1.478	4.91E+00	8.44E-02	8.48E-01	1.07E+01	9.59E-02	4.61E-01
	69.36	3.017	0.128	0.350	1.349	4.31E+00	6.64E-02	8.95E-01	9.33E+00	5.57E-02	5.19E-01
	88.69	2.780	0.088	0.232	1.256	3.94E+00	4.90E-02	9.22E-01	9.49E+00	3.17E-02	5.42E-01
N_2	**11.09**	1.380	0.045	0.061	1.145	3.39E+02	5.21E-05	8.74E-01	1.68E+02	5.15E-04	2.93E-01
	30.50	1.221	0.036	0.043	1.121	2.83E+02	5.32E-05	8.93E-01	1.12E+03	5.62E-05	2.41E-01
	49.95	0.953	0.034	0.032	1.120	2.51E+02	4.40E-05	8.93E-01	1.35E+02	3.13E-04	3.03E-01
	69.37	0.885	0.027	0.024	1.101	2.36E+02	4.04E-05	9.08E-01	6.15E+03	6.64E-06	1.92E-01
	88.76	0.443	0.040	0.018	1.147	1.59E+02	3.00E-05	8.72E-01	1.49E+04	2.48E-06	1.62E-01
O_2	**11.20**	1.666	0.033	0.054	1.105	2.15E+00	2.32E-02	9.75E-01	3.54E+00	1.61E-02	7.43E-01
	30.58	1.473	0.026	0.039	1.086	2.49E+00	1.33E-02	9.64E-01	1.95E+01	2.18E-03	4.83E-01
	50.02	0.975	0.030	0.029	1.100	2.12E+00	1.09E-02	9.46E-01	3.10E+01	1.10E-03	3.99E-01
	69.44	1.509	0.014	0.021	1.057	3.58E+01	3.96E-04	9.47E-01	2.12E+02	1.10E-04	3.62E-01
	88.79	0.479	0.037	0.018	1.130	7.49E+00	1.13E-03	8.90E-01	1.75E+02	1.46E-04	2.61E-01
Ar	**11.14**	1.043	0.058	0.060	1.193	1.98E+01	1.04E-03	8.44E-01	2.25E+04	7.39E-06	1.51E-01
	30.52	1.228	0.034	0.041	1.115	4.40E+02	3.24E-05	8.97E-01	1.03E+02	5.05E-04	3.31E-01
	49.93	1.026	0.030	0.031	1.108	2.16E+01	7.35E-04	9.06E-01	1.58E+02	2.50E-04	3.08E-01
	69.33	1.125	0.021	0.024	1.089	2.17E+02	4.84E-05	9.18E-01	1.71E+02	1.63E-04	3.25E-01
	88.70	0.510	0.037	0.019	1.128	2.05E+00	5.83E-03	9.10E-01	5.11E-01	3.73E-02	9.88E-01

AIV.5. Bibliography

1. Rao, A. V., Kalesh, R. R. & Pajonk, G. M. Hydrophobicity and Physical Properties of TEOS Based Silica Aerogels using Phenyltriethoxysilane as a Synthesis Component. *J. Mater. Sci.* **38,** 4407–4413 (2003).

2. Wagh, P. B. & Ingale, S. V. Comparison of Some Physico-Chemical Properties of Hydrophilic and Hydrophobic Silica Aerogels. *Ceram. Int.* **28,** 43–50 (2002).

3. Venkateswara Rao, A., Kulkarni, M. M., Amalnerkar, D. P. & Seth, T. Surface Chemical Modification of Silica Aerogels using Various Alkyl-Alkoxy/Chloro Silanes. *Appl. Surf. Sci.* **206,** 262–270 (2003).

4. Gorle, B. S. K., Smirnova, I. & McHugh, M. A. Adsorption and Thermal Release of Highly Volatile Compounds in Silica Aerogels. *J. Supercrit. Fluids* **48,** 85–92 (2009).

Appendix V

Supplementary Information

for

"Effect of Pore Size and Heterogeneous Surface on the Adsorption of CO_2, N_2, O_2, and Ar on Carbon Aerogel, RF Aerogel, and Activated Carbons"

Sean M.W. Wilson, Fatma Al-Enzi, Vida A. Gabriel, and F. Handan Tezel

Department of Chemical and Biological Engineering, University of Ottawa, 161 Louis-Pasteur, Ottawa, Ontario K1N 6N5 Canada

Submitted to: Microporous and Mesoporous Materials 2020

Contents

AV.1. Gravimetric System

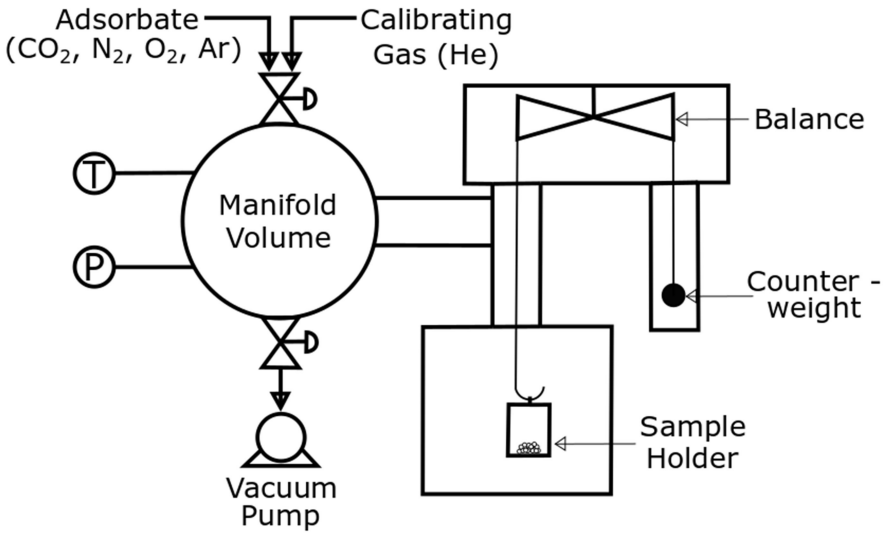

Figure AV.1 - Schematic diagram of the VTI Scientific Instruments GHP Gravimetric system that is used in this study.

AV.2. Isotherms Data Points

Table AV.1 – Carbon dioxide equilibrium adsorption capacities for carbon aerogel. Exact temperature for the isotherm is included above each isotherm.

11.04 °C		30.57 °C		50.19 °C		69.78 °C		89.34 °C	
Pressure Atm	q_e mmol/g	Pressure Atm	q_e mmol/g	Pressure Atm	q_e mmol/g	Pressure Atm	q_e mmol/g	Pressure Atm	q_e mmol/g
0.0000	0.0000	0.0000	0.0000	0.0000	0.0000	0.0000	0.0000	0.0000	0.0000
0.0332	0.4553	0.0333	0.2557	0.0333	0.1426	0.0333	0.0833	0.0332	0.0500
0.0664	0.7130	0.0665	0.4270	0.0665	0.2520	0.0665	0.1521	0.0665	0.0935
0.1328	1.0599	0.1327	0.6783	0.1328	0.4261	0.1329	0.2691	0.1328	0.1714
0.1939	1.2913	0.1993	0.8696	0.1993	0.5670	0.1992	0.3685	0.1992	0.2406
0.4008	1.8133	0.3971	1.2738	0.3968	0.8813	0.3958	0.6047	0.3967	0.4144
0.7968	2.4051	0.7902	1.7843	0.7919	1.3079	0.7924	0.9497	0.7883	0.6807
1.5330	3.0917	1.5349	2.3812	1.5343	1.8294	1.5387	1.3872	1.5394	1.0471
3.2109	3.8787	3.2139	3.1181	3.2174	2.5061	3.2103	2.0028	3.2122	1.5832
6.3761	4.7814	6.3771	3.9172	6.3782	3.2394	6.3895	2.6961	6.3886	2.2172
1.5449	3.1120	1.5430	2.3931	1.5324	1.8343	1.5680	1.4060	1.5368	1.0499
0.4033	1.8433	0.3954	1.2856	0.3982	0.8945	0.4039	0.6220	0.3992	0.4241

Table AV.2 – Nitrogen equilibrium adsorption capacities for carbon aerogel. Exact temperature for the isotherm is included above each isotherm.

10.87 °C		30.51 °C		50.19 °C		69.81 °C		89.41 °C	
Pressure Atm	q_e mmol/g	Pressure Atm	q_e mmol/g	Pressure Atm	q_e mmol/g	Pressure Atm	q_e mmol/g	Pressure Atm	q_e mmol/g
0.0000	0.0000	0.0000	0.0000	0.0000	0.0000	0.0000	0.0000	0.0000	0.0000
0.0333	0.0225	0.0333	0.0149	0.0333	0.0106	0.0333	0.0088	0.0333	0.0079
0.0666	0.0448	0.0665	0.0285	0.0665	0.0197	0.0665	0.0154	0.0666	0.0125
0.1330	0.0861	0.1330	0.0547	0.1329	0.0371	0.1329	0.0271	0.1329	0.0212
0.1995	0.1248	0.1996	0.0798	0.1997	0.0538	0.1993	0.0387	0.1992	0.0299
0.3934	0.2242	0.3979	0.1489	0.3985	0.1015	0.3973	0.0725	0.3972	0.0540
0.7676	0.3828	0.7938	0.2686	0.7942	0.1880	0.7915	0.1343	0.7959	0.1008
1.5405	0.6292	1.5403	0.4507	1.5435	0.3275	1.5428	0.2398	1.5387	0.1780
3.2177	0.9962	3.2240	0.7536	3.2172	0.5714	3.2202	0.4292	3.2176	0.3338
6.3906	1.4372	6.3888	1.1370	6.3945	0.8979	6.3940	0.7099	6.3960	0.5640
1.5217	0.6281	1.5634	0.4571	1.5396	0.3277	1.5138	0.2358	1.5300	0.1764
0.3932	0.2312	0.3989	0.1522	0.3940	0.1026	0.4045	0.0749	0.4079	0.0559

Table AV.3 – Oxygen equilibrium adsorption capacities for carbon aerogel. Exact temperature for the isotherm is included above each isotherm.

10.90 °C		30.55 °C		50.22 °C		69.85 °C		89.44 °C	
Pressure Atm	q_e mmol/g	Pressure Atm	q_e mmol/g	Pressure Atm	q_e mmol/g	Pressure Atm	q_e mmol/g	Pressure Atm	q_e mmol/g
0.0000	0.0000	0.0000	0.0000	0.0000	0.0000	0.0000	0.0000	0.0000	0.0000
0.0333	0.0240	0.0333	0.0141	0.0333	0.0103	0.0333	0.0087	0.0333	0.0082
0.0666	0.0457	0.0666	0.0273	0.0666	0.0190	0.0666	0.0154	0.0666	0.0130
0.1329	0.0853	0.1331	0.0517	0.1330	0.0353	0.1331	0.0270	0.1329	0.0216
0.1994	0.1230	0.1993	0.0759	0.1993	0.0514	0.1995	0.0383	0.1995	0.0302
0.3992	0.2249	0.3994	0.1432	0.3978	0.0975	0.3985	0.0716	0.3985	0.0548
0.7764	0.3903	0.7773	0.2582	0.7776	0.1795	0.7751	0.1303	0.7753	0.0989
1.5326	0.6542	1.5357	0.4546	1.5326	0.3241	1.5327	0.2388	1.5479	0.1822
3.2003	1.0743	3.2004	0.7876	3.2009	0.5864	3.1994	0.4434	3.2023	0.3398
6.3785	1.6095	6.3794	1.2401	6.3805	0.9637	6.3819	0.7505	6.3819	0.5898
1.5269	0.6608	1.5433	0.4634	1.5419	0.3341	1.5350	0.2491	1.5252	0.1948
0.4062	0.2423	0.3976	0.1536	0.4032	0.1105	0.3988	0.0860	0.3935	0.0740

Table AV.4 – Argon equilibrium adsorption capacities for carbon aerogel. Exact temperature for the isotherm is included above each isotherm.

11.01 °C		30.59 °C		50.23 °C		69.80 °C		89.39 °C	
Pressure Atm	q_e mmol/g	Pressure Atm	q_e mmol/g	Pressure Atm	q_e mmol/g	Pressure Atm	q_e mmol/g	Pressure Atm	q_e mmol/g
0.0000	0.0000	0.0000	0.0000	0.0000	0.0000	0.0000	0.0000	0.0000	0.0000
0.0333	0.0313	0.0333	0.0155	0.0333	0.0103	0.0333	0.0077	0.0333	0.0073
0.0666	0.0549	0.0665	0.0292	0.0666	0.0195	0.0665	0.0139	0.0665	0.0118
0.1331	0.0968	0.1330	0.0548	0.1330	0.0361	0.1331	0.0254	0.1330	0.0202
0.1995	0.1346	0.1992	0.0786	0.1994	0.0525	0.1994	0.0367	0.1994	0.0284
0.3979	0.2366	0.3979	0.1465	0.3977	0.0990	0.3978	0.0695	0.3971	0.0524
0.7958	0.4073	0.7956	0.2672	0.7953	0.1850	0.7935	0.1315	0.7982	0.0990
1.5376	0.6569	1.5399	0.4570	1.5363	0.3264	1.5395	0.2381	1.5421	0.1780
3.2182	1.0636	3.2194	0.7864	3.2106	0.5856	3.2141	0.4416	3.2123	0.3354
6.3888	1.5758	6.3859	1.2269	6.3801	0.9522	6.3884	0.7521	6.3908	0.5870
1.5479	0.6540	1.5521	0.4581	1.5429	0.3260	1.5447	0.2393	1.5472	0.1774
0.4024	0.2303	0.4073	0.1489	0.3980	0.0986	0.3965	0.0703	0.4025	0.0541

Table AV.5 – Carbon dioxide equilibrium adsorption capacities for RF aerogel. Exact temperature for the isotherm is included above each isotherm.

10.94 °C		30.53 °C		50.18 °C		69.76 °C		89.34 °C	
Pressure Atm	q_e mmol/g	Pressure Atm	q_e mmol/g	Pressure Atm	q_e mmol/g	Pressure Atm	q_e mmol/g	Pressure Atm	q_e mmol/g
0.0000	0.0000	0.0000	0.0000	0.0000	0.0000	0.0000	0.0000	0.0000	0.0000
0.0332	0.1600	0.0333	0.0844	0.0333	0.0471	0.0333	0.0291	0.0333	0.0233
0.0671	0.2647	0.0666	0.1447	0.0665	0.0809	0.0665	0.0479	0.0665	0.0347
0.1330	0.4094	0.1328	0.2391	0.1330	0.1394	0.1328	0.0825	0.1328	0.0555
0.1928	0.5085	0.1992	0.3146	0.1991	0.1888	0.1992	0.1137	0.1995	0.0756
0.3969	0.7501	0.3965	0.4844	0.3976	0.3097	0.3969	0.1948	0.3968	0.1294
0.7989	1.0665	0.7973	0.7242	0.7882	0.4867	0.7887	0.3231	0.7908	0.2200
1.5344	1.4682	1.5343	1.0329	1.5318	0.7281	1.5350	0.5067	1.5403	0.3562
3.2122	2.0870	3.2155	1.5084	3.1848	1.0991	3.2137	0.8038	3.2195	0.5983
6.3830	2.9357	6.3802	2.1493	6.3784	1.6243	6.3814	1.2359	6.3793	0.9647
1.5338	1.4782	1.5437	1.0426	1.5730	0.7466	1.5424	0.5127	1.5683	0.3704
0.3935	0.7604	0.3993	0.4946	0.3932	0.3138	0.3981	0.2009	0.4003	0.1362

Table AV.6 – Nitrogen equilibrium adsorption capacities for RF aerogel. Exact temperature for the isotherm is included above each isotherm.

11.01 °C		30.53 °C		50.20 °C		69.84 °C		89.42 °C	
Pressure Atm	q_e mmol/g	Pressure Atm	q_e mmol/g	Pressure Atm	q_e mmol/g	Pressure Atm	q_e mmol/g	Pressure Atm	q_e mmol/g
0.0000	0.0000	0.0000	0.0000	0.0000	0.0000	0.0000	0.0000	0.0000	0.0000
0.0333	0.0159	0.0333	0.0084	0.0333	0.0053	0.0333	0.0038	0.0333	0.0028
0.0666	0.0218	0.0665	0.0116	0.0665	0.0073	0.0666	0.0055	0.0665	0.0046
0.1330	0.0322	0.1329	0.0173	0.1329	0.0112	0.1330	0.0079	0.1331	0.0068
0.1992	0.0401	0.1991	0.0220	0.1991	0.0143	0.1996	0.0103	0.1994	0.0090
0.3986	0.0661	0.3977	0.0374	0.3973	0.0243	0.3977	0.0179	0.3975	0.0154
0.7975	0.1093	0.7915	0.0627	0.7912	0.0416	0.7939	0.0308	0.7937	0.0250
1.5439	0.1763	1.5417	0.1073	1.5453	0.0741	1.5360	0.0523	1.5366	0.0377
3.2212	0.3001	3.2162	0.1948	3.2186	0.1376	3.2174	0.0940	3.2195	0.0819
6.3966	0.4851	6.3854	0.3287	6.3961	0.2415	6.3909	0.1590	6.3927	0.1324
1.5194	0.1602	1.5343	0.1012	1.5271	0.0695	1.5174	0.0496	1.5376	0.0349
0.4019	0.0555	0.4041	0.0349	0.3944	0.0228	0.4011	0.0169	0.4050	0.0144

Table AV.7 – Oxygen equilibrium adsorption capacities for RF aerogel. Exact temperature for the isotherm is included above each isotherm.

10.85 °C		30.52 °C		50.22 °C		69.87 °C		89.43 °C	
Pressure Atm	q_e mmol/g	Pressure Atm	q_e mmol/g	Pressure Atm	q_e mmol/g	Pressure Atm	q_e mmol/g	Pressure Atm	q_e mmol/g
0.0000	0.0000	0.0000	0.0000	0.0000	0.0000	0.0000	0.0000	0.0000	0.0000
0.0334	0.0133	0.0333	0.0107	0.0333	0.0050	0.0333	0.0043	0.0333	0.0029
0.0665	0.0199	0.0665	0.0168	0.0666	0.0098	0.0666	0.0082	0.0666	0.0056
0.1329	0.0315	0.1330	0.0261	0.1329	0.0193	0.1329	0.0146	0.1331	0.0105
0.1997	0.0425	0.1995	0.0356	0.1996	0.0289	0.1994	0.0212	0.1993	0.0145
0.4014	0.0734	0.3975	0.0588	0.4007	0.0515	0.3997	0.0352	0.3999	0.0275
0.7770	0.1237	0.7754	0.0975	0.7748	0.0837	0.7795	0.0592	0.7756	0.0430
1.5351	0.2147	1.5317	0.1682	1.5329	0.1429	1.5355	0.1009	1.5322	0.0783
3.2021	0.3834	3.1874	0.3020	3.1990	0.2538	3.2013	0.1769	3.2000	0.1507
6.3781	0.6362	6.3790	0.5142	6.3799	0.4225	6.3798	0.3113	6.3785	0.2627
1.5334	0.2317	1.5257	0.1855	1.5433	0.1633	1.5320	0.1170	1.5464	0.0981
0.3944	0.1014	0.4073	0.0802	0.4049	0.0704	0.3970	0.0515	0.4014	0.0446

Table AV.8 – Argon equilibrium adsorption capacities for RF aerogel. Exact temperature for the isotherm is included above each isotherm.

10.94 °C		30.54 °C		50.18 °C		69.80 °C		89.37 °C	
Pressure Atm	q_e mmol/g	Pressure Atm	q_e mmol/g	Pressure Atm	q_e mmol/g	Pressure Atm	q_e mmol/g	Pressure Atm	q_e mmol/g
0.0000	0.0000	0.0000	0.0000	0.0000	0.0000	0.0000	0.0000	0.0000	0.0000
0.0333	0.0078	0.0333	0.0054	0.0333	0.0039	0.0333	0.0034	0.0333	0.0026
0.0666	0.0124	0.0666	0.0086	0.0666	0.0062	0.0666	0.0053	0.0666	0.0048
0.1332	0.0218	0.1329	0.0145	0.1331	0.0098	0.1330	0.0084	0.1331	0.0072
0.1989	0.0302	0.1996	0.0202	0.1991	0.0145	0.1990	0.0116	0.1992	0.0100
0.3982	0.0570	0.3978	0.0368	0.3975	0.0262	0.3984	0.0205	0.3970	0.0167
0.7953	0.1045	0.7945	0.0671	0.7963	0.0484	0.7975	0.0371	0.7983	0.0293
1.5352	0.1842	1.5343	0.1200	1.5391	0.0872	1.5409	0.0641	1.5362	0.0449
3.2200	0.3386	3.2139	0.2284	3.2176	0.1692	3.2197	0.1264	3.2185	0.0922
6.3799	0.5660	6.3838	0.3935	6.3850	0.3035	6.3812	0.2244	6.3823	0.1679
1.5399	0.1820	1.5526	0.1184	1.5459	0.0849	1.5396	0.0615	1.5306	0.0460
0.4072	0.0572	0.3988	0.0365	0.3932	0.0255	0.3938	0.0186	0.4021	0.0161

Table AV.9 – Carbon dioxide equilibrium adsorption capacities for activated carbon clothe (ACC). Exact temperature for the isotherm is included above each isotherm.

10.93 °C		30.54 °C		50.17 °C		69.76 °C		89.33 °C	
Pressure Atm	q_e mmol/g	Pressure Atm	q_e mmol/g	Pressure Atm	q_e mmol/g	Pressure Atm	q_e mmol/g	Pressure Atm	q_e mmol/g
0.0000	0.0000	0.0000	0.0000	0.0000	0.0000	0.0000	0.0000	0.0000	0.0000
0.0333	0.3055	0.0333	0.1658	0.0333	0.0953	0.0333	0.0592	0.0333	0.0419
0.0666	0.5485	0.0665	0.3077	0.0665	0.1793	0.0665	0.1117	0.0666	0.0759
0.1326	0.9545	0.1331	0.5586	0.1329	0.3351	0.1330	0.2113	0.1329	0.1416
0.1989	1.3034	0.1992	0.7806	0.1994	0.4786	0.1993	0.3049	0.1995	0.2049
0.3958	2.1602	0.3971	1.3504	0.3971	0.8579	0.3971	0.5622	0.3968	0.3818
0.7933	3.5084	0.7944	2.2797	0.7886	1.4965	0.7899	1.0137	0.7931	0.7062
1.5361	5.3520	1.5326	3.6088	1.5430	2.4810	1.5342	1.7262	1.5363	1.2405
3.2098	8.0515	3.2118	5.7558	3.2156	4.1317	3.2126	3.0106	3.1835	2.2122
6.3761	10.8313	6.3814	8.2761	6.3826	6.2671	6.3847	4.7674	6.3798	3.6566
1.5422	5.3715	1.5532	3.6431	1.5431	2.4842	1.5337	1.7277	1.5477	1.2477
0.4015	2.1960	0.4021	1.3707	0.4000	0.8687	0.4084	0.5806	0.3997	0.3876

Table AV.10 – Nitrogen equilibrium adsorption capacities for activated carbon clothe (ACC). Exact temperature for the isotherm is included above each isotherm.

10.87 °C		30.53 °C		50.20 °C		69.84 °C		89.44 °C	
Pressure	q_e	Pressure	q_e	Pressure	q_e	Pressure	q_e	Pressure	q_e
Atm	mmol/g	Atm	mmol/g	Atm	mmol/g	Atm	mmol/g	Atm	mmol/g
0.0000	0.0000	0.0000	0.0000	0.0000	0.0000	0.0000	0.0000	0.0000	0.0000
0.0334	0.0280	0.0333	0.0184	0.0333	0.0145	0.0333	0.0122	0.0333	0.0116
0.0666	0.0508	0.0666	0.0333	0.0666	0.0241	0.0666	0.0196	0.0665	0.0173
0.1328	0.0930	0.1330	0.0612	0.1328	0.0429	0.1328	0.0334	0.1329	0.0276
0.1996	0.1331	0.1995	0.0878	0.1991	0.0614	0.1992	0.0471	0.1994	0.0379
0.3985	0.2483	0.3967	0.1650	0.3977	0.1159	0.3978	0.0871	0.3977	0.0682
0.7975	0.4595	0.7957	0.3125	0.7894	0.2190	0.7993	0.1652	0.7999	0.1276
1.5419	0.8003	1.5397	0.5616	1.5364	0.4026	1.5353	0.3003	1.5355	0.2296
3.2145	1.4147	3.2140	1.0343	3.2128	0.7647	3.2196	0.5764	3.2192	0.4470
6.3861	2.2803	6.3896	1.7345	6.3921	1.3304	6.3836	1.0325	6.3973	0.8219
1.5420	0.7893	1.5331	0.5524	1.5240	0.3971	1.5150	0.2948	1.5351	0.2289
0.4048	0.2434	0.3915	0.1593	0.4003	0.1156	0.3918	0.0850	0.3970	0.0681

Table AV.11 – Oxygen equilibrium adsorption capacities for activated carbon clothe (ACC). Exact temperature for the isotherm is included above each isotherm.

10.88 °C		30.52 °C		50.18 °C		69.81 °C		89.43 °C	
Pressure	q_e	Pressure	q_e	Pressure	q_e	Pressure	q_e	Pressure	q_e
Atm	mmol/g	Atm	mmol/g	Atm	mmol/g	Atm	mmol/g	Atm	mmol/g
0.0000	0.0000	0.0000	0.0000	0.0000	0.0000	0.0000	0.0000	0.0000	0.0000
0.0334	0.0195	0.0333	0.0123	0.0333	0.0091	0.0333	0.0069	0.0333	0.0059
0.0666	0.0386	0.0666	0.0245	0.0666	0.0178	0.0666	0.0133	0.0665	0.0113
0.1328	0.0743	0.1330	0.0482	0.1330	0.0348	0.1302	0.0253	0.1328	0.0209
0.1994	0.1094	0.1991	0.0719	0.1994	0.0515	0.1958	0.0371	0.1995	0.0306
0.3972	0.2097	0.4012	0.1419	0.3976	0.1007	0.4009	0.0754	0.3988	0.0587
0.7764	0.3935	0.7770	0.2686	0.7745	0.1929	0.7776	0.1441	0.7765	0.1116
1.5338	0.7394	1.5342	0.5146	1.5337	0.3699	1.5306	0.2766	1.5341	0.2145
3.2010	1.3686	3.1986	0.9823	3.1991	0.7263	3.1988	0.5500	3.1978	0.4288
6.3813	2.3344	6.3803	1.7339	6.3796	1.3195	6.3803	1.0243	6.3687	0.8061
1.5372	0.7426	1.5210	0.5118	1.5375	0.3723	1.5295	0.2780	1.5200	0.2148
0.3990	0.2151	0.3982	0.1435	0.3962	0.1035	0.3962	0.0777	0.3948	0.0624

Table AV.12 – Argon equilibrium adsorption capacities for activated carbon clothe (ACC). Exact temperature for the isotherm is included above each isotherm.

10.95 °C		30.54 °C		50.20 °C		69.81 °C		89.39 °C	
Pressure	q_e	Pressure	q_e	Pressure	q_e	Pressure	q_e	Pressure	q_e
Atm	mmol/g	Atm	mmol/g	Atm	mmol/g	Atm	mmol/g	Atm	mmol/g
0.0000	0.0000	0.0000	0.0000	0.0000	0.0000	0.0000	0.0000	0.0000	0.0000
0.0333	0.0185	0.0333	0.0136	0.0333	0.0115	0.0333	0.0096	0.0333	0.0095
0.0667	0.0362	0.0666	0.0255	0.0666	0.0197	0.0665	0.0159	0.0665	0.0142
0.1329	0.0707	0.1328	0.0489	0.1330	0.0364	0.1330	0.0286	0.1330	0.0240
0.2027	0.1066	0.1995	0.0719	0.1995	0.0528	0.1995	0.0406	0.1995	0.0335
0.3980	0.2033	0.3976	0.1395	0.3986	0.1013	0.3979	0.0764	0.3980	0.0612
0.7958	0.3902	0.7904	0.2687	0.7924	0.1954	0.7938	0.1472	0.7942	0.1159
1.5429	0.7348	1.5373	0.5032	1.5420	0.3689	1.5368	0.2751	1.5367	0.2146
3.2208	1.3390	3.2124	0.9593	3.2163	0.7170	3.2217	0.5386	3.2173	0.4228
6.3882	2.2489	6.3888	1.6779	6.3855	1.2831	6.3844	0.9867	6.3807	0.7818
1.5485	0.7352	1.5317	0.4996	1.5773	0.3750	1.5398	0.2751	1.5303	0.2122
0.3995	0.2044	0.3929	0.1372	0.3990	0.1007	0.3921	0.0755	0.3931	0.0606

Table AV.13 – Carbon dioxide equilibrium adsorption capacities for BPL. Exact temperature for the isotherm is included above each isotherm.

10.97 °C		30.54 °C		50.16 °C		69.77 °C		89.33 °C	
Pressure	q_e	Pressure	q_e	Pressure	q_e	Pressure	q_e	Pressure	q_e
Atm	mmol/g	Atm	mmol/g	Atm	mmol/g	Atm	mmol/g	Atm	mmol/g
0.0000	0.0000	0.0000	0.0000	0.0000	0.0000	0.0000	0.0000	0.0000	0.0000
0.0333	0.2817	0.0333	0.1560	0.0333	0.0884	0.0333	0.0530	0.0333	0.0334
0.0665	0.4725	0.0665	0.2750	0.0666	0.1623	0.0665	0.0990	0.0665	0.0629
0.1328	0.7657	0.1328	0.4685	0.1330	0.2895	0.1329	0.1820	0.1328	0.1180
0.1993	1.0019	0.1993	0.6305	0.1993	0.3995	0.1994	0.2574	0.1992	0.1694
0.3888	1.5256	0.3963	1.0145	0.3968	0.6731	0.3962	0.4509	0.3974	0.3073
0.7952	2.3421	0.7899	1.5935	0.7922	1.1030	0.7902	0.7685	0.7889	0.5408
1.5385	3.3773	1.5360	2.3868	1.5343	1.7058	1.5393	1.2372	1.5357	0.9035
3.2117	4.8390	3.2129	3.5897	3.2150	2.6759	3.2145	2.0178	3.2102	1.5299
6.3810	6.3737	6.3845	4.9736	6.3848	3.8729	6.3853	3.0363	6.3891	2.3822
1.5426	3.3953	1.5523	2.4068	1.5418	1.7143	1.5404	1.2404	1.5436	0.9105
0.4074	1.5869	0.3982	1.0272	0.3978	0.6815	0.3995	0.4596	0.3920	0.3086

Table AV.14 – Nitrogen equilibrium adsorption capacities for BPL. Exact temperature for the isotherm is included above each isotherm.

10.88 °C		30.52 °C		50.18 °C		69.81 °C		89.40 °C	
Pressure	q_e	Pressure	q_e	Pressure	q_e	Pressure	q_e	Pressure	q_e
Atm	mmol/g	Atm	mmol/g	Atm	mmol/g	Atm	mmol/g	Atm	mmol/g
0.0000	0.0000	0.0000	0.0000	0.0000	0.0000	0.0000	0.0000	0.0000	0.0000
0.0334	0.0238	0.0333	0.0145	0.0333	0.0103	0.0333	0.0080	0.0333	0.0075
0.0666	0.0424	0.0665	0.0260	0.0665	0.0178	0.0665	0.0133	0.0665	0.0116
0.1332	0.0764	0.1330	0.0474	0.1330	0.0321	0.1328	0.0234	0.1330	0.0191
0.1990	0.1069	0.1996	0.0679	0.1995	0.0460	0.1993	0.0334	0.1996	0.0267
0.3977	0.1936	0.3980	0.1260	0.3977	0.0863	0.3982	0.0627	0.3978	0.0486
0.7932	0.3433	0.7946	0.2318	0.7971	0.1628	0.7910	0.1183	0.7898	0.0903
1.5370	0.5750	1.5354	0.4030	1.5418	0.2919	1.5432	0.2173	1.5385	0.1649
3.2169	0.9724	3.2154	0.7153	3.2158	0.5368	3.1871	0.4009	3.2103	0.3147
6.3850	1.5021	6.3896	1.1534	6.3847	0.8976	6.3836	0.7044	6.3959	0.5604
1.5638	0.5769	1.5415	0.4023	1.5231	0.2883	1.5663	0.2188	1.5331	0.1640
0.4044	0.1902	0.4022	0.1261	0.3922	0.0857	0.3955	0.0628	0.4061	0.0499

Table AV.15 – Oxygen equilibrium adsorption capacities for BPL. Exact temperature for the isotherm is included above each isotherm.

10.89 °C		30.52 °C		50.19 °C		69.82 °C		89.44 °C	
Pressure	q_e	Pressure	q_e	Pressure	q_e	Pressure	q_e	Pressure	q_e
Atm	mmol/g	Atm	mmol/g	Atm	mmol/g	Atm	mmol/g	Atm	mmol/g
0.0000	0.0000	0.0000	0.0000	0.0000	0.0000	0.0000	0.0000	0.0000	0.0000
0.0333	0.0156	0.0333	0.0111	0.0333	0.0089	0.0333	0.0080	0.0333	0.0075
0.0666	0.0307	0.0665	0.0208	0.0666	0.0157	0.0677	0.0130	0.0666	0.0114
0.1331	0.0593	0.1332	0.0397	0.1313	0.0283	0.1329	0.0224	0.1288	0.0182
0.1996	0.0873	0.1990	0.0579	0.1950	0.0407	0.1995	0.0316	0.1938	0.0253
0.3993	0.1668	0.3994	0.1115	0.4029	0.0798	0.3995	0.0592	0.4010	0.0467
0.7782	0.3059	0.7750	0.2071	0.7763	0.1477	0.7749	0.1096	0.7746	0.0848
1.5318	0.5479	1.5313	0.3813	1.5303	0.2759	1.5341	0.2060	1.5340	0.1587
3.2023	0.9842	3.2022	0.7111	3.1994	0.5263	3.2006	0.3981	3.1986	0.3076
6.3789	1.6162	6.3784	1.2108	6.3805	0.9271	6.3814	0.7191	6.3837	0.5658
1.5385	0.5513	1.5274	0.3813	1.5429	0.2783	1.5345	0.2064	1.5209	0.1596
0.3914	0.1671	0.3927	0.1118	0.4056	0.0816	0.3973	0.0604	0.3992	0.0487

Table AV.16 – Argon equilibrium adsorption capacities for BPL. Exact temperature for the isotherm is included above each isotherm.

10.95 °C		30.53 °C		50.18 °C		69.78 °C		89.34 °C	
Pressure	q_e	Pressure	q_e	Pressure	q_e	Pressure	q_e	Pressure	q_e
Atm	mmol/g	Atm	mmol/g	Atm	mmol/g	Atm	mmol/g	Atm	mmol/g
0.0000	0.0000	0.0000	0.0000	0.0000	0.0000	0.0000	0.0000	0.0000	0.0000
0.0333	0.0143	0.0333	0.0109	0.0333	0.0087	0.0333	0.0076	0.0333	0.0075
0.0666	0.0285	0.0666	0.0203	0.0666	0.0153	0.0666	0.0124	0.0666	0.0112
0.1331	0.0560	0.1330	0.0386	0.1329	0.0280	0.1331	0.0216	0.1331	0.0183
0.1995	0.0827	0.1995	0.0566	0.1997	0.0407	0.1995	0.0308	0.1997	0.0252
0.3976	0.1583	0.3978	0.1084	0.3975	0.0771	0.3977	0.0578	0.3975	0.0456
0.7956	0.2980	0.7888	0.2048	0.7902	0.1471	0.7899	0.1097	0.7929	0.0853
1.5339	0.5239	1.5405	0.3731	1.5452	0.2725	1.5366	0.2035	1.5374	0.1563
3.2161	0.9414	3.2169	0.6919	3.2191	0.5179	3.2248	0.3946	3.2154	0.3031
6.3878	1.5359	6.3779	1.1686	6.3791	0.9009	6.3797	0.7035	6.3900	0.5519
1.5467	0.5282	1.5376	0.3724	1.5428	0.2719	1.5360	0.2023	1.5363	0.1544
0.4007	0.1613	0.3994	0.1096	0.3976	0.0779	0.3988	0.0582	0.3993	0.0462

Table AV.17 – Carbon dioxide equilibrium adsorption capacities for F-600. Exact temperature for the isotherm is included above each isotherm.

10.96 °C		30.54 °C		50.18 °C		69.76 °C		89.34 °C	
Pressure	q_e	Pressure	q_e	Pressure	q_e	Pressure	q_e	Pressure	q_e
Atm	mmol/g	Atm	mmol/g	Atm	mmol/g	Atm	mmol/g	Atm	mmol/g
0.0000	0.0000	0.0000	0.0000	0.0000	0.0000	0.0000	0.0000	0.0000	0.0000
0.0333	0.3389	0.0333	0.1868	0.0333	0.1059	0.0333	0.0617	0.0332	0.0391
0.0665	0.5607	0.0665	0.3258	0.0665	0.1917	0.0665	0.1148	0.0665	0.0725
0.1329	0.8907	0.1326	0.5459	0.1331	0.3373	0.1328	0.2096	0.1326	0.1342
0.1995	1.1475	0.1995	0.7271	0.1995	0.4612	0.1990	0.2939	0.1990	0.1917
0.3970	1.7108	0.3962	1.1382	0.3958	0.7586	0.3971	0.5077	0.3975	0.3431
0.7896	2.4681	0.7866	1.7191	0.7882	1.2033	0.7908	0.8434	0.7905	0.5918
1.5330	3.3750	1.5358	2.4566	1.5422	1.8008	1.5359	1.3121	1.5338	0.9615
3.2112	4.4718	3.2141	3.4625	3.2132	2.6599	3.2128	2.0415	3.2176	1.5598
6.3833	5.4406	6.3785	4.4531	6.3824	3.6044	6.3854	2.8946	6.3821	2.3073
1.5553	3.4050	1.5395	2.4643	1.5457	1.8063	1.5320	1.3128	1.5374	0.9659
0.4072	1.7528	0.4022	1.1587	0.3996	0.7709	0.4007	0.5177	0.3998	0.3509

Table AV.18 – Nitrogen equilibrium adsorption capacities for F-600. Exact temperature for the isotherm is included above each isotherm.

10.87 °C		30.53 °C		50.20 °C		69.82 °C		89.41 °C	
Pressure Atm	q_e mmol/g	Pressure Atm	q_e mmol/g	Pressure Atm	q_e mmol/g	Pressure Atm	q_e mmol/g	Pressure Atm	q_e mmol/g
0.0000	0.0000	0.0000	0.0000	0.0000	0.0000	0.0000	0.0000	0.0000	0.0000
0.0333	0.0285	0.0333	0.0148	0.0333	0.0110	0.0333	0.0088	0.0333	0.0079
0.0666	0.0505	0.0665	0.0273	0.0666	0.0195	0.0666	0.0146	0.0665	0.0123
0.1331	0.0894	0.1331	0.0513	0.1330	0.0356	0.1328	0.0258	0.1330	0.0203
0.1994	0.1247	0.1993	0.0740	0.1995	0.0511	0.1993	0.0366	0.1991	0.0283
0.3979	0.2223	0.3976	0.1385	0.3978	0.0960	0.3974	0.0684	0.3980	0.0517
0.7924	0.3871	0.7943	0.2545	0.7958	0.1792	0.7975	0.1291	0.7894	0.0960
1.5365	0.6335	1.5356	0.4378	1.5394	0.3165	1.5444	0.2327	1.5363	0.1734
3.2186	1.0355	3.2216	0.7595	3.1870	0.5653	3.2168	0.4265	3.2180	0.3287
6.3889	1.5381	6.3880	1.1844	6.3879	0.9217	6.3907	0.7274	6.3889	0.5717
1.5191	0.6215	1.5348	0.4362	1.5250	0.3120	1.5170	0.2277	1.5323	0.1733
0.3973	0.2143	0.3942	0.1374	0.3999	0.0957	0.4059	0.0697	0.3963	0.0519

Table AV.19 – Oxygen equilibrium adsorption capacities for F-600. Exact temperature for the isotherm is included above each isotherm.

10.87 °C		30.52 °C		50.21 °C		69.83 °C		89.43 °C	
Pressure Atm	q_e mmol/g	Pressure Atm	q_e mmol/g	Pressure Atm	q_e mmol/g	Pressure Atm	q_e mmol/g	Pressure Atm	q_e mmol/g
0.0000	0.0000	0.0000	0.0000	0.0000	0.0000	0.0000	0.0000	0.0000	0.0000
0.0333	0.0178	0.0333	0.0123	0.0333	0.0091	0.0333	0.0074	0.0333	0.0064
0.0666	0.0351	0.0666	0.0230	0.0666	0.0163	0.0665	0.0126	0.0666	0.0107
0.1330	0.0677	0.1329	0.0439	0.1329	0.0304	0.1330	0.0225	0.1329	0.0180
0.1994	0.0990	0.1992	0.0639	0.1992	0.0438	0.1995	0.0323	0.1994	0.0252
0.4002	0.1868	0.3990	0.1220	0.3973	0.0841	0.3979	0.0609	0.4016	0.0470
0.7770	0.3353	0.7763	0.2247	0.7777	0.1580	0.7772	0.1142	0.7743	0.0860
1.5353	0.5869	1.5356	0.4075	1.5320	0.3013	1.5314	0.2149	1.5314	0.1607
3.1969	1.0111	3.2027	0.7350	3.2010	0.5526	3.1993	0.4069	3.2006	0.3124
6.3786	1.5857	6.3805	1.2048	6.3780	0.9325	6.3787	0.7196	6.3826	0.5595
1.5340	0.5896	1.5235	0.4071	1.5280	0.3027	1.5329	0.2172	1.5259	0.1630
0.4044	0.1944	0.4033	0.1270	0.3941	0.0869	0.3928	0.0636	0.3966	0.0509

Table AV.20 – Argon equilibrium adsorption capacities for F-600. Exact temperature for the isotherm is included above each isotherm.

10.90 °C		30.54 °C		50.20 °C		69.84 °C		89.41 °C	
Pressure	q_e	Pressure	q_e	Pressure	q_e	Pressure	q_e	Pressure	q_e
Atm	mmol/g	Atm	mmol/g	Atm	mmol/g	Atm	mmol/g	Atm	mmol/g
0.0000	0.0000	0.0000	0.0000	0.0000	0.0000	0.0000	0.0000	0.0000	0.0000
0.0333	0.0114	0.0333	0.0111	0.0333	0.0096	0.0333	0.0091	0.0333	0.0071
0.0666	0.0330	0.0666	0.0218	0.0666	0.0168	0.0666	0.0141	0.0665	0.0110
0.1331	0.0665	0.1330	0.0419	0.1328	0.0306	0.1330	0.0237	0.1329	0.0183
0.1995	0.0965	0.1994	0.0613	0.1993	0.0436	0.1991	0.0332	0.1995	0.0253
0.4042	0.1796	0.3985	0.1160	0.3975	0.0817	0.3985	0.0605	0.3987	0.0460
0.7863	0.3169	0.7945	0.2168	0.7942	0.1542	0.7904	0.1126	0.7916	0.0852
1.5387	0.5629	1.5387	0.3878	1.5361	0.2781	1.5417	0.2053	1.5422	0.1546
3.2121	0.9496	3.2195	0.6959	3.2203	0.5172	3.2165	0.3886	3.2198	0.2968
6.3830	1.4753	6.3766	1.1322	6.3748	0.8797	6.3881	0.6810	6.3790	0.5342
1.5760	0.5749	1.5378	0.3894	1.5436	0.2790	1.5353	0.2050	1.5491	0.1546
0.3959	0.1795	0.4067	0.1210	0.3990	0.0819	0.3985	0.0612	0.4028	0.0464

Table AV.21 – Carbon dioxide equilibrium adsorption capacities for M-30. Exact temperature for the isotherm is included above each isotherm.

10.95 °C		30.54 °C		50.17 °C		69.78 °C		89.34 °C	
Pressure	q_e	Pressure	q_e	Pressure	q_e	Pressure	q_e	Pressure	q_e
Atm	mmol/g	Atm	mmol/g	Atm	mmol/g	Atm	mmol/g	Atm	mmol/g
0.0000	0.0000	0.0000	0.0000	0.0000	0.0000	0.0000	0.0000	0.0000	0.0000
0.0333	0.1770	0.0333	0.1018	0.0333	0.0620	0.0333	0.0423	0.0333	0.0295
0.0665	0.3313	0.0665	0.1931	0.0665	0.1182	0.0665	0.0790	0.0665	0.0545
0.1329	0.6086	0.1329	0.3629	0.1329	0.2257	0.1330	0.1500	0.1328	0.1031
0.1992	0.8620	0.1993	0.5214	0.1995	0.3285	0.1993	0.2185	0.1990	0.1508
0.3961	1.5359	0.3957	0.9518	0.3967	0.6136	0.3961	0.4132	0.3959	0.2876
0.7850	2.7116	0.7855	1.7209	0.7879	1.1347	0.7897	0.7794	0.7895	0.5515
1.5325	4.6344	1.5323	3.0036	1.5382	2.0228	1.5373	1.4161	1.5379	1.0184
3.2154	8.0947	3.2092	5.4194	3.2158	3.7515	3.2106	2.6854	3.2121	1.9653
6.3788	12.7446	6.3844	8.9652	6.3893	6.4166	6.3802	4.7207	6.3811	3.5373
1.5429	4.6666	1.5543	3.0420	1.5511	2.0402	1.5491	1.4271	1.5379	1.0175
0.3994	1.5587	0.3938	0.9545	0.3958	0.6174	0.4059	0.4266	0.4028	0.2964

Table AV.22 – Nitrogen equilibrium adsorption capacities for M-30. Exact temperature for the isotherm is included above each isotherm.

10.94 °C		30.53 °C		50.19 °C		69.84 °C		89.41 °C	
Pressure Atm	q_e mmol/g	Pressure Atm	q_e mmol/g	Pressure Atm	q_e mmol/g	Pressure Atm	q_e mmol/g	Pressure Atm	q_e mmol/g
0.0000	0.0000	0.0000	0.0000	0.0000	0.0000	0.0000	0.0000	0.0000	0.0000
0.0333	0.0204	0.0333	0.0144	0.0333	0.0120	0.0333	0.0101	0.0333	0.0100
0.0665	0.0387	0.0666	0.0273	0.0666	0.0212	0.0666	0.0168	0.0665	0.0156
0.1330	0.0740	0.1330	0.0515	0.1330	0.0389	0.1330	0.0300	0.1329	0.0262
0.1996	0.1081	0.1995	0.0754	0.1994	0.0562	0.1996	0.0432	0.1990	0.0366
0.3978	0.2080	0.3982	0.1455	0.3973	0.1075	0.3981	0.0822	0.3978	0.0671
0.7934	0.3970	0.7965	0.2815	0.7964	0.2090	0.7977	0.1597	0.7907	0.1264
1.5403	0.7256	1.5416	0.5217	1.5411	0.3906	1.5406	0.2981	1.5364	0.2360
3.1867	1.3565	3.1905	0.9999	3.2134	0.7636	3.2243	0.5950	3.2210	0.4720
6.3884	2.3679	6.3859	1.7925	6.3931	1.3880	6.3842	1.0990	6.3879	0.8796
1.5413	0.7192	1.5309	0.5147	1.5210	0.3832	1.5364	0.2959	1.5284	0.2335
0.4066	0.2078	0.4037	0.1455	0.3988	0.1073	0.3942	0.0809	0.3931	0.0663

Table AV.23 – Oxygen equilibrium adsorption capacities for M-30. Exact temperature for the isotherm is included above each isotherm.

10.88 °C		30.53 °C		50.20 °C		69.84 °C		89.44 °C	
Pressure Atm	q_e mmol/g	Pressure Atm	q_e mmol/g	Pressure Atm	q_e mmol/g	Pressure Atm	q_e mmol/g	Pressure Atm	q_e mmol/g
0.0000	0.0000	0.0000	0.0000	0.0000	0.0000	0.0000	0.0000	0.0000	0.0000
0.0333	0.0190	0.0333	0.0126	0.0333	0.0105	0.0333	0.0096	0.0333	0.0084
0.0666	0.0356	0.0666	0.0236	0.0666	0.0186	0.0666	0.0160	0.0665	0.0137
0.1329	0.0670	0.1329	0.0451	0.1328	0.0346	0.1330	0.0282	0.1329	0.0235
0.1997	0.0983	0.1993	0.0664	0.1995	0.0505	0.1992	0.0402	0.1994	0.0333
0.3995	0.1880	0.4005	0.1303	0.4001	0.0976	0.3972	0.0761	0.3975	0.0615
0.7757	0.3538	0.7779	0.2483	0.7744	0.1848	0.7781	0.1442	0.7786	0.1152
1.5336	0.6961	1.5315	0.4795	1.5312	0.3556	1.5309	0.2749	1.5309	0.2196
3.1984	1.3200	3.1994	0.9455	3.2010	0.7136	3.1984	0.5496	3.2008	0.4374
6.3799	2.3588	6.3785	1.7407	6.3840	1.3346	6.3795	1.0509	6.3802	0.8415
1.5287	0.6971	1.5297	0.4811	1.5250	0.3565	1.5371	0.2792	1.5243	0.2227
0.3982	0.1954	0.4041	0.1360	0.3922	0.0999	0.4016	0.0822	0.4038	0.0690

Table AV.24 – Argon equilibrium adsorption capacities for M-30. Exact temperature for the isotherm is included above each isotherm.

10.94 °C		30.53 °C		50.18 °C		69.78 °C		89.36 °C	
Pressure Atm	q_e mmol/g	Pressure Atm	q_e mmol/g	Pressure Atm	q_e mmol/g	Pressure Atm	q_e mmol/g	Pressure Atm	q_e mmol/g
0.0000	0.0000	0.0000	0.0000	0.0000	0.0000	0.0000	0.0000	0.0000	0.0000
0.0333	0.0148	0.0333	0.0124	0.0333	0.0102	0.0333	0.0087	0.0333	0.0078
0.0667	0.0300	0.0666	0.0232	0.0666	0.0182	0.0665	0.0150	0.0665	0.0130
0.1332	0.0602	0.1331	0.0447	0.1330	0.0341	0.1330	0.0274	0.1330	0.0226
0.1996	0.0903	0.1995	0.0658	0.1993	0.0498	0.1996	0.0393	0.1995	0.0325
0.3977	0.1776	0.3984	0.1286	0.3980	0.0966	0.3977	0.0752	0.3976	0.0607
0.7999	0.3508	0.7892	0.2498	0.7898	0.1878	0.7900	0.1456	0.7911	0.1162
1.5328	0.6521	1.5424	0.4760	1.5413	0.3582	1.5430	0.2776	1.5354	0.2171
3.2211	1.2803	3.2235	0.9433	3.2154	0.7153	3.2148	0.5559	3.2199	0.4406
6.3855	2.3036	6.3816	1.7285	6.3854	1.3355	6.3836	1.0544	6.3875	0.8488
1.5363	0.6524	1.5476	0.4757	1.5445	0.3576	1.5385	0.2757	1.5284	0.2172
0.4044	0.1811	0.4006	0.1287	0.4075	0.0989	0.4065	0.0767	0.4051	0.0618

Table AV.25 – Carbon dioxide equilibrium adsorption capacities for NZ-AC. Exact temperature for the isotherm is included above each isotherm.

10.95 °C		30.53 °C		50.16 °C		69.75 °C		89.31 °C	
Pressure Atm	q_e mmol/g	Pressure Atm	q_e mmol/g	Pressure Atm	q_e mmol/g	Pressure Atm	q_e mmol/g	Pressure Atm	q_e mmol/g
0.0000	0.0000	0.0000	0.0000	0.0000	0.0000	0.0000	0.0000	0.0000	0.0000
0.0333	0.3755	0.0333	0.1886	0.0333	0.1153	0.0333	0.0750	0.0332	0.0513
0.0666	0.6176	0.0664	0.3298	0.0665	0.2033	0.0664	0.1319	0.0665	0.0898
0.1328	1.0033	0.1329	0.5693	0.1327	0.3562	0.1330	0.2331	0.1328	0.1587
0.1994	1.3288	0.1989	0.7766	0.1993	0.4935	0.1993	0.3251	0.1991	0.2222
0.3960	2.1131	0.3970	1.3003	0.3973	0.8475	0.3966	0.5683	0.3970	0.3932
0.7915	3.3433	0.7895	2.1397	0.7858	1.4294	0.7929	0.9895	0.7867	0.6924
1.5342	5.0859	1.5359	3.3898	1.5338	2.3311	1.5370	1.6440	1.5401	1.1886
3.2113	7.7907	3.2132	5.4362	3.2134	3.8872	3.2120	2.8312	3.2140	2.0989
6.3811	10.9933	6.3824	8.0589	6.3852	6.0005	6.3859	4.5337	6.3929	3.4530
1.5354	5.1172	1.5513	3.4296	1.5404	2.3457	1.5756	1.6827	1.5420	1.1949
0.4089	2.2018	0.4065	1.3498	0.3966	0.8587	0.3965	0.5776	0.4054	0.4083

Table AV.26 – Nitrogen equilibrium adsorption capacities for NZ-AC. Exact temperature for the isotherm is included above each isotherm.

10.88 °C		30.52 °C		50.18 °C		69.80 °C		89.38 °C	
Pressure Atm	q_e mmol/g	Pressure Atm	q_e mmol/g	Pressure Atm	q_e mmol/g	Pressure Atm	q_e mmol/g	Pressure Atm	q_e mmol/g
0.0000	0.0000	0.0000	0.0000	0.0000	0.0000	0.0000	0.0000	0.0000	0.0000
0.0333	0.0480	0.0333	0.0191	0.0333	0.0119	0.0333	0.0096	0.0333	0.0091
0.0665	0.0700	0.0665	0.0324	0.0665	0.0206	0.0666	0.0160	0.0666	0.0144
0.1330	0.1076	0.1330	0.0556	0.1331	0.0364	0.1328	0.0278	0.1330	0.0240
0.1995	0.1408	0.1994	0.0770	0.1995	0.0517	0.1992	0.0391	0.1993	0.0329
0.3980	0.2357	0.3976	0.1396	0.3982	0.0958	0.3976	0.0722	0.3982	0.0586
0.7978	0.4078	0.7883	0.2552	0.7910	0.1795	0.7919	0.1352	0.7940	0.1078
1.5464	0.6918	1.5426	0.4608	1.5417	0.3300	1.5452	0.2500	1.5369	0.1948
3.2113	1.2163	3.2158	0.8554	3.2127	0.6322	3.2198	0.4854	3.2184	0.3798
6.3867	1.9960	6.3872	1.4652	6.3861	1.1167	6.3936	0.8835	6.3979	0.6973
1.5184	0.6740	1.5327	0.4522	1.5228	0.3231	1.5175	0.2434	1.5346	0.1934
0.3972	0.2239	0.4075	0.1394	0.4015	0.0954	0.4006	0.0723	0.3951	0.0586

Table AV.27 – Oxygen equilibrium adsorption capacities for NZ-AC Exact temperature for the isotherm is included above each isotherm.

10.93 °C		30.56 °C		50.23 °C		69.84 °C		89.44 °C	
Pressure Atm	q_e mmol/g	Pressure Atm	q_e mmol/g	Pressure Atm	q_e mmol/g	Pressure Atm	q_e mmol/g	Pressure Atm	q_e mmol/g
0.0000	0.0000	0.0000	0.0000	0.0000	0.0000	0.0000	0.0000	0.0000	0.0000
0.0333	0.0631	0.0333	0.0136	0.0333	0.0114	0.0333	0.0103	0.0333	0.0080
0.0666	0.0832	0.0665	0.0242	0.0666	0.0191	0.0666	0.0166	0.0665	0.0129
0.1329	0.1158	0.1330	0.0441	0.1329	0.0332	0.1330	0.0276	0.1329	0.0206
0.1993	0.1464	0.1995	0.0633	0.1995	0.0474	0.1996	0.0386	0.1993	0.0279
0.3997	0.2284	0.3998	0.1187	0.3994	0.0876	0.3975	0.0690	0.4008	0.0481
0.7779	0.3741	0.7807	0.2195	0.7765	0.1613	0.7755	0.1254	0.7746	0.0832
1.5367	0.6426	1.5307	0.4082	1.5329	0.3033	1.5329	0.2337	1.5317	0.1517
3.2027	1.1583	3.1987	0.7872	3.2008	0.5908	3.2005	0.4514	3.1989	0.2949
6.3798	1.9777	6.3800	1.4123	6.3811	1.0761	6.3817	0.8384	6.3792	0.5394
1.5536	0.6616	1.5371	0.4205	1.5299	0.3139	1.5391	0.2480	1.5254	0.1516
0.4057	0.2567	0.3990	0.1365	0.3916	0.1038	0.4007	0.0893	0.3918	0.0501

Table AV.28 – Argon equilibrium adsorption capacities for NZ-AC. Exact temperature for the isotherm is included above each isotherm.

10.99 °C		30.57 °C		50.21 °C		69.82 °C		89.39 °C	
Pressure Atm	q_e mmol/g	Pressure Atm	q_e mmol/g	Pressure Atm	q_e mmol/g	Pressure Atm	q_e mmol/g	Pressure Atm	q_e mmol/g
0.0000	0.0000	0.0000	0.0000	0.0000	0.0000	0.0000	0.0000	0.0000	0.0000
0.0333	0.0173	0.0333	0.0119	0.0333	0.0077	0.0333	0.0063	0.0333	0.0057
0.0666	0.0329	0.0666	0.0219	0.0666	0.0145	0.0665	0.0115	0.0665	0.0101
0.1330	0.0616	0.1331	0.0411	0.1330	0.0282	0.1330	0.0219	0.1330	0.0184
0.1996	0.0894	0.1996	0.0597	0.1996	0.0415	0.1994	0.0319	0.1996	0.0266
0.3979	0.1686	0.3970	0.1140	0.3987	0.0813	0.3975	0.0619	0.3974	0.0500
0.7907	0.3183	0.8007	0.2215	0.7919	0.1583	0.7924	0.1207	0.7930	0.0959
1.5352	0.5816	1.5347	0.4068	1.5367	0.2990	1.5400	0.2283	1.5405	0.1784
3.2195	1.1052	3.2201	0.7927	3.2196	0.5942	3.2121	0.4528	3.2201	0.3605
6.3852	1.9226	6.3810	1.4168	6.3876	1.0870	6.3813	0.8448	6.3811	0.6755
1.5404	0.5830	1.5491	0.4087	1.5418	0.2990	1.5340	0.2265	1.5457	0.1769
0.3978	0.1709	0.3976	0.1139	0.4008	0.0819	0.4036	0.0629	0.4017	0.0506

Table AV.29 – Carbon dioxide equilibrium adsorption capacities for OLC. Exact temperature for the isotherm is included above each isotherm.

10.97 °C		30.55 °C		50.20 °C		69.80 °C		89.37 °C	
Pressure Atm	q_e mmol/g	Pressure Atm	q_e mmol/g	Pressure Atm	q_e mmol/g	Pressure Atm	q_e mmol/g	Pressure Atm	q_e mmol/g
0.0000	0.0000	0.0000	0.0000	0.0000	0.0000	0.0000	0.0000	0.0000	0.0000
0.0333	0.3948	0.0333	0.2162	0.0333	0.1220	0.0333	0.0725	0.0332	0.0450
0.0666	0.6595	0.0665	0.3793	0.0665	0.2223	0.0665	0.1347	0.0665	0.0846
0.1326	1.0602	0.1327	0.6432	0.1329	0.3943	0.1327	0.2462	0.1328	0.1578
0.1989	1.3804	0.1993	0.8634	0.1992	0.5430	0.1991	0.3469	0.1992	0.2264
0.3975	2.1052	0.3971	1.3805	0.3965	0.9092	0.3966	0.6055	0.3958	0.4076
0.7916	3.1091	0.7873	2.1284	0.7882	1.4695	0.7896	1.0226	0.7885	0.7150
1.5329	4.3470	1.5385	3.1217	1.5331	2.2412	1.5342	1.6241	1.5342	1.1832
3.2119	5.9150	3.2116	4.5042	3.2106	3.4076	3.2150	2.5910	3.2165	1.9700
6.3800	7.3411	6.3791	5.9309	6.3805	4.7310	6.3811	3.7604	6.3804	2.9824
1.5704	4.4050	1.5483	3.1366	1.5449	2.2545	1.5504	1.6364	1.5459	1.1909
0.3956	2.1148	0.4011	1.3980	0.4067	0.9326	0.3988	0.6131	0.3991	0.4150

Table AV.30 – Nitrogen equilibrium adsorption capacities for OLC. Exact temperature for the isotherm is included above each isotherm.

10.88 °C		30.51 °C		50.18 °C		69.79 °C		89.41 °C	
Pressure Atm	q_e mmol/g	Pressure Atm	q_e mmol/g	Pressure Atm	q_e mmol/g	Pressure Atm	q_e mmol/g	Pressure Atm	q_e mmol/g
0.0000	0.0000	0.0000	0.0000	0.0000	0.0000	0.0000	0.0000	0.0000	0.0000
0.0333	0.0338	0.0333	0.0177	0.0333	0.0120	0.0333	0.0096	0.0333	0.0081
0.0666	0.0593	0.0666	0.0326	0.0666	0.0216	0.0665	0.0162	0.0665	0.0135
0.1331	0.1048	0.1331	0.0606	0.1330	0.0400	0.1327	0.0293	0.1329	0.0232
0.1996	0.1458	0.1993	0.0867	0.1990	0.0581	0.1996	0.0422	0.1989	0.0327
0.3980	0.2604	0.3978	0.1632	0.3981	0.1107	0.3984	0.0798	0.3975	0.0605
0.7894	0.4553	0.7898	0.2998	0.7990	0.2103	0.7940	0.1517	0.7979	0.1146
1.5412	0.7577	1.5435	0.5276	1.5378	0.3756	1.5369	0.2764	1.5410	0.2077
3.1884	1.2507	3.2191	0.9237	3.2141	0.6851	3.2134	0.5178	3.2251	0.3954
6.3840	1.8985	6.3881	1.4649	6.3883	1.1321	6.3921	0.8950	6.3967	0.6955
1.5644	0.7589	1.5291	0.5195	1.5202	0.3692	1.5385	0.2757	1.5629	0.2083
0.4081	0.2554	0.4069	0.1639	0.3974	0.1094	0.3986	0.0798	0.4056	0.0612

Table AV.31 – Oxygen equilibrium adsorption capacities for OLC. Exact temperature for the isotherm is included above each isotherm.

10.89 °C		31.21 °C		50.17 °C		69.80 °C		89.39 °C	
Pressure Atm	q_e mmol/g	Pressure Atm	q_e mmol/g	Pressure Atm	q_e mmol/g	Pressure Atm	q_e mmol/g	Pressure Atm	q_e mmol/g
0.0000	0.0000	0.0000	0.0000	0.0000	0.0000	0.0000	0.0000	0.0000	0.0000
0.0333	0.0208	0.0333	0.0120	0.0333	0.0087	0.0333	0.0067	0.0333	0.0058
0.0665	0.0403	0.0666	0.0242	0.0666	0.0170	0.0666	0.0130	0.0665	0.0104
0.1329	0.0776	0.1330	0.0478	0.1327	0.0333	0.1331	0.0248	0.1298	0.0188
0.1995	0.1138	0.1991	0.0708	0.1991	0.0494	0.1994	0.0363	0.2016	0.0282
0.4007	0.2166	0.3997	0.1382	0.3996	0.0969	0.4011	0.0709	0.3996	0.0535
0.7799	0.3942	0.7774	0.2583	0.7749	0.1827	0.7810	0.1342	0.7750	0.1004
1.5338	0.6988	1.5314	0.4730	1.5329	0.3426	1.5321	0.2515	1.5330	0.1901
3.2006	1.2309	3.2019	0.8734	3.2011	0.6505	3.2027	0.4882	3.1880	0.3666
6.3797	1.9710	6.3803	1.4626	6.3800	1.1250	6.3805	0.8673	6.3808	0.6776
1.5307	0.6992	1.5390	0.4759	1.5434	0.3456	1.5419	0.2542	1.5247	0.1921
0.4030	0.2223	0.3972	0.1399	0.3968	0.0989	0.3985	0.0728	0.3969	0.0568

Table AV.32 – Argon equilibrium adsorption capacities for OLC. Exact temperature for the isotherm is included above each isotherm.

10.95 °C		30.54 °C		50.17 °C		69.75 °C		89.36 °C	
Pressure Atm	q_e mmol/g	Pressure Atm	q_e mmol/g	Pressure Atm	q_e mmol/g	Pressure Atm	q_e mmol/g	Pressure Atm	q_e mmol/g
0.0000	0.0000	0.0000	0.0000	0.0000	0.0000	0.0000	0.0000	0.0000	0.0000
0.0333	0.0186	0.0333	0.0124	0.0333	0.0086	0.0333	0.0061	0.0333	0.0051
0.0666	0.0373	0.0666	0.0245	0.0665	0.0169	0.0665	0.0121	0.0665	0.0098
0.1330	0.0731	0.1330	0.0479	0.1330	0.0330	0.1331	0.0238	0.1330	0.0187
0.1996	0.1082	0.1997	0.0711	0.1995	0.0492	0.1994	0.0353	0.1997	0.0276
0.3978	0.2071	0.3980	0.1378	0.3973	0.0958	0.3980	0.0692	0.3978	0.0528
0.7998	0.3914	0.7949	0.2637	0.7973	0.1868	0.7902	0.1348	0.7919	0.1022
1.5345	0.6845	1.5369	0.4777	1.5378	0.3436	1.5416	0.2537	1.5368	0.1914
3.2171	1.2175	3.2123	0.8806	3.2201	0.6543	3.2212	0.4914	3.2240	0.3764
6.3838	1.9557	6.3867	1.4737	6.3830	1.1322	6.3902	0.8761	6.3834	0.6866
1.5353	0.6848	1.5486	0.4803	1.5423	0.3440	1.5365	0.2525	1.5473	0.1915
0.4056	0.2124	0.4038	0.1403	0.4057	0.0981	0.4058	0.0707	0.3985	0.0532

AV.3. Ash Content Calculations

The ash content values were calculated from the SEM-EDS data assuming that the oxidation states of Mg, Al, Si, P, S, K, Ca, and Fe were 2, 3, 4, 5, 0, 1, 2, and 3, respectively, and that the hydrogen content makes up an insignificant amount of the total mass of the activated carbon. By summing the mass of the oxygen that is present within the ash content using the oxidation state with the mass of the elemental ashes the total mass of ash content was calculated. This total mass of ash content was then divided by the total mass of carbon, oxygen, and phosphorus present in the activated carbon (excluding the oxygen from the ash content) and multiplying it by 100% to acquire the ash content in mass%.

AV.4. Raw BET Data

Table AV.33 – Nitrogen BET isotherms (P/P_0 vs cm^3/g STP) at 77K for Carbon Aerogel, RF Aerogel, ACC, BPL, F-600, M-30, and NZ-AC.

Carbon Aerogel		RF Aerogel		ACC		BPL		F-600		M-30		NZ-AC	
P/P_0	q (cm^3/g)	P/P_0	q (cm^3/g)	P/P_0	q (cm^3/g)	P/P_0	q (cm^3/g)	P/P_0	q (cm^3/g)	P/P_0	q (cm^3/g)	P/P_0	q (cm^3/g)
1.077E-02	139.0569	1.063E-02	67.7522	5.379E-08	2.82075	2.157E-07	2.86168	2.567E-07	2.91478	1.916E-03	440.0806	6.870E-08	2.84951
3.185E-02	152.3595	3.383E-02	84.8154	9.504E-08	5.63762	4.032E-07	5.75367	4.692E-07	5.82936	2.977E-03	465.1787	1.636E-07	5.71724
6.273E-02	161.6328	6.420E-02	96.0837	1.483E-07	8.47571	6.951E-07	8.62468	8.172E-07	8.74793	4.007E-03	482.2631	3.664E-07	8.57611
8.023E-02	165.5833	7.978E-02	100.4363	2.130E-07	11.3224	1.044E-06	11.5124	1.255E-06	11.665	4.990E-03	494.3768	5.918E-07	11.4334
1.012E-01	169.6089	1.009E-01	105.3283	2.872E-07	14.1677	1.465E-06	14.3901	1.805E-06	14.5967	6.028E-03	504.573	8.435E-07	14.3075
1.209E-01	173.0715	1.206E-01	109.3975	3.675E-07	17.0101	1.928E-06	17.2851	2.437E-06	17.5266	6.950E-03	512.1851	1.168E-06	17.1677
1.409E-01	176.3484	1.409E-01	113.2012	4.596E-07	19.8568	2.466E-06	20.1826	3.148E-06	20.4561	8.041E-03	519.9561	1.526E-06	20.0465
1.616E-01	179.567	1.610E-01	116.701	5.607E-07	22.6867	3.076E-06	23.0762	3.926E-06	23.3502	9.185E-03	527.0842	1.905E-06	22.8902
1.818E-01	182.62	1.812E-01	119.9681	6.751E-07	25.5263	3.723E-06	25.9647	4.777E-06	26.2648	9.887E-03	531.0536	2.367E-06	25.7432
2.016E-01	185.5319	2.014E-01	123.1818	8.012E-07	28.3555	4.440E-06	28.8566	5.728E-06	29.1903	2.205E-02	578.9778	2.861E-06	28.6268
2.485E-01	192.182	2.502E-01	130.3703	9.402E-07	31.1951	5.228E-06	31.7465	6.699E-06	32.0792	2.983E-02	600.8857	3.400E-06	31.4887
3.019E-01	199.7607	3.029E-01	137.9743	1.095E-06	34.0254	6.079E-06	34.6425	7.748E-06	34.9897	3.956E-02	624.7545	3.961E-06	34.3498
3.528E-01	207.0659	3.531E-01	145.2622	1.262E-06	36.8625	7.010E-06	37.5332	8.879E-06	37.9117	4.825E-02	644.3543	4.595E-06	37.2289
3.995E-01	214.0318	4.007E-01	152.4063	1.448E-06	39.7056	8.011E-06	40.4274	1.010E-05	40.8265	5.835E-02	666.1098	5.286E-06	40.1088

Appendix V

4.490E-01	221.6702	4.511E-01	160.328	1.652E-06	42.5411	9.073E-06	43.313	1.134E-05	43.742	6.932E-02	688.7037	5.994E-06	42.9805
5.004E-01	230.0682	5.010E-01	168.866	1.886E-06	45.3583	1.023E-05	46.2147	1.265E-05	46.6462	7.946E-02	708.6978	6.777E-06	45.8622
5.501E-01	238.8184	5.511E-01	178.3377	2.116E-06	48.1896	1.146E-05	49.1127	1.404E-05	49.5677	8.899E-02	727.4245	7.581E-06	48.7104
5.998E-01	248.523	6.008E-01	188.7932	2.390E-06	51.0035	1.279E-05	52.0056	1.552E-05	52.4597	9.879E-02	746.0314	8.463E-06	51.5878
6.500E-01	259.8198	6.505E-01	200.9333	2.668E-06	53.8391	1.422E-05	54.9025	1.704E-05	55.3514	1.160E-01	778.0801	9.392E-06	54.4634
6.996E-01	273.0901	7.003E-01	215.6554	2.982E-06	56.6725	1.572E-05	57.7878	1.871E-05	58.237	1.364E-01	814.86	1.038E-05	57.343
7.491E-01	289.4846	7.505E-01	233.9406	3.305E-06	59.4868	1.736E-05	60.6742	2.047E-05	61.15	1.564E-01	849.7804	1.142E-05	60.2194
7.982E-01	311.099	7.998E-01	257.8672	3.696E-06	62.3051	1.912E-05	63.5861	2.220E-05	64.073	1.763E-01	884.0756	1.252E-05	63.0978
8.207E-01	323.9398	8.220E-01	272.5662	4.075E-06	65.1297	2.097E-05	66.4658	2.418E-05	66.9871	1.969E-01	918.069	1.369E-05	65.9826
8.490E-01	344.2735	8.515E-01	295.8384	4.496E-06	67.9622	2.300E-05	69.3655	2.634E-05	69.9011	2.179E-01	951.0425	1.492E-05	68.8349
8.733E-01	367.1084	8.750E-01	321.0132	4.970E-06	70.779	2.513E-05	72.2454	2.868E-05	72.8219	2.399E-01	984.2837	1.619E-05	71.687
8.974E-01	398.1956	9.005E-01	358.1497	5.449E-06	73.6203	2.745E-05	75.1426	3.127E-05	75.7484	2.624E-01	1015.897	1.755E-05	74.5543
9.211E-01	444.0247	9.241E-01	410.6076	5.977E-06	76.4614	2.964E-05	78.0362	3.405E-05	78.6384	2.848E-01	1045.42	1.899E-05	77.4338
9.427E-01	514.6858	9.474E-01	498.3973	6.538E-06	79.297	3.218E-05	80.9301	3.711E-05	81.5444	3.067E-01	1071.588	2.049E-05	80.3018
9.686E-01	719.3857	9.717E-01	765.4842	7.175E-06	82.1245	3.530E-05	83.8162	4.055E-05	84.4678	3.290E-01	1094.679	2.207E-05	83.1571
9.727E-01	812.0336	9.744E-01	837.9506	7.781E-06	84.957	3.825E-05	86.708	4.439E-05	87.3961	3.508E-01	1114.683	2.374E-05	86.0327
9.822E-01	1282.783	9.858E-01	1486.189	8.430E-06	87.7594	4.156E-05	89.602	4.849E-05	90.3055	3.593E-01	1121.5	2.548E-05	88.9
9.967E-01	1744.455	9.969E-01	1602.32	9.165E-06	90.5799	4.507E-05	92.4962	5.337E-05	93.2247	3.801E-01	1135.982	2.731E-05	91.7591
9.752E-01	1738.761	9.795E-01	1585.454	9.943E-06	93.4145	4.905E-05	95.3914	5.873E-05	96.1484	4.007E-01	1147.399	2.922E-05	94.6106
9.728E-01	1716.016	9.690E-01	1559.636	1.080E-05	96.2219	5.317E-05	98.2841	6.496E-05	99.0537	4.200E-01	1155.682	3.123E-05	97.4632
9.561E-01	1330.225	9.541E-01	1073.793	1.162E-05	99.0494	5.789E-05	101.193	7.192E-05	101.975	4.394E-01	1162.791	3.331E-05	100.316
9.293E-01	676.1676	9.223E-01	668.9037	1.253E-05	101.866	6.286E-05	104.087	8.009E-05	104.896	4.606E-01	1168.949	3.552E-05	103.19
8.974E-01	481.0293	9.022E-01	517.4133	1.349E-05	104.678	6.832E-05	106.98	8.979E-05	107.809	4.796E-01	1173.748	3.782E-05	106.069
8.753E-01	420.7393	8.747E-01	407.9836	1.453E-05	107.501	7.440E-05	109.871	1.012E-04	110.724	5.003E-01	1178.177	4.024E-05	108.943
8.565E-01	387.1655	8.541E-01	361.4807	1.559E-05	110.325	8.086E-05	112.766	1.150E-04	113.639	5.201E-01	1181.953	4.286E-05	111.798
8.306E-01	354.7353	8.179E-01	308.3234	1.676E-05	113.139	8.822E-05	115.652	1.324E-04	116.553	5.405E-01	1185.402	4.551E-05	114.667
8.035E-01	330.8434	7.936E-01	284.6733	1.796E-05	115.948	9.606E-05	118.546	1.532E-04	119.473	5.601E-01	1188.682	4.835E-05	117.553
7.533E-01	300.8279	7.552E-01	257.2984	1.926E-05	118.768	1.050E-04	121.444	1.793E-04	122.397	5.806E-01	1191.813	5.130E-05	120.421
7.030E-01	280.4522	7.026E-01	231.2342	2.062E-05	121.606	1.146E-04	124.317	2.115E-04	125.322	6.002E-01	1194.622	5.434E-05	123.278
6.538E-01	265.3691	6.536E-01	213.6821	2.205E-05	124.436	1.255E-04	127.211	2.529E-04	128.243	6.202E-01	1197.527	5.762E-05	126.156
6.018E-01	252.7105	6.036E-01	199.4194	2.358E-05	127.252	1.374E-04	130.11	3.065E-04	131.156	6.406E-01	1200.195	6.105E-05	129.011
5.515E-01	242.214	5.513E-01	186.9829	2.517E-05	130.073	1.508E-04	133.002	3.762E-04	134.069	6.599E-01	1202.893	6.466E-05	131.864
5.011E-01	232.8789	5.012E-01	176.754	2.686E-05	132.894	1.658E-04	135.895	4.683E-04	136.977	6.807E-01	1205.599	6.851E-05	134.733
4.510E-01	224.3942	4.513E-01	167.7194	2.866E-05	135.715	1.822E-04	138.786	5.892E-04	139.886	7.002E-01	1208.04	7.243E-05	137.575
4.012E-01	216.4814	4.006E-01	159.3019	3.062E-05	138.514	2.009E-04	141.667	7.493E-04	142.775	7.202E-01	1210.569	7.656E-05	140.441
3.510E-01	208.8555	3.509E-01	151.4995	3.253E-05	141.328	2.223E-04	144.558	9.602E-04	145.637	7.404E-01	1212.998	8.091E-05	143.318
3.006E-01	201.4687	3.011E-01	144.0347	3.468E-05	144.13	2.462E-04	147.46	1.240E-03	148.501	7.601E-01	1215.397	8.549E-05	146.179
2.508E-01	194.3145	2.508E-01	136.5628	3.686E-05	146.952	2.733E-04	150.347	1.607E-03	151.355	7.803E-01	1217.836	9.031E-05	149.052
2.010E-01	187.1441	2.013E-01	129.0432	3.918E-05	149.778	3.046E-04	153.231	2.085E-03	154.181	8.000E-01	1220.416	9.532E-05	151.936
1.410E-01	178.1761	1.409E-01	118.9714	4.175E-05	152.582	3.400E-04	156.122	2.703E-03	156.99	8.208E-01	1222.728	1.005E-04	154.783
				4.429E-05	155.406	3.813E-04	159.01	3.495E-03	159.766	8.397E-01	1225.008	1.060E-04	157.659
				4.700E-05	158.224	4.285E-04	161.896	4.491E-03	162.511	8.601E-01	1227.839	1.116E-04	160.513
				4.995E-05	161.035	4.835E-04	164.783	5.728E-03	165.185	8.806E-01	1230.677	1.176E-04	163.395
				5.297E-05	163.827	5.477E-04	167.662	7.243E-03	167.786	9.000E-01	1233.552	1.239E-04	166.259
				5.631E-05	166.635	6.228E-04	170.544	9.096E-03	170.351	9.247E-01	1238.005	1.307E-04	169.113
				5.968E-05	169.453	7.099E-04	173.425	1.135E-02	172.85	9.497E-01	1243.866	1.377E-04	171.986
				6.333E-05	172.233	8.136E-04	176.307	1.433E-02	175.544	9.727E-01	1253.575	1.450E-04	174.835
				6.704E-05	175.054	9.346E-04	179.173	1.961E-02	179.118	9.867E-01	1268.511	1.528E-04	177.704
				7.116E-05	177.866	1.077E-03	182.029	2.445E-02	181.612	9.662E-01	1259.411	1.607E-04	180.589
				7.549E-05	180.674	1.245E-03	184.875	2.863E-02	183.379	9.421E-01	1249.548	1.690E-04	183.434
				7.997E-05	183.493	1.443E-03	187.73	3.402E-02	185.278	9.135E-01	1242.966	1.780E-04	186.279
				8.476E-05	186.315	1.675E-03	190.57	3.977E-02	186.956	8.862E-01	1238.561	1.874E-04	189.135
				8.994E-05	189.121	1.948E-03	193.416	4.461E-02	188.165	8.645E-01	1235.73	1.970E-04	192.01
				9.524E-05	191.937	2.264E-03	196.232	4.961E-02	189.259	8.445E-01	1232.989	2.074E-04	194.893
				1.010E-04	194.75	2.635E-03	199.052	5.781E-02	190.782	8.407E-01	1231.94	2.181E-04	197.745
				1.072E-04	197.553	3.062E-03	201.861	7.071E-02	192.709	8.180E-01	1229.964	2.298E-04	200.607
				1.136E-04	200.355	3.550E-03	204.643	8.089E-02	193.959	7.855E-01	1226.35	2.416E-04	203.463
				1.204E-04	203.149	4.109E-03	207.418	9.154E-02	195.079	7.798E-01	1225.403	2.544E-04	206.34
				1.277E-04	205.956	4.733E-03	210.148	1.024E-01	196.081	7.582E-01	1223.099	2.679E-04	209.211
				1.359E-04	208.741	5.442E-03	212.878	1.236E-01	197.735	7.418E-01	1221.25	2.820E-04	212.089
				1.441E-04	211.519	6.230E-03	215.583	1.529E-01	199.618	7.203E-01	1218.846	2.972E-04	214.948
				1.528E-04	214.292	7.111E-03	218.271	1.828E-01	201.258	7.004E-01	1216.541	3.130E-04	217.822
				1.622E-04	217.085	8.069E-03	220.928	2.101E-01	202.581	6.803E-01	1214.203	3.297E-04	220.689
				1.722E-04	219.871	9.121E-03	223.554	2.354E-01	203.707	6.605E-01	1211.917	3.478E-04	223.561
				1.829E-04	222.655	1.027E-02	226.178	2.585E-01	204.663	6.407E-01	1209.434	3.666E-04	226.419
				1.942E-04	225.439	1.470E-02	234.638	2.816E-01	205.564	6.202E-01	1206.827	3.869E-04	229.273
				2.065E-04	228.218	1.952E-02	241.868	3.049E-01	206.423	6.005E-01	1204.198	4.082E-04	232.132
				2.198E-04	230.994	2.442E-02	248.089	3.293E-01	207.275	5.802E-01	1201.513	4.308E-04	234.969
				2.341E-04	233.768	2.974E-02	253.948	3.543E-01	208.104	5.606E-01	1198.705	4.548E-04	237.827
				2.492E-04	236.537	3.380E-02	257.996	3.742E-01	208.74	5.403E-01	1195.721	4.806E-04	240.686
				2.657E-04	239.307	3.890E-02	262.637	4.001E-01	209.518	5.204E-01	1192.803	5.082E-04	243.556
				2.832E-04	242.069	4.441E-02	267.207	4.243E-01	210.216	5.007E-01	1189.585	5.374E-04	246.4
				3.024E-04	244.821	4.830E-02	270.209	4.495E-01	210.92	4.814E-01	1185.109	5.685E-04	249.25
				3.229E-04	247.567	5.902E-02	277.689	4.743E-01	211.588	4.590E-01	1179.997	6.022E-04	252.121
				3.451E-04	250.317	6.653E-02	282.383	4.992E-01	212.244	4.407E-01	1175.652	6.384E-04	254.966
				3.694E-04	253.066	7.939E-02	289.578	5.244E-01	212.9	4.220E-01	1169.161	6.764E-04	257.815
				3.957E-04	255.801	8.979E-02	294.786	5.490E-01	213.522	4.025E-01	1157.827	7.182E-04	260.679
				4.246E-04	258.537	1.002E-01	299.565	5.744E-01	214.164	3.789E-01	1142.309	7.620E-04	263.53
				4.552E-04	261.256	1.218E-01	308.251	5.997E-01	214.814	3.599E-01	1128.731	8.097E-04	266.383
				4.888E-04	263.965	1.540E-01	319.135	6.246E-01	215.456	3.409E-01	1113.141	8.609E-04	269.25
				5.253E-04	266.637	1.848E-01	327.942	6.493E-01	216.105	3.207E-01	1093.771	9.157E-04	272.085
				5.645E-04	269.305	2.123E-01	334.949	6.745E-01	216.8	3.003E-01	1071.243	9.743E-04	274.922
				6.074E-04	271.968	2.393E-01	341.232	6.992E-01	217.512	2.799E-01	1046.454	1.039E-03	277.764
				6.545E-04	274.629	2.607E-01	345.952	7.243E-01	218.293	2.605E-01	1020.498	1.107E-03	280.613
				7.056E-04	277.274	2.830E-01	350.682	7.495E-01	219.161	2.400E-01	990.9999	1.181E-03	283.463
				7.609E-04	279.884	3.046E-01	355.139	7.943E-01	220.989	2.202E-01	960.5336	1.262E-03	286.303
				8.212E-04	282.475	3.289E-01	360.03	8.466E-01	223.935	1.997E-01	928.0947	1.346E-03	289.115
				8.869E-04	285.059	3.537E-01	364.92	8.944E-01	228.194	1.804E-01	895.8214	1.440E-03	291.956
				9.579E-04	287.622	3.742E-01	368.921	9.088E-01	230.005	1.622E-01	864.5387	1.540E-03	294.785
				1.035E-03	290.149	3.999E-01	373.909	9.201E-01	231.692	1.461E-01	836.1387	1.649E-03	297.606
				1.119E-03	292.659	4.245E-01	378.611	9.297E-01	233.286	1.201E-01	788.7413	1.766E-03	300.411
				1.209E-03	295.153	4.497E-01	383.412	9.393E-01	235.147	1.001E-01	750.8287	1.892E-03	303.211
				1.308E-03	297.611	4.748E-01	388.171	9.494E-01	237.333	9.076E-02	732.8855	2.027E-03	306.002
				1.413E-03	300.026	4.998E-01	392.9	9.592E-01	239.765	8.239E-02	716.5471	2.175E-03	308.805
				1.526E-03	302.413	5.248E-01	397.623	9.688E-01	242.632	7.028E-02	692.1643	2.333E-03	311.613
				1.648E-03	304.785	5.502E-01	402.412	9.782E-01	246.46	6.005E-02	671.0247	2.507E-03	314.412

1.779E-03	307.127	5.748E-01	407.054	9.861E-01	251.488	5.034E-02	650.3462	2.691E-03	317.189
1.919E-03	309.438	5.997E-01	411.782	9.891E-01	256.264	4.034E-02	627.8802	2.890E-03	319.982
2.067E-03	311.708	6.250E-01	416.597	9.780E-01	248.906	3.047E-02	603.8213	3.106E-03	322.751
2.227E-03	313.951	6.503E-01	421.445	9.683E-01	245.841	2.067E-02	576.0692	3.332E-03	325.529
2.392E-03	316.131	6.746E-01	426.13	9.611E-01	244.198	1.033E-02	535.3996	3.577E-03	328.271
2.568E-03	318.292	6.997E-01	431.006	9.462E-01	241.393	9.170E-03	529.0453	3.841E-03	331.015
2.754E-03	320.403	7.249E-01	435.976	9.359E-01	239.852	8.285E-03	523.33	4.124E-03	333.735
2.952E-03	322.52	7.502E-01	441.032	9.262E-01	238.526	7.265E-03	516.5893	4.423E-03	336.442
3.155E-03	324.554	7.956E-01	450.284	9.158E-01	237.233	6.183E-03	507.84	4.748E-03	339.141
3.371E-03	326.57	8.487E-01	461.673	9.057E-01	236.047	5.155E-03	497.96	5.088E-03	341.848
3.593E-03	328.535	8.980E-01	473.234	8.558E-01	231.029	4.135E-03	486.0099	5.454E-03	344.519
3.831E-03	330.503	9.100E-01	476.274	7.998E-01	226.799	3.114E-03	469.6885	5.839E-03	347.205
4.074E-03	332.423	9.201E-01	478.945	7.521E-01	224.15	2.093E-03	442.3227	6.249E-03	349.878
4.329E-03	334.297	9.301E-01	481.781	7.272E-01	223.013			6.687E-03	352.533
4.591E-03	336.138	9.397E-01	484.627	7.014E-01	221.968			7.142E-03	355.143
4.866E-03	337.975	9.499E-01	487.851	6.755E-01	221.032			7.620E-03	357.756
5.147E-03	339.745	9.594E-01	491.118	6.511E-01	220.232			8.127E-03	360.351
5.439E-03	341.521	9.694E-01	494.916	6.254E-01	219.456			8.659E-03	362.957
5.737E-03	343.229	9.791E-01	499.188	6.005E-01	218.755			9.219E-03	365.52
6.048E-03	344.939	9.903E-01	504.364	5.754E-01	218.082			9.802E-03	368.089
6.361E-03	346.595	9.706E-01	497.955	5.507E-01	217.455			1.523E-02	387.708
6.687E-03	348.236	9.505E-01	491.693	5.254E-01	216.829			1.903E-02	398.232
7.017E-03	349.834	9.350E-01	487.422	5.011E-01	216.15			2.398E-02	410.001
7.357E-03	351.423	9.261E-01	485.105	4.752E-01	213.537			2.963E-02	421.594
7.705E-03	352.98	9.153E-01	482.421	4.466E-01	211.799			3.467E-02	430.771
8.060E-03	354.523	9.058E-01	480.101	4.281E-01	210.94			3.841E-02	436.984
8.423E-03	356.024	8.513E-01	467.526	4.009E-01	209.91			4.312E-02	444.33
8.785E-03	357.481	8.009E-01	456.643	3.760E-01	209.085			4.873E-02	452.427
9.162E-03	358.963	7.514E-01	446.426	3.510E-01	208.299			5.979E-02	466.632
9.537E-03	360.379	7.258E-01	441.299	3.256E-01	207.467			6.922E-02	477.332
1.496E-02	377.568	7.004E-01	436.291	3.003E-01	206.594			7.899E-02	487.247
2.000E-02	388.961	6.758E-01	431.537	2.755E-01	205.691			8.927E-02	496.661
2.441E-02	397.09	6.508E-01	426.73	2.504E-01	204.72			9.962E-02	505.189
2.971E-02	405.39	6.252E-01	421.881	2.254E-01	203.673			1.202E-01	519.638
3.479E-02	412.094	6.007E-01	417.282	2.004E-01	202.556			1.534E-01	537.635
3.981E-02	417.816	5.755E-01	412.56	1.756E-01	201.338			1.829E-01	549.348
4.485E-02	422.85	5.507E-01	407.954	1.506E-01	199.973			2.122E-01	558.11
5.371E-02	430.192	5.255E-01	403.271	1.284E-01	198.581			2.398E-01	564.462
5.898E-02	433.868	5.006E-01	398.568	1.011E-01	196.508			2.660E-01	569.194
6.985E-02	440.083	4.803E-01	392.965	9.041E-02	195.523			2.892E-01	572.617
7.994E-02	444.617	4.505E-01	385.071	8.013E-02	194.45			3.110E-01	575.342
9.007E-02	448.283	4.237E-01	379.249	7.059E-02	193.298			3.316E-01	577.578
1.001E-01	451.225	4.023E-01	374.884	6.272E-02	192.191			3.545E-01	579.747
1.235E-01	456.234	3.757E-01	369.642	5.092E-02	190.155			3.747E-01	581.42
1.510E-01	460.133	3.507E-01	364.765	4.620E-02	189.184			3.994E-01	583.257
1.764E-01	462.731	3.258E-01	359.855	4.034E-02	187.79			4.246E-01	584.906
2.018E-01	464.772	3.005E-01	354.76	3.522E-02	186.351			4.492E-01	586.353
2.269E-01	466.429	2.757E-01	349.637	3.045E-02	184.788			4.746E-01	587.728
2.516E-01	467.854	2.508E-01	344.294	2.566E-02	182.91			4.994E-01	588.949
2.766E-01	469.115	2.257E-01	338.673	2.059E-02	180.458			5.242E-01	590.103
3.013E-01	470.187	2.010E-01	332.722	1.570E-02	177.412			5.495E-01	591.169
3.262E-01	471.177	1.761E-01	326.196	1.044E-02	172.805			5.744E-01	592.162
3.512E-01	472.051	1.518E-01	319.112	5.231E-03	165.287			5.992E-01	593.088
3.743E-01	472.769	1.265E-01	310.714					6.242E-01	593.98
3.997E-01	473.501	1.016E-01	300.953					6.493E-01	594.808
4.248E-01	474.162	9.107E-02	296.214					6.743E-01	595.605
4.497E-01	474.784	8.214E-02	291.864					6.997E-01	596.38
4.748E-01	475.314	7.060E-02	285.679					7.245E-01	597.097
4.996E-01	475.753	6.052E-02	279.612					7.497E-01	597.781
5.245E-01	476.185	5.165E-02	273.623					7.980E-01	599.035
5.495E-01	476.592	4.520E-02	268.806					8.504E-01	600.301
5.748E-01	476.929	4.030E-02	264.839					8.999E-01	601.498
5.997E-01	477.237	3.543E-02	260.554					9.105E-01	601.764
6.247E-01	477.566	3.143E-02	256.731					9.204E-01	602.005
6.495E-01	477.854	2.555E-02	250.476					9.302E-01	602.253
6.748E-01	478.076	2.102E-02	244.976					9.402E-01	602.507
7.000E-01	478.299	1.566E-02	237.292					9.500E-01	602.772
7.254E-01	478.431	1.043E-02	227.739					9.606E-01	603.07
7.507E-01	478.583	5.241E-03	213.499					9.707E-01	603.386
7.987E-01	478.795							9.806E-01	603.761
8.507E-01	478.976							9.905E-01	604.256
9.007E-01	479.135							9.624E-01	603.401
9.103E-01	479.158							9.406E-01	602.86
9.204E-01	479.149							9.257E-01	602.525
9.295E-01	479.192							9.151E-01	602.272
9.402E-01	479.219							9.053E-01	602.046
9.496E-01	479.267							8.561E-01	600.952
9.601E-01	479.265							8.006E-01	599.691
9.708E-01	479.346							7.502E-01	598.461
9.802E-01	479.492							7.250E-01	597.818
9.900E-01	479.69							7.002E-01	597.152
9.607E-01	479.39							6.750E-01	596.438
9.305E-01	479.307							6.501E-01	595.697
9.152E-01	479.295							6.253E-01	594.913
9.049E-01	479.279							6.009E-01	594.096
8.538E-01	479.222							5.751E-01	593.19
7.997E-01	479.153							5.502E-01	592.265
7.497E-01	478.916							5.257E-01	591.307
7.257E-01	478.794							5.003E-01	590.252
7.005E-01	478.629							4.759E-01	588.862
6.749E-01	478.452							4.500E-01	587.222
6.506E-01	478.267							4.255E-01	585.484
6.250E-01	478.009							4.003E-01	583.574
6.000E-01	477.697							3.752E-01	581.653
5.750E-01	477.337							3.506E-01	579.597
5.505E-01	476.996							3.259E-01	577.195

5.255E-01	476.57
5.002E-01	476.132
4.749E-01	475.604
4.500E-01	474.966
4.251E-01	474.279
4.000E-01	473.636
3.752E-01	472.906
3.500E-01	472.107
3.252E-01	471.259
3.000E-01	470.286
2.752E-01	469.188
2.500E-01	467.943
2.251E-01	466.52
2.001E-01	464.858
1.751E-01	462.87
1.501E-01	460.328
1.252E-01	456.816
1.013E-01	451.852
9.018E-02	448.655
8.011E-02	445.044
7.021E-02	440.661
6.029E-02	435.11
5.037E-02	428.057
4.516E-02	423.605
4.017E-02	418.689
3.523E-02	413.12
3.028E-02	406.7
2.608E-02	400.354
2.037E-02	390.153
1.576E-02	379.956
1.004E-02	363.234
5.063E-03	340.381
3.005E-01	574.337
2.758E-01	570.972
2.508E-01	566.865
2.262E-01	561.856
2.013E-01	555.538
1.767E-01	547.587
1.505E-01	536.838
1.264E-01	524.063
1.008E-01	506.738
9.292E-02	500.457
8.053E-02	489.453
7.048E-02	479.429
6.190E-02	469.915
5.176E-02	457.289
4.626E-02	449.769
4.161E-02	442.895
3.585E-02	433.631
3.121E-02	425.432
2.529E-02	413.689
2.094E-02	403.813
1.558E-02	389.523
1.054E-02	372.019
1.023E-02	371.065
5.312E-03	345.095
5.240E-03	344.574

AV.5. Surface Area and Pore Volume Distribution

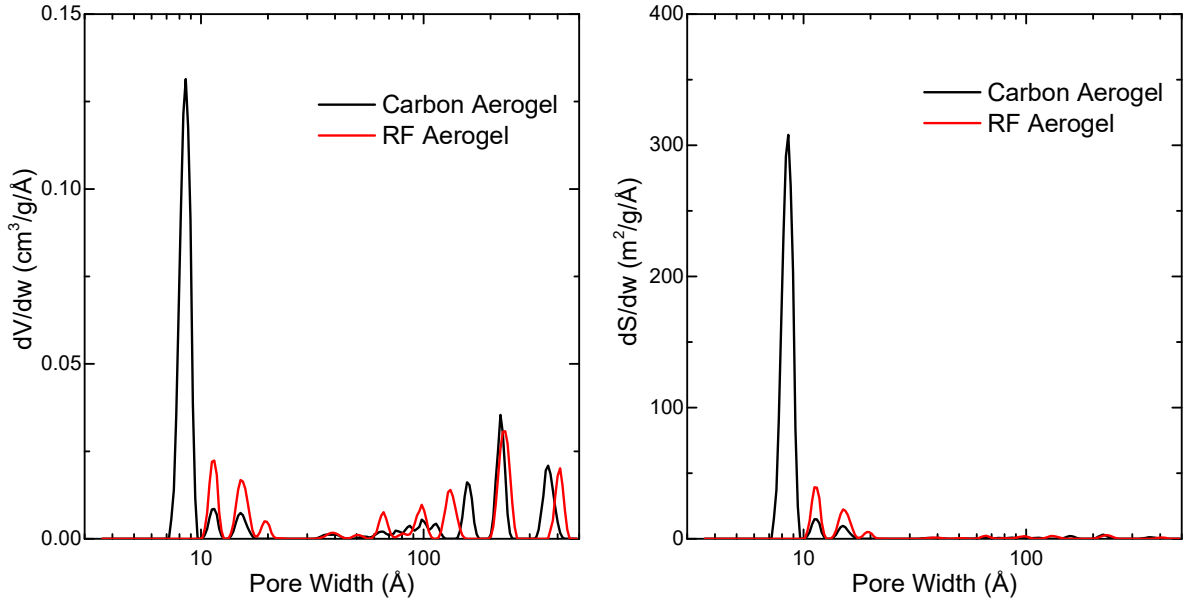

Figure AV.2 – Surface area and pore volume distribution relative to pore width using 2D-NLDFT-HS analysis for carbon aerogel and RF aerogel.

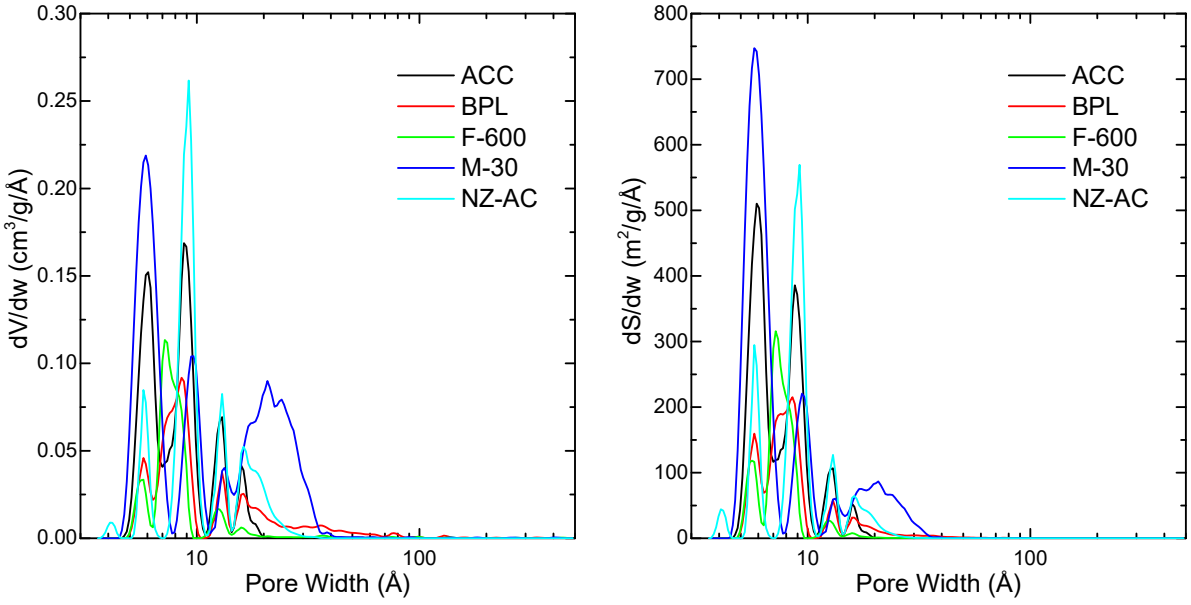

Figure AV.3 – Surface area and pore volume distribution relative to pore width using 2D-NLDFT-HS analysis for ACC, BPL, F-600, M-30, and NZ-AC.

AV.6. Isotherm Model Parameters

Table AV.34 - Adsorption isotherm model parameters for carbon aerogel for CO_2, N_2, O_2, and Ar at 10°C, 30°C, 50°C, 70°C, and 90°C. Associated equations are located in Methods section.

		Langmuir		Freundlich		Sips			Toth		
	T	q_s	β	k	n	q_s	β	n	q_s	β	t
	(°C)	mmol/g	Atm^{-1}	$\frac{mmol}{g\ atm}$		mmol/g	Atm^{-1}		mmol/g	Atm^{-1}	
CO_2	11.04	4.9091	1.4444	2.4589	2.6493	8.20E+00	2.72E-01	5.78E-01	1.37E+01	5.32E+00	2.91E-01
	30.57	4.3036	0.9737	1.8402	2.3385	6.67E+00	2.65E-01	6.51E-01	1.06E+01	1.92E+00	3.49E-01
	50.19	3.8596	0.6599	1.3736	2.0734	5.66E+00	2.33E-01	7.18E-01	8.82E+00	8.57E-01	4.06E-01
	69.78	3.5365	0.4516	1.0230	1.8548	5.13E+00	1.78E-01	7.66E-01	8.40E+00	4.36E-01	4.35E-01
	89.34	3.2329	0.3233	0.7579	1.6863	4.56E+00	1.45E-01	8.12E-01	7.60E+00	2.51E-01	4.76E-01
N_2	10.87	2.3409	0.2423	0.4469	1.5552	3.02E+00	1.40E-01	8.73E-01	4.44E+00	1.79E-01	5.80E-01
	30.51	2.1616	0.1715	0.3172	1.4310	2.72E+00	1.09E-01	9.07E-01	4.04E+00	1.15E-01	6.25E-01
	50.19	1.9958	0.1271	0.2286	1.3411	2.44E+00	8.77E-02	9.33E-01	3.52E+00	8.36E-02	6.80E-01
	69.81	1.8969	0.0930	0.1660	1.2689	2.79E+00	4.82E-02	9.13E-01	7.27E+00	3.08E-02	5.14E-01
	89.41	1.7396	0.0748	0.1250	1.2257	2.80E+00	3.46E-02	9.14E-01	1.10E+01	1.52E-02	4.61E-01
O_2	10.90	2.9127	0.1903	0.4646	1.4682	3.87E+00	1.07E-01	8.82E-01	6.29E+00	1.21E-01	5.65E-01
	30.55	2.7212	0.1303	0.3183	1.3476	3.42E+00	8.53E-02	9.25E-01	5.28E+00	8.01E-02	6.43E-01
	50.22	2.5552	0.0945	0.2259	1.2680	3.25E+00	6.25E-02	9.39E-01	5.43E+00	5.10E-02	6.49E-01
	69.85	2.3033	0.0755	0.1665	1.2243	3.28E+00	4.25E-02	9.31E-01	7.92E+00	2.60E-02	5.58E-01
	89.44	2.0434	0.0633	0.1261	1.1977	4.19E+00	2.11E-02	9.02E-01	6.10E+01	3.07E-03	3.35E-01
Ar	11.01	2.7119	0.2115	0.4721	1.5156	4.09E+00	8.93E-02	8.36E-01	8.77E+00	1.12E-01	4.50E-01
	30.59	2.6033	0.1383	0.3210	1.3674	3.44E+00	8.15E-02	9.07E-01	5.93E+00	7.68E-02	5.86E-01
	50.23	2.4208	0.1011	0.2275	1.2841	3.10E+00	6.56E-02	9.34E-01	5.23E+00	5.45E-02	6.37E-01
	69.80	2.4051	0.0710	0.1641	1.2120	3.32E+00	4.23E-02	9.39E-01	7.73E+00	2.56E-02	5.79E-01
	89.39	2.1709	0.0578	0.1227	1.1815	4.17E+00	2.17E-02	9.15E-01	5.03E+01	3.39E-03	3.62E-01

Table AV.35 - Adsorption isotherm model parameters for RF aerogel for CO_2, N_2, O_2, and Ar at 10°C, 30°C, 50°C, 70°C, and 90°C. Associated equations are located in Methods section.

		Langmuir		Freundlich		Sips			Toth		
	T	q_s	β	k	n	q_s	β	n	q_s	β	t
	(°C)	mmol/g	Atm^{-1}	$\frac{mmol}{g\ atm}$		mmol/g	Atm^{-1}		mmol/g	Atm^{-1}	
CO_2	10.94	3.6050	0.5269	1.1650	1.9960	1.82E+01	7.65E-03	5.48E-01	9.73E+02	7.08E-01	1.06E-01
	30.53	2.8559	0.4097	0.7927	1.8394	8.26E+00	2.98E-02	6.31E-01	9.25E+01	2.41E-01	1.74E-01
	50.18	2.4137	0.2975	0.5432	1.6753	5.90E+00	3.91E-02	7.00E-01	4.87E+01	9.74E-02	2.19E-01
	69.76	2.1301	0.2073	0.3692	1.5238	5.42E+00	3.05E-02	7.46E-01	7.15E+01	2.83E-02	2.22E-01
	89.34	2.0063	0.1417	0.2580	1.4017	9.48E+00	8.71E-03	7.53E-01	2.00E+04	1.94E-04	1.16E-01
N_2	11.01	1.0177	0.1390	0.1301	1.4087	8.05E+01	1.20E-04	7.12E-01	3.25E+03	4.49E-04	1.30E-01
	30.53	0.8992	0.0893	0.0776	1.2826	3.37E+01	4.31E-04	7.84E-01	1.19E+04	3.48E-05	1.34E-01
	50.20	0.8342	0.0633	0.0522	1.2115	2.91E+01	4.88E-04	8.29E-01	6.58E+03	2.27E-05	1.59E-01
	69.84	0.4309	0.0905	0.0375	1.2836	2.99E+01	1.93E-04	7.81E-01	2.80E+05	1.76E-06	9.63E-02
	89.42	0.3908	0.0803	0.0304	1.2544	1.55E+00	9.26E-03	8.36E-01	4.01E+03	3.05E-05	1.44E-01
O_2	10.85	1.6142	0.1009	0.1542	1.3029	5.65E+00	1.25E-02	8.16E-01	1.07E+04	8.09E-05	1.39E-01
	30.52	1.3959	0.0904	0.1216	1.2844	4.91E+01	4.70E-04	7.83E-01	8.75E+04	9.72E-06	1.18E-01
	50.22	1.0177	0.1108	0.1028	1.3070	6.88E+00	4.71E-03	7.76E-01	5.19E+04	2.24E-05	1.11E-01
	69.87	0.9152	0.0796	0.0713	1.2605	3.44E+01	4.30E-04	7.97E-01	1.66E+05	2.79E-06	1.13E-01
	89.43	0.9410	0.0605	0.0559	1.1950	3.59E+00	8.50E-03	8.70E-01	2.87E+03	4.54E-05	1.80E-01
Ar	10.94	1.6259	0.0833	0.1290	1.2468	2.64E+00	3.73E-02	9.06E-01	1.04E+01	1.74E-02	4.48E-01
	30.54	1.3597	0.0636	0.0841	1.1976	2.55E+00	2.41E-02	9.10E-01	2.55E+01	4.67E-03	3.68E-01
	50.18	1.3814	0.0440	0.0602	1.1449	4.47E+00	8.68E-03	9.06E-01	9.14E+01	8.94E-04	3.21E-01
	69.80	0.9616	0.0476	0.0455	1.1593	7.39E+00	3.02E-03	8.77E-01	1.73E+02	4.00E-04	2.70E-01
	89.37	0.8077	0.0409	0.0336	1.1542	3.09E+01	3.88E-04	8.69E-01	2.47E+02	2.07E-04	2.54E-01

Table AV.36 - Adsorption isotherm model parameters for activated carbon clothe (ACC) for CO_2, N_2, O_2, and Ar at 10°C, 30°C, 50°C, 70°C, and 90°C. Associated equations are located in Methods section.

		Langmuir		Freundlich		Sips			Toth		
	T	q_s	β	k	n	q_s	β	n	q_s	β	t
	(°C)	mmol/g	Atm^{-1}	$\frac{mmol}{g\ atm}$		mmol/g	Atm^{-1}		mmol/g	Atm^{-1}	
CO_2	10.93	15.1157	0.3761	3.9088	1.7596	2.03E+01	1.86E-01	8.15E-01	2.97E+01	3.35E-01	5.14E-01
	30.54	13.3072	0.2500	2.6163	1.5781	1.90E+01	1.15E-01	8.35E-01	3.39E+01	1.64E-01	4.85E-01
	50.17	11.7676	0.1754	1.7687	1.4464	1.72E+01	8.20E-02	8.62E-01	3.61E+01	8.68E-02	4.83E-01
	69.76	10.5237	0.1285	1.2223	1.3495	1.52E+01	6.50E-02	8.92E-01	3.16E+01	5.70E-02	5.25E-01
	89.33	9.5088	0.0974	0.8666	1.2786	1.37E+01	5.21E-02	9.14E-01	3.27E+01	3.57E-02	5.29E-01
N_2	10.87	5.4937	0.1104	0.5590	1.3080	7.53E+00	6.28E-02	9.14E-01	1.49E+01	5.05E-02	5.66E-01
	30.53	5.1438	0.0794	0.3887	1.2327	6.80E+00	5.01E-02	9.40E-01	1.30E+01	3.59E-02	6.20E-01
	50.20	4.9184	0.0579	0.2770	1.1777	6.96E+00	3.40E-02	9.46E-01	1.75E+01	1.84E-02	5.80E-01
	69.84	4.6119	0.0451	0.2055	1.1462	1.11E+01	1.31E-02	9.18E-01	9.47E+02	3.20E-04	2.72E-01
	89.44	4.4386	0.0354	0.1574	1.1226	5.99E+01	1.33E-03	8.97E-01	1.49E+04	1.64E-05	2.10E-01
O_2	10.88	7.5521	0.0700	0.5061	1.2057	9.06E+00	5.22E-02	9.63E-01	1.42E+01	4.03E-02	7.17E-01
	30.52	7.1871	0.0498	0.3487	1.1508	7.95E+00	4.28E-02	9.84E-01	1.08E+01	3.44E-02	8.21E-01
	50.18	7.1182	0.0356	0.2503	1.1117	8.23E+00	2.91E-02	9.84E-01	1.26E+01	2.07E-02	7.87E-01
	69.81	7.2150	0.0259	0.1858	1.0837	9.29E+00	1.86E-02	9.80E-01	2.51E+01	7.77E-03	6.59E-01
	89.43	6.5520	0.0220	0.1439	1.0732	1.13E+01	1.11E-02	9.68E-01	1.00E+02	1.56E-03	4.86E-01
Ar	10.95	6.8653	0.0761	0.4963	1.2191	7.53E+00	6.53E-02	9.78E-01	9.61E+00	5.70E-02	8.20E-01
	30.54	6.5977	0.0533	0.3423	1.1617	7.68E+00	4.23E-02	9.75E-01	1.14E+01	3.25E-02	7.68E-01
	50.20	6.1755	0.0410	0.2494	1.1284	7.61E+00	3.04E-02	9.74E-01	1.32E+01	2.02E-02	7.27E-01
	69.81	5.7022	0.0327	0.1855	1.1077	1.16E+01	1.27E-02	9.45E-01	2.02E+02	1.09E-03	3.85E-01
	89.39	4.8961	0.0297	0.1455	1.1015	2.54E+01	3.74E-03	9.23E-01	1.34E+03	1.38E-04	2.92E-01

Table AV.37 - Adsorption isotherm model parameters for BPL for CO_2, N_2, O_2, and Ar at 10°C, 30°C, 50°C, 70°C, and 90°C. Associated equations are located in Methods section.

		Langmuir		Freundlich		Sips			Toth		
	T	q_s	β	k	n	q_s	β	n	q_s	β	t
	(°C)	mmol/g	Atm^{-1}	$\frac{mmol}{g\ atm}$		mmol/g	Atm^{-1}		mmol/g	Atm^{-1}	
CO_2	10.97	8.0333	0.5237	2.5451	1.9531	1.30E+01	1.49E-01	7.08E-01	2.60E+01	5.83E-01	3.49E-01
	30.54	6.9377	0.3662	1.7778	1.7620	1.17E+01	1.04E-01	7.41E-01	2.87E+01	2.70E-01	3.45E-01
	50.16	6.0386	0.2672	1.2517	1.6148	1.02E+01	8.29E-02	7.80E-01	2.79E+01	1.40E-01	3.62E-01
	69.77	5.3667	0.1987	0.8923	1.4951	8.83E+00	7.12E-02	8.22E-01	2.43E+01	8.33E-02	3.97E-01
	89.33	4.7956	0.1522	0.6432	1.4021	7.41E+00	6.57E-02	8.63E-01	1.91E+01	5.90E-02	4.49E-01
N_2	10.88	2.9902	0.1558	0.4087	1.4087	4.48E+00	7.11E-02	8.67E-01	1.03E+01	6.74E-02	4.73E-01
	30.52	2.7760	0.1105	0.2828	1.3088	3.87E+00	6.10E-02	9.10E-01	8.05E+00	4.81E-02	5.51E-01
	50.18	2.6346	0.0807	0.2022	1.2363	3.54E+00	4.96E-02	9.37E-01	6.98E+00	3.52E-02	6.08E-01
	69.81	2.5408	0.0599	0.1482	1.1854	4.34E+00	2.64E-02	9.23E-01	2.56E+01	7.53E-03	4.31E-01
	89.40	2.3212	0.0496	0.1136	1.1602	5.67E+00	1.38E-02	9.10E-01	6.00E+02	2.99E-04	2.56E-01
O_2	10.89	4.2137	0.0971	0.3816	1.2743	5.50E+00	6.11E-02	9.32E-01	1.01E+01	4.76E-02	6.13E-01
	30.52	3.8851	0.0708	0.2638	1.2094	4.99E+00	4.74E-02	9.51E-01	9.26E+00	3.32E-02	6.48E-01
	50.19	3.6678	0.0529	0.1895	1.1635	5.20E+00	3.14E-02	9.50E-01	1.45E+01	1.51E-02	5.71E-01
	69.82	3.4207	0.0416	0.1408	1.1345	6.78E+00	1.60E-02	9.34E-01	1.19E+02	1.50E-03	3.65E-01
	89.44	3.0268	0.0359	0.1086	1.1222	2.35E+01	2.59E-03	9.02E-01	2.15E+03	7.26E-05	2.47E-01
Ar	10.95	3.9464	0.0993	0.3645	1.2790	5.00E+00	6.58E-02	9.38E-01	8.43E+00	5.38E-02	6.42E-01
	30.53	3.6576	0.0734	0.2569	1.2161	4.66E+00	4.96E-02	9.51E-01	8.36E+00	3.58E-02	6.55E-01
	50.18	3.4386	0.0556	0.1860	1.1700	4.56E+00	3.61E-02	9.56E-01	9.68E+00	2.17E-02	6.32E-01
	69.78	3.2199	0.0437	0.1389	1.1394	5.39E+00	2.10E-02	9.43E-01	3.43E+01	4.83E-03	4.57E-01
	89.34	2.7959	0.0384	0.1069	1.1290	1.31E+01	5.00E-03	9.06E-01	1.43E+03	1.09E-04	2.52E-01

Table AV.38 - Adsorption isotherm model parameters for F-600 for CO_2, N_2, O_2, and Ar at 10°C, 30°C, 50°C, 70°C, and 90°C. Associated equations are located in Methods section.

		Langmuir		Freundlich		Sips			Toth		
	T	q_s	β	k	n	q_s	β	n	q_s	β	t
	(°C)	mmol/g	Atm^{-1}	$\frac{mmol}{g\ atm}$		mmol/g	Atm^{-1}		mmol/g	Atm^{-1}	
CO_2	10.96	6.1378	0.9192	2.5545	2.2981	8.32E+00	3.82E-01	7.16E-01	1.11E+01	1.43E+00	4.47E-01
	30.54	5.4752	0.5895	1.8389	2.0077	7.79E+00	2.31E-01	7.42E-01	1.18E+01	6.96E-01	4.32E-01
	50.18	4.9016	0.4021	1.3234	1.7961	7.10E+00	1.62E-01	7.78E-01	1.19E+01	3.58E-01	4.42E-01
	69.76	4.4200	0.2850	0.9527	1.6325	6.32E+00	1.27E-01	8.20E-01	1.11E+01	2.02E-01	4.73E-01
	89.34	3.9893	0.2099	0.6881	1.5076	5.64E+00	1.02E-01	8.55E-01	1.03E+01	1.25E-01	5.01E-01
N_2	10.87	2.7098	0.2012	0.4530	1.4937	3.85E+00	9.73E-02	8.57E-01	7.14E+00	1.16E-01	5.02E-01
	30.53	2.5437	0.1353	0.3075	1.3594	3.22E+00	8.68E-02	9.20E-01	5.00E+00	8.31E-02	6.34E-01
	50.20	2.3272	0.1022	0.2209	1.2873	2.96E+00	6.70E-02	9.35E-01	4.79E+00	5.74E-02	6.50E-01
	69.82	2.2857	0.0727	0.1599	1.2192	3.61E+00	3.50E-02	9.19E-01	1.35E+01	1.55E-02	4.73E-01
	89.41	2.0648	0.0597	0.1204	1.1872	4.06E+00	2.15E-02	9.11E-01	5.61E+01	3.07E-03	3.47E-01
O_2	10.87	3.4096	0.1352	0.4115	1.3581	4.30E+00	8.73E-02	9.21E-01	6.70E+00	8.31E-02	6.35E-01
	30.52	3.1724	0.0956	0.2832	1.2697	3.93E+00	6.59E-02	9.44E-01	6.19E+00	5.54E-02	6.75E-01
	50.21	2.8766	0.0751	0.2055	1.2170	3.23E+00	6.20E-02	9.73E-01	4.20E+00	5.41E-02	8.03E-01
	69.83	2.8788	0.0521	0.1468	1.1620	4.34E+00	2.83E-02	9.44E-01	1.57E+01	1.11E-02	5.21E-01
	89.43	2.5269	0.0445	0.1109	1.1425	4.64E+00	1.87E-02	9.35E-01	5.32E+01	2.61E-03	3.94E-01
Ar	10.90	3.0622	0.1442	0.3899	1.3759	3.80E+00	9.54E-02	9.22E-01	5.71E+00	9.33E-02	6.46E-01
	30.54	2.9253	0.0986	0.2684	1.2767	3.63E+00	6.78E-02	9.43E-01	5.71E+00	5.74E-02	6.71E-01
	50.20	2.8259	0.0707	0.1921	1.2119	4.15E+00	3.82E-02	9.31E-01	1.19E+01	2.02E-02	5.29E-01
	69.84	2.5767	0.0561	0.1415	1.1771	5.20E+00	1.97E-02	9.13E-01	9.39E+01	2.15E-03	3.35E-01
	89.41	2.4467	0.0436	0.1061	1.1452	1.07E+01	5.89E-03	8.97E-01	2.49E+03	6.93E-05	2.25E-01

Table AV.39 - Adsorption isotherm model parameters for M-30 for CO_2, N_2, O_2, and Ar at 10°C, 30°C, 50°C, 70°C, and 90°C. Associated equations are located in Methods section.

		Langmuir		Freundlich		Sips			Toth		
	T	q_s	β	k	n	q_s	β	n	q_s	β	t
	(°C)	mmol/g	Atm^{-1}	$\frac{mmol}{g\ atm}$		mmol/g	Atm^{-1}		mmol/g	Atm^{-1}	
CO_2	10.95	27.6699	0.1325	3.3064	1.3607	4.26E+01	5.95E-02	8.77E-01	1.13E+02	4.75E-02	4.62E-01
	30.54	23.5788	0.0954	2.1176	1.2774	3.96E+01	3.94E-02	8.91E-01	1.71E+02	1.89E-02	4.17E-01
	50.17	20.4426	0.0713	1.4050	1.2162	3.47E+01	3.08E-02	9.12E-01	1.89E+02	1.02E-02	4.21E-01
	69.78	18.2649	0.0545	0.9730	1.1700	2.87E+01	2.76E-02	9.37E-01	1.82E+02	6.74E-03	4.42E-01
	89.34	16.7640	0.0418	0.6922	1.1337	2.84E+01	1.99E-02	9.44E-01	2.17E+02	3.81E-03	4.42E-01
N_2	10.94	8.5159	0.0602	0.4968	1.1827	1.14E+01	3.83E-02	9.51E-01	2.57E+01	2.23E-02	6.09E-01
	30.53	8.0711	0.0446	0.3539	1.1395	1.06E+01	2.99E-02	9.64E-01	2.43E+01	1.60E-02	6.39E-01
	50.19	7.4567	0.0357	0.2637	1.1145	1.07E+01	2.18E-02	9.64E-01	3.39E+01	8.51E-03	5.85E-01
	69.84	7.5066	0.0268	0.2007	1.0887	1.31E+01	1.30E-02	9.61E-01	1.59E+02	1.42E-03	4.40E-01
	89.41	6.3251	0.0253	0.1599	1.0871	3.47E+01	3.13E-03	9.32E-01	2.49E+03	7.90E-05	2.91E-01
O_2	10.88	10.4704	0.0455	0.4667	1.1400	1.24E+01	3.56E-02	9.76E-01	2.05E+01	2.44E-02	7.41E-01
	30.53	10.7283	0.0303	0.3224	1.0966	1.30E+01	2.33E-02	9.81E-01	2.52E+01	1.34E-02	7.26E-01
	50.20	10.1310	0.0238	0.2396	1.0779	1.44E+01	1.51E-02	9.76E-01	5.69E+01	4.47E-03	5.91E-01
	69.84	10.2471	0.0179	0.1839	1.0631	1.14E+02	1.12E-03	9.45E-01	6.06E+02	3.33E-04	4.01E-01
	89.44	8.7385	0.0167	0.1467	1.0612	2.25E+02	4.22E-04	9.44E-01	4.24E+02	3.75E-04	4.15E-01
Ar	10.94	11.8071	0.0379	0.4410	1.1182	1.35E+01	3.15E-02	9.84E-01	2.06E+01	2.25E-02	7.88E-01
	30.53	10.9377	0.0294	0.3187	1.0940	1.35E+01	2.21E-02	9.81E-01	2.74E+01	1.22E-02	7.14E-01
	50.18	10.3564	0.0232	0.2390	1.0761	1.47E+01	1.48E-02	9.76E-01	6.29E+01	4.03E-03	5.82E-01
	69.78	10.1668	0.0181	0.1843	1.0621	2.77E+01	5.43E-03	9.61E-01	2.50E+02	7.93E-04	4.60E-01
	89.36	10.8806	0.0132	0.1449	1.0494	1.16E+02	9.20E-04	9.57E-01	4.38E+02	3.50E-04	4.44E-01

Table AV.40 - Adsorption isotherm model parameters for NZ-AC for CO_2, N_2, O_2, and Ar at 10°C, 30°C, 50°C, 70°C, and 90°C. Associated equations are located in Methods section.

		Langmuir		Freundlich		Sips			Toth		
	T	q_s	β	k	n	q_s	β	n	q_s	β	t
	(°C)	mmol/g	Atm^{-1}	$\frac{mmol}{g\ atm}$		mmol/g	Atm^{-1}		mmol/g	Atm^{-1}	
CO_2	10.95	15.9488	0.3249	3.7986	1.7129	3.04E+01	7.19E-02	7.28E-01	1.14E+02	1.79E-01	2.88E-01
	30.53	13.3967	0.2279	2.4835	1.5550	2.54E+01	5.85E-02	7.76E-01	1.08E+02	7.80E-02	3.11E-01
	50.16	11.3372	0.1720	1.6919	1.4518	2.29E+01	4.29E-02	8.01E-01	1.49E+02	3.29E-02	2.96E-01
	69.75	9.8328	0.1319	1.1799	1.3691	2.16E+01	3.13E-02	8.22E-01	2.57E+02	1.20E-02	2.74E-01
	89.31	8.4912	0.1061	0.8430	1.3096	1.91E+01	2.62E-02	8.45E-01	3.30E+02	5.77E-03	2.72E-01
N_2	10.88	4.7936	0.1103	0.4969	1.3291	1.95E+01	1.02E-02	7.95E-01	8.24E+04	5.10E-05	1.22E-01
	30.52	4.7355	0.0698	0.3201	1.2147	9.06E+00	2.52E-02	9.01E-01	9.30E+01	5.13E-03	3.55E-01
	50.18	4.5825	0.0503	0.2265	1.1590	7.81E+00	2.30E-02	9.34E-01	5.05E+01	5.56E-03	4.39E-01
	69.80	4.5895	0.0372	0.1699	1.1238	1.36E+01	8.64E-03	9.21E-01	2.16E+03	1.12E-04	2.58E-01
	89.38	3.7144	0.0360	0.1339	1.1248	1.25E+02	4.67E-04	8.92E-01	2.72E+04	8.08E-06	1.94E-01
O_2	10.93	5.4173	0.0890	0.4701	1.2915	1.21E+03	3.97E-05	7.75E-01	1.24E+06	3.47E-06	1.06E-01
	30.56	6.3425	0.0448	0.2802	1.1431	1.14E+01	1.93E-02	9.36E-01	1.15E+02	3.04E-03	4.06E-01
	50.23	5.5423	0.0377	0.2073	1.1236	1.27E+01	1.22E-02	9.32E-01	3.64E+02	7.27E-04	3.36E-01
	69.84	4.7674	0.0333	0.1593	1.1161	9.92E+01	7.86E-04	9.00E-01	4.53E+03	5.00E-05	2.43E-01
	89.44	2.6546	0.0398	0.1060	1.1392	2.07E+02	1.80E-04	8.79E-01	8.38E+03	2.13E-05	2.03E-01
Ar	10.99	7.1449	0.0575	0.4001	1.1767	1.04E+01	3.24E-02	9.43E-01	3.17E+01	1.50E-02	5.42E-01
	30.57	6.6817	0.0421	0.2772	1.1328	9.37E+00	2.60E-02	9.60E-01	2.73E+01	1.13E-02	5.88E-01
	50.21	6.6510	0.0306	0.2013	1.0973	7.95E+00	2.40E-02	9.83E-01	1.38E+01	1.52E-02	7.55E-01
	69.82	6.2344	0.0245	0.1524	1.0810	1.01E+01	1.31E-02	9.68E-01	8.23E+01	2.02E-03	4.90E-01
	89.39	5.6086	0.0214	0.1203	1.0732	1.57E+01	6.07E-03	9.53E-01	8.74E+01	1.49E-03	4.84E-01

Table AV.41 - Adsorption isotherm model parameters for OLC for CO_2, N_2, O_2, and Ar at 10°C, 30°C, 50°C, 70°C, and 90°C. Associated equations are located in Methods section.

		Langmuir		Freundlich		Sips			Toth		
	T	q_s	β	k	n	q_s	β	n	q_s	β	t
	(°C)	mmol/g	Atm^{-1}	$\frac{mmol}{g\ atm}$		mmol/g	Atm^{-1}		mmol/g	Atm^{-1}	
CO_2	10.97	8.5869	0.7551	3.2669	2.1648	1.18E+01	3.13E-01	7.31E-01	1.63E+01	1.04E+00	4.48E-01
	30.55	7.6395	0.4890	2.3171	1.9019	1.10E+01	1.92E-01	7.58E-01	1.77E+01	5.04E-01	4.33E-01
	50.20	6.8064	0.3369	1.6440	1.7106	1.00E+01	1.35E-01	7.92E-01	1.81E+01	2.59E-01	4.39E-01
	69.80	6.1223	0.2417	1.1747	1.5645	8.94E+00	1.06E-01	8.31E-01	1.71E+01	1.48E-01	4.66E-01
	89.37	5.5677	0.1776	0.8442	1.4490	7.97E+00	8.65E-02	8.67E-01	1.58E+01	9.29E-02	5.00E-01
N_2	10.88	3.5268	0.1795	0.5402	1.4552	5.12E+00	8.49E-02	8.62E-01	1.03E+01	9.25E-02	4.91E-01
	30.51	3.3535	0.1206	0.3677	1.3283	4.27E+00	7.75E-02	9.25E-01	6.84E+00	7.04E-02	6.35E-01
	50.18	3.1405	0.0880	0.2602	1.2521	3.88E+00	6.14E-02	9.48E-01	6.09E+00	5.07E-02	6.85E-01
	69.79	3.1131	0.0630	0.1899	1.1915	4.48E+00	3.57E-02	9.40E-01	1.24E+01	1.84E-02	5.51E-01
	89.41	2.7332	0.0532	0.1427	1.1684	5.15E+00	2.09E-02	9.22E-01	5.93E+01	3.21E-03	3.74E-01
O_2	10.89	4.6333	0.1154	0.4882	1.3151	5.81E+00	7.67E-02	9.32E-01	9.15E+00	6.84E-02	6.51E-01
	31.21	4.3304	0.0797	0.3273	1.2297	5.09E+00	6.11E-02	9.63E-01	7.35E+00	5.08E-02	7.40E-01
	50.17	4.0779	0.0596	0.2351	1.1779	4.65E+00	4.87E-02	9.76E-01	6.43E+00	3.96E-02	7.90E-01
	69.80	3.8293	0.0459	0.1720	1.1416	4.66E+00	3.44E-02	9.73E-01	7.83E+00	2.36E-02	7.29E-01
	89.39	3.7863	0.0341	0.1283	1.1122	8.37E+00	1.18E-02	9.39E-01	2.30E+02	6.90E-04	3.49E-01
Ar	10.95	4.7511	0.1091	0.4761	1.2999	5.74E+00	7.77E-02	9.44E-01	8.16E+00	7.14E-02	7.05E-01
	30.54	4.3882	0.0790	0.3289	1.2280	5.11E+00	6.13E-02	9.64E-01	7.26E+00	5.14E-02	7.50E-01
	50.17	4.2271	0.0572	0.2345	1.1718	4.84E+00	4.65E-02	9.76E-01	6.88E+00	3.69E-02	7.81E-01
	69.75	4.0776	0.0428	0.1712	1.1325	4.76E+00	3.42E-02	9.79E-01	7.60E+00	2.39E-02	7.60E-01
	89.36	3.9380	0.0330	0.1290	1.1067	6.00E+00	1.87E-02	9.62E-01	2.98E+01	4.82E-03	5.23E-01

AV.7. Comparison of CO_2 and N_2 BPL Isotherms to Literature

Adsorption isotherm data were given for BPL carbon for the gases used in this study in figures from Sircar and Golden (2000) as well as McEwen et al. (2013). These figures were converted from images to graphical data points using a web plot digitalizer app at "https://apps.automeris.io/wpd/" and fitted to Sips isotherm. The isotherm parameters are presented in Table AV.42.

Table AV.42 – Sips adsorption isotherm parameters used for comparison modeled from literature data for BPL.

		Sips			
Gas	T	q_s	β	n	Ref.
	°C	mmol/g	Atm^{-1}		
CO_2	30	12.34	0.0968	0.7594	Sircar and Golden (2000)
N_2	30	5.547	0.0339	0.8959	
CO_2	25	16.76	0.0656	0.7168	McEwen et al (2013)
N_2	25	7.894	0.0412	1.0285	

AV.8. Selectivity (CO_2/N_2 Adsorption Capacity)

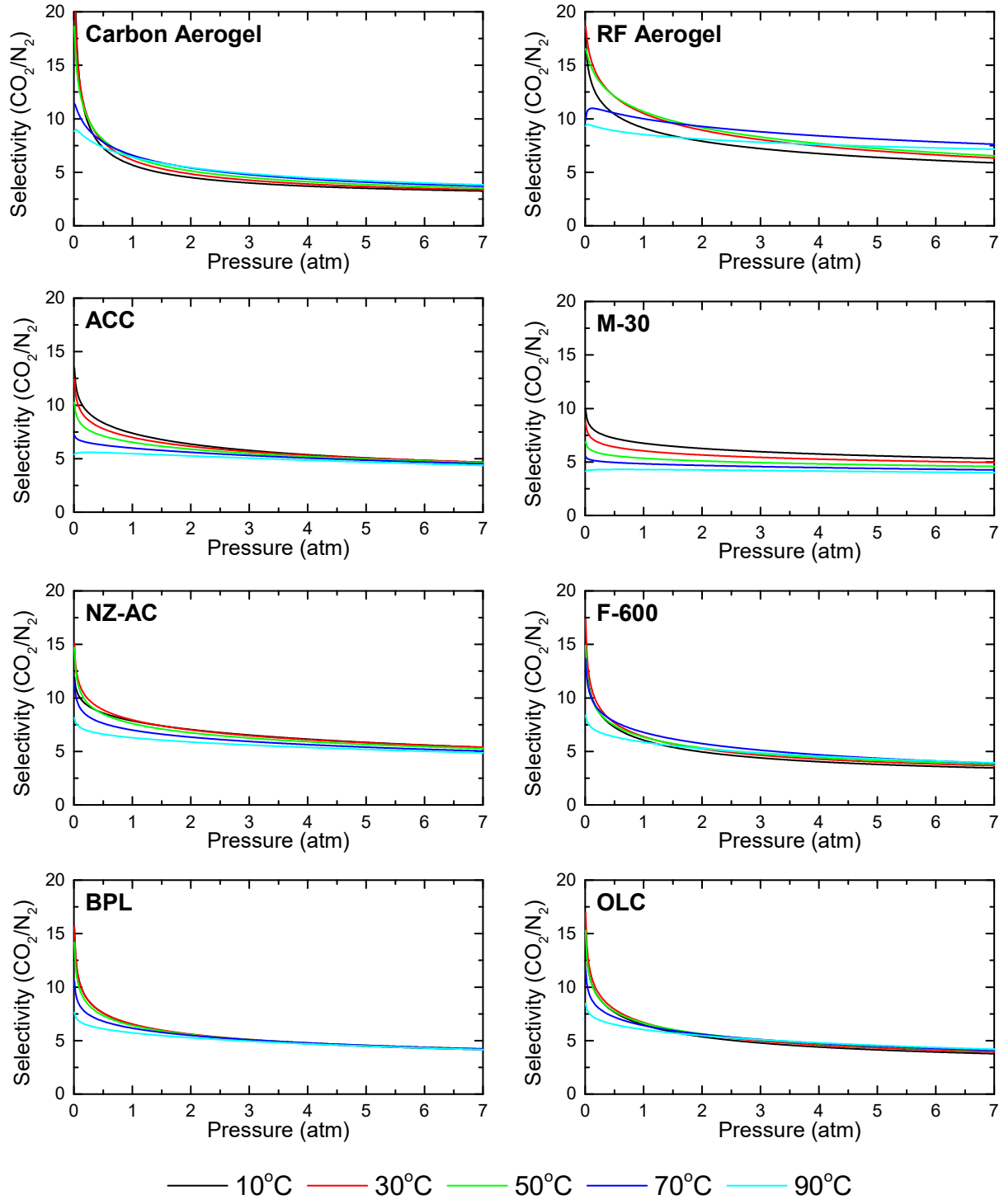

Figure AV.4 – Adsorption selectivity of CO_2 over N_2 for the carbon adsorbents tested in this study at 10°C, 30°C, 50°C, 70°C, and 90°C.

AV.9. Pore Size, Surface Area, and %Oxidation

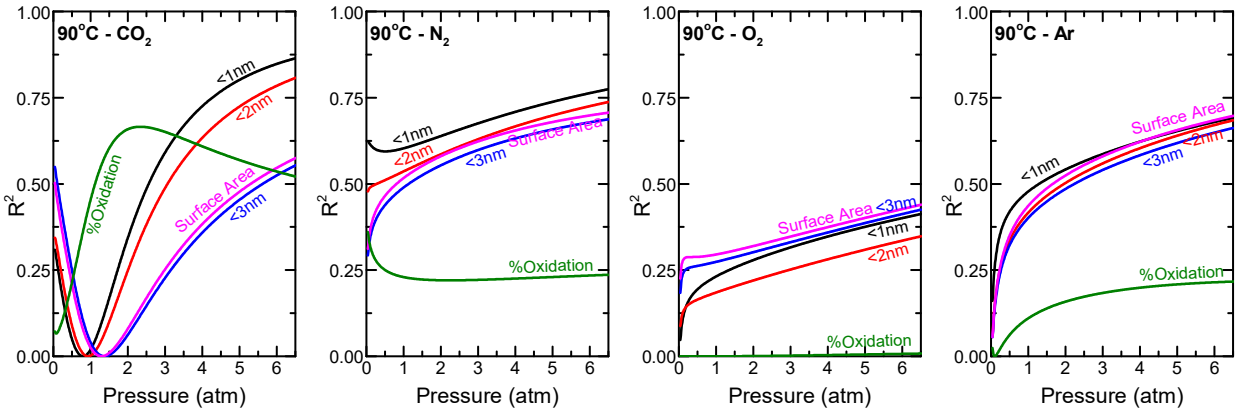

Figure AV.5 – Coefficient of determination with respect to pressure between adsorption capacity (CO_2, N_2, O_2, and Ar) at 90°C and five parameters: cumulative pore size <1 nm, <2nm, and <3nm, surface area, and %oxidation.

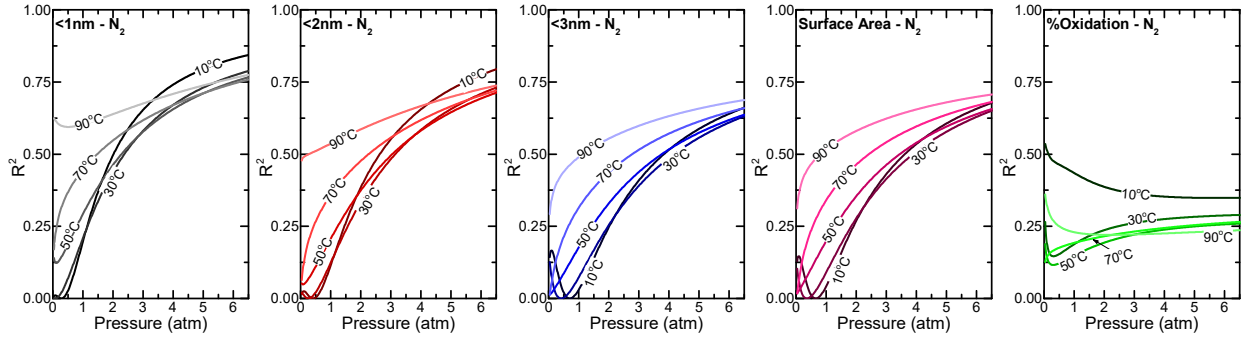

Figure AV.6 – Effect of temperature on the coefficient of determination with respect to pressure between adsorption capacity of N_2 and five parameters: cumulative pore size <1 nm, <2nm, and <3nm, surface area, and %oxidation.

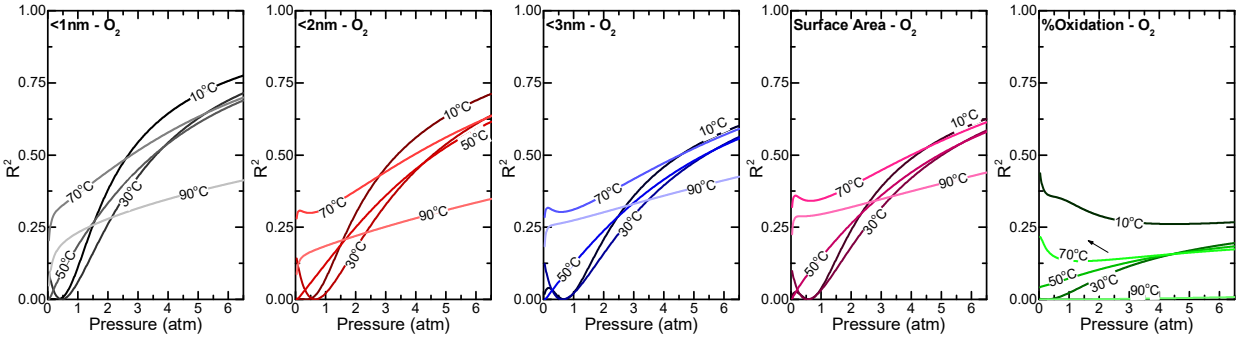

Figure AV.7 – Effect of temperature on the coefficient of determination with respect to pressure between adsorption capacity of O_2 and five parameters: cumulative pore size <1 nm, <2nm, and <3nm, surface area, and %oxidation.

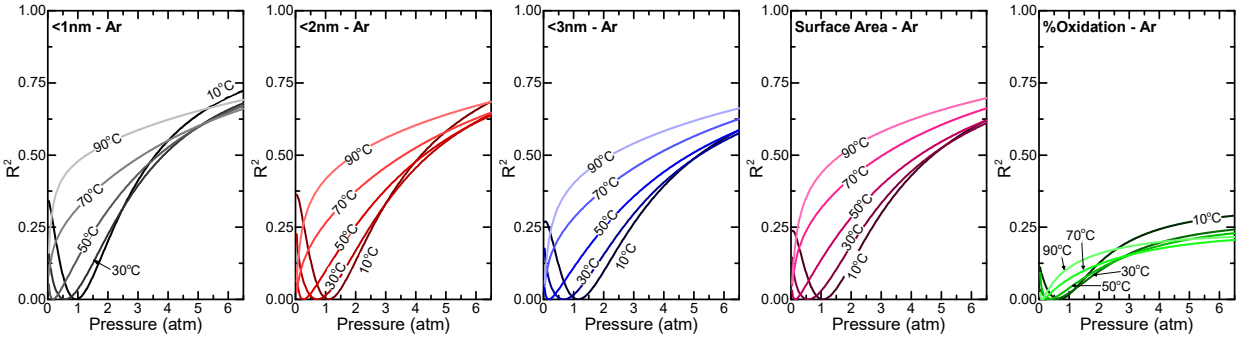

Figure AV.8 – Effect of temperature on the coefficient of determination with respect to pressure between adsorption capacity of Ar and five parameters: cumulative pore size <1 nm, <2nm, and <3nm, surface area, and %oxidation.

AV.10. Temperature Dependant Toth (TD-Toth)

Table AV.43 – The fitted parameters for the empirical TD-Toth model for carbons in this study for CO_2, N_2, O_2, and Ar adsorption. T_0 is equal to 284 K.

		q_{so}	β_o	Q/RT_0	t_o	α	χ
		(mmol/g)	(atm^{-1})				
Carbon Aerogel	CO_2	1.118E+01	4.360E+00	1.333E+01	3.318E-01	6.136E-02	-5.952E-01
	N_2	4.345E+00	1.815E-01	7.684E+00	5.875E-01	2.256E-01	7.041E-02
	O_2	5.936E+00	1.241E-01	8.382E+00	5.851E-01	6.290E-02	-6.348E-01
	Ar	7.329E+00	1.226E-01	1.064E+01	4.908E-01	1.490E-01	-1.725E+00
RF Aerogel	CO_2	3.046E+02	7.664E-01	2.766E+01	1.282E-01	4.128E-02	-6.557E+00
	N_2	6.396E+01	7.699E-03	3.647E+01	2.212E-01	-4.882E-01	-2.483E+01
	O_2	4.657E+04	2.598E-05	3.083E+00	1.204E-01	7.487E-02	3.440E+00
	Ar	1.552E+01	1.188E-02	6.977E+00	4.082E-01	3.987E-03	0.000E+00
ACC	CO_2	3.023E+01	3.343E-01	1.100E+01	5.070E-01	-1.361E-01	-1.082E+00
	N_2	1.559E+01	4.884E-02	7.656E+00	5.562E-01	2.269E-01	-5.494E-01
	O_2	1.330E+01	4.264E-02	6.922E+00	7.379E-01	8.955E-02	-5.469E-01
	Ar	1.027E+01	5.356E-02	6.255E+00	7.949E-01	-8.200E-02	-1.244E-01
BPL	CO_2	2.566E+01	5.880E-01	1.232E+01	3.507E-01	1.826E-02	-1.178E+00
	N_2	9.400E+00	7.191E-02	9.178E+00	4.923E-01	1.535E-01	-1.255E+00
	O_2	1.046E+01	4.619E-02	7.020E+00	6.046E-01	1.134E-01	-3.186E-01
	Ar	8.926E+00	5.119E-02	5.960E+00	6.274E-01	2.556E-01	4.129E-01
F-600	CO_2	1.112E+01	1.434E+00	1.156E+01	4.450E-01	-6.629E-03	-4.803E-01
	N_2	6.292E+00	1.243E-01	9.556E+00	5.370E-01	3.282E-02	-1.338E+00
	O_2	6.497E+00	8.461E-02	6.650E+00	6.463E-01	2.552E-01	3.217E-01
	Ar	6.044E+00	8.908E-02	7.567E+00	6.284E-01	2.302E-01	-2.867E-01
M-30	CO_2	1.218E+02	4.486E-02	1.030E+01	4.489E-01	2.592E-02	-1.278E+00
	N_2	2.675E+01	2.147E-02	6.022E+00	6.025E-01	1.565E-01	-2.208E-01
	O_2	2.257E+01	2.219E-02	7.096E+00	7.204E-01	-2.453E-02	-1.153E+00
	Ar	2.600E+01	1.803E-02	5.254E+00	7.244E-01	8.909E-02	4.898E-02
NZ-AC	CO_2	1.085E+02	1.812E-01	1.438E+01	2.938E-01	-1.730E-03	-2.588E+00
	N_2	5.034E+02	2.753E-03	1.860E+01	2.263E-01	1.499E-01	-7.077E+00
	O_2	5.772E+03	2.265E-04	1.266E+01	1.831E-01	1.818E-01	-2.280E+00
	Ar	2.819E+01	1.662E-02	7.513E+00	5.630E-01	1.170E-01	-1.112E+00
OLC	CO_2	1.640E+01	1.047E+00	1.162E+01	4.455E-01	-4.825E-02	-7.583E-01
	N_2	8.762E+00	1.020E-01	9.506E+00	5.318E-01	1.473E-01	-1.271E+00
	O_2	8.584E+00	7.169E-02	7.413E+00	6.730E-01	9.071E-02	-3.708E-01
	Ar	8.169E+00	7.139E-02	6.820E+00	7.043E-01	1.347E-01	-8.237E-02